Top quark pair production in proton antiproton collisions

Top quark pair production in proton antiproton collisions

ACADEMISCH PROEFSCHRIFT

ter verkrijging van de graad van doctor
aan de Universiteit van Amsterdam
op gezag van de Rector Magnificus
prof.mr. P.F. van der Heijden
ten overstaan van
een door het college voor promoties ingestelde commissie,
in het openbaar te verdedigen
in de Aula der Universiteit
op Vrijdag 1 april 2005, te 14:00 uur

door

Freya Blekman

geboren te Amsterdam

Promotores: Prof.dr. M.W.J.M. Demarteau
Prof.dr. F.L. Linde

Co-promotor: Dr. M. Vreeswijk

Faculteit der Natuurwetenschappen, Wiskunde en Informatica

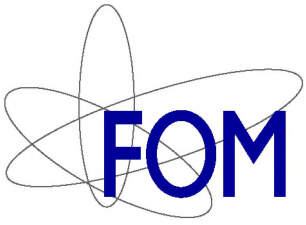

The work described in this thesis is part of the research programme of the 'Nationaal Instituut voor Kernfysica en Hoge-Energie Fysica' (NIKHEF) in Amsterdam, the Netherlands.
The author was financially supported by the 'Stichting voor Fundamenteel Onderzoek der Materie' (FOM).

ISBN 90-646-4135-8.

voor Henk en Ineke

Contents

Acknowledgments **155**

Introduction

By nature, Homo Sapiens is curious. We take an interest in our surroundings and try to understand what they are made of. Today, our curiosity has led to an understanding of the world around us that is astoundingly accurate: particle physics predicts the behavior of things that are invisible to the naked eye, but also invisible with most tools like microscopes.

In the search to understand the world around us, we have evolved from believing that the world was made of four building blocks; the elements water, fire, air and earth. This was an established point of view for ancient Greeks and Romans. Even in the Middle Ages, people still commonly believed the world solely consisted of these four elements.

In the 18^{th} and 19^{th} century people found out that the building blocks of matter came in a multitude of flavors, called (again) elements. After the discovery of the atom, early 20^{th} century, scientists discovered that elements are not elementary at all: the atom is made of electrons and a nucleus, which contains protons and neutrons. The number of protons in the atom determines the type of element.

The twentieth century has been very eventful in the perspective from the description of the matter in our universe. In the 1960s, it was discovered that even neutrons and protons were not elementary; they are made of particles called quarks. Almost all matter around us is made of quarks called up (u) and down (d), and electrons (e). There are also electron neutrinos (ν_e), which are created in radio-active processes like β-decay. This set of four particles together is called a generation. In the 1970s and 1980s it was discovered that there are three generations of quarks and leptons. The second and third generations are similar to the first, but heavier. The higher-generation particles eventually decay to their lighter counterparts, which is why the matter around us mainly consists of the lightest generation. Or, at least, that is the status at the start of the 21^{st} century. The behavior, the 'physics', of elementary particles is described by physics theory. This theory is very convincing, it is possible to verify the predictions up to great accuracy. Chapter 1 of this thesis gives an overview of the present theory, which is called the Standard Model.

In their search for smaller and smaller constituents of matter, physicists have become more and more dependent on technology. The curiosity for the minute particles has led to the development of intricate tools, tools that shoot particles against other particles and record the effect of these collisions. Such a tool is called a particle accelerator, and the result of the collisions is studied by gigantic detectors that enclose the collision point, looking for the remnants of elementary particle collisions.

In fact, only very few of these particle accelerators are able to probe up to the energies needed to test the predictions of the Standard Model. Chapter 2 of this thesis describes

one of the particle accelerators (the Tevatron, near Chicago, USA) and the detector (called DØ) that is used to study the remnants of proton-antiproton collisions. Chapter 3 describes the event reconstruction from the output of the DØ detector. These events are used to test the Standard Model.

Chapters 4 through 7 describe a measurement of the production rate of one of the particles that is currently regarded as being truly elementary: the top quark (t), the heaviest quark in the third generation. Top quarks are rarely produced, and there are background processes which completely overwhelm the signal: there are in the order of 10^6 background events for every $t\bar{t}$ event. The analysis mostly concentrates on rejecting collisions where *no* top quarks were made.

Top quarks decay to a W boson and a b quark, which leads to a typical event signature. Only $t\bar{t}$ events where both W bosons decay to quarks are considered, this is called the $t\bar{t}$ to all-jets channel. Detecting the presence of a b quark and exploiting the top event signature reduces the background to an acceptable level. The silicon tracker is used to detect the (long lived) decay products of the b. This thesis describes the first measurement that uses this method in the $t\bar{t}$ to all-jets channel with the DØ detector.

After rejection of the remaining background collisions the number of top quarks is counted, and the result is compared to the theoretical predictions.

Chapter 1

Theory

1.1 The Standard Model of particle physics

Modern physics at a sub-nuclear scale is described by relativistic quantum field theory. A particular model that has been extremely successful is called the Standard Model (SM). The SM and particle physics theory in general have been described in a multitude of textbooks [1, 2, 3], so only a short overview of the issues relevant to this thesis will be presented here.

The SM encompasses different types of particle interactions, of which the electromagnetic is the most commonly known. The electro-magnetic force, described by Quantum Electro Dynamics (QED), and the weak force are combined in the electroweak sector of the SM. The strong nuclear force is described in the SM by the field theory called Quantum Chromo Dynamics (QCD).

Quarks and Leptons

In quantum field theory elementary particles are described by spinors[1]. Spin $\frac{1}{2}\hbar$ spinors describe the fermions and can be used to represent the leptons $\ell = e, \nu_e, \mu, \nu_\mu, \tau, \nu_\tau$ and quarks $q = d, u, s, c, b, t$. Requiring the Lagrangian of the quantum fields to be invariant under gauge transformation of several symmetry groups leads to a natural description of elementary particles and their interactions. Gauge bosons are described by spin $1\hbar$ spinors and are the mediators of the interactions.

Requiring that the theory is invariant under transformation of the $SU(3) \otimes SU(2)_L \otimes U(1)$ symmetry groups, each with its own coupling constant, leads to a quantum description of the strong and electroweak interaction. The group $SU(3)$, with coupling constant α_S (the strong coupling constant), describes the strong force or Quantum Chromo Dynamics (QCD) mediated by eight different gauge bosons called gluons, g. The groups $SU(2)_L \otimes U(1)$, with coupling constants equivalent to G_F (the Fermi constant) and α (the fine structure constant), describe the electroweak interactions, mediated by the gauge bosons W and Z for the weak force and the photon γ for the electromagnetic force. The

[1] Enrico Fermi first defined the field-theory for half-integer spin particles. Satyendranath Bose worked on whole-integer spin particle fields. Paul Dirac introduced the terms bosons and fermions.

quarks participate in all three interactions. The charged leptons only experience the electroweak force. The neutrinos only interact through the weak force.

The coupling strength of the interactions is different for QCD, weak and electromagnetic interactions. The coupling constants G_F, α and α_S change as a function of the energy scale in the particle interaction, and in some speculative extensions of the SM there exists a certain scale where the coupling constants are expected to be identical. The idea that all forces in the SM can be combined into one force is obviously very compelling, but currently has not been proven. The value of this 'Grand Unification' scale where the three couplings are unified to one coupling is not exactly known. The predictions depend on models which use measurements as input.

Antimatter, generations and mixing

Quarks and leptons all have their own antiparticle, which is represented by the same symbol but carries a bar above it, so the antiparticle of the top quark t is the $\bar{t}$. Antiparticles have the same mass but opposite quantum numbers.

The quarks are grouped into the generations (u, d), (c, s) and (t, b). The generations for leptons are (e, ν_e), (μ, ν_μ) and (τ, ν_τ). Each generation of quarks or leptons replicates quark and lepton properties with one exception: the mass is completely different from generation to generation. Lepton interactions are characterized by the conservation of lepton number, where each (anti-)particle from a generation is assigned a unique lepton number of $(-)1$. For instance $\mu \rightarrow \bar{\nu}_e \nu_\mu e$ decay is only possible by the creation of the additional two neutrinos.

Weak interactions between quarks from different generations are common. The quark mass eigenstates are not the same as the weak eigenstates. The weak decay of a quark to a quark of another flavor is governed by a 3×3 mixing matrix named the CKM matrix, after Cabibbo, Kobayashi and Maskawa.

Composite objects

In QCD the equivalent of electric charge is called 'color'. Color is used to define three different possible states: red, blue and green. Leptons do not have color. Color interactions are mediated by the gluons g. There are 8 different color interactions possible, so there are 8 gluons. Quarks and gluons cannot exist as free particles in nature. All free particles in nature are color neutral. The SM predicts that unbound quarks will connect to other unbound quarks and form composite objects. It is possible to construct composite fermions and bosons from quarks. The half integer spin bound states (fermions) are called baryons, and consist of bound states of three valence quarks. The integer spin bound states (bosons) are called mesons and consist of systems of a valence quark-antiquark pair.

Higgs mechanism

When, locally, the gauge invariance of the electroweak $SU(2)_L \otimes U(1)$ symmetry group is broken, the quarks, leptons and gauge bosons acquire mass. The method used for

electroweak symmetry breaking is called the Higgs mechanism. The success of this method is already shown from the fact that, in the electroweak sector, only one gauge boson remains massless: the photon. The Higgs mechanism thus transforms the SM to a theory that describes what we observe in nature: the gauge bosons W and Z *are* massive, the photon is massless. The Higgs mechanism also gives rise to an additional massive boson called the Higgs boson.

The SM has been shown to be predictive and agrees with the experimental data in many respects. All but one of the predicted particles have been observed: The last missing particle, the Higgs boson, has not been observed, and it is being searched for actively by the particle physics community.

The Higgs boson interacts with the quarks and leptons in the SM. In the interaction, the quarks and leptons acquire mass. The strength of the interaction is dependent on the mass of the fermion. As the heaviest known elementary particle, the top quark has the strongest coupling to the Higgs boson. Hence, accurate measurements of top quark properties are used as one of the inputs for an indirect measurement of the Higgs mass, as will be discussed in Section 1.4.

Standard Model parameters

If only three generations of quarks and leptons are included, the SM describes the behavior of strong and electroweak reactions between 25 particles: Six quarks; six leptons; twelve gauge bosons and the Higgs boson. If neutrinos are considered massless, the basic SM interactions are described by 19 parameters: The vacuum expectation and self-coupling of the Higgs field (v and λ); the nine fermion masses (m_i); the weak mixing angle ($\sin\theta_W$); the coupling constants of the three fundamental interactions (g_S, g and g') and four parameters used to describe the CKM quark mixing matrix[2].

Not all of these parameters can be measured directly, so usually more convenient parameters are used. For instance, at tree-level g, g' and v can be transformed into accurately measurable parameters like the aforementioned α and G_F structure constants, and the mass of the Z boson M_Z:

$$\alpha = \frac{1}{4\pi}\frac{g^2 g'^2}{g^2 + g'^2} = 7.297352568(24) \cdot 10^{-3}; \tag{1.1}$$

$$G_F = \frac{1}{v^2\sqrt{2}} = 1.16637(1) \cdot 10^{-5}\ \text{GeV}^{-2}; \tag{1.2}$$

and

$$M_Z = \frac{v}{2}\sqrt{g^2 + g'^2} = 91.1876(21)\ \text{GeV}, \tag{1.3}$$

where the uncertainties in the last digits are given in parentheses [9], and $\hbar = c = 1$. Analyses which compare precision measurements of one SM parameter to predictions derived from the remaining parameters are called 'Standard Model fits'.

[2]Including massive neutrino adds three more mass parameters and an additional mixing matrix, similar to the CKM matrix but describing the difference between the neutrino mass and electroweak eigenstates.

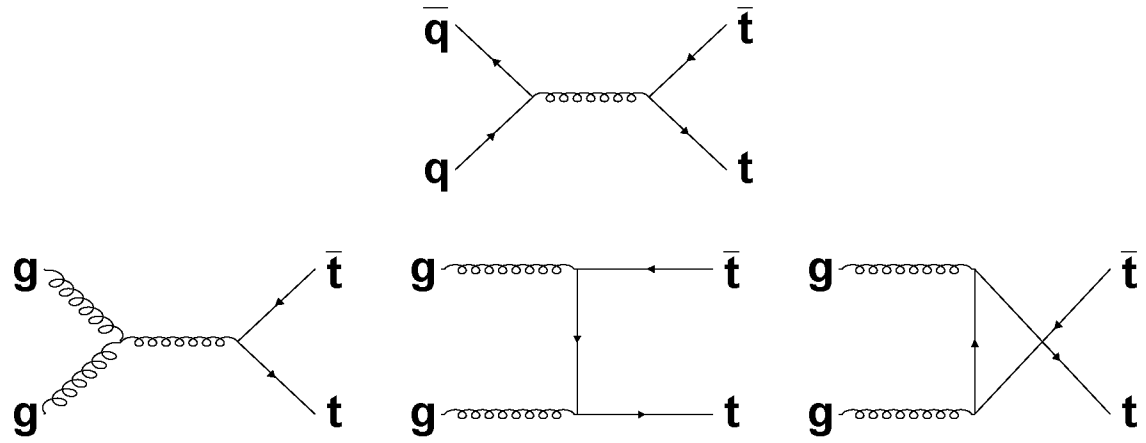

Figure 1.1: *The leading order Feynman diagrams for $t\bar{t}$ production.*

1.2 Top quark production

In hadron collisions, the top quark is primarily produced via the strong interaction. The Tevatron collides protons (p) on antiprotons ($\bar{p}$).

The cross section for $p\overline{p} \rightarrow t\bar{t}$ at a $p\overline{p}$ invariant mass of $\sqrt{s}$ can be written as:

$$\sigma_{t\bar{t}} = \sum_{a,b} \int \mathrm{d}x_a \, \mathrm{d}x_b \, f_a^p(x_a, \mu^2) f_b^{\bar{p}}(x_b, \mu^2) \, \hat{\sigma}(ab \rightarrow t\bar{t}; \hat{s}, \mu^2, m_t), \tag{1.4}$$

where the summation over indices a and b runs over either light quarks or gluons in the proton (a) and antiproton (b). Here μ^2 is an energy scale, to be discussed in detail further on in this section. $\hat{\sigma}$ is the cross section at parton level, where a and b are the partons that carry a fraction x_a and x_b of the (anti-)proton momentum, respectively. Both $\hat{\sigma}$ and σ depend on the top quark mass, m_t [4].

The parton momenta inside the (anti-)proton are described by the parton distribution functions f_a^p and $f_b^{\bar{p}}$. The light quark masses are considered negligible with respect to the top quark mass. The parton-level cross section $\hat{\sigma}$ depends on the energy of the parton-parton interaction, $\sqrt{\hat{s}} = \sqrt{x_a x_b s}$. At leading order, there are only a few processes which contribute to $\hat{\sigma}$:

$$q \, + \, \overline{q} \, \rightarrow \, t \, + \, \overline{t} \, , \tag{1.5}$$

quark-antiquark annihilation, and

$$g \, + \, g \, \rightarrow \, t \, + \, \overline{t} \, , \tag{1.6}$$

when gluons fuse to produce top quarks in the final state. Figure 1.1 shows the leading order Feynman diagrams, and Table 1.1 lists the relative contributions of both processes.

The cross section σ also depends on the factorization and renormalization scale. The latter is introduced during the renormalization procedure. The factorization scale comes from the splitting (factorizing) of the perturbative ($\hat{\sigma}$) and non-perturbative parts (f_a^p, $f_b^{\bar{p}}$)

	$q\bar{q} \rightarrow t\bar{t}$	$gg \rightarrow t\bar{t}$
Tevatron ($\sqrt{s}$ = 1.8 TeV $p\bar{p}$)	90 %	10 %
Tevatron ($\sqrt{s}$ = 2.0 TeV $p\bar{p}$)	85 %	15 %
LHC ($\sqrt{s}$ = 14 TeV pp)	10 %	90 %

Table 1.1: *Theoretical predictions for the relative contributions from the quark-antiquark annihilation and gluon fusion processes in $t\bar{t}$ production at the Tevatron and LHC [7].*

	$\sqrt{s}$ = 1.8 TeV		$\sqrt{s}$ = 2.0 TeV	
$\mu = \mu_F = \mu_R$	NLO [pb]	NNLO [pb]	NLO [pb]	NNLO [pb]
$\mu/c^2 = m_t/2$	5.4	6.4	7.4	8.9
$\mu/c^2 = m_t$	5.2	6.3	7.1	8.8
$\mu/c^2 = 2m_t$	4.7	6.3	6.5	8.8

Table 1.2: *Theoretical predictions for the top pair production cross section at NLO and NNLO. The same energy scale μ is used for the factorization, μ_F, and renormalization, μ_R, scale.*

of the cross section. As both scales are arbitrary, the same scale, μ, is used for both. A common choice for μ is the energy needed at production threshold per parton ($\mu = m_t c^2$). The uncertainty that is created by the choice of energy scale is estimated by varying μ over an arbitrary range, such as $\frac{1}{2}m_t < \mu/c^2 < 2m_t$. In the ideal case, there should be no dependence on μ in the final result, as the renormalization and factorization scales have no physical significance.

With the extension of the Feynman diagrams, e.g. involving gluon radiation in the initial and final state, the theoretical prediction of the $t\bar{t}$ cross section has been calculated up to Next-to-Leading-Order (NLO) and even Next-to-Next-to-Leading-Order (NNLO, or order $(\alpha_s)^4$) precision [5, 6]. The predictions for a top mass of 175 GeV/c^2 and $\sqrt{s}$ of 1.8 and 2.0 TeV are listed in Table 1.2.

Top production at future colliders

For a comparison, the $t\bar{t}$ cross section at the next collider, the Large Hadron Collider (LHC) will also be briefly discussed here. The LHC will collide protons on protons, with an interaction energy of $\sqrt{s} = 14$ TeV. The NLO prediction for the $t\bar{t}$ production cross section at the LHC is $\sigma_{t\bar{t}} = 800 \pm 150$ pb. Table 1.1 lists the relative contribution of the two different production processes, which change from the Tevatron to the LHC. To understand this change, one has to remember that the parton content in the proton changes as a function of $x_{a/b}$ in Equation 1.4 [3]. As the LHC will collide protons, this effect

[3] At large x, only the u, d valence quarks of the proton are probed. If there is more energy available in the interaction, the x needed for production will drop, and gluon and quark pairs from vacuum interactions will also be probed. For top production at threshold, at the Tevatron $x_{a/b} \approx 0.18$, while at the LHC $x_{a/b} \approx 0.025$.

is amplified by the absence of anti-valence quarks in the interaction. Consequently, at the LHC the relative gluon contribution in the proton-proton interaction is significantly larger than in the $p\overline{p}$ collisions at the Tevatron.

1.3 Top decay

Top quarks are expected to decay through the process

$$t \rightarrow W^{+}b \text{ (or } \bar{t} \rightarrow W^{-}\bar{b}) \ , \tag{1.7}$$

for which the branching fraction is nearly 100%. The top decay to Ws and Wd is suppressed by the square of the CKM matrix elements V_{ts} and V_{td}. With the SM prediction of $V_{tb} : V_{ts} : V_{td} = 0.99 : 0.04 : 0.01$ [9], the decay is dominated by V_{tb}.

The SM predicts the top quark decay width to be [10, 9]:

$$\Gamma_t = \frac{G_F m_t^3}{8\pi\sqrt{2}} \left(1 - \frac{M_W^2}{m_t^2}\right)^2 \left(1 + 2\frac{M_W^2}{m_t^2}\right)^2 \left[1 - \frac{2\alpha_s}{3\pi}\left(\frac{2\pi^2}{3} - \frac{5}{2}\right)\right]. \tag{1.8}$$

Terms of order m_b^2/m_t^2, α_S^2 and $(\alpha_S/\pi)M_W^2/m_t^2$ and higher are neglected. When the higher order electroweak and order α_S^2 QCD corrections are included, the overall theoretical uncertainty of Γ_t is less than 1%. Using accurately measured [9] values for G_F, α_s and M_W, and $m_t = 175$ GeV/c^2, this leads to a width of the order of 1.5 GeV/c^2. Because of the large width, and corresponding short lifetime (in the order of 10^{-24} s) , the top quark is expected to decay before it can hadronize to top-flavored hadrons or $t\bar{t}$ mesons (toponium).

The b quarks from $t \rightarrow Wb$ decay

The presence of b quarks in $t\bar{t}$ events is a distinguishing signature for top quark production. Direct (QCD) $b\bar{b}$ production tends to produce b quark pairs that have a rapidly falling energy spectrum [12]. The b quarks from the decay of the top quarks, on the other hand, are much more energetic since they come from the decay of a single massive particle. As will be shown in Figure 4.10, the transverse energy (E_T) of the b quarks from top decays peaks around 50 GeV, and even larger transverse energies can be observed.

1.3.1 Top decay channels

With the top quark's CKM preferred decay to Wb pairs, there is a limited number of final states possible. Hence, top final states are classified by the decay products of the W boson. W bosons can decay to leptons and quarks. Rougly, the probability for a W boson to decay to quarks is 2/3, while the remaining 1/3 of the W boson decays has leptons in the final state. The experimental numbers differ slightly [9]; the quark contribution is increased by QCD effects.

So-called 'jets' of particles from quark hadronization are used as the experimental signature for energetic light and b quarks. For $t\bar{t}$ production, three classes of final states are distinguished:

decay channel	W boson decays		branching fraction [%]
dilepton	$\ell\nu_\ell$	$\ell\nu_\ell$	10.27 $\pm$ 0.17
lepton + jets	$q\bar{q}$	$\ell\nu_\ell$	43.49 $\pm$ 0.27
all-jets	$q\bar{q}$	$q\bar{q}$	46.19 $\pm$ 0.48

Table 1.3: *Predicted branching fractions (in %) for the respective $t\bar{t}$ final states [9]. Both $\bar{\ell}\nu_\ell$ and $\ell\bar{\nu}_\ell$ W boson decays are possible, but are not separately listed.*

1. $t\bar{t} \to W^+bW^-\bar{b} \to q\bar{q}bq\bar{q}\bar{b}$, where both W bosons decay hadronically to $q = u, d, s, c$ (light) quarks.
2. $t\bar{t} \to W^+bW^-\bar{b} \to q\bar{q}b\ell\bar{\nu}_\ell\bar{b} + \bar{\ell}\nu_\ell bq\bar{q}\bar{b}$, where one W boson decays hadronically, while the other decays to leptons $\ell = e, \mu, \tau$.
3. $t\bar{t} \to W^+bW^-\bar{b} \to \bar{\ell}\nu_\ell b\ell\bar{\nu}_\ell\bar{b}$, where both W bosons decay leptonically.

The different final states are referred to as the all-jets, lepton+jets and dilepton channels, respectively. Table 1.3 lists the different branching fractions for the three classes of final states.

The analysis presented in this thesis deals with $t\bar{t}$ production in the all-jets channel. The all-jets channel is considered experimentally the most difficult to measure, as there is significantly more background than in the other decay channels. The main background is QCD multijet production, which overwhelms the signal by three to four orders of magnitude.

1.4 Top mass

The top mass is one of the input parameters of the SM. The top quark is very heavy, around 190 times the proton mass. Because of its large mass, the top quark plays an important role in precision electroweak analyses, particularly analyses related to the Higgs boson, which couples to mass [9, 10, 13].

At tree level, the mass of the W boson is predicted completely from M_Z through the weak mixing angle $\sin\theta_W$[4]. The W boson mass can be written as [10]:

$$M_W^2 = \frac{\sqrt{2}G_F}{\pi\alpha}\frac{1}{\sin^2\theta_W}. \tag{1.9}$$

When higher-order corrections are included, this expression becomes:

$$M_W^2 = \frac{\sqrt{2}G_F}{\pi\alpha}\frac{1}{\sin^2\theta_W(1-\Delta r)} \tag{1.10}$$

[4]The definition used $\sin^2\theta_W = 1 - \frac{M_W^2}{M_Z^2}$, is the so-called *on-shell* definition, because it is defined in terms of physical (on-shell) quantities.

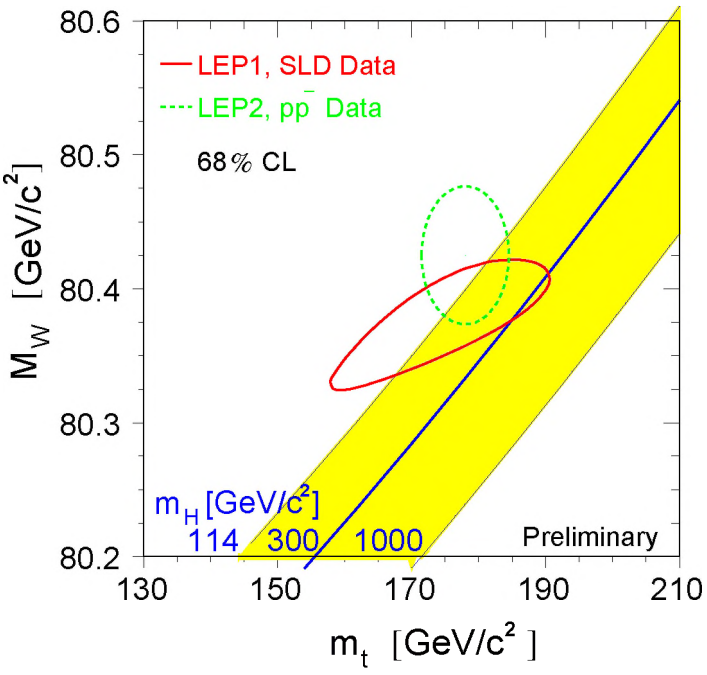

Figure 1.2: *W mass vs. top mass. The two ellipses show the current limits on the top and W mass for direct (dashed line) and indirect (solid line) measurements. The diagonal lines give the theoretical dependence of $M_W(m_t)$, for different masses of the Higgs boson. Preliminary results from new Tevatron direct top mass measurements are included [13].*

where Δr contains the radiative corrections on $\sin\theta_W$. The Δr contribution coming from top quarks is:

$$(\Delta r)_t \approx -\frac{3G_F m_t^2}{8\sqrt{2}\pi^2}\frac{1}{\tan^2\theta_W}. \tag{1.11}$$

Here, only the $W \to bt \to W$ and $Z \to t\bar{t} \to Z$ one-loop corrections are taken into account.

Obviously, corrections of the type listed in Equation 1.11 also exist for the other quarks. However, with the top mass in the numerator, the top quark is expected to dominate the contributions coming from other quarks, which is why they are ignored in this comparison.

Combining Equations 1.10 and 1.11, one can observe that M_W^2 has a linear dependence on m_t^2.

The dashed ellipse in Figure 1.2 indicates the 68% confidence level limits on M_W and m_t coming from direct measurements. The current world average from direct measurements is [9]:

$$m_t = 174.3 \pm 5.1 \text{ GeV/c}^2. \tag{1.12}$$

There is a new, preliminary, more accurate measurement for m_t. This improved measurement of m_t is mainly influenced by an improved DØ measurement [14]. The current preliminary world average is [13]

$$m_t = 178.0 \pm 4.3 \text{ GeV/c}^2, \tag{1.13}$$

which is significantly higher than the previous world average.

It is also possible to measure the top mass indirectly, for instance through higher order corrections to e^+e^- annihilation asymmetries near the Z resonance. Historically, these

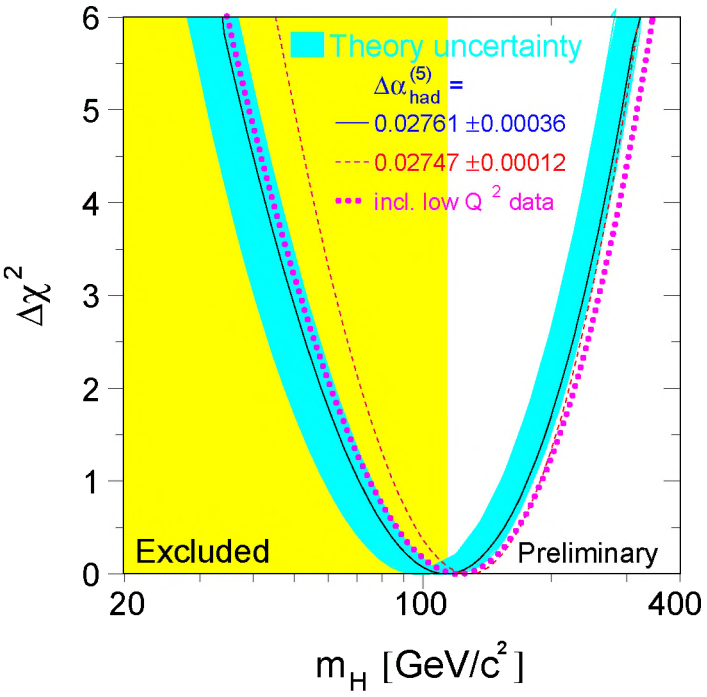

Figure 1.3: *Quality ($\Delta\chi^2$) of the SM fit of M_W and m_t as a function of the mass of the Higgs boson. Shown are the probability for a certain Higgs mass and its uncertainty, and the mass range already excluded by direct searches. Preliminary results from new Tevatron direct top mass measurements are included. The dotted and dashed curves show the probability for different values of the hadronic contribution to α [13].*

neutral current measurements were actually used to predict the top quark mass several years before it was discovered[5]. The world average from these indirect measurements is [9]

$$m_t = 178.1^{+10.4}_{-8.3}\ \mathrm{GeV/c^2}. \tag{1.14}$$

The solid ellipse in Figure 1.2 shows the limits set by these indirect neutral current precision measurements.

The Higgs boson also adds a correction to the W boson mass [10]:

$$(\Delta r)_H = \frac{11 G_F M_Z^2 \cos^2\theta_W}{24\sqrt{2}\pi^2} \ln\frac{m_H^2}{M_Z^2}, \tag{1.15}$$

which yields an additional logarithmic dependence on m_H to the offset of $M_W(m_t)$. Figure 1.2 shows the dependence of M_W versus m_t, for different Higgs masses.

Given that within the framework of the SM (some) quantities depend on the Higgs mass, the data, notably the measurement of M_W and m_t, can be used to predict the Higgs mass. The information contained in Figure 1.2 is presented as a likelihood $\Delta\chi^2$. The preliminary value of m_t is used. $\Delta\chi^2$ is, within the framework of the SM, a function of the Higgs boson mass. The minimum value of the parabola, which represents the theoretical prediction, indicates the preferred mass of the Higgs boson. Also shown is the Higgs mass range which is already excluded by searches [13]. The Higgs mass that is preferred by the SM seems to be only slightly above the mass exclusion limit of 114.4 GeV/c^2:

$$m_H^{preferred} = 123.3\ \mathrm{GeV/c^2}, \tag{1.16}$$

[5]Even before the e^+e^- annihilation asymmetry measurements, the measurements on b quark mixing already hinted that the top quark was relatively heavy.

while the 95% confidence level upper limit on m_H is

$$m_H < 260 \text{ GeV/c}^2. \tag{1.17}$$

1.5 Other properties of the top quark

For completeness, the following section will briefly discuss other relevant subjects in top physics that are not studied in this thesis.

1.5.1 Top spin

A remarkable property of the top quark is the fact that its spin orientation is transferred to its decay products and should be directly observable. This is a consequence of the very short lifetime of the top quark. If the top quark would hadronize, the spin information would be lost when the quark depolarizes in mesons. Hence, direct observation of quark spin is only possible in top quark decays.

In $p\overline{p}$ collisions, the $t\bar{t}$ pair is expected to be mainly produced through an s-channel gluon (See Figure 1.1 for the tree-level Feynman diagrams). Since the gluon is a spin $1\hbar$ state, the spin of the two top quarks in the final state is expected to be strongly correlated. Measurement of the top pair spin correlation [15] is an interesting way to check this basic physical principle.

1.5.2 Single top

Top quarks are produced in pairs through the strong interaction. In the weak interaction, top quarks are produced together with a b quark in the final state, or with a W boson through bg fusion. These types of processes are called single top production, and have not been observed yet. Cross sections are predicted to be of the order of 1 to 2 pb [16].

Single top production is interesting because it is possible to directly measure the coupling constant of $W^+ \rightarrow \bar{b} + t$, V_{tb}. Another aspect of single top production is that it provides us with another method to probe the b-quark content in the proton and antiproton.

In single top production, the spin of the top quark is predicted to be completely correlated to the spin of the quarks that produced it, (the $t\bar{b}$ pair couples only to the spin-$1\hbar$ W). This correlation makes single top events a probe of the spin of the quarks in the (anti)proton [10].

1.6 Signal simulation

Monte Carlo $t\bar{t}$ signal generated at the Tevatron Run 2 center of mass ($\sqrt{s} = 1.96$ TeV/c^2) is used to simulate $t\bar{t}$ all-jets events. The hard scattering process is simulated by ALPGEN 1.2 [17] for the top pair production. In the main signal sample, the two W bosons in the event are forced to decay to quarks. PYTHIA 6.2 [26] is used for the rest of the $t\bar{t}$ decay. Table 1.4 lists what processes are taken into account by what Monte Carlo generator.

ALPGEN	PYTHIA
$p\bar{p} \rightarrow t\bar{t}$	final state radiation
initial state radiation	$t\bar{t} \rightarrow W^+bW^-\bar{b} \rightarrow q\bar{q}bq\bar{q}\bar{b}$
	quark hadronization

Table 1.4: *A list of the processes necessary to simulate $p\bar{p} \rightarrow t\bar{t} \rightarrow$ all-jets events. The different processes are listed by Monte Carlo generator, we use a stacked simulation with ALPGEN and PYTHIA.*

PYTHIA adds additional final state radiation and simulates the production of decay products and hadronization. ALPGEN has the advantage that it is possible to include the full spin correlation for the top quarks, while PYTHIA simulates the hadronization and parton showering as observed in data. PYTHIA uses a model called string fragmentation, which uses 'color strings' that create particles according to the initial quark or gluon momentum. This method has the advantage that it correctly describes the behavior of the color flow in the jet. ALPGEN, on the other hand, is tuned to accurately predict the kinematics of $p\bar{p} \rightarrow t\bar{t} \rightarrow X$ processes at the level of the matrix element.

One of the inputs for both PYTHIA and ALPGEN is the scale for the calculation of the $t\bar{t}$ processes. Here, the scale used is $m_t c^2$, which is similar to the values used in the theoretical (N)NLO cross section calculations (Section 1.2). The set of parton distribution functions used by ALPGEN for modeling the proton and antiproton is CTEQ6.1M [27]. The decay in PYTHIA uses CTEQ5L [28][6]. The various branching fractions and lifetimes of long-lived b quark states are modeled by EVTGEN [29].

The top quark mass is set to 175 GeV/c^2 in the main sample. Two smaller samples at masses of 165 and 185 GeV/c^2 are used for studies of top mass dependence. Another control sample is generated for systematic studies, here only one W boson decays hadronically and the other W boson decays to leptons $\ell = e, \mu, \tau$. The theoretical prediction of the Monte Carlo $t\bar{t}$ production cross section is set to 6.5 pb. The signal sample consists of 48k events. The $t\bar{t}$ Monte Carlo sample contains a hundredfold more events than theoretically predicted in the data sample at hand.

1.7 Backgrounds for $t\bar{t}$ production in the all-jets channel

Events with six or more jets from light quarks or gluons are the dominant background for the $t\bar{t}$ to all-jets measurement.

Full matrix element calculations for high-multiplicity QCD processes exist only to leading order, and are accessible through the ALPGEN [17] Monte Carlo generator. The largest number of 'hard' partons in these Monte Carlo simulations is six. Next-to-leading

[6]The choice to use different parton distribution functions is merely technical. The version of the DØ software environment used in this thesis was only able to run this version of PYTHIA within the timespan of the completion of the analysis.

order calculations are only available for two- and three parton final states [18]. The studies of the most recent $p\overline{p}$ data at the Tevatron are not yet published.

At the Tevatron $p\overline{p}$ interactions, the cross section for six-jet events at $\sqrt{s} = 1.8$ TeV/c^2 (Run 1) has been studied using the ALPGEN LO Monte Carlo simulations [17, 22]. The expected cross section depends very strongly on the jet E_T cut. For $E_T > 30$ GeV the cross section is expected to be around 50-100 pb. The experimental (Run 1) result is in agreement: the CDF experiment has measured 48 ± 1 pb with similar jet requirements. When the jet threshold is loosened, the cross section increases rapidly, at $E_T > 15$ GeV the predicted cross section at LO increases by around a factor 100.

The quality of the QCD predictions of this type have been studied experimentally by the DØ collaboration for events with up to four jets, and then mainly in the high transverse energy range [19]. Typically there are requirements on the E_T of jets in the order of 30 GeV or more. Similar measurements have also been performed by the CDF collaboration [20][7]. Both results were obtained during the Run 1 period of the Tevatron.

The main conclusions of both measurements are that the commonly used Monte Carlo generators are good at predicting jet kinematic distributions for two- and three-jet events, but at higher jet multiplicities the predictions become less reliable and the Monte Carlo parameters have to be finely tuned to agree with data. The jet multiplicity distributions are usually predicted correctly, but jet transverse energy (E_T) spectra already disagree for events with four jets. This is the reason that for these QCD measurements the requirements on the jet energy are quite tight.

The Monte Carlo fine tuning has not been done on the current Tevatron data, which are taken at a larger interaction center of mass energy. Because the Monte Carlo fails to accurately describe the data, the analysis presented in this thesis will solely rely on data for the estimation of the background.

Other backgrounds

Another background that should be considered is the production of a (hadronically) decaying W boson with four extra jets. The cross sections for $W + 4$ jets and $t\bar{t}$ production are of similar size [23], so processes like this can be ignored with respect to the overwhelming QCD background. However, if the presence of b quarks is required, the $p\bar{p} \rightarrow W + bX$ cross section is negligible with respect to the $t\bar{t}$ cross section [24].

[7] The CDF collaboration has measured up to six-jet multiplicities. Discrepancies were observed between different Monte Carlo generators and the data.

Chapter 2

Experimental Setup

In the early 1990's the DØ experiment was installed at the Tevatron proton-antiproton collider at Fermi National Accelerator Laboratory, in Batavia (near Chicago), Illinois, United States of America. The DØ experiment received its name from its location on the collider ring, which has a lattice consisting of six segments labeled A to F, which are subdivided in eight segments numbered 0 through 7. The other experiment at the Tevatron is called the *Collider Detector at Fermilab* (CDF) and is located at location BØ on the ring. Initially, the high energy physics community anticipated to use only the CDF experiment, but already in the early stages of detector development people realized that a second experiment would be necessary to provide the necessary scientific verification.

DØ became operational in 1992 [33]. Its main features were good energy measurement, with a very granular, high precision liquid Argon/Uranium sampling calorimeter, and large angular coverage, also in the muon detector. As any extra material would decrease the energy resolution, no solenoid was placed inside the calorimeter. The lack of a central magnetic field had as consequence that the inner tracking at DØ could not be used to measure the momentum of charged particles, so would only focus on distinction between charged and neutral particles.

The CDF and DØ collaboration simultaneously published the discovery of the top quark at the Tevatron in 1995 [34]. DØ takes a leading role in the measurement of jet spectra and other QCD phenomena.

2.1 The Tevatron

The Tevatron accelerator became operational in 1983, providing several fixed target experiments at Fermilab with a 800 GeV proton beam. Proton-antiproton collisions were established in 1986, with a maximal operating energy of 900 GeV per beam.

In 2001 the Tevatron started a new era with a proton and antiproton beam of 980 GeV, an improvement in beam-optics and a decrease in bunch spacing which greatly improves the Run 2 performance. Table 2.1 gives the design operating parameters for Tevatron's Runs 1 and 2. Typical average values of the instantaneous luminosity are around 30×10^{30} for the data studied in this thesis.

	Run 1	Run 2	
Running period (*expected*)	1993 - 1995	2001 - *2009*	delivered
p bunches	6	36	36
p / bunch	2.3×10^{11}	2.7×10^{11}	2×10^{11}
$\overline{p}$ bunches	6	36	36
$\overline{p}$ / bunch	5.5×10^{10}	4.2×10^{10}	3×10^{10}
bunch spacing [nsec]	3500	396	396
interactions/crossing	2.5	2.3	1.5
typical luminosity [$\mathrm{cm}^{-2}\mathrm{s}^{-1}$]	0.16×10^{32}	2.0×10^{32}	1.0×10^{32}
integrated luminosity [pb^{-1}/week]	3.2	17.3	18.6

Table 2.1: *Design operating parameters for the Tevatron collider for Run 1 and Run 2. Also listed are the record values that are achieved up to 2004. For the current status of the Tevatron beam see [25]*

2.1.1 Tevatron operation

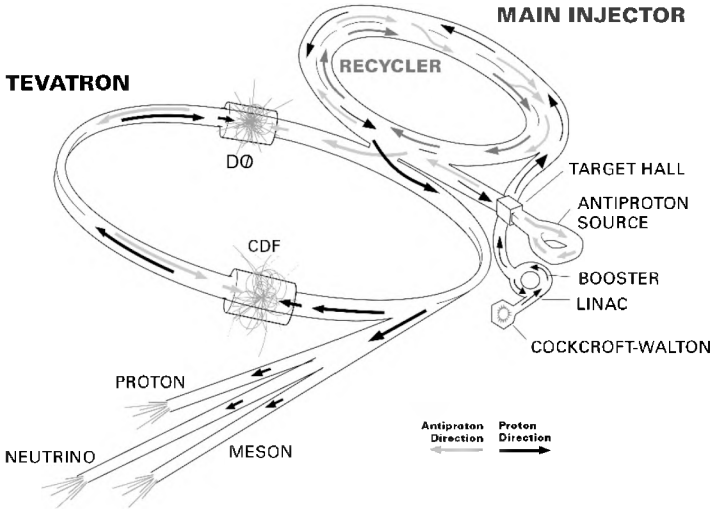

Figure 2.1: *Schematic view of the Tevatron configuration for Run 2.*

The Tevatron is supported by a chain of pre-accelerators (Figure 2.1):

- The Cockroft-Walton accelerator is used to accelerate bunches of (negatively charged) hydrogen ions to an energy of 750 keV;
- The hydrogen ions are then accelerated up to 400 MeV by a linear accelerator. After the LINAC, the ions are sent through a carbon foil, which strips the electrons and leaves the bare protons;
- The first synchrotron accelerator, the booster, is then used to accelerate the protons to an energy of 8 GeV;

- The protons are now ready to be inserted into the main injector. The Main Injector is positioned in a separate beam tunnel adjacent to the Tevatron, as can be seen in Figure 2.1[1]. The main injector can be used to accelerate protons and antiprotons up to an energy of 150 GeV. Antiprotons are produced by shooting a 120 GeV proton beam on a nickel target. In the overwhelming amount of secondary particles from these proton-nucleus collisions a small amount of antiprotons is produced (typically, one needs 10^5 proton collisions to collect one antiproton). The antiprotons are 'stacked' in the antiproton accumulator, until enough have been collected. The antiprotons are then sent to the main injector for injection into the Tevatron;

- The final accelerator is the Tevatron itself. It accelerates the bunches of protons and antiprotons to an energy of 980 GeV. There are two points where the beams collide: CDF and DØ. In parallel, a fraction of the protons is used to feed Fermilab's fixed target experiments.

2.2 The DØ Detector

This section describes the configuration of the DØ experiment during the collection period of the data used in this thesis. Figure 2.2 shows a three-dimensional representation of the DØ detector.

The DØ detector consists of a collection of different sub-detectors around the $p\overline{p}$ interaction point. From the interaction point outward they are:

- a vertex detector, the Silicon Microstrip Tracker (SMT);
- a central tracker, the Central Fiber Tracker (CFT);
- a solenoid magnet to provide the central magnetic field;
- a calorimeter in three cryostats;
- a muon system with a toroid magnet.

In the following sections, the different sub-detectors are discussed in more detail, concentrating on systems which are particularly important to the analysis presented in this thesis.

2.2.1 Coordinate system

Detector coordinates

The standard DØ coordinate system is defined as:

[1]During the Run 1 period, the 'Main Ring' accelerator used for injection was situated in the same tunnel as the Tevatron. As a consequence of the storage beam passing through the detector volume, DØ could not use 25% of the $p\overline{p}$ collisions because of this [35]. CDF did not have this problem, the Main Ring passed outside its active detector volume.

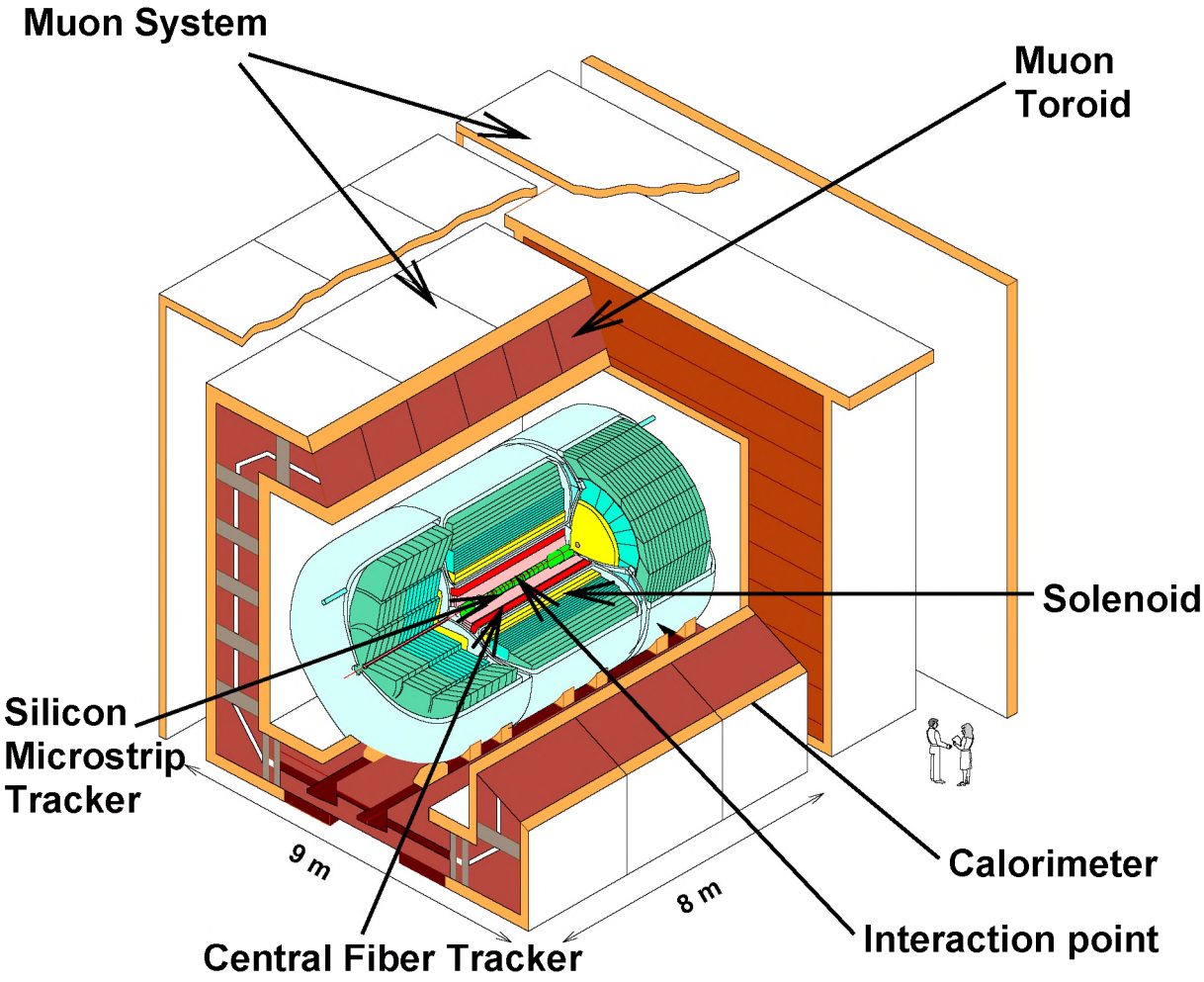

Figure 2.2: *A view of the DØ Run 2 detector. Shown are, from the interaction point outward: the tracking detectors Silicon Microstrip Tracker (SMT) and Central Fiber Tracker (CFT) with their solenoid magnet, the calorimeter in its three cryostats and the three-layer muon system with its toroidal magnet.*

- the x-axis points horizontally away from the center of the Tevatron ring;
- the y-axis points upward;
- the z-axis points along the proton beam.

Whenever a cylindrical coordinate system is used, ϕ is defined as the polar angle. The radial coordinate r is the radial distance from the z-axis. Occasionally, an additional coordinate θ is used, which is equivalent to the azimuthal angle. By definition, $\theta = 0$ is along the proton beam direction, while $\phi = 0$ is at the positive x-axis.

At hadron colliders, it is useful to work with variables which are not very sensitive to the boost of the particle interaction. As the initial momentum transfer of the $p\overline{p}$ interaction is not known, most coordinates are parametrized as Lorentz-vectors as a function of energy E, transverse energy $E_T = \sqrt{E_x^2 + E_y^2}$ (sometimes the transverse momentum $p_T = \sqrt{p_x^2 + p_y^2}$ is used), ϕ, and pseudo-rapidity η, which is defined as:

$$\eta \equiv -\ln\left(\tan\frac{\theta}{2}\right). \tag{2.1}$$

η approximates the true rapidity of a particle, $y = \frac{1}{2}\ln((E + p_z)/(E - p_z))$. Translations in y are invariant under Lorentz-transformation in the z direction, which means that differences in y are also Lorentz-invariant in z.

Physics coordinates

This coordinate system describes the relevant physical quantities of the observed particle, and is hence called the *physics* coordinate system. The physics coordinate system is clearly distinguished from the system where η is measured from the absolute center of the detector ($z = 0$). This coordinate system is labeled the detector coordinate system, and the pseudo-rapidity is referred to as 'detector η' or η_{det}. In the physics coordinate system η_{phys} is used, which is usually just written as η. In this thesis physics coordinates are used, unless stated otherwise.

The proton-antiproton collisions at DØ occur over a 1 m region of z. The Interaction Point or Primary Vertex (PV) can be reconstructed by several different methods, and η, ϕ and E_T are measured with respect to this point.

Cone space

It is often convenient to parametrize the distance between objects in η, ϕ space. These distances are measured using the 'cone' distance dR:

$$dR = \sqrt{(\Delta\phi)^2 + (\Delta\eta)^2}, \tag{2.2}$$

where $\Delta\phi$ and $\Delta\eta$ are the distances between two objects in ϕ and η coordinates.

2.2.2 Luminosity measurement

The instantaneous luminosity of $p\overline{p}$ interactions is determined by measuring the total inelastic $p\overline{p}$ interaction rate. DØ uses the world average total $p\overline{p}$ cross section to obtain a total inelastic cross section within the DØ acceptance of 59.3 $\pm$ 2.3 mb at 1.8 TeV center of mass energy [36], which is then corrected to the current Tevatron energy of $\sqrt{s}$ = 1.96 TeV. The $p\overline{p}$ interaction rate is measured by scintillator counters close to the beam.

The interaction rate changes per bunch crossing, as not every proton or antiproton bunch in the beam necessarily has the same intensity. A database is used to store the different luminosities per bunch. The instantaneous luminosity a particular trigger is exposed to is calculated from the stored bunch crossing information [37, 39]. This method measures the instantaneous luminosity with an accuracy of 6.5%.

2.2.3 Magnets

The measurement of charged particle momenta is determined from the curvature of the track in a magnetic (B) field. The B field inside the calorimeter is provided by a superconducting solenoid, which has a two-layer coil with a radius of 60 cm. The solenoid produces a magnetic field of 2 T in the proton or antiproton direction. To provide a uniform value of the B field integral, $\sin\theta \int B_z \mathrm{d}l$, the ends of the solenoid coil have higher current density.

Outside the calorimeter, the toroidal magnet, which was inherited from Run 1, is used for muon momentum measurement. The (toroidal) magnetic field in the muon system has field lines perpendicular to the beam axis, and has a field strength of 1.8 T. The iron of the muon toroid also serves as the return yoke for the central solenoid. The local values of the B fields in the tracking volume and muon system are stored in a field map.

2.2.4 Tracking

The Silicon Microstrip Tracker

Figure 2.3 shows the DØ Silicon Microstrip Tracker (SMT). The upgraded DØ tracking system is designed to have a large pseudo-rapidity coverage in combination with a high resolution vertex identification, to provide secondary vertex identification for a variety of physics processes like b-physics and top-physics. Besides these physics-based requirements, the Run 2 running conditions and small confinement inside the calorimeter add some extra constraints to the Silicon Tracker design.

The DØ SMT is placed in the center of the DØ detector. The SMT has an outer radius of 16 cm (26 cm for H-disks), covering a pseudo-rapidity range of $|\eta_{det}| < 3$. In total, the SMT reads out almost 800 k channels. An elaborate description of the SMT geometry can be found in [38, 41].

The SMT contains six barrel-shaped, eight-layer micro-strip detectors, each consisting of four ϕ-hermetic combinations of two layers. The barrels are shown in Figure 2.3. Both single-sided and double-sided micro-strip detectors are used, where the latter measure

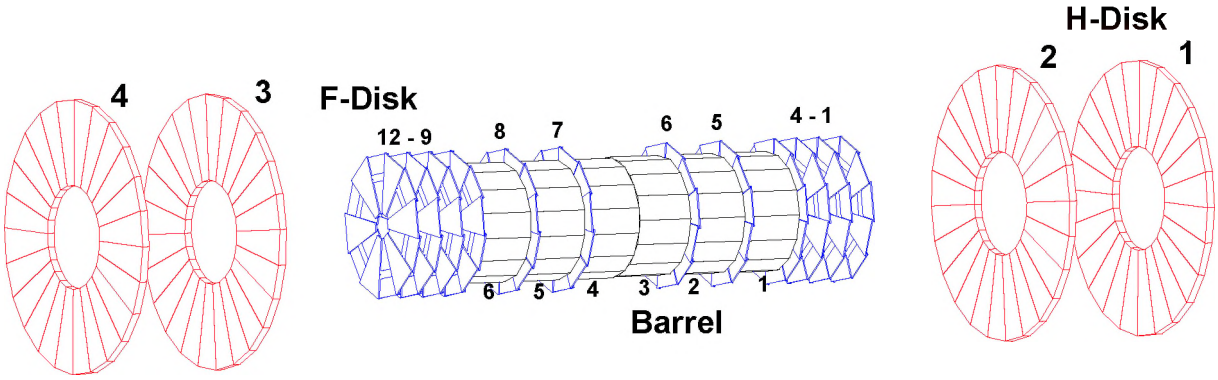

Figure 2.3: *View of the DØ SMT. Shown are the six barrels, twelve F-disks and four H-disks.*

	channels	sensor type	stereo angle	# chips	strip pitch
barrels 2-5	276.5 k	double-sided	90°	6	50/153 μm
(High Occup.)		double-sided	2°	9	50/67 μm
barrels 1 and 6	111.0 k	single-sided	-	3	50 μm
(Low Occup.)		double-sided	2°	9	50/67 μm
F-disk	258 k	double-sided	$\pm$15°	14	63 μm
H-disk	107 k	single-sided	$\pm$7.5°	6 $\times$ 2	80 μm

Table 2.2: *Summary of SMT sub-detector and sensors. Listed are the number of channels for the different types of barrel and disk detectors, the type of microstrip sensor technology used, the stereo angle (if applicable), the number of readout chips and the pitch, the distance between two strips.*

the z-coordinate by means of a stereo angle between the strips, as listed in Table 2.2. Besides the barrels, the SMT also contains disk-shaped detectors of two kinds, 12 F-disks which are placed between and outside the barrel detectors and, placed further away, 4 H-disks covering the high $|\eta_{det}|$ range. F-disks consist of trapezoidal double-sided micro-strip detectors. H-disks are constructed of two single-sided micro-strip detectors that are glued back-to-back. Figure 2.3 displays the configuration of the different disks.

The SMT modules are read out with SVX2*e* chips, which are able to measure the deposited charge per strip, using analogue pipeline technology. Each chip has 128 readout channels [40]. The number of chips used to read out a detector varies per detector type, but all SVX2*e* chips are read out via a readout hybrid, which is called a High Density Interconnect (HDI). Table 2.2 lists the various silicon detector types used in the SMT.

Every silicon module is aligned with an accuracy of 10 μm. The silicon is cooled by means of a mixture of water and glycol to a temperature of -7°C.

The Scintillating Fiber Tracker

The part of the tracking volume between the silicon and pre-shower detector is filled by a scintillating fiber tracker. The Central Fiber Tracker (CFT) covers the central pseudo-rapidity region. The CFT provides track reconstruction for charged particles within a range of $|\eta_{det}| < 2.0$, and provides tracking information to the trigger. The triggering range for the CFT is $|\eta_{det}| < 1.6$.

The fiber tracker consists of 76,800 scintillating fibers that are mounted on 8 concentric cylinders. The fibers are positioned with an accuracy of 25 μm. A hit in the CFT system is measured with an accuracy of 100 μm in r, ϕ. Each cylinder contains two layers, one for axial readout and one at a 3° stereo angle, to make it possible to also reconstruct the z coordinate. The stereo layers are alternating in negative and positive stereo angles. There are no geometric gaps in a layer, and a minimum of 2 potential hits per cylinder. CFT fibers scintillate in the yellow-green part of the spectrum, the emission wavelength is around 530 nm.

A minimum ionizing particle produces only few photons by scintillation. To detect the photons a Visible Light Photon Counter (VLPC) is used, a device based on a chilled solid-state photomultiplier. Digitization is provided by the SVX2e chip, that is also used to read out the DØ silicon.

For lowest-level triggering, the CFT signal is split off between the VLPC and SVX2e chip, and read out by amplifier and discriminator pairs. These provide the input to a fast programmable hardware trigger, based on $r-\phi$ patterns in 4.5 degree sections of the central axial layers.

Pre-shower Detectors

The DØ pre-shower detectors are placed between solenoid and calorimeter. The pre-shower detectors operate as a thin scintillator calorimeter layer. The energy deposited in the pre-shower detector is included in the measurement of the electromagnetic energy. This way the detector can be used to identify EM objects[2] that have already started an electromagnetic cascade in the solenoid magnet. They also provide an extra track position measurement. As the scintillator technology used is almost identical to the Central Fiber Tracker, the pre-shower detectors are read out with VLPCs.

2.2.5 Calorimetry

The DØ experiment prides itself with a liquid argon sampling calorimeter. Though the DØ calorimeter itself has not been changed since the start of the experiment, for Run 2 the readout electronics have been replaced to be able to read out at the higher bunch-crossing rates.

Liquid argon has the disadvantage that an intricate cryogenic system is necessary to operate the calorimeter at very low temperatures. However, once installed, liquid argon calorimeters are radiation-hard and easy to maintain. The calorimeter is divided into

[2]Electrons should be read as *electrons and positrons*. The combination of electrons, positrons and photons is referred to as electromagnetic (EM) objects, unless stated otherwise.

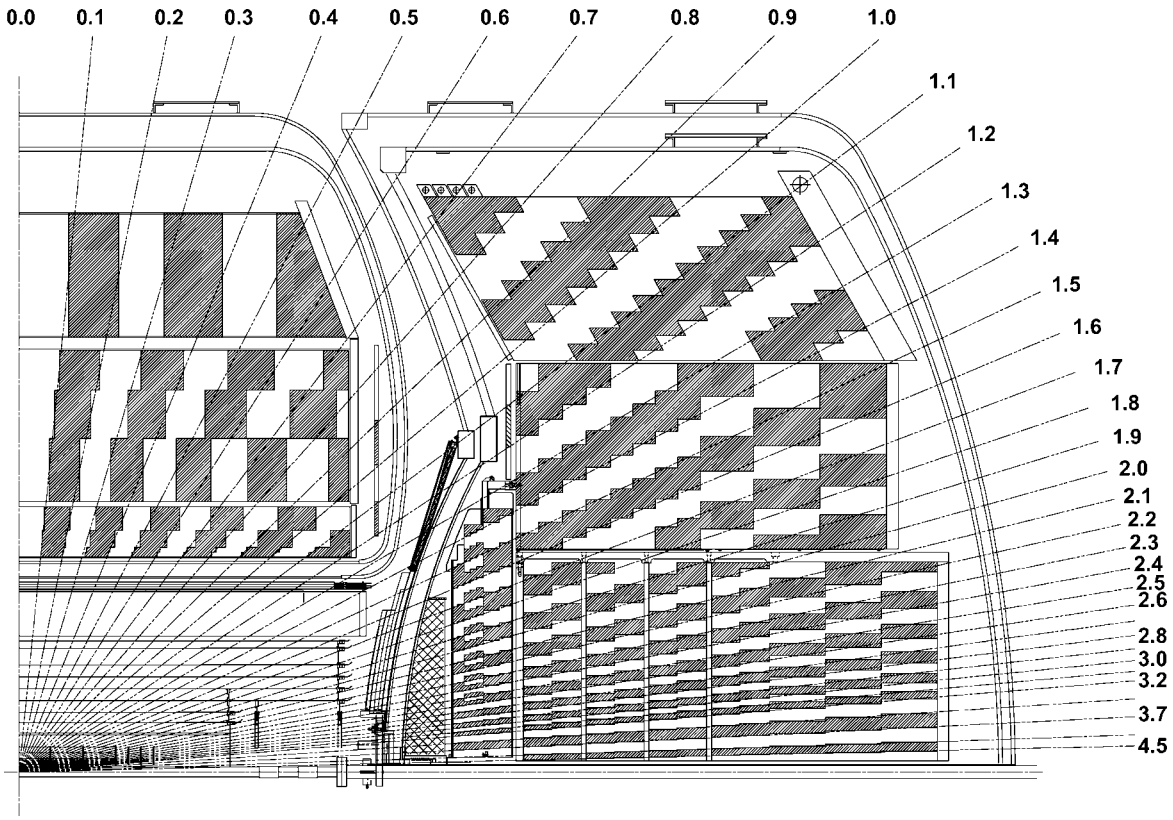

Figure 2.4: *Side view of a quarter of the calorimeter, cut at the $y-z$ plane, with the central barrel calorimeter and end cap calorimeter in separate cryostats. The pseudo-projective towers in η_{det} are also indicated.*

three cryostats, one central barrel and two end caps. Figure 2.4 shows a cross section of the calorimeter in the $y - z$ plane.

Figure 2.5 shows the layout of a basic calorimeter readout cell, consisting of metal absorber plates and resistive pads with the intermediate gap filled with liquid Argon. The gap is the same for all calorimeter readout cells. Depending on the location in the calorimeter, depleted uranium, copper or stainless steel absorbers are used to induce electro-magnetic and hadronic showering. Table 2.3 lists the use of these materials in the different calorimeter regions. The secondary particles in the shower ionize the argon atoms that fill the gaps between the absorber plates. As a potential is applied, the electrons from the argon ionization drift across the gap toward the resistive pads, which are anodes covered by a dielectric. The induced charge on the pads can be integrated, and is proportional to the energy of the particles in the shower. Several of these unit cells are stacked together, and these *readout* cells are the basic units of energy measurement with the DØ calorimeter. The number of unit cells per readout cell depends on the location in

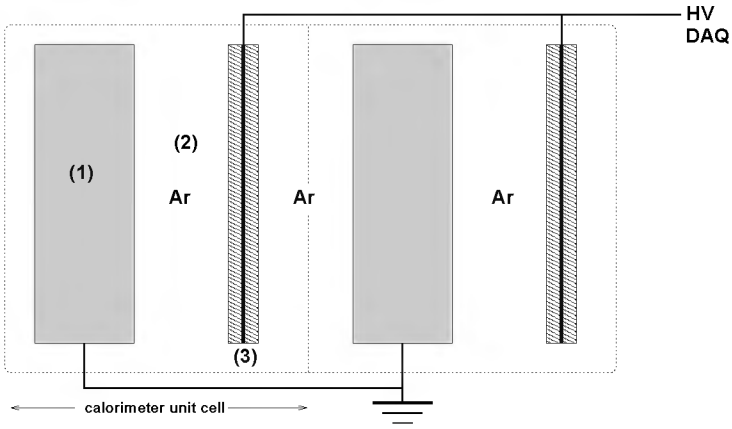

Figure 2.5: *A calorimeter unit cell. A voltage of approximately 1.7 kV is maintained between the grounded absorber plates (1) and the resistive pads (3). Electrons drift through the electric field in the 2.3 mm gap filled with liquid argon (2) in about 450 ns.*

Calorimeter section	Absorber used	# layers	tower $\Delta\phi \times \Delta\eta$
Central, Electro-magnetic	Uranium	4	0.05×0.05 *
Central, Fine hadronic	Uranium	3	0.1×0.1
Central, Coarse hadronic	Copper	1	0.1×0.1
Forward, Electro-magnetic	Uranium	4	0.05×0.05 *
Forward, Fine hadronic	Stainless Steel/Uranium	3/4	0.1×0.1
Forward, Coarse hadronic	Stainless Steel	1/3	0.1×0.1

Table 2.3: *Parameter table for the different calorimeter sub-detectors. Only the electro-magnetic sections (marked $\star$) have the fine granularity in one layer, the rest of the EM sections has* 0.1×0.1 *size readout towers.*

the calorimeter.

The choice of absorber material is particularly important in the inner region of the calorimeter, where both photons, electrons and hadrons interact. In this electro-magnetic calorimeter, depleted uranium is used. The electro-magnetic calorimeter covers approximately 20 radiation lengths. The calorimeter section that uses Uranium is almost *compensating*, meaning that it provides the same energy response to hadrons (E_π) and EM objects (E_{em}) of the same energy. The ratio E_{em}/E_π has been measured to be between 1.11 at 10 GeV and 1.04 at 150 GeV. At the depth that the electro-magnetic shower is expected to deposit most of its energy, the electromagnetic calorimeter cells have finer segmentation to provide higher position accuracy, see Table 2.3.

Outside the electro-magnetic calorimeter resides the hadronic calorimeter, which does not need to be as finely segmented, as hadronic showers are larger than electro-magnetic ones. Typically, this part of the calorimeter is used to measure jets of particles, created by a hadronizing parton, and these jets will be covering several towers. The hadronic calorimeter region is split up in sections with fine and coarse cell depths, which cover approximately 95 and 35 radiation lengths, respectively. The coarse hadronic calorimeter is mostly used to measure all energy that has not been absorbed by the previous layers. After almost 150 electro-magnetic radiation lengths, or 8-10 hadronic interaction lengths, the DØ calorimeter is not expected to have a significant fraction of punch through par-

ticles. As a consequence, only minimum interacting particles (muons) are expected to travel into the muon spectrometer.

Inter-Cryostat Detector

There is a small gap between the central and forward calorimeters, see also Figure 2.4. This volume in the detector is mainly filled by cryostat walls, support structures and cabling. To improve the jet identification in the $0.8 < \eta_{det} < 1.4$ range, the inter-cryostat region is equipped with scintillating tiles. The Inter-Cryostat Detector (ICD) consists of a layer of $\Delta\eta \times \Delta\phi = 0.1 \times 0.1$ tiles, matching the towers in the calorimeter. Note that in the whole ICD region, there is always still a significant part of either the central or forward calorimeter that provides coverage.

Calorimeter resolution

The energy resolution of the calorimeter has been parametrized in terms of

$$\frac{\sigma}{E} = \frac{N}{E} \oplus \frac{S}{\sqrt{E}} \oplus C \tag{2.3}$$

where N is the energy smearing caused by the noise of the read-out electronics and uranium decay, S is the smearing caused by the fluctuations in energy sampling and C the calibration error. The measured values are $N = 0.140$ GeV, $S = 14.8\%\ \sqrt{\text{GeV}}$ and $C = 0.3\%$ for $e^{\pm}/\gamma$ and $N = 1.28$ GeV, $S = 44.6\%\ \sqrt{\text{GeV}}$ and $C = 3.9\%$ for charged pions, see [42]. In this thesis, the calorimeter is mainly used to measure composite jet objects, that consist of both EM objects and pions. The resolution for jets, collections of pions, electrons and photons, is dominated by the non-linearities of the calorimeter(S and C), and was measured to be $S = 90.2\%\ \sqrt{\text{GeV}}$ and $C = 5.2\%$.

2.2.6 Muon system

There is a central and a forward muon system, see Figure 2.2. The central muon system has coverage up to $|\eta_{det}| = 1$; the forward system extends from the central system to $|\eta_{det}| = 2$. The system uses proportional drift tubes (PDTs) in the central system, and mini-drift tubes (MDTs) in the forward region. The choice to use a different detector technology is motivated by the fact that there is significantly more radiation in the forward muon detector region, and MDTs are less sensitive to high-radiation environments.

The muon system of the DØ detector consists of three multi-layers of drift tubes, labeled A, B and C, where the latter is furthest from the interaction point. Each multi-layer consists of three (four for the A layer) layers of drift tubes, so it is possible to reconstruct a track segment within one multi-layer. The muon chambers do not provide full coverage in ϕ. There is no coverage in the bottom A-layer in the central muon system, from $\phi_{det} = 225°$ to $\phi_{det} = 310°$. This area is occupied by the calorimeter support structure.

The central inner and outer multi-layer also have an extra layer of $\Delta\eta_{det} \times \Delta\phi_{det} = 0.1 \times 4.5°$ scintillation counters (tiles), which can be used for triggering and cosmic ray rejection. In the forward region every layer has scintillator counters.

The accuracy with which the muon momentum can be measured using only the muon system is about $\Delta p/p = 20(40)$ % for muons with a momentum around 10(50) GeV/c. The spatial resolution for a hit is around 1 mm for both the PDTs and MDTs. More detailed studies can be found in [11].

In this thesis, muons reconstructed in the muon system are matched to tracks from the central tracking system, which means the central track resolution dominates the resolution on the muon momentum.

2.3 The DØ trigger system

At DØ, the bunch-crossing rate is around 2.5 MHz. The DØ collaboration does not have the capability (caused by dead time of readout electronics) or the financial means (computer farms to reconstruct every $p\overline{p}$ collision) to look at every event that is created at the interaction point. This means that also 'hard' inelastic $p\overline{p}$ interactions will have to be rejected. As a result, the trigger selection is motivated by the physics program of the DØ collaboration.

The task of the DØ trigger system is to sieve through the 1.7 million interactions per second. The final output rate is limited to 50 Hz. The events are selected based on the presence of objects that are likely to come from inelastic interactions with high transverse energy, events containing leptons, events with many or very energetic jets and events where the transverse momentum is unbalanced.

We use a trigger system consisting of three steps (trigger levels), which is described in more detail in the following pages. We focus on calorimeter and jet triggering, which are most relevant for the analysis discussed in this thesis.

2.3.1 First level trigger

The first level trigger (L1) is a hardware based system. It takes information from the calorimeter, muon system, pre-shower detector and fiber tracker. It is designed to provide a 10 kHz output rate, independent of the input rate.

The L1 system provides simple detector information in objects called L1 terms. It is possible to combine these L1 terms with simple logic, like AND and OR operations. A designated computer system called the trigger framework manages all the available information. The L1 trigger system is designed to store the events in a large buffer, which means that there is 3.3 μs available to make a decision. There is only a limited number (256) L1 terms available, which can be used by different higher-level triggers. If any of the L1 terms has fired, the event is passed to the second-level trigger. The typical dead time of the L1 trigger is around 1-5%.

L1 calorimeter triggers

The L1 calorimeter tower objects are defined as projective trigger towers with size $\Delta\eta_{det} \times \Delta\phi_{det} = 0.2 \times 0.2$, or 2×2 calorimeter readout cells. It is possible to combine only the information from the electro-magnetic section of the calorimeter (for electron and photon triggers) or the entire calorimeter (for jets). The coarse hadronic calorimeter is not used in the L1 trigger. The L1 calorimeter trigger is instrumented up to $|\eta_{det}| < 3.2$ for most of the data used in this thesis. A small sub-set is from an earlier period, when the calorimeter trigger was implemented to $|\eta_{det}| < 2.4$

The electro-magnetic triggers are named CEM(n, x), and the calorimeter L1 terms are called CJT(n, x), where n is the number of trigger towers to be required over an energy threshold of x GeV. Typical threshold values are of the order of 5 GeV, but much higher values are used for specific physics triggers.

L1 track trigger

The L1 track trigger only uses the axial layers of the CFT, which are divided in projective wedges with an opening angle of 4.5°. The measured hit pattern is compared to pre-defined patterns for four different track transverse momentum bins. The hit patterns are only defined for single tracks at low occupancy, which are not relevant for the analysis discussed in this dissertation.

L1 muon trigger

The L1 muon system is divided in 8 segments, for both the central and forward muon chambers. Muons are detected in the first level trigger system by requiring a coincidence of scintillator tiles in two of the three muon system layers. There is a limited time window for this coincidence, to reject cosmic rays. Most muon triggers also require a hit in the drift chambers.

2.3.2 Second level trigger

The second level trigger (L2) consists of programmable hardware and microprocessors. All subsystems use similar technology, and all information is then combined in one processor which makes the global L2 trigger decision. The L2 system is designed to provide a data-reduction of a factor 10, and has around 100 μs to make this decision. Most systems use the information already available from the first trigger level to define regions of interest for the L2 trigger. At the second trigger level, simple physics object information is already available, so more complicated trigger requirements can be made.

L2 calorimeter trigger

The L2 calorimeter trigger is designed to run algorithms for electron/photon, jet and missing transverse energy ($\not\!\!E_T$) identification. At the second trigger level, the precision calorimeter readout is used, which improves the jet energy measurement. However, not

the full granularity is available at L2 as there is not sufficient time to consider the entire calorimeter. Instead, the L1 calorimeter information is used as seeds to select the calorimeter towers for the L2 triggers.

For L2 jets, the algorithm combines 5×5 trigger towers, where a fired L1 tower over threshold is used as the seed. The sum of E_T of all towers in the L2 jet is used as the trigger. It is also possible to construct composite objects, like the sum of the E_T of the jets in the event.

Photons and electrons are identified using L1 EM towers as seeds. Only the four most energetic towers nearest to the L1 seed are used. These electro-magnetic trigger towers are used to calculate the L2 E_T. A comparison is made to the energy measured in the hadronic calorimeter, only L2 EM objects of which 50% or more of the total transverse energy comes from the EM calorimeter are triggered.

The missing transverse energy, $\not\!\!E_T$, is just the vector sum of the E_T of the individual trigger towers. This variable is used to identify particles that were not detected in the calorimeter, for example energetic neutrinos.

L2 tracks and vertices

The L2 tracking uses the same data as the first level tracker, but extracts more information from it. At the second trigger level, it is possible to measure the track p_T by reconstructing a (coarse) track from the L1 hits. A more accurate ϕ coordinate is derived from the information of the innermost CFT layer. The track coordinates are also extrapolated to the calorimeter radius, to make it possible to match the track to calorimeter electrons.

L2 muon trigger

At the second trigger level, there is complete, calibrated, timing information available from the muon system. As there is enough information to reject poorly identified muons and cosmic rays, it is possible to loosen the (tight) L1 timing requirements on the scintillator hits. Loosening the scintillator timing requirement improves the efficiency and accuracy of the track measurement. The second level muon trigger uses information from the scintillator and drift chamber hits, and makes use of reconstructed track segments from the muon and the central tracking system. The L2 muon trigger can be tuned, for instance, to trigger on energetic isolated muons for W and Z physics, and on non-isolated muons in jets for $b\bar{b}$ production.

2.3.3 Third level trigger

The third trigger system (L3) consists of a collection of Linux PCs which reconstruct the event, based on all data coming from the detector. The L3 system consists of a modular system of software tools and filters. The L3 code structure is similar to the structure used in the event reconstruction that is run offline, but less options are available.

In principle, all algorithms are able to run both on the L3 and reconstruction PC farms, but usually the algorithm implementation is limited by processing time. At the third trigger level, the available time per event is 100 ms. When at least one L2 trigger

has fired, all (digitized) data is collected from the different sub-detectors and collected on one PC, on which a complete event reconstruction is done.

Because of the plethora of available triggers and triggering algorithms (tracking, muons, electrons, b-vertex finding, etc.), the only trigger that is relevant to the analysis discussed in this thesis is discussed below.

At the third trigger level, only one type of jet algorithm is currently run: The cone algorithm, which is discussed in section 3.1.2. We use a cone size of $R = 0.7$, with no splitting or merging. In addition, the L3 jet trigger requires the presence of a primary vertex. The scalar sum of the p_T of the tracks assigned to the vertex has to be over a threshold of $p_T^{L3PV} > 1$ GeV/c. The mild vertex requirement is used to reject fake jets that consist of calorimeter noise. The exact configuration of all trigger levels used for data collection is described in Section 4.1.2.

Chapter 3

Object Identification

In this chapter, we describe the physical objects that are measured in the DØ detector. For the $t\bar{t}$ analysis presented in this thesis, calorimeter jets play a major role, and will be described in more detail.

3.1 Calorimeter jets

3.1.1 Noise suppression and the T42 algorithm

At the start of Run 2, the DØ collaboration was unpleasantly surprised by the presence of noise in the calorimeter readout electronics. We use the T42 algorithm [47] for suppression of this calorimeter noise.

The noise of a calorimeter signal, indicated by σ_{ped}, is the root mean square (RMS) of the calorimeter pedestal in ADC counts. The ADC pedestals are measured per calorimeter readout cell in dedicated calibration runs.

The T42 algorithm removes isolated moderately energetic calorimeter cells, which are mostly caused by electronics noise. Cells with a calorimeter energy of less than $2.5\sigma_{ped}$ are ignored by the offline reconstruction. If a cell energy between $2.5\sigma_{ped}$ and $4.0\sigma_{ped}$ is observed, the cell is removed only if it is isolated. An isolated cell is defined as being not adjacent to another cell that passes the pedestal threshold. We do not apply the T42 algorithm in the first layer of the electro-magnetic calorimeter, and also not in the coarse hadronic layers of the inter-cryostat region[1]. Cells with negative energies are always rejected.

Depending on the type of data sample, the ratio of T42-rejected cells over the total number of cells in the entire calorimeter ranges from 30% to 60%. The fraction of rejected cells *in jets* corresponds to the number of cells expected from a Gaussian distribution (between 2.5 and 4σ), and the effect is not dependent on the transverse energy (E_T) of the reconstructed jet [48], which confirms that the T42 algorithm indeed reduces the number of noise cells.

[1] In these regions the rejection of cells between $2.5\sigma_{ped}$ and $4.0\sigma_{ped}$ does not improve the calorimeter performance, either because the signal is too similar to noise or because the loss of signal does not compensate for the rejected noise.

3.1.2 Cone algorithm

DØ uses the Improved Legacy Cone Algorithm (ILCA) to reconstruct jets in its calorimeters [49].

The calorimeter energy is recorded in cells, which have an η_{det} and ϕ_{det} coordinate. At this stage, the center of the detector is still used as a reference point. Massless four-vectors are used to represent the cells. The spatial component in these four-vectors has as length the energy of the cell, E, and points along the object's direction with respect to the center of the detector. The basic idea behind ILCA is that jets can be contained in cones in (η, ϕ) space.

To start clustering, the algorithm chooses *seeds*. These are typically calorimeter towers over a certain threshold. The distance between a tower object and seed in cone space is then defined as

$$dR = \sqrt{(\Delta\eta_{det})^2 + (\Delta\phi_{det})^2}, \tag{3.1}$$

where $\Delta\eta_{det}$ and $\Delta\phi_{det}$ are the angles between object and seed. If dR is smaller than the chosen cone size R, typically 0.3 to 0.7, the cell's four-vector is added to the seed four-vector. The spatial components of the two four-vectors are added according to their transverse energy. The process is re-iterated over all cells in the event until there is a collection of stable seeds that contain most of the energy in the cones. The collections of cells are then defined as the proto-jets in the event.

It can happen that two proto-jets overlap. One then has to decide whether two proto-jets should be merged or kept as separate proto-jets. Here, a parameter called the split/merge fraction f is used, which is defined as the ratio of the shared energy of the proto-jets and the energy of the least energetic proto-jet. If the fraction is larger than f a new center value is calculated for the proto-jet, and the cells outside its cone are rejected. Otherwise, the cells are split between the proto-jets. In both cases, the algorithm is then further iterated until a stable axis for the proto-jets is reestablished.

When all proto-jets are stable, the cells belonging to each proto-jet are used to calculate the four-vector in physics coordinates. The stable and thus final proto-jets are called jets. The jets in this thesis are reconstructed with a cone algorithm with a seed $E_T > 1$ GeV. A cone size of $R = 0.5$ and $f = 0.5$ are used. Before any additional corrections are applied, reconstructed jets with $E_T < 8$ GeV are rejected.

3.1.3 Jet ID

After reconstructing the jets, one has to reject poorly reconstructed jet objects, and electrons and photons mis-identified as jets. Figures 3.1 and 3.2 show the selection criteria used to reject fake jets, as applied to a very clean sample of back-to-back di-jet events:

- It is unlikely that much hadronic energy is deposited in the coarse hadronic calorimeter section. The coarse hadronic calorimeter is also more sensitive to noise because of the large size of the readout cells. We require $CHF < 0.4$, where CHF is the fraction of energy in the jet coming from the coarse hadronic part of the calorimeter;

- There is also a requirement on EMF, the fraction of energy coming from the electromagnetic (EM) calorimeter: $0.05 < EMF < 0.95$. One has to remember that particle jets also have a significant π^0 content, which mostly decay to two photons that will shower in the EM calorimeter, so very low EMF values are unlikely. High values of EMF are caused by electrons and photons that are mis-identified as jets;

- After application of these selection criteria, there are still some hot cells present in our sample. Hot cells are defined as single cells that contain (a large amount of) unattributed energy. The ratio of the transverse energy in the leading cell in the jet to the next-to-highest leading cell in the event ($HotF$) should reject jets that are clustered from hot cells. We require $HotF < 10$;

- It is possible to reconstruct a jet that consists of one, single calorimeter cell. These jets, created by single hot cells, are rejected by requiring that the number of towers containing 90% of the jet energy ($n90$) is greater than 1;

- The noise in the precision readout electronics does not influence the energy measured by the first-level jet trigger. We require that at least a fraction of the jet energy is already present at the first trigger level. For this, we define the variable $L1SET$, which is the scalar sum of the transverse energy in all the L1 trigger towers in the jet cone. We require that

$$\frac{L1SET}{E_T(1-CHF)} > 0.4 \tag{3.2}$$

  in the central and end cap calorimeter, and

$$\frac{L1SET}{E_T(1-CHF)} > 0.2 \tag{3.3}$$

  in the inter-cryostat detector (ICD) region, where there is no full L1 trigger coverage. The $L1SET$ cut is applied before corrections to the jet energy scale;

- There is a minimum jet energy:

$$E_T > 15 \text{ GeV}. \tag{3.4}$$

  This cut is made after energy scale and resolution corrections, as will be discussed in the following sections.

3.1.4 Jet Energy scale

The jet energy that is measured in the calorimeter is not equal to sum of the energies of the particles that created the jet in the detector. The difference is caused by detector effects like non-uniform response to the deposited energy and calorimeter noise. It is also possible that part of the shower falls outside the jet cone.

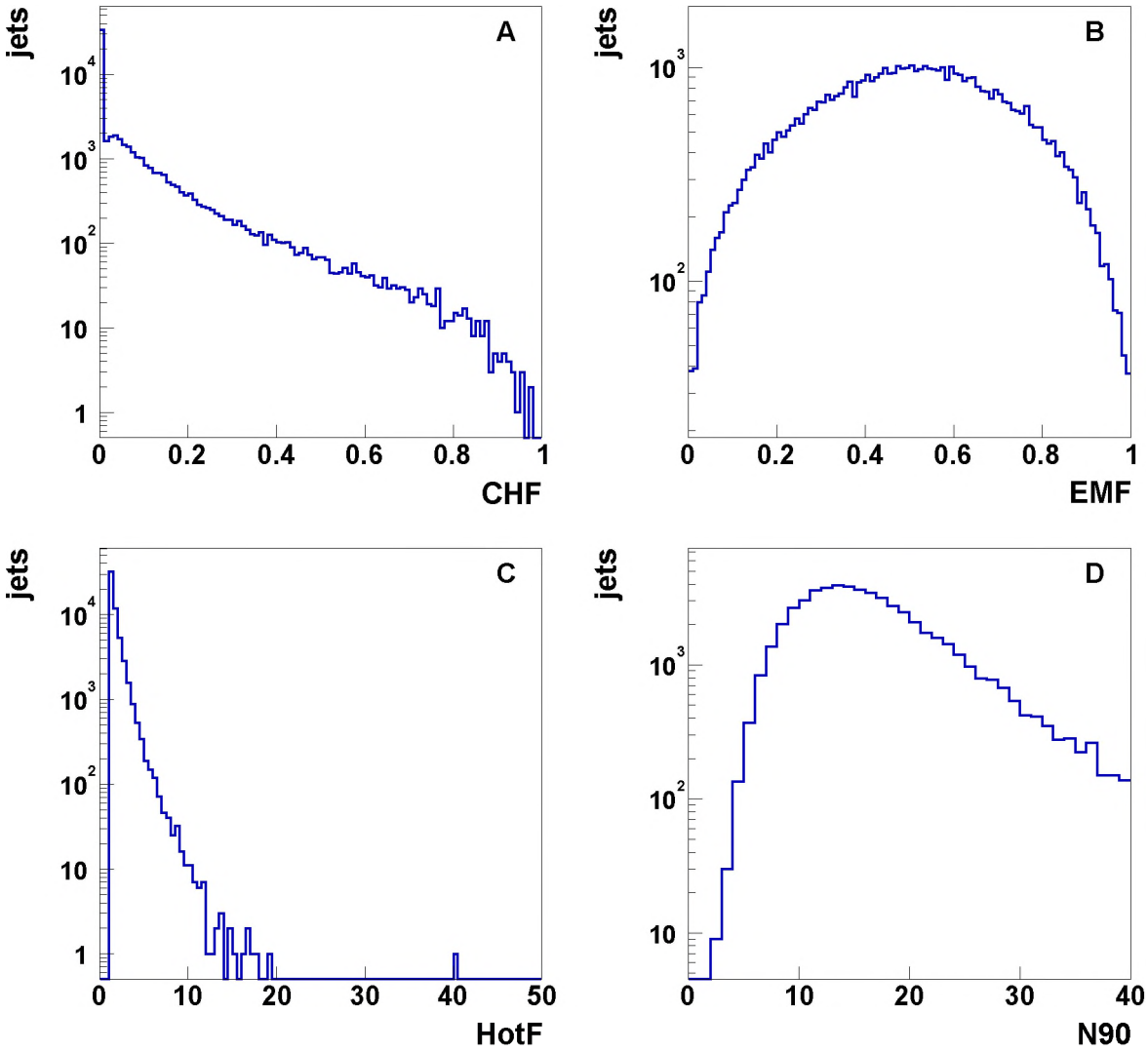

Figure 3.1: *Quantities used for jet identification: (A) the coarse hadronic fraction (CHF); (B) the electromagnetic fraction (EMF); (C) the hot cell fraction (HotF) and (D) the number of towers containing 90% of the jet energy (n90).*

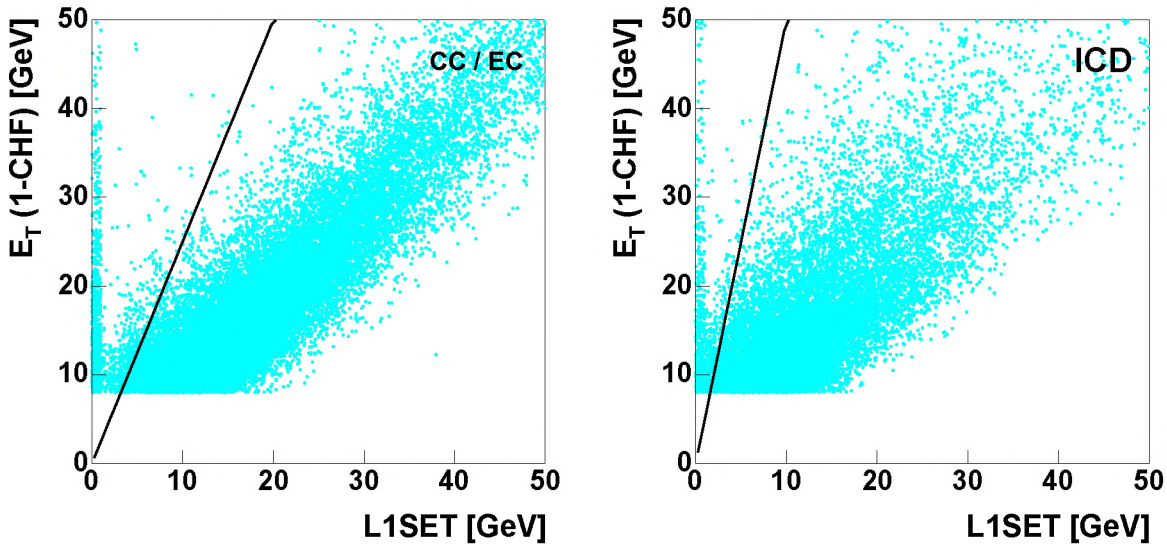

Figure 3.2: *L1SET versus $E_T(1-CHF)$ for central and forward jets (left) and jets in the ICD region (right).*

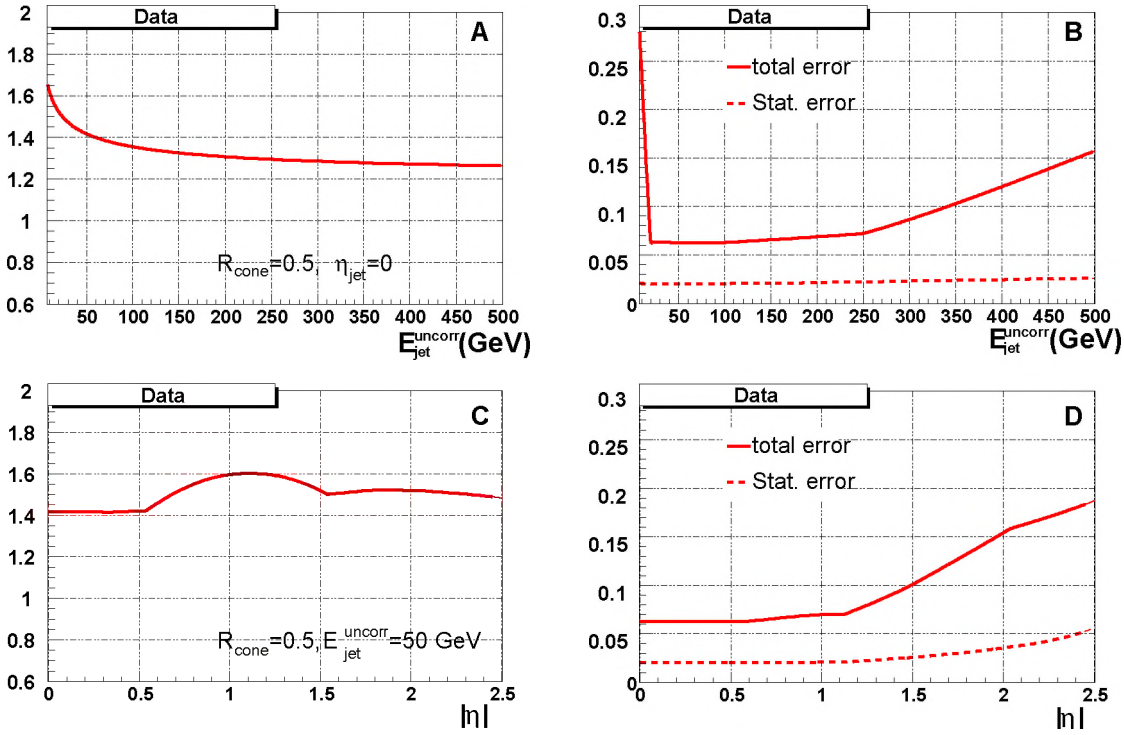

Figure 3.3: *Jet Energy Scale correction and errors for jets in data. Shown are the correction as a function of jet energy E (A) and pseudo-rapidity $|\eta|$ (C). Also shown are the uncertainties of the correction as a function of E (B) and $|\eta|$ (D).*

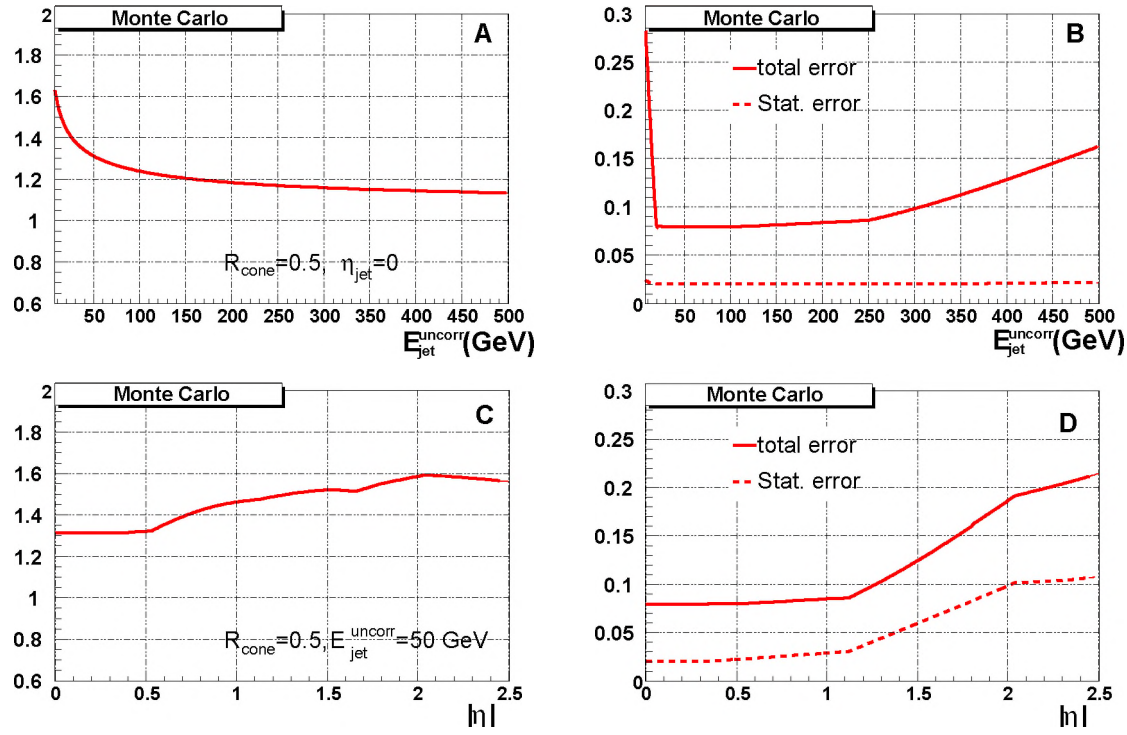

Figure 3.4: *Jet Energy Scale correction and errors for jets in Monte Carlo. Shown are the correction as a function of jet energy E (A) and pseudo-rapidity $|\eta|$ (C). Also shown are the uncertainties of the correction as a function of E (B) and $|\eta|$ (D).*

To correct the calorimeter jet energies back to parton level, a jet energy scale (JES) correction C^{JES} is applied. As the calorimeter behavior is not necessarily correctly modeled in Monte Carlo simulation, it is also necessary to correct simulated jets. The JES is also used to correct the missing transverse energy $\not\!\!E_T$ in the calorimeter.

The particle level or true jet energy, E_{jet}^{part}, reconstructed with a cone algorithm with cone size R, is obtained from the measured jet energy E_{jet}^{meas} using the relation

$$E_{jet}^{part} = \frac{E_{jet}^{meas} - E_O(R,\eta,\mathcal{L})}{\mathcal{R}_{jet}(R,\eta,E)S(R,\eta,E)} = C^{JES}(E_{jet}^{meas},\eta,R,\mathcal{L}) \cdot E_{jet}^{meas}. \quad (3.5)$$

Usually, the total correction is applied to the initial energy E_{jet}^{meas} as a multiplicative factor $C^{JES}(E_{jet}^{meas},\eta,R,\mathcal{L})$. The inputs for C^{JES} are:

- $E_O(R,\eta,\mathcal{L})$ is the offset created by detector and electronic noise, pile-up energy from previous collisions and the extra energy added by the underlying physics event and possible additional events. The dependence on the luminosity $\mathcal{L}$ is caused by the fact that the number of additional interactions is dependent on the luminosity;

- $\mathcal{R}_{jet}(R,\eta,E)$ parametrizes the energy response of the calorimeter. In principle this should only be dependent of η and E, but the dependence on R is caused by the

fact that only part of the jet energy is measured in the cone. Hence, the response is different for jets with different cone sizes;

- $S(R, \eta, E)$ represents the fraction of the particle jet that is deposited inside the jet cone. This out-of-cone showering correction depends on the cone size, and also slightly on the energy of the jet and location in the calorimeter.

The JES is measured directly using E_T conservation in γ + jet events. In the simplest case, the jet balances the photon in the transverse plane. As the energy of the photon is measured accurately[2], the true jet energy can be derived. The η and E distributions of the jets are fit, where there are uncertainties coming from the fit (statistical) and the method (systematic).

Figures 3.3 and 3.4 show the JES corrections C and errors dC on the measurements for data and Monte Carlo events, respectively. Shown are the JES scale factors for uncorrected jets, as a function of the (uncorrected) reconstructed jet energy and η. Typical scale factors are around 1.4 ± 0.06 for jets from data (E_{jet}^{meas} around 50GeV), and 1.3 ± 0.08 for Monte Carlo jets. The uncertainties, which are dominated by the systematic correction for the out-of-cone showering $S(R, \eta, E)$, become very large ($0.2 - 0.3$, approximately 15-20% of the total correction) at low jet energies. The errors are uncorrelated for the Monte Carlo and data.

3.1.5 Jet energy resolution

The jet energy resolution, which is very similar to the calorimeter energy resolution (Section 2.2.5), can be measured in γ + jet data (for low jet energies) and di-jet data for higher jet energies using the asymmetry $(E_{T_1} - E_{T_2})/(E_{T_1} + E_{T_2})$ [51].

The jet energy resolution:

$$\frac{\sigma_{E_T}}{E_T} = \frac{N}{E_T} \oplus \frac{S}{\sqrt{E_T}} \oplus C \tag{3.6}$$

is measured in different bins of η_{det} of the jet, and is limited by low statistics in the γ + jet sample. The data are fit to the function given in Equation 3.6. See Tables 3.1 and 3.2 for the fit values. The measured values of N, S and C are different for data and Monte Carlo jets. The di-jet sample is not available for lower energy measurements because it is collected on a single-jet trigger which is not fully efficient for jets with $E_T < 50$ GeV.

3.1.6 Jet efficiency

The jet identification is on average over 99% efficient [51] above a threshold of $E_T > 50$ GeV. The fake rate was measured to be 4%, where both di-jet events with extra (fake) jets and W+4 jet data for jets without tracking confirmation yielded the same result.

[2]The electro-magnetic calorimeter response of photons and electrons can be measured using different mass resonances like $Z \to e^+e^-$, $J/\psi \to e^+e^-$ and $\pi^0 \to \gamma\gamma$ data [50]. As the masses of these particles are known up to high accuracy, they can be used to determine the energy scale for electrons (and consequently photons).

	N [GeV]	S [GeV$^{0.5}$]	C
$0.0 < \lvert\eta_{det}\rvert < 0.5$	4.26	0.658	0.0436
$0.5 < \lvert\eta_{det}\rvert < 1.0$	4.61	0.621	0.0578
$1.0 < \lvert\eta_{det}\rvert < 1.5$	3.08	0.816	0.0729
$1.5 < \lvert\eta_{det}\rvert < 2.0$	4.83	0.0	0.0735

Table 3.1: *Jet resolution constants for Monte Carlo jets.*

	N [GeV]	S [GeV$^{0.5}$]	C
$0.0 < \lvert\eta_{det}\rvert < 0.5$	5.05	0.753	0.0893
$0.5 < \lvert\eta_{det}\rvert < 1.0$	0.0	1.200	0.0870
$1.0 < \lvert\eta_{det}\rvert < 1.5$	2.24	0.924	0.1350
$1.5 < \lvert\eta_{det}\rvert < 2.0$	6.42	0.0	0.0974

Table 3.2: *Jet resolution constants for data jets.*

However, the efficiency to reconstruct *and* identify a jet is a more useful figure of merit. Table 3.3 lists the combined jet identification and reconstruction efficiency for the three different calorimeter ranges.

3.2 Tracks

The passage of charged particles through the SMT and CFT detectors results in a collection of hits containing 2D or 3D position information. A tracking algorithm reconstructs the trajectory of the particle by combining the corresponding hits in a particle track. The DØ tracking algorithm is based on Kalman filtering [43, 44].

3.2.1 Track resolution and efficiency

The momentum resolution of a track is given by

$$\frac{\sigma_{p_T}}{p_T} = \sqrt{0.015^2 + (\frac{0.014\ p_T}{\text{GeV/c}})^2} \tag{3.7}$$

The impact parameter resolution of a reconstructed track is measured to be 21 μm for tracks with $p_T > 10$ GeV/c[55]. The tracking efficiency depends on the location in the detector and the track p_T. For $Z \rightarrow \mu^+\mu^-$ data (track $p_T > 10$ GeV/c), the efficiency to reconstruct a track is 99%, with a fake rate of 2%. For tracks with lower p_T ($p_T > 0.5$ GeV/c) the efficiency is 92%, with a fake rate of 3% [45].

The tracking inefficiency in Monte Carlo is around 10-40% smaller, again dependent on η_{det} and p_T.

calorimeter region	efficiency [%]
central ($\|\eta_{det}\| < 0.8$)	98.5 ± 0.4
ICD ($0.8 \leq \|\eta_{det}\| < 1.5$)	94.8 ± 0.5
end cap ($\|\eta_{det}\| \geq 1.5$)	97.8 ± 0.6

Table 3.3: *Average jet identification+reconstruction efficiency for the three different calorimeter ranges [52]. The listed efficiencies are for jets with* $E_T > 50$ GeV/c^2.

3.2.2 Tracks in jets

It is only possible to reconstruct secondary vertices within a jet if two (or more) tracks are present inside the jet cone. Jets which pass this requirement are considered taggable. The efficiency for a jet to be taggable is called taggability. Taggable jets are jets which:

- contain at least two tracks with $p_T > 0.5$ GeV/c and $\chi^2/N_{DOF} < 3$ of the track fit, both within a distance of $dR < 0.5$ with respect to the jet axis;
- all tracks should have least two SMT hits in the two inner layers of the silicon. Tracks that do not pass this requirement but have three or more SMT hits are also used.

Figure 3.5 shows the fraction of taggable jets in data and Monte Carlo, as a function of the jet E_T and η. The average taggability is 82.1% on data. For Monte Carlo jets, the average taggability is 93.7%. The difference between data and Monte Carlo events is directly connected to the difference in tracking efficiency as described in Section 3.2.1. Only events with six or more jets are used, as the taggability has been shown to be dependent on the number of jets in the event [46].

3.3 Electrons

The reconstruction of EM objects is based on calorimeter cells from the electromagnetic layers in the calorimeter. However, the first layer of the hadronic calorimeter is included in the energy measurement. A cone algorithm with $R = 0.2$ is used to reconstruct the calorimeter EM objects. For electrons, the EM object is matched to a central track, where the track is required to be within $\Delta\eta < 0.05$ and $\Delta\phi < 0.05$. The axis of the EM object in the calorimeter is used for the electron coordinates.

3.4 Muons

To reconstruct a muon, two different detector systems are used: The muon detector and the central tracker. The tracking algorithm used for reconstruction of tracks in the muon system is similar to the algorithm used in central track reconstruction (Section 3.2).

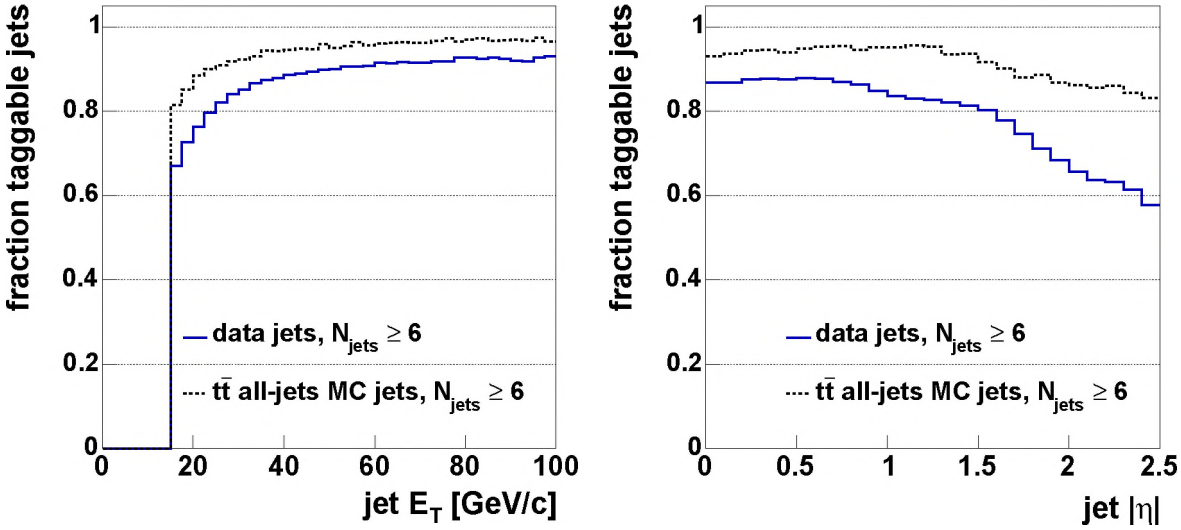

Figure 3.5: *The taggability of jets as a function of the jet E_T (left) and $|\eta|$. Shown are the distribution for data jets in events with six or more jet events (line) and jets in $t\bar{t}$ all-jets Monte Carlo events, also with six or more jets.*

3.4.1 Local muons

A local muon consists of a track that has been reconstructed using only information from the muon system.

The algorithm first reconstructs separate track segments in the three different layers of the muon system. Segments from different layers are combined in a local muon track. Only muons constructed of segments from all three layers of the muon system are used in this analysis.

An extra requirement is made on the timing information of the scintillator hits. Muons collected outside a time window of ±10 ns of the beam crossing are rejected because they are most likely created by muons coming from cosmic ray background.

3.4.2 Global muons

Local muon tracks can be combined (matched) with a central track. Muons that have a central track match are referred to as global muons. A reliable central track match is important, since the central track momentum is measured with much better resolution than the local muon.

The efficiency of the complete global muon selection was measured to be $\varepsilon_{data} = 65 \pm 5$ % for data, and $\varepsilon_{MC} = 71 \pm 1\%$ for Monte Carlo muons. The ratio, $\varepsilon_{data}/\varepsilon_{MC}$, is compatible with unity [53, 51]. Muons with a transverse momentum (p_T^μ) of $p_T^\mu < 4$ GeV/c are rejected. Also, the muon is required to be within $|\eta_{det}| < 2$.

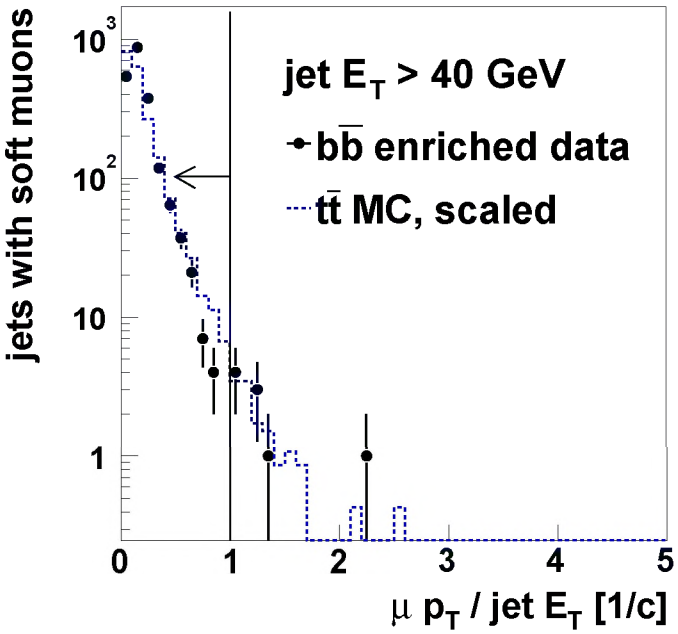

Figure 3.6: *Distribution of p_T^μ / E_T^{jet} for di-jet $b\bar{b}$ enriched data (markers) and b-jets from $t\bar{t}$ Monte Carlo events (histogram).*

3.4.3 Muons in jets

A jet is considered a heavy quark candidate if at least one global muon with $p_T^\mu > 4$ GeV/c is found inside the jet cone, so $dR < 0.5$ between the muon and the jet. Some additional requirements are made to further reject background of high-energy cosmic rays and energetic muons coming from decays other than the jet decay:

- The distance of closest approach in z, Δz, is required to be less than 5 cm between the track and the primary vertex. This requirement is used to reduce remaining background from cosmic ray muons and badly reconstructed tracks. As the typical decay length of a B meson is in the order of a few mm, this does not influence the selection of b candidate jets containing muons.

- The maximum p_T^μ is limited by the jet E_T; muons at very high p_T^μ (> 100 GeV/c) are not consistent with the heavy-quark jet hypothesis, and are expected to be caused by muons from other physics processes that just happen to be caught inside the jet cone. A cut of $p_T^\mu / E_T^{jet} < 1c^{-1}$ is required.

Soft muon tag efficiency

The soft muon tagging efficiency has been measured using several methods to reduce the systematic uncertainty. Di-jet data and $b\bar{b}$, $c\bar{c}$ and QCD Monte Carlo events are studied. The reconstruction efficiencies for low p_T(< 20 GeV/c) muons are found to agree within errors:

$$\frac{\varepsilon_{data}}{\varepsilon_{MC}} = \frac{(69.2 \pm 3.8)\%}{(67.5 \pm 1.2)\%} = 1.025 \pm 0.060. \tag{3.8}$$

This value is used to correct the muon-tagging efficiencies estimated in Monte Carlo events, and shows no significant dependence on η or ϕ. The discrepancies between MC and data become smaller when the jet E_T is increased.

Figure 3.6 shows the distribution of p_T^{μ}/E_T^{jet} for high-E_T di-jet $b\bar{b}$ events. These events were selected by a study of back to back di-jet events with a muon in the leading jet. The away jet is then searched for a muon. If a muon is present, the away jet is used for efficiency studies. The efficiency of the $p_T^{\mu}E_T^{jet} < 1$ cut is 0.975 ± 0.009 for any jet, and increases to 0.99 ± 0.02 for jets with $E_T > 40$ GeV, the E_T regime of the jets from $t\bar{t}$ decays. Again, there are no discrepancies between data and muon tagged b-jets coming from $t\bar{t}$ Monte Carlo events.

3.5 Isolated leptons

Leptons coming from processes like W and Z decay are expected to be very energetic and isolated from any other physics objects in the detector [51]. Events that contain isolated leptons are rejected, as no isolated leptons are expected in the $t\bar{t}$ all-jets event signature.

Isolated muons are required to have $p_T^{\mu} > 15$ GeV/c, and should be associated with a track that originates from the PV. There are also requirements on the (lack of) calorimeter energy near the muon and there is a veto on the presence of additional tracks very close to the muon track [51].

Isolated electrons are also required to have $p_T^{ele} > 15$ GeV/c. Most of the electron's energy is required to come from the electro-magnetic calorimeter, no energy contribution from the coarse hadronic calorimeter section is allowed. The electro-magnetic shower shape is required to be consistent with an electron. The associated track has to originate from the PV. An electron likelihood discriminant [54] is used to reject fake electrons.

3.6 Vertices

At DØ, we distinguish between the primary vertex (PV), which comes from the hard $p\overline{p}$ scattering process, and possible secondary vertices (SV), which come from particles that travel a distance before decaying to other particles.

3.6.1 Primary vertex

To measure the location of the primary vertex, we go through the following steps:

- The tracks are required to originate from near the beam line. The algorithm locates the beam, the location in x, y space where the $p\overline{p}$ beam passes through the detector. Only tracks with a distance of closest approach (DCA, see Figure 3.7) in the x, y plane which is consistent with the beam line are included in the fit. The requirement on the track is made by a cut on the DCA significance $\frac{DCA_{xy}}{\sigma_{DCA_{xy}}} \equiv S_{(0,0)} < 100$ with respect to the beam line;

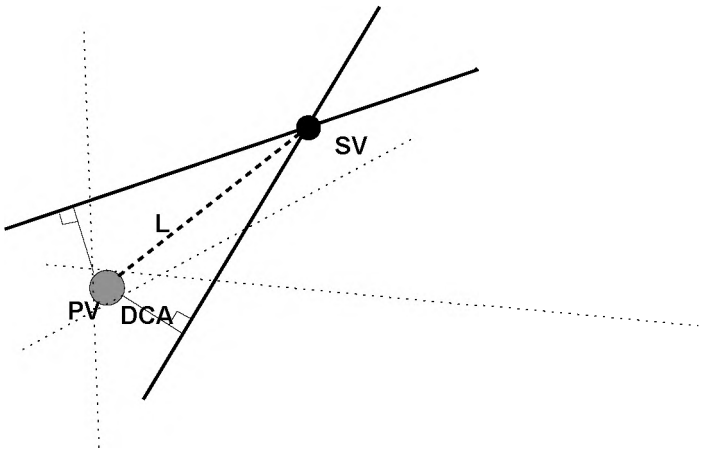

Figure 3.7: *Definition of some track and vertex parameters: The distance of closest approach (DCA) of a track (line) to the primary vertex (PV) and the decay length L (dashed line) of a secondary vertex (SV), the distance between the PV and SV. The dotted lines represent tracks from the PV.*

- Only tracks of good quality are used. At least two SMT hits are required, $p_T \geq 0.5$ GeV/c and the DCA significance (measured in x, y, z), $S_{0,0,0}$, is required to be less than 5. The selected tracks are assigned to the vertex candidates, and the candidate with the largest average track p_T is identified as the primary vertex;

- Events with a primary vertex outside the tracking volume are rejected by requiring $|z_{PV}| < 60$ cm.

The average efficiency of the PV reconstruction has been measured to be 98% on multijet data. The inefficiency originates from events with a PV outside the SMT barrel volume. Inside the SMT barrel the PV reconstruction efficiency is 100%. The accuracy to reconstruct a primary vertex is approximately 15 μm in x, y and 30 μm in z.

3.6.2 Secondary vertices

The (relatively) long lifetime of the B meson makes it possible to identify the location of the decay vertex of the B meson. It is necessary to know both the primary vertex and the track location up to 10-50 μm accuracy to make a reliable reconstruction of the secondary vertex.

We use an algorithm called the secondary vertex tagger (SVT), which reconstructs secondary vertices from the tracks in the event. A very detailed description of the algorithm for primary and secondary vertex reconstruction can be found in [55]. The SVT algorithm consists of the following steps:

- Construct track-jets with the cone algorithm, using tracks instead of calorimeter cells. Only tracks with $p_T > 1$ GeV/c and DCA significance $S_{DCA} > 3$ are considered, where the DCA is with respect to the primary vertex. Every track-jet with at least two selected tracks is searched for secondary vertices;

- We then use the *build-up* algorithm to build secondary vertices. The algorithm fits all combinations of tracks in the jet. The next step is to attach additional tracks to the secondary vertex. Tracks can be assigned to several secondary vertices;

- Extra requirements are placed on the candidate secondary vertices: the transverse decay length[3] $|L_{xy}| < 2.6$ cm, the lifetime significance $|\frac{L_{xy}}{\sigma_{L_{xy}}}| > 7$, collinearity > 0.9 and the $\chi^2/dof < 10$ of the secondary vertex fit. The vertex transverse decay length L_{xy} is defined as the distance between the SV and PV (Fig 3.7) in the transverse plane. The collinearity gives a measure for how much the tracks assigned to the SV actually point toward the PV;

- Since we use the SV to identify the presence of a B meson in the jet, we reject secondary vertices that are consistent with K^0_S, Λ^0 and $\gamma \rightarrow e^+e^-$;

- Next, the track-jets are matched to calorimeter jets. The track-jet is required to be within $dR < 0.5$ of the calorimeter jet.

A calorimeter jet is considered tagged if it contains a track-jet with a selected secondary vertex. We do not consider vertices with a negative lifetime.

3.6.3 Secondary vertex tagging efficiency

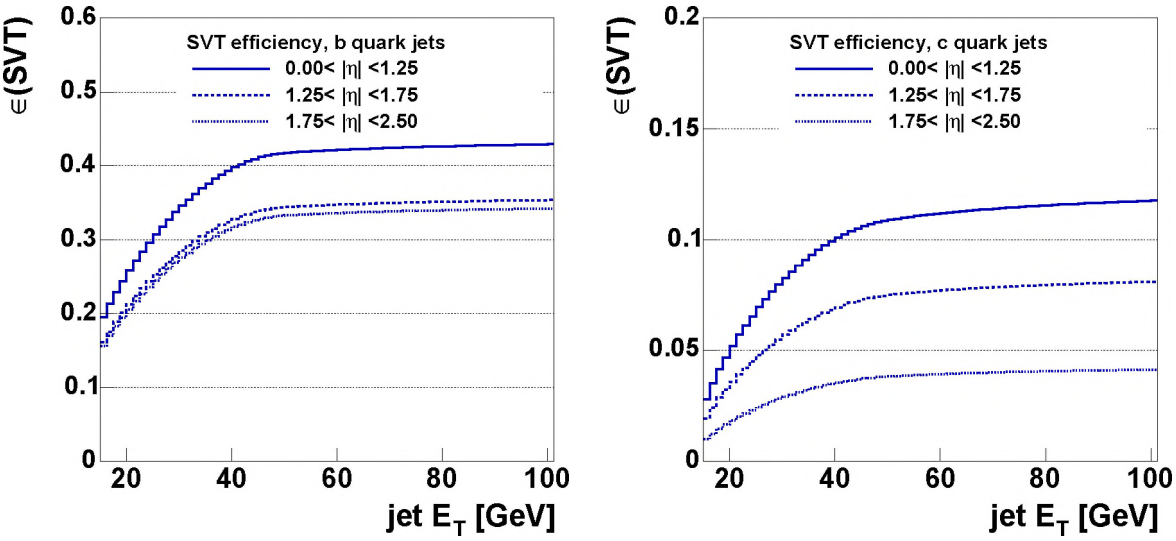

Figure 3.8: *Measured SVT-tagging probabilities, derived from a muon-tagged di-jet data sample. The probability to tag a b jet as measured in data is shown on the left; the right plot is the efficiency to identify jets coming from a c-quark. The solid curve represents jets in the central detector region ($\eta < 1.25$). The dashed and dotted lines represent more forward jets, respectively in the range $1.25 < \eta < 1.75$ and $1.75 < \eta < 2.5$.*

The SVT tagging efficiency is measured on a sample enriched in $b\bar{b}$ production, as described in [46]. A sample of back-to-back di-jet events is used, where the b-content is increased by the requirement of one jet with a soft muon tag. Additional cuts are used

[3]The inner radius of the silicon detector is $r = 2.6$ cm.

	SVT efficiency per jet flavor	
	MC	data
b-jets	0.52	0.39
c-jet	0.13	0.11
light q-jet	0.003	0.006

Table 3.4: *The probability to tag jets of different flavor, for jets from a $t\bar{t}$ all-jets Monte Carlo sample after preselection. These jets are central ($|\eta| < 2$) and have a typical E_T of around 50 GeV. Shown are the efficiencies measured on Monte Carlo jets (MC tagging) and efficiencies when the behavior of data-jets is used. The errors on these numbers are completely dominated by Monte Carlo statistics and do not represent the uncertainty on the b/c/light quark tagging efficiency.*

to further increase the b and c quark content of the sample[4]. As the away jet is expected to also come from the $b\bar{b}$ decay, the efficiency to tag this jet is used to derive the SVT tagging efficiency for b jets in data. All efficiency measurements are done as a function of jet E_T and in three η bins.

The SVT efficiencies are different for Monte Carlo simulation and data. This is dominated by the difference in tracking efficiency, particularly in the low p_T regime. There also is a separate correction for the difference in taggability in Monte Carlo simulation and data (See Section 3.2.2).

The b tagging efficiency is corrected for the ratio in efficiency, SF_b, of the away jets of soft lepton tagged $b\bar{b}$ events in data and Monte Carlo:

$$SF_b(E_T, \eta) = \frac{\varepsilon_b^{data}(E_T, \eta)}{\varepsilon_b^{MC}(E_T, \eta)}. \tag{3.9}$$

SF_b is measured as a function of jet E_T and η, see [46] for details. It is not straightforward to measure the c quark content in data, so we assume that the c jets behave relatively the same as b jets in data and Monte Carlo simulation: $SF_b = SF_c$.

Figure 3.8 shows the efficiencies to tag b and c quarks as a function of jet E_T and η. Typical b tagging efficiencies are around 42% for central jets with E_T around 50 GeV. The efficiency to identify c jets is 11%. The light quark efficiency is also measured in data, using a γ+jets sample, where the b content is suppressed. Table 3.4 lists the average efficiency per jet, for jets in $t\bar{t}$ all-jets Monte Carlo events. Two methods are used: just applying the SVT algorithm on the Monte Carlo jets ('direct MC tagging') and applying the efficiency as a function of the jet's η and E_T, measured on data as described in the previous paragraphs.

[4]To increase the b content of the μ-tagged jet, a cut is placed on a variable called $p_{T_{rel}}$. $p_{T_{rel}}$ is defined as the relative transverse momentum of a muon with respect to the jet axis. Muons originating from weak (b) decays are expected to have a larger $p_{T_{rel}}$ than muons coming from light quark and pion decays. This variable is not used directly in the analysis presented in this thesis; further detailed studies can be found in [12].

Chapter 4

Event samples

In this Chapter we will define the different event samples used in this thesis. First, the data collection with the DØ detector and trigger system will be discussed. Then, the samples of simulated $t\bar{t}$ to all-jets signal events will be studied. Finally, the preselection criteria will be presented.

4.1 Dataset selection

This section describes the processing of events to provide the datasets used in this thesis.

4.1.1 Data quality requirements

Only data that passed the following quality criteria are used [51]:

- The run has to pass certain detector quality requirements. This information is provided by the particular sub-detector working group, and is either determined by the shifter during data taking or by a detector expert doing raw data quality studies. The main purpose of this selection is to immediately reject runs where certain sub-detectors are turned off. The state of each sub-detector for data taking is stored in a database [56].

- The reconstructed physics objects have to be of sufficiently good quality. This is again dependent on the detector performance, but is determined after reconstruction of the data. The quality is determined by comparing measured quantities to typical averages. For instance, runs with an average $\not\!\!E_T$ significantly different from 0 are indicative of malfunctioning calorimeter regions and are thus rejected.

- The luminosity is measured per trigger and per luminosity block, which is typically about one minute of data taking. If there is a problem with the trigger configuration or luminosity measurement, the appropriate luminosity block is flagged as bad. We reject the corresponding data from the luminosity calculation and the analysis.

Two different good-run configurations are used. Both require good calorimeter and tracking performance, including reasonable muon system performance. For analyses that use

soft muons we also require that the muon system is good, which reduces the available sample.

4.1.2 Trigger requirements

The data collection at DØ is done with sets of triggers to record the events of interest. For the data collection period covered in this thesis various triggers were used. Occasionally the trigger configuration and the trigger requirements change. As there are limitations to the total output rate, the triggers have to be adapted to provide the same output rate when the instantaneous luminosity increases. A complete set of triggers running simultaneously is called a trigger list.

Trigger lists are distinguished using version numbers. The dataset used in this analysis uses trigger lists ranging from version 8 (v8) through 12 (v12). Events were collected using the 4JT10 trigger (lists v8 through v11) or 4JT12 trigger (v12 trigger list). Both triggers were optimized for collection of $t\bar{t}$ all-jets events. The triggers are configured in such a way that they are also sensitive to other physics processes with similar (multijet) event signature.

Both triggers require at least 4 jets, and there is also a requirement on the total transverse energy in the event. The definition of the triggers used in this analysis is:

- 4JT10; used in trigger lists v8 - v11:

  L1: CJT(4,5)

  - Four trigger towers with $E_T > 5$ GeV.

  L2: 3jet8_ht90

  - Three jets with $E_T > 8$ GeV and total $L2HT > 90$ GeV.
    The $L2$ H_T cut is not applied in trigger list v8.

  L3: mp160_JET(SCJET_9,4,10.)_JET(SCJET _9,2,20.)

  - Four jets with $E_T > 10$ GeV, of which two with $E_T > 20$ GeV.
    The JET(SCJET_9,2,20.) cut was not made in trigger list v8.

- 4JT12; used in trigger list v12:

  L1: CJT(3,5)

  - Three trigger towers with $E_T > 5$ GeV.

  L2: 3jet8_ht50

  - Three jets with $E_T > 8$ GeV and total $L2HT > 50$ GeV.

  L3: mp160_JET(SCJET_9,4,12.)_JET(SCJET_9,3,15.)_JET(SCJET_9,2,25.)

  - Four jets with $E_T > 12$ GeV, of which three with $E_T > 15$ GeV and two with $E_T > 25$ GeV.

The efficiency of these trigger terms will be studied in Section 4.3.

4.2 Integrated luminosity

trigger list	name	$\mathcal{L}$ (standard)	$\mathcal{L}$ (good μ)	all recorded $\mathcal{L}$
v8	4JT10	20.8 pb^{-1}	20.7 pb^{-1}	25.8 pb^{-1}
v9	4JT10	29.1 pb^{-1}	19.8 pb^{-1}	32.6 pb^{-1}
v10	4JT10	15.8 pb^{-1}	15.5 pb^{-1}	16.2 pb^{-1}
v11	4JT10	57.8 pb^{-1}	57.7 pb^{-1}	60.7 pb^{-1}
v12	4JT12	38.9 pb^{-1}	36.1 pb^{-1}	40.3 pb^{-1}
v8-12	total	162.5 pb^{-1}	149.9 pb^{-1}	175.6 pb^{-1}

Table 4.1: *Integrated luminosities for the different trigger list versions. The standard sample is used for the main analysis in this thesis.*

The integrated luminosity of a data sample is measured for the trigger version used to collect the sample. Table 4.1 shows the collected luminosity per trigger version, after application of the good run list. The loose muon sample, with an integrated luminosity of $\mathcal{L} = 162.5$ pb^{-1}, is used when no tight requirements on the muon quality are needed. Further on in this thesis, an analysis that uses muons for b jet identification is presented. The tighter requirement on the muon reconstruction then reduces the size of the usable data sample for the muon tag analysis to $\mathcal{L} = 149.9$ pb^{-1}.

4.3 Trigger efficiency

The probability that an event passes the different trigger levels is parametrized as a function of individual trigger objects. For jet triggers, the trigger efficiency is measured as a function of the transverse momentum of the reconstructed jet. From the single object efficiencies, the efficiency per event can be calculated. This method can also be used to calculate other efficiencies where the efficiency is known on jet-level.

Under the assumption that the probability to trigger on a given jet has no dependence on whether other jets in the event also fired the trigger, the event probability can be expressed as a product of the individual jet probabilities P_i, where i are the different jets in the event. For example, one can write the probability for an event to have exactly no jet trigger in an event with N jets as

$$P_{event}(0, N) = \prod_{i=1}^{i \leq N} (1 - P_i). \tag{4.1}$$

In general, the probability that k jets fire the trigger in an event with N jets is written as

$$P_{event}(k, N) = \sum_{all\ perm.}^{i,j \leq N} \left(\prod_{i=1}^{i \leq k} P_i \prod_{j \neq i}^{k < j \leq N} (1 - P_j) \right). \tag{4.2}$$

Combining trigger requirements

In the analysis discussed in this thesis, several trigger levels are combined. To determine the trigger efficiency for a given event, the overall trigger efficiency can be written as

$$P(L1 \times L2 \times L3) = P(L1) \times P(L2|L1) \times P(L3|L1\ L2) \tag{4.3}$$

where $P(L1)$ is the probability that the event passes the level 1 trigger, $P(L2|L1)$ is the probability that an event that passes the first level trigger also passes the L2 trigger and $P(L3|L1\ L2)$ is the probability that an event that passed trigger levels 1 and 2 also passes the third trigger level. The next sections describe the efficiency of the $t\bar{t}$ all-jets triggers more elaborately.

Single object trigger efficiencies

The probability to fire a jet trigger can be parametrized in terms of the (JES corrected) E_T, and detector η of the jet : $P_{jet}(E_T, \eta_{det})$. A dedicated dataset is used to measure jet trigger efficiencies. This dataset is collected with single electron triggers, to avoid a trigger bias. We require the events in our sample to pass the following requirements:

- **good run list.** The event should pass all detector and data acquisition quality cuts that are also applied in the $t\bar{t}$ analyses;
- **good electron.** The event should contain exactly one electron. The single electron should have fired the electron trigger with which this data sample was collected. If any other electrons are present in the event it is possible that ambiguities are introduced, as electrons can also fire jet triggers. The electron is required to have an energy above 10 GeV on the second trigger level, and 15 GeV after the full reconstruction;
- **jet multiplicity.** To include possible effects due to high calorimeter occupancy, we disregard events with three or less jets; this accounts for possible correlations in the jet trigger.

L1 turn-on curves

We now measure the first level trigger efficiencies for three different bins of detector η: The central calorimeter (CC, $|\eta_{det}| < 0.8$), the inter-cryostat region (ICD, $0.8 < |\eta_{det}| < 1.5$) and the end-cap calorimeter (EC, $|\eta_{det}| > 1.5$). Figure 4.1 shows the measured L1 efficiencies at the jet-level. The trigger behavior is fitted with a basic turn-on curve:

$$f(x) = \frac{1}{2}p\big(1 + \mathrm{Erf}(\frac{x-h}{s\sqrt{x}})\big), \tag{4.4}$$

where p is the value of the function plateau, h is the value of x where $f(x)$ is equal to half the plateau and s is the slope of $f(x)$ in h. Erf is the basic Gaussian error function.

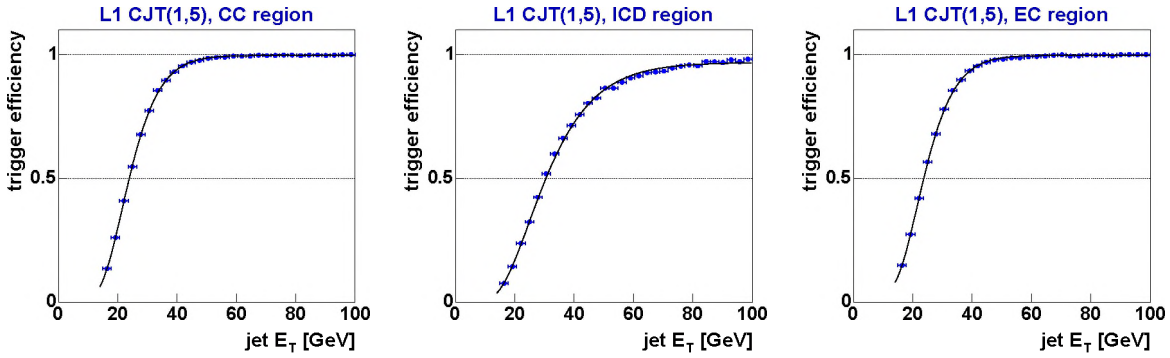

Figure 4.1: *First level trigger efficiencies for the three different calorimeter ranges, as a function of the JES corrected jet E_T. The line represents a fit to the data, using a basic turn-on function.*

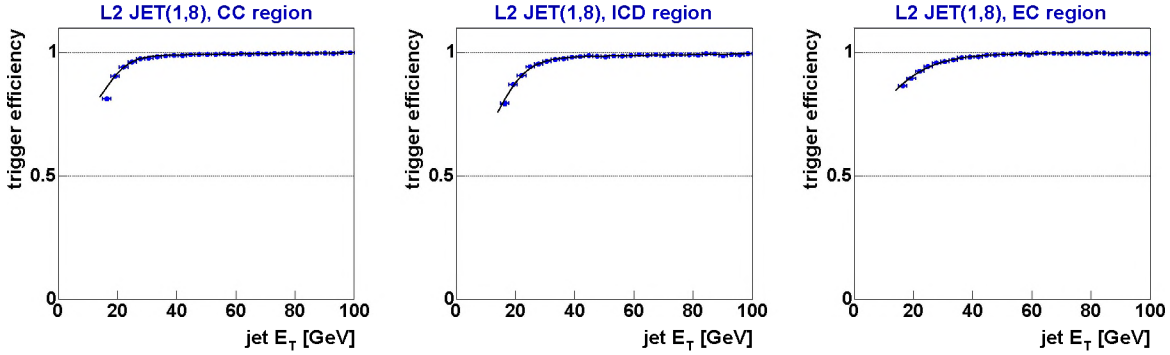

Figure 4.2: *Second level trigger efficiencies for the three different calorimeter ranges, as a function of the E_T of jets, after JES correction. Only jets that pass the L1 trigger are used. The line represents a basic turn-on curve that is fitted to the data. The errors on the fit will be taken into account as a systematic uncertainty on the trigger efficiencies.*

In the CC and EC calorimeter the L1 trigger becomes fully efficient above approximately $E_T > 60$ GeV, while in the ICD region the turn-on is even more slow. The errors on the plateau efficiency are of the order of 0.4%. Typical jets in a $t\bar{t}$ all-jets event have an E_T around 50 GeV. The slow turn-on at the first trigger level is the most important source of inefficiency for the signal.

Higher level trigger turn-on curves

On the second and third trigger level, the focus is more on background rejection as the signal efficiency is approximately 100%.

On the second trigger level the jets are again parametrized in three bins of η_{det}. Figure 4.2 shows the three second level trigger efficiencies as a function of jet E_T. As only jets that passed the L1 trigger are used, and the L1 information is also used as seed for the L2 jets, the efficiency for reconstructed jets over 15 GeV is already at its maximum for jets near the E_T threshold of 15 GeV.

Additionally, an global event-based requirement is used. The variable H_T, which is

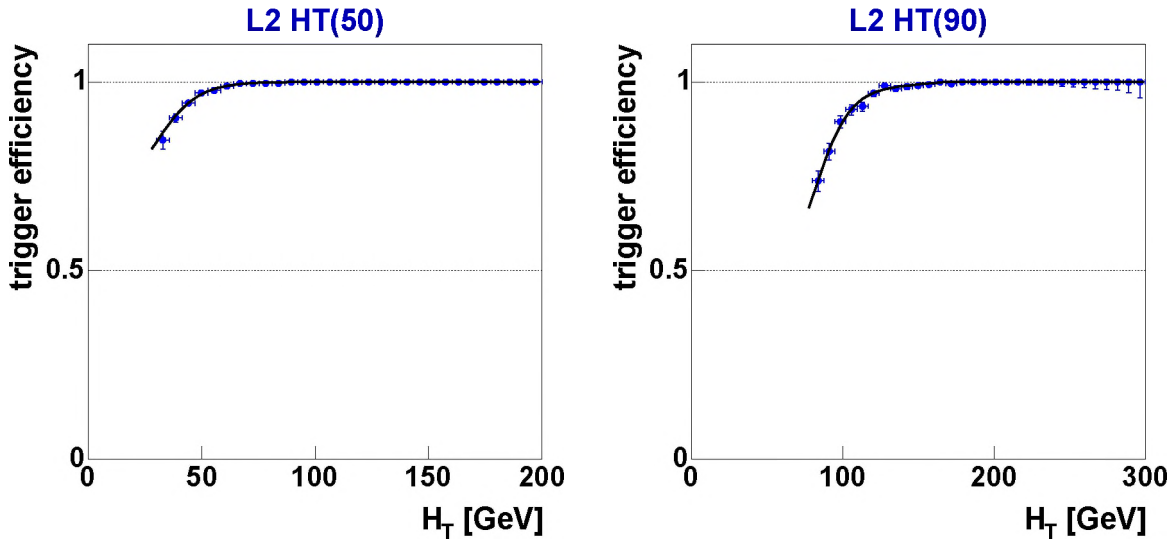

Figure 4.3: *Second level trigger efficiencies for two different L2HT cuts, as a function of the sum of the transverse energies of all jets, H_T. Only events that pass the L1 trigger CJT(3,5) are used. The line represents a basic turn-on curve that is fitted to the data. The errors on the fit will be taken into account as a systematic uncertainty on the trigger efficiencies.*

used very often in this thesis, is defined as:

$$H_T = \sum_{jet=1}^{N_{jets}} E_T(\text{jet}), \tag{4.5}$$

the scalar sum of the E_T's of the jets in the event. This variable is a good probe for energetic multijet physics, for example hadronic $t\bar{t}$ or Higgs production, where we expect large values of H_T. At the second trigger level, there is a requirement on $L2HT$, the sum of the E_T of all L2 jets in the event. Figure 4.3 shows the behavior of the $L2HT$ trigger as a function of the reconstructed H_T. For both the L2 jets and $L2HT$ efficiencies the data is fit with the same function as the L1 trigger efficiency (line).

The instantaneous luminosity of the Tevatron determines the number of hard interactions per second. During the collection of the data used in this thesis, the instantaneous luminosity increased significantly. The third level jet trigger requirements change drastically per version of the trigger list, as the L3 trigger is used to fix the output rate of the all-jets triggers to about 5 Hz. Most of the third level triggers have tight requirements on the two most energetic jets, to reduce the background rate from QCD di-jet events. Four jets are required to have fired in total. The efficiency of the L3 jet triggers for the v8 through v11 trigger lists is shown in Figure 4.4, where in the v8 list only the 10 GeV L3 jet E_T requirement was used. The efficiencies for the jet trigger requirements used in the v12 trigger configuration can be seen in Figure 4.5. Again, the triggers are parametrized in the three different detector η bins that represent the CC, ICD and EC calorimeter region. Only jets that passed L1 and L2 are used.

The L3 trigger uses the precision readout which is known to add additional noise. At the third-level trigger there is also the requirement of the presence of a primary vertex, to reject events that consist only of calorimeter readout electronics noise. The slope in the efficiency plateau is caused by the requirement of the presence of a well-defined primary vertex at L3. The slow saturation after the initial sharp turn-on is attributed to remaining noise jets in the sample, which lower the measured efficiency. The basic fit function for the turn-on curves was modified to include the slope in the plateau. However, even after the correction for this slope the fit is not optimal. This effect is included in the error estimate on the L3 jet triggers. The errors on fits for the trigger efficiency will be taken into account as a systematic uncertainty on the trigger efficiency.

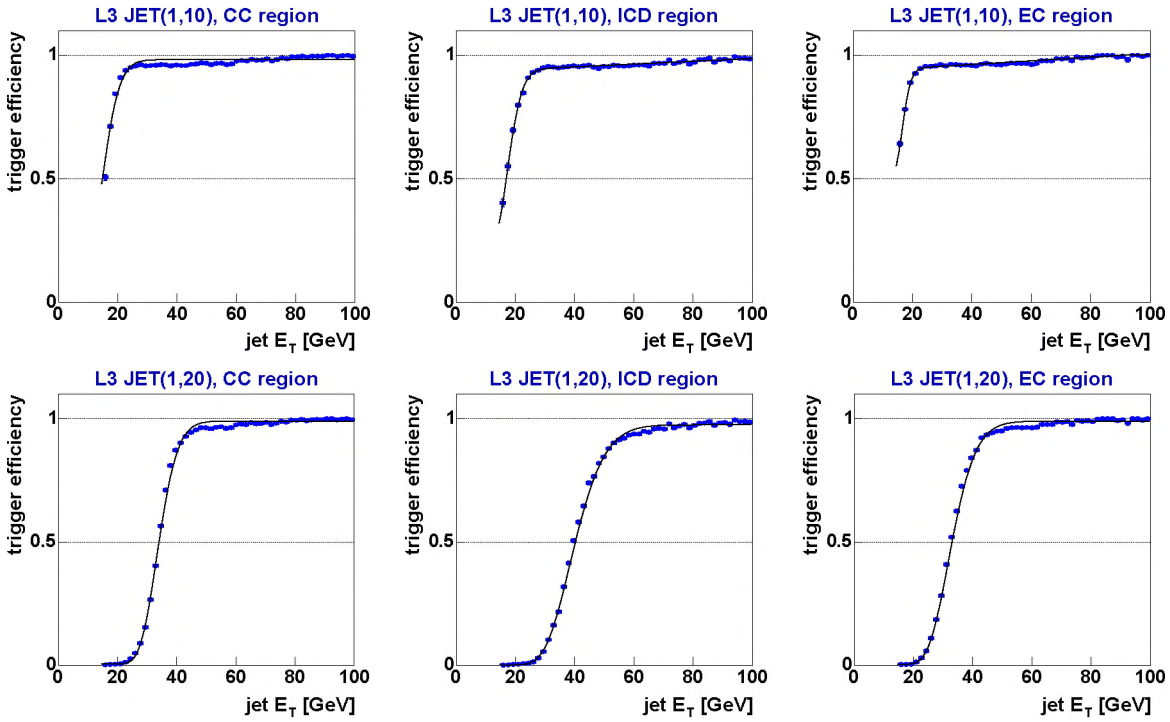

Figure 4.4: *Third level trigger efficiencies for the three different calorimeter ranges, as a function of jet E_T. The terms shown are used in the v11 and earlier versions of the trigger. Only jets that pass the L1 and L2 trigger requirements are used. The line represents the fit of a turn-on function with an additional slope. The errors on the fit are taken into account as a systematic uncertainty on the trigger efficiencies.*

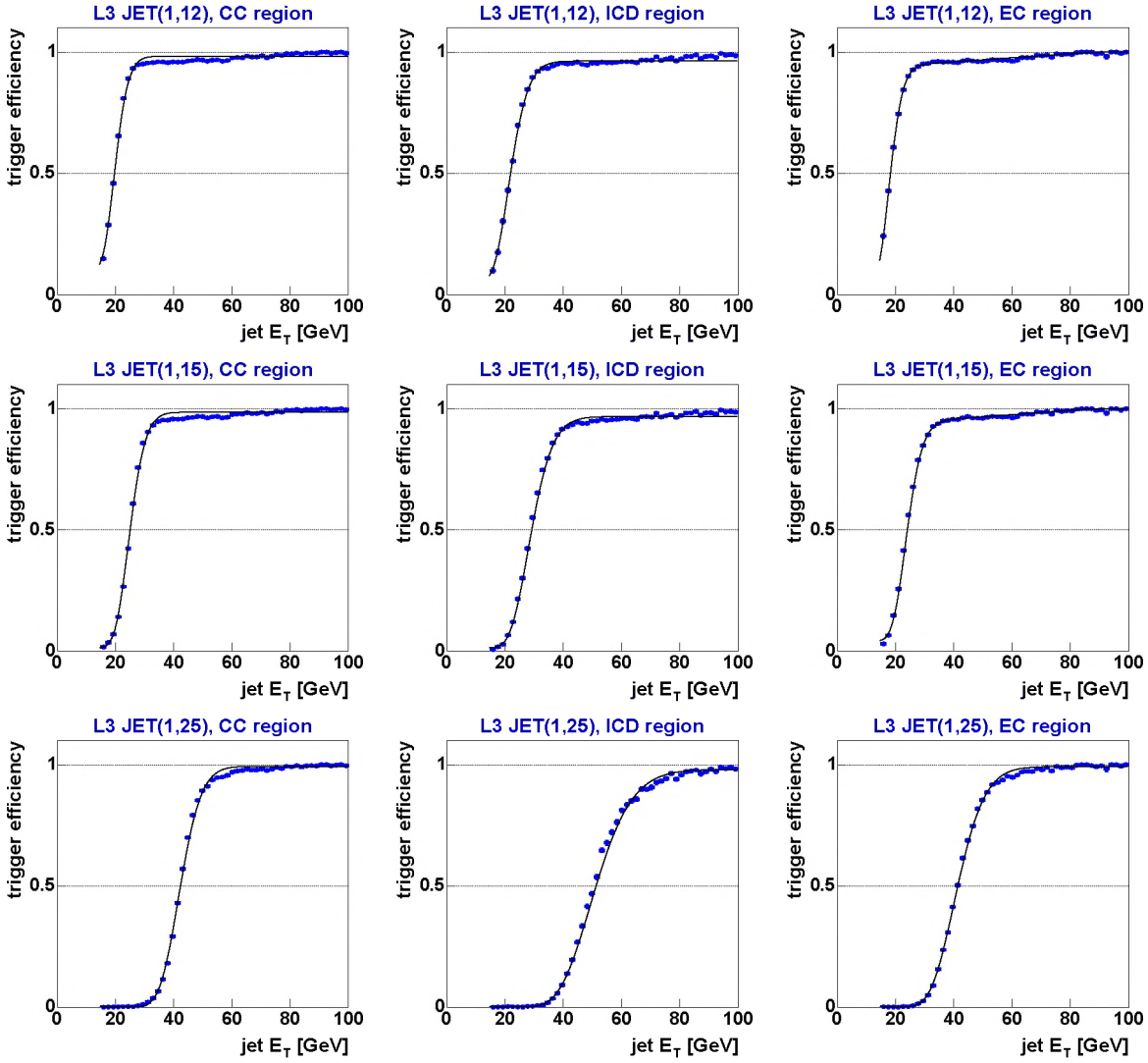

Figure 4.5: *Third level trigger efficiencies for the three different calorimeter ranges, as a function of jet E_T. Shown are the terms used in the v12 version of the trigger. Only jets that pass the L1 and L2 trigger requirements are used. The line represents the fit of a error function with an additional slope. The errors on the fit are taken into account as a systematic uncertainty on the trigger efficiencies.*

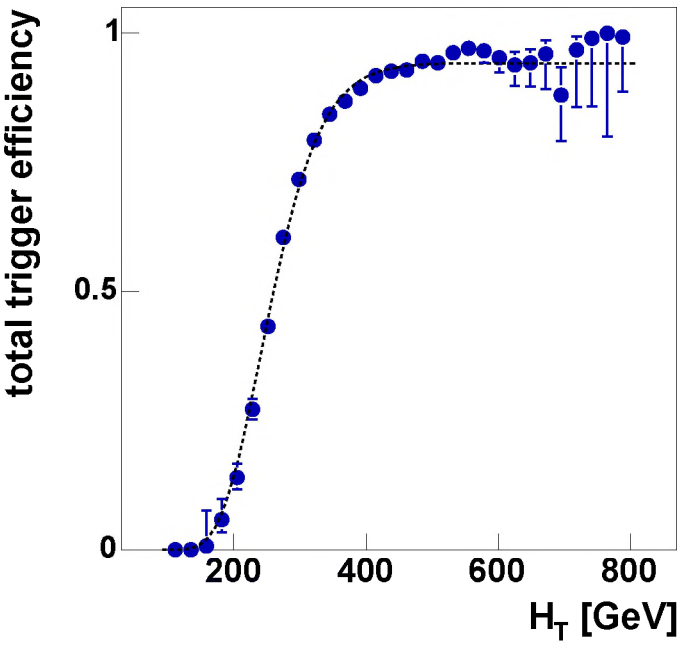

Figure 4.6: *The total (L1×L2×L3) trigger efficiency as a function of H_T, determined for $t\bar{t}$ all-jets Monte Carlo by using efficiencies determined on data. The efficiency is obtained by convolution with the jet-based turn-on curves from Figures 4.1 through 4.5.*

4.3.1 Overall trigger efficiency

Luminosity weighting

It is now possible to determine the efficiency to collect a $t\bar{t}$ all-jets event with the signal triggers. Since the efficiency depends on the version of the trigger, the total trigger efficiency is defined as the luminosity weighted average of the separate trigger efficiencies ε_i^{trig}, so

$$\varepsilon_{tot}^{trig} = \frac{\varepsilon_{\mathrm{v8}}^{trig} \cdot \mathcal{L}_{\mathrm{v8}} + \varepsilon_{\mathrm{v9}}^{trig} \cdot \mathcal{L}_{\mathrm{v9}} + \varepsilon_{\mathrm{v10}}^{trig} \cdot \mathcal{L}_{\mathrm{v10}} + \varepsilon_{\mathrm{v11}}^{trig} \cdot \mathcal{L}_{\mathrm{v11}} + \varepsilon_{\mathrm{v12}}^{trig} \cdot \mathcal{L}_{\mathrm{v12}}}{\mathcal{L}_{tot}}, \tag{4.6}$$

where $\mathcal{L}_i$ are the luminosities for the different trigger versions as listed in Table 4.1 and ε_i^{trig} changes per trigger configuration as described in Section 4.1.2.

Trigger efficiency

The total trigger efficiency ε_{tot}^{trig} is calculated on an event-by-event basis, and depends of the number of jets in the event and on H_T. Figure 4.6 shows the total trigger efficiency, ε_{tot}^{trig}, as a function of the JES corrected H_T for a sample of six-jet $t\bar{t}$ all-jets events. In the regime where the $t\bar{t}$ all-jets events are expected (six or more jets, $H_T > 350$ GeV), the efficiency is over 85%. Above $H_T > 400$ GeV, the plateau efficiency is 0.943 ± 0.004. The average efficiency for the different trigger levels is presented in Figure 4.7. The loss in efficiency for $t\bar{t}$ signal is dominated by the L1 inefficiency. The trigger efficiency on an event basis is used as an event weight in the final efficiency calculation.

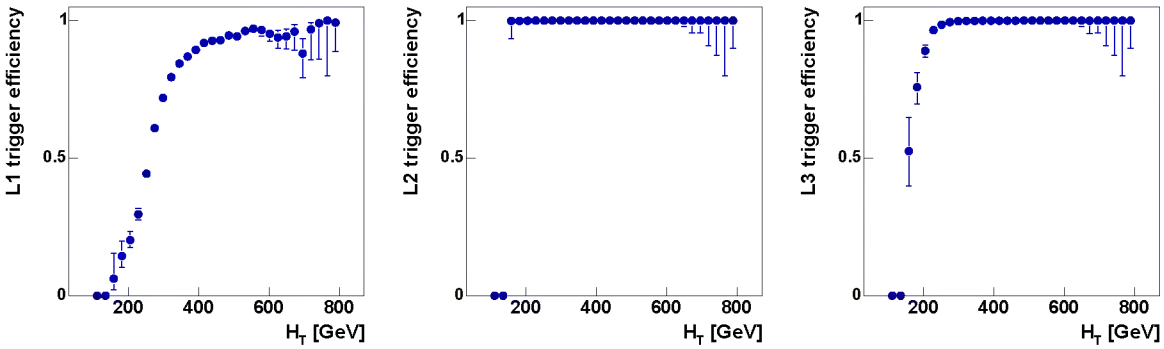

Figure 4.7: *Efficiency for $t\bar{t}$ all-jets Monte Carlo events, as a function of JES corrected H_T, for the three different trigger levels. As can be observed from the leftmost figure, the inefficiency is almost completely dominated by L1.*

Rates

The average triggering rate for the v11-v12 triggers is around 35-40 Hz at L1, 10-20 Hz at L2 and 4-5 Hz at L3, for runs with an instantaneous luminosity of around $80 \cdot 10^{30}$ $\mathrm{cm}^{-2}\mathrm{s}^{-1}$, which is typical for the period when the data was collected. Higher instantaneous luminosities mainly affect the first and second level trigger rates, particularly in the v12 trigger.

4.3.2 Trigger simulation and Monte Carlo

For comparison, we also simulate the trigger response using Monte Carlo techniques [59].

During the development of the 4JT10 and 4JT11 triggers, the predicted efficiency was between 98% (v8 version) and 91% (v12 version), which is consistent with the results measured in data. The major difference between data and Monte Carlo is that in the simulation the L1 efficiency has a faster turn-on, which also causes the total trigger efficiency to become fully efficient earlier.

To study the trigger simulation, we compare it to the efficiency measured using turn-on curves similar to Figures 4.1 through 4.5, but measured on trigger simulated $t\bar{t}$ all-jets Monte Carlo events instead of data. Figure 4.8 shows the performance of the complete trigger chain as a function of H_T, from Monte Carlo and through application of the turn-on curves. The difference between the two curves is a measure for how well the jet-based parametrization method predicts the total efficiency. The trigger simulation also models the correlations between the triggered jets. The fact that there is only a small difference between the two curves means that the correlation between the jets is a small effect. The difference between the two fitted curves in Figure 4.8 is used as a systematic uncertainty on the measurement of the trigger efficiency.

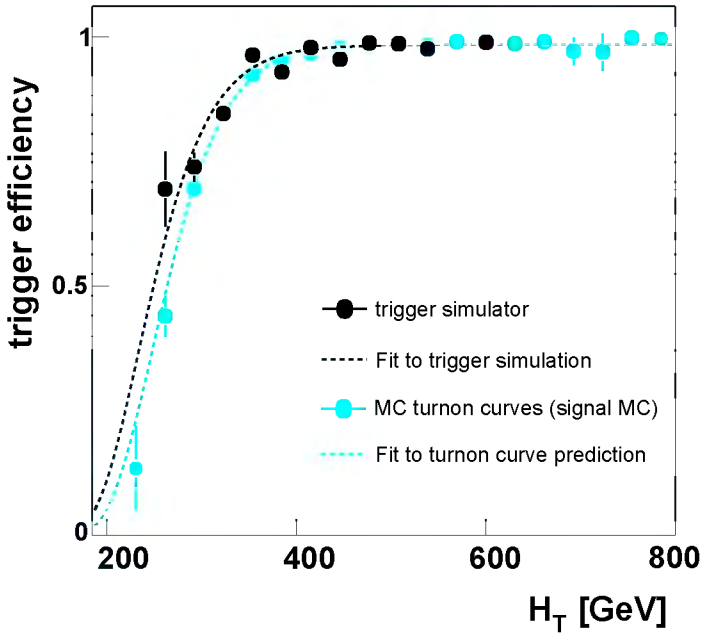

Figure 4.8: *The total (L1×L2×L3) trigger efficiency as a function of H_T. Shown are the efficiencies measured by direct simulation (black markers) and by application of Monte-Carlo simulation based turn-on curves (Grey markers).*

4.4 Simulated signal

In the Monte Carlo simulation, a top mass of $m_t = 175$ GeV/c^2 (with $\Gamma_t = 0$) is used. The W boson mass is set to 80.4 GeV/c^2. After the Monte Carlo event generation, the particles from simulated $t\bar{t}$ events are processed through D0GSTAR [30], a GEANT3 [31] simulation of the DØ detector. D0GSTAR is a full detector simulation, including the plate geometry of the calorimeter. Additional minimum bias proton-antiproton events are added to the Monte Carlo events. The number of minimum bias events follows a Poisson distribution with a mean of 0.8. The detector response is simulated by d0sim [32]. The simulated $t\bar{t}$ events are reconstructed with the same reconstruction chain as data.

We will examine how well the $t\bar{t}$ events can be reconstructed after the whole detector simulation and reconstruction is applied.

4.4.1 Parton-level kinematics

To compare Monte Carlo events to data, we can only use reconstructed physics objects. In the $t\bar{t}$ all-jet channel we are experimentally restricted to jets that originate from quarks and gluons. This section studies the behavior of jets that are matched to partons.

Jet matching

To define a jet as coming from a certain Monte Carlo parton, we require the parton from t or W decay to be close to the jet axis. A requirement in η, ϕ space of $dR < 0.3$ is used to match the jet and the Monte Carlo parton. The dR distribution between jets and partons in $t\bar{t}$ all-jets events can be seen in Figure 4.9. If a jet is within $dR < 0.3$ of a Monte Carlo parton, the jet is referred to as 'Monte Carlo matched'. This method

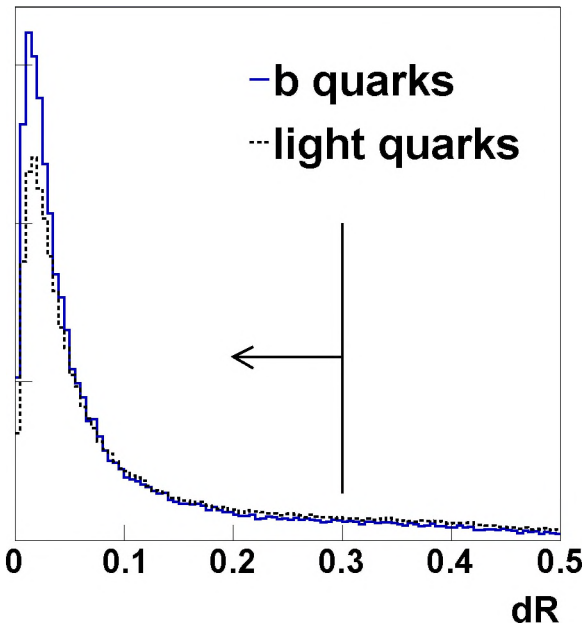

Figure 4.9: *Distance in R space between Monte Carlo parton and closest jet, as observed in $t\bar{t}$ all-jets Monte Carlo. A cut of $dR < 0.3$ is applied for the jet to be considered matched to a parton. The solid (dashed) curve represents the distribution for b (light) quarks.*

matches 93% of all partons from the hard interaction to a jet. Only 19% of all $t\bar{t}$ all-jets events have *all* partons matched to jets. The reason for this will become clear shortly.

W bosons and b jets

To identify top events, first it is necessary to identify the decay products of the top quark: W bosons and b quarks.

The jets are selected with the same selection criteria as in data: $E_T > 15$ GeV. The left-hand plot in Figure 4.10 shows the E_T distribution of jets matched to a b quark. The E_T distribution is expected to be diluted by neutrinos from the B-meson decay that cannot be detected. The jet energy scale correction does not account for this effect, which explains the shift to lower jet E_T. For W bosons in $t\bar{t}$ all-jets events, two jets have to be identified. The right-hand plot in Figure 4.10 suggests that there is a bias towards higher transverse momenta, which is to be expected given the jet E_T requirement.

The result of the mass reconstruction of the W bosons in $t\bar{t}$ all-jets events can be seen in Figure 4.11. Figure 4.11 only shows those $t\bar{t}$ events that have all jets matched to a quark (19% of the total number of events). From a Gaussian fit to this distribution we obtain:

$$M_W = 83.7 \pm 0.12 \text{ GeV/c}^2; \tag{4.7}$$

and

$$\sigma_W = 12.3 \pm 0.2 \text{ GeV/c}^2. \tag{4.8}$$

Thus, given the input W boson mass of 80.4 GeV/c^2, there is a bias towards larger reconstructed invariant masses. Furthermore, the M_W distribution in Figure 4.11 exhibits a non-Gaussian tail at high invariant masses.

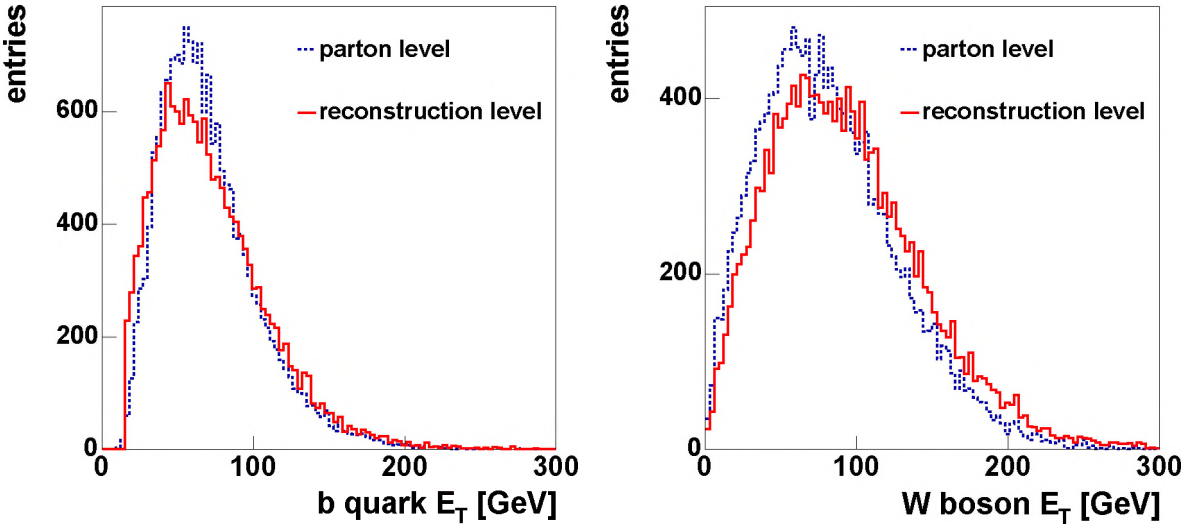

Figure 4.10: *Transverse energy of b quarks (left) and di-jet reconstructed W bosons (right) in $t\bar{t} \rightarrow$ all-jets events, for parton-level (dashed line) and reconstructed jet-level (solid line).*

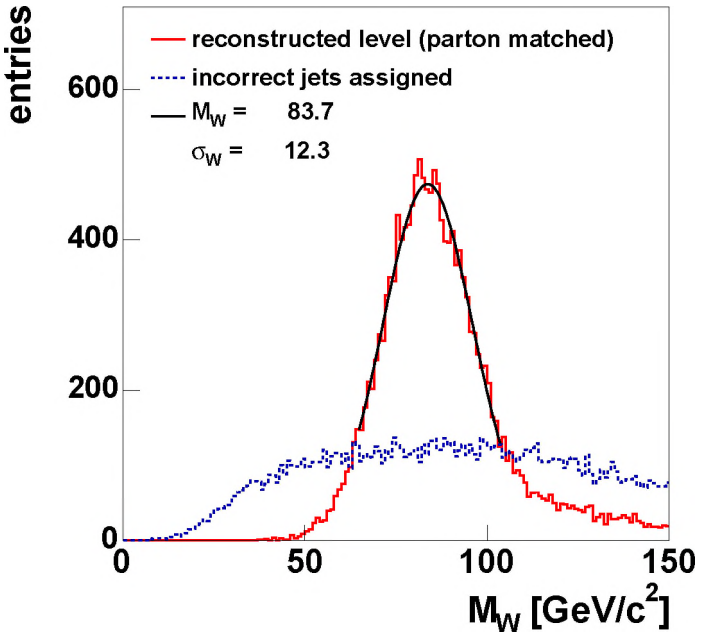

Figure 4.11: *Reconstructed mass of W bosons, where all partons have a reconstructed jet matched to them within $dR < 0.3$. The jets are used to calculate the invariant mass. Also shown is the distribution when the jets are not correctly assigned to the W boson (dashed histogram). The curve is a Gaussian fit.*

The origin of the tail in the W boson mass spectrum can be seen from Figure 4.12, which shows the observed transverse energy of the jet as a function of the transverse energy of the matched quark. There is a significant fraction of jets that have additional energy, which can be attributed to gluon radiation off other partons in the event and reconstruction effects like the splitting and merging of jets. We apply an additional requirement of $|E_T(\text{quark}) - E_T(\text{jet})| = \Delta(E_T) < 16$ GeV to remove badly matched jets. This requirement is illustrated by the dashed lines in Figure 4.12. Figure 4.13 shows the resulting M_W distribution. Now the reconstructed W boson mass is near the input value, $M_W = 80.2 \pm 0.13$ GeV/c^2.

The bias in the reconstructed W boson mass is thus created by effects which are also expected to occur in data. We take into account the shifted W boson mass in the $t\bar{t}$ cross section measurement.

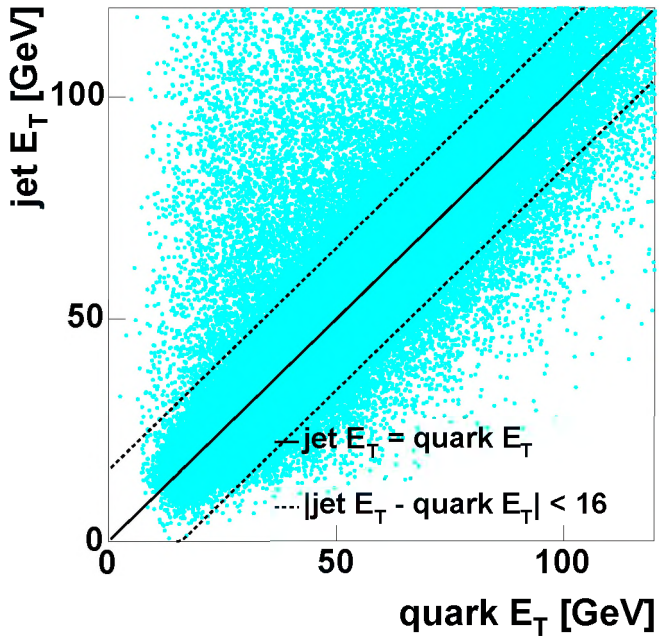

Figure 4.12: *The E_T of the matched jet as a function of the quark E_T. The dashed lines represent a $\Delta(E_T) = |\text{jet } E_T - \text{quark } E_T| < 16$ GeV requirement, the solid line indicates where $E_T(\text{jet}) = E_T(\text{quark})$.*

Top quark reconstruction

Once the jets of W boson and b quark are matched, we can extract the top mass. To match we only require that the jet-parton distance $dR < 0.3$. Figure 4.14 shows the top mass when all jets are matched to the correct partons

$$m_t = 178.7 \pm 0.3 \text{ GeV/c}^2. \tag{4.9}$$

Again, there is a slight bias in the invariant top mass. The width and mean value come from a fit of a Gaussian function to the distribution of correctly reconstructed events. The width of the mass peak is completely dominated by smearing effects, and can be interpreted as a resolution

$$\sigma_t = 23.4 \pm 0.3 \text{ GeV/c}^2. \tag{4.10}$$

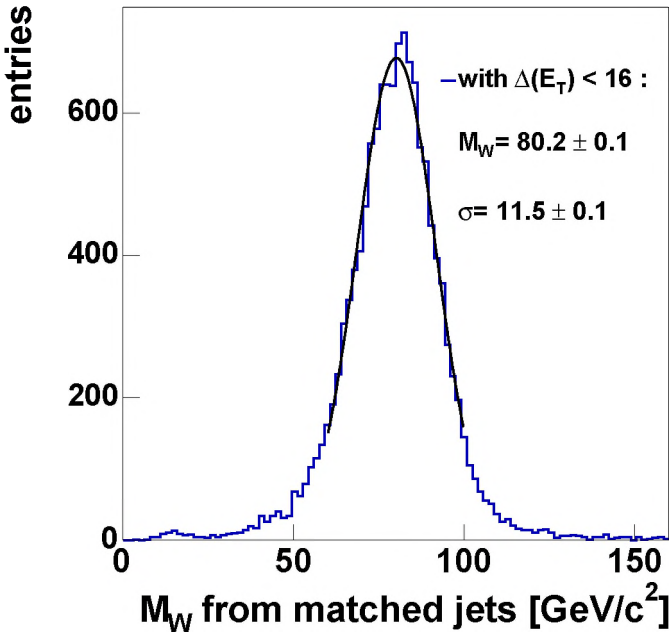

Figure 4.13: *The invariant mass (histogram) of the W boson after a* $\Delta(E_T) < 16$ GeV *requirement. The curve represents a Gaussian fit.*

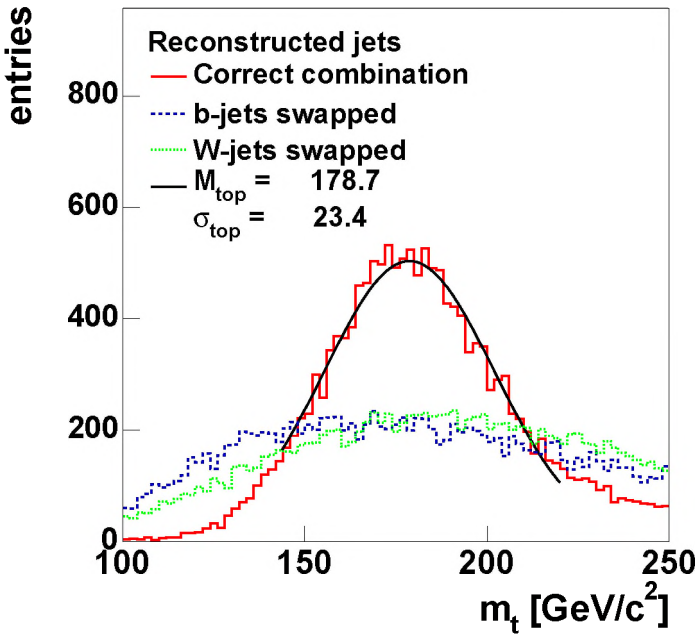

Figure 4.14: *Reconstructed top mass, where all partons have a matched reconstructed jet within* $dR < 0.3$. *Shown are the correct jet-assignments (histogram), the solid curve represents a fit using a Gaussian function. Also shown are the results if b jets are swapped (dashed histogram) or jets for W bosons are incorrectly assigned (dotted histogram).*

The large value of σ_t suggests that it is not easy to measure the genuine top width in this top production channel, as it is dominated by jet smearing.

We can also swap the jets of W bosons or b quarks that originate from different top quarks. The results for these wrongly assigned jets are also shown. Finding the correct jet combination for the two W bosons will be a great challenge.

4.5 Preselection of events

Before starting the actual analysis, the data and Monte Carlo event samples are filtered to optimize signal purity. In this process, called preselection, events of a global type which is similar to the expected signal are selected by making some cuts which maximize the background rejection.

As the analysis presented here tries to identify $t\bar{t}\rightarrow$ all-jets events, our expected final state consists of events with six or more jets and no isolated leptons.

Table 4.2 lists all the efficiencies for the different preselection cuts, which are presented in the following paragraphs. The effect of the consecutive cuts on the data set is listed in Table 4.3.

preselection cut	cut efficiency	total efficiency
isolated μ veto	1.0000 ± 0.0005	1.0000 ± 0.0005
isolated electron veto	1.0000 ± 0.0005	1.0000 ± 0.0005
$N_{vertex} = 1$	0.9645 ± 0.0065	0.9645 ± 0.0065
$N_{jets} \geq 6$	0.3405 ± 0.0045	0.3284 ± 0.0035

Table 4.2: *Efficiencies of the different preselection cuts for $t\bar{t}$ all-jets Monte Carlo. Shown are the efficiencies of the individual cuts, and overall efficiency after each cut. The uncertainties are caused by the limited size of the Monte Carlo event sample.*

preselection cut	events rejected	events left	fraction rejected
4JT10/4JT12 trigger	-	855k	-
data quality	182k	671k	0.213
isolated μ veto	9	671k	0
isolated electron veto	70	671k	0
$N_{vertex} \neq 0$	5k	666k	0.007
$N_{jets} \geq 6$	383k	283k	0.575
$N_{vertex} = 1$	84k	199k	0.297

Table 4.3: *Number of data events rejected in the preselection.*

4.5.1 Isolated lepton veto

The analysis discussed in this thesis studies events without isolated, high p_T leptons. Not accidentally, the veto on isolated leptons is exactly orthogonal to the selection done on isolated leptons in DØ's lepton+jets analyses [51]. Any event that passes these lepton isolation requirements will be considered a $t\bar{t} \rightarrow$ lepton+jets candidate, and should hence be removed from the dataset. Tables 4.2 shows that the lepton veto has no effect on signal Monte Carlo.

4.5.2 Primary vertex veto

Events that do not have a correctly reconstructed vertex are rejected. This happens rarely in our data sample. As already shown in Section 3.6.1, the efficiency to reconstruct a primary vertex in data is 100% in the central detector region. This can also be seen in Table 4.3: practically no events are rejected.

Multiple interactions

At the Tevatron, it is not unlikely that there is more than one $p\overline{p}$ interaction per beam-crossing. Of events with six or more jets, around 13% of the events[1] is expected to come from multiple interaction events, where the second interaction is also a hard QCD process [22]. As the whole interaction region spans an area of $|z| < 50$ cm, these double-vertex events can be removed by looking at the location of the second primary vertex. We reject events that have two well-defined primary vertices, with the following requirements:

- We demand that at least two tracks from a PV are inside the $dR < 0.5$ jet cone for the jet to be assigned to that particular PV;
- If two unique, well defined PVs are found, which are more than 3 cm apart and both have at least three jets assigned, the event is rejected.

Figure 4.15 shows the distribution of the primary vertices in z. The right plot in Figure 4.15 shows the difference in z, δz, if additional primary vertices are found (markers). The dashed histogram shows the expected distribution if the additional PV is randomly drawn from the z distribution. The two distributions agree within statistical uncertainties.

The effect of the PV selection criteria on Monte Carlo events is small, as can be observed in Table 4.2. The veto on a second PV decreases the efficiency for $t\bar{t}$ all-jet events by 4%. This requirement on QCD data reduces the event sample by 30%, as listed in Table 4.3.

[1] In this case the second $p\overline{p}$ interaction is an actual, hard, QCD multijet process. The observed cross section for these depends on the requirements on the energy of the jets. The contribution of this type of background events is very dependent on the E_T cut of the jet system. For a jet $E_T > 10$ GeV, 20% of the rate is expected to come from multiple interactions, at $E_T > 20$ GeV this is already down to 2% [22]. The value of 13% was derived through intrapolation of the exponential behaviour of the multijet cross sections in QCD (ALPGEN) Monte Carlo at $\sqrt{s}$ =1.8 GeV. All these numbers come from Run 1 Monte Carlo studies and have significant uncertainties.

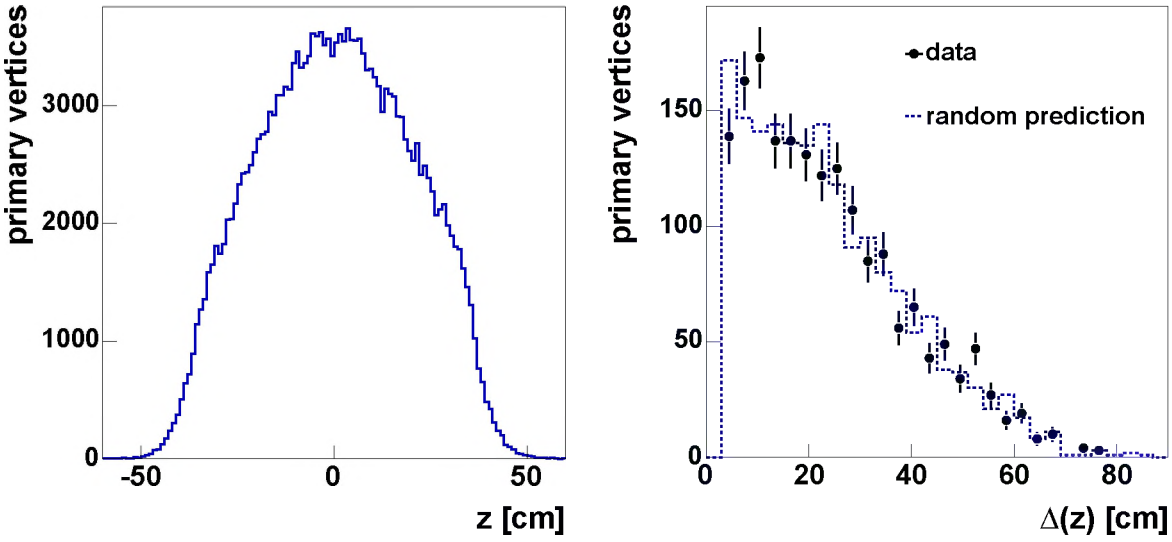

Figure 4.15: *Left: The z distribution for all primary vertices with at least three associated jets. Right: The difference in z between the first and second vertex (both are required to have three associated jets). The markers show the distribution as observed in six-jet data, the dashed histogram represents the expected distribution for random additional interactions.*

4.5.3 Jet multiplicity

Figure 4.16 shows the number of jets present in Monte Carlo $t\bar{t}$ all-jets events. As can be observed, the majority of events does actually not have six separate reconstructed jets within the detector acceptance. There is a requirement on the number of jets to be over the six-jet threshold:

$$N_{jets} \geq 6, \tag{4.11}$$

which is motivated by the following arguments:

- in QCD, the jet multiplicity falls off exponentially, so requiring many jets reduces our background more than it reduces our signal;
- if less than six jets are required, it would be practically impossible to reconstruct two top masses in the events.

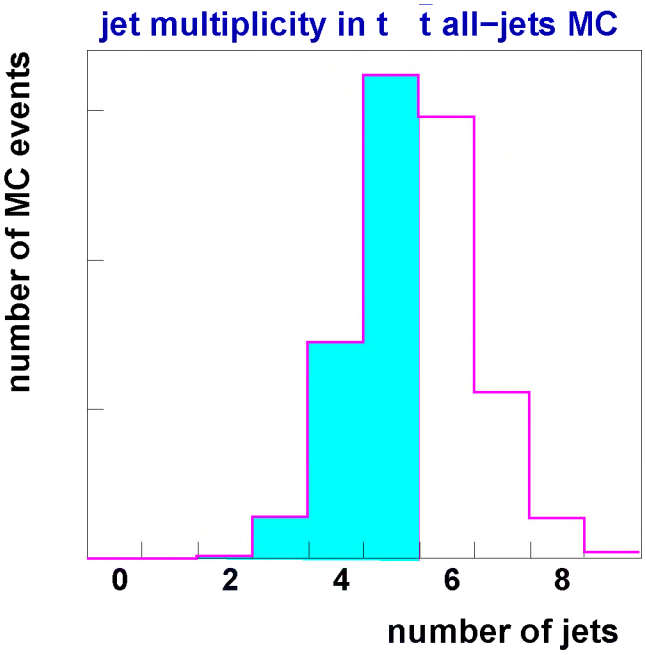

Figure 4.16: *Number of jets reconstructed in $t\bar{t}$ Monte Carlo events. Events with less than six jets are rejected from the analysis.*

Chapter 5

Signal extraction

The analysis that is presented in the following chapters searches for $t\bar{t}$ events with six or more jets. The data sample, after preselection, consists of almost 200k events, and is dominated by QCD multijet background. The event selection is aimed at reducing this background.

5.1 Analysis outline

An important characteristic of $t\bar{t}$ events is the presence of two b quarks in the final state. Although b quarks are also produced directly in QCD, the $b\bar{b}$+4 jets cross section is expected to be about three orders of magnitude smaller than the $q\bar{q}$+4 jets cross section. In a small fraction of the $q\bar{q}$+4 jet events (around 2%) a light quark jet (or jet originating from a gluon) is wrongly identified as a b jet. By requiring the presence of a candidate b jet (see next paragraph), the background is suppressed by two orders of magnitude, while $t\bar{t}$ events are not rejected in the ideal case. The efficiency for signal depends on the method of b jet identification, but is typically between 20-50%. The identification of b candidates can thus be used to enhance the $t\bar{t}$ content in the sample.

In this thesis, the method to identify the b jet candidates is the detection of a secondary vertex: b quarks hadronize to B mesons which have a relatively long lifetime, caused by the fact that b quarks primarily decay through weak interactions. With a typical lifetime of around $2{\cdot}10^{-12}$ s, the B mesons are expected to travel distances of the order of 4 mm[1]. The decay of the B meson leads to a displaced, or secondary vertex. The algorithm used for secondary vertex reconstruction is called Secondary Vertex Tagger (SVT) and is described in Section 3.6.2. An event that contains at least one b jet candidate is considered 'tagged'. The b identification is discussed in Section 5.2.

The dataset is divided in two samples containing tagged and untagged events, respectively. At this stage both tagged and untagged samples are dominated by QCD background. Around 50-100 $t\bar{t}$ events are expected in the dataset of 16k tagged events. Furthermore, no kinematic or topological differences are expected between tagged and untagged background events. In the final analysis we measure the $t\bar{t}$ cross-section in the

[1]Typical γ factors are around 7

tagged sample. As will be shown, even after additional selection requirements this sample is still dominated by background. To predict the number of background events we use the whole (tagged and untagged) data sample to parametrize the background content in the tagged data. This analysis step will be explained in Section 5.2.2.

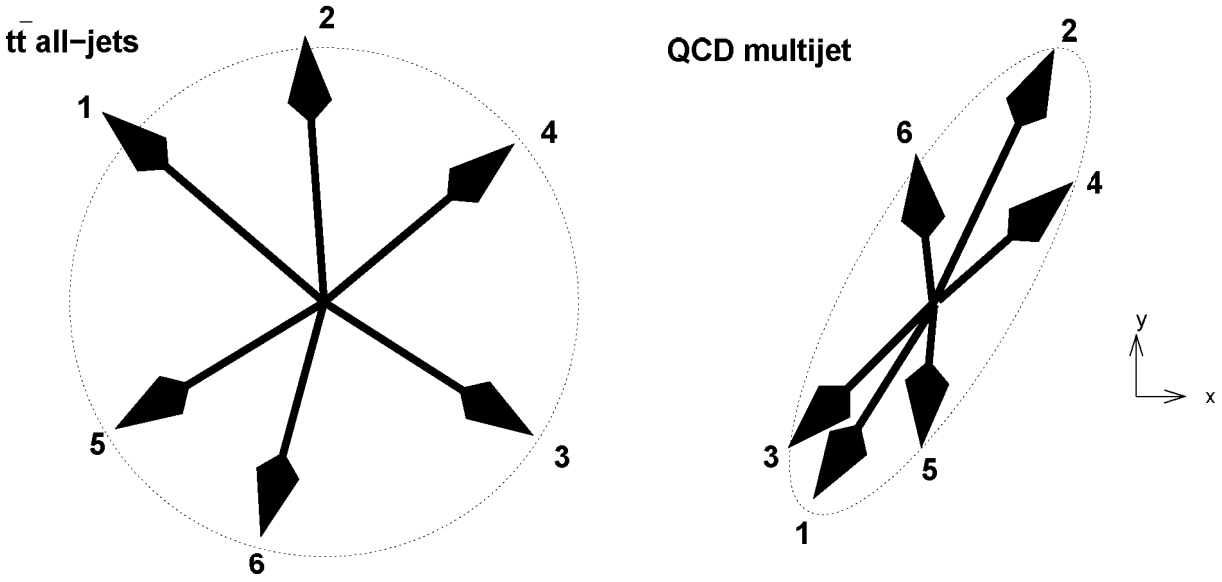

Figure 5.1: *A graphical representation in the x, y plane of the detector for six-jet $t\bar{t}$ all-jets events (left) and QCD multijet events (right). The length of the arrows represents the energy of the jets.*

After b tagging, it is possible to use the kinematic and topological difference between QCD and $t\bar{t}$ events to further reduce the background. Figure 5.1 illustrates the difference between a 'typical' $t\bar{t}$ all-jets event and a QCD multijet event. The QCD event is created by a basic $p\bar{p} \rightarrow q\bar{q}/gg+X$ process, where 'soft' extra jets are created through higher order processes. The background QCD events come mainly from the production of light quarks. Since relatively little energy is needed to produce light quarks and a large range in x of the parton distribution function can be probed, the final quark system can have a significant amount of (longitudinal) momentum along the beam axis. A significant fraction of the QCD multijet events can hence be expected to have more jets at high values of $|\eta|$, or whole events can be skewed towards the (anti)proton direction.

For $t\bar{t}$ production the boosting of events is much more unlikely, as there is barely enough energy available for the tops to acquire substantial additional momentum. Consequently, top quark pairs are produced nearly at rest and the jets in $t\bar{t}$ events are more central. Also, the jets in $t\bar{t}$ events tend to have roughly the same transverse momentum, no matter if the jet originated from a b quark or from the hadronic W decay.

The background for hadronic $t\bar{t}$ signal is further reduced by looking at a set of global event quantities that are sensitive to the differences between multijet QCD and $t\bar{t}$ signal. There are *many* observables that probe the difference between multijet QCD data and $t\bar{t}$ events in global distributions, but no single observable has enough discriminating power. In Section 5.3 a variety of these observables are discussed. It is possible to combine these

quantities in one variable that discriminates between $t\bar{t}$ and QCD events. In this case, an artificial neural network (ANN) is used, as is discussed in Section 5.4. Combining the variables in an ANN has the advantage that the correlation between the quantities used is taken into account, which leads to a more effective background rejection. As will be shown, these techniques reduce the background to a level where the $t\bar{t}$ signal becomes statistically significant.

5.2 Event tagging

The presence of two b quarks in $t\bar{t}$ decays leads to a relatively high yield of b candidate jets. First, the effect of the secondary vertex tag requirement on $t\bar{t}$ signal events will be discussed. Secondly, the behavior of the vertex tag on the background will be investigated. The overwhelming presence of QCD events in the tagged (and untagged) sample allows for a straightforward measurement of the probability that a secondary vertex is assigned to a jet. As, even in the tagged sample, the top content is completely negligible with respect to the background, there is no significant $t\bar{t}$ contribution to the tagging probabilities that are thus derived.

The probability function that a jet contains any (fake or real) secondary vertex is called a Tag Rate Function (TRF). The TRF is defined as the probability to tag a background event in the (background-dominated) sample, where no distinction is made between tagged jets originating from b, c, light quarks or gluons. The TRF is measured per jet on the complete sample. The probability to find a secondary vertex associated with a jet in the sample is then used to calculate the probability that an event contains one or more tagged jets. These probabilities are derived using the technique described in Section 4.3.

5.2.1 Tagging $t\bar{t}$ events

Using the SVT tagging efficiencies per jet as measured in data (Section 3.6.3), the SVT-tagging efficiency for $t\bar{t}$ all-jets events can be derived on an event-by-event basis, using the method from Section 4.3. The average efficiency to tag a $t\bar{t}$ all-jets event with six or more jets is determined to be:

$$\varepsilon_{t\bar{t}}^{SVT} = 0.564 \pm 0.014, \tag{5.1}$$

which also includes the accidental tagging of the jets from W boson decays. Combining this with the preselection efficiencies of 33.0% (Table 4.2), trigger efficiency of 85% (Section 4.3.1), the total sample is expected to contain around 90 signal events, in a sample of 16k tagged events. The final event tagging efficiency is obtained after all selection criteria, to account for the dependence on the event shape. The used method is discussed in Section 6.1.

5.2.2 TRF measurement

An accurate prediction of the number of background events is necessary to observe a relatively small excess of $t\bar{t}$ candidate events in the tagged sample. In this analysis, the

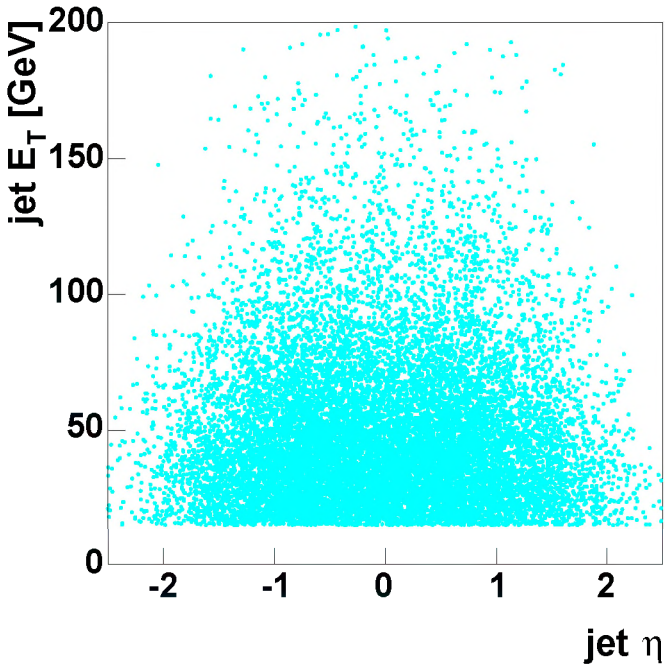

Figure 5.2: *Jet E_T and η for jets with an SVT tag.*

tagging probability is measured on the same complete, tagged and untagged data sample. The use of the same data sample is crucial to the analysis, as the value and shape of the TRF depends on jet multiplicity, energy scale and flavor content of the sample. For reasons we will explain in Section 5.2.3, we exclude double-tagged events with $dR_{tags} < 1.5$ between the b candidate jets from the TRF measurement.

The TRF is modeled as function of the transverse energy and rapidity of the jets. Figure 5.2 shows the jet E_T versus jet η for the tagged sample. If we assume that there are no η and E_T correlations, the tag rate function p^{jet} factorizes:

$$p^{jet}(E_T, \eta) = f(E_T)g(\eta), \tag{5.2}$$

with $f(E_T)$ the probability that a jet with transverse energy E_T has an SVT tag, $g(\eta)$ the probability that a jet at η is tagged. p^{jet} corresponds to the absolute probability to tag a jet. In Figures 5.3 and 5.4 the individual functions $f(E_T)$ and $g(\eta)$ have been normalized to the same absolute probability as $p(E_T, \eta)$. Obviously, only jets that contain tracks can be used to construct secondary vertices, so only *taggable* jets are taken into account. The definition of jet taggability can be found in Section 3.2.2. The shape of the TRF function depends on the energy scale of the event. To take this dependence into account, the TRF is measured in four bins of H_T.

Figure 5.3 shows the behavior of the jet TRF for different H_T bins:

$$p^{jet}(E_T, \eta, H_T) = \frac{N_{tagged}(E_T, \eta, H_T)}{N_{taggable}(E_T, \eta, H_T)}, \tag{5.3}$$

as function of the jet E_T, in four bins of H_T. Shown are the observed TRFs as a function of E_T (markers), and the fitted distributions (line) with their uncertainties (dashed error

band). The function $f(E_T)$ (line) is fitted to these distributions, using a parametrization of the form:

$$f(E_T) = a_1 \cdot 0.5(1 + \mathrm{Erf}(\frac{E_T - a_2}{a_3\sqrt{E_T}})),$$

where Erf is the standard Gaussian error function.

The function $g(\eta)$ is obtained in a similar manner and is parametrized as:

$$g(\eta) = b_1 + b_2\eta^2 + b_3\eta^4 + b_4\eta^6 + b_5\eta^8 \exp(b_6\eta^2). \tag{5.4}$$

If $g(\eta)$ returns a negative value it is fixed to zero. Figure 5.4 shows the observed TRF in data as a function of η, and the fitted distribution of $g(\eta)$ (solid line) with its uncertainty band (dashed line). The tagged (and untagged) jet sample is observed to be independent of ϕ.

The values of the parameters of $f(E_T)$ and $g(\eta)$ are listed in Table 5.1. As can be observed from Figures 5.3 and 5.4 there are significant uncertainties on the shape and size of the tagging probability per-jet; the dashed lines represent the uncertainty on the shown TRF parametrization. The uncertainty on the TRF fit will be taken into account in the systematic uncertainty of the background prediction.

parameter	$0 < H_T < 200$	$200 < H_T < 300$	$300 < H_T < 400$	$H_T > 400$
a_1 [GeV$^{-0.5}$]	0.0267	0.0284	0.0351	0.0356
a_2	29.44	28.89	35.89	32.96
a_3 [GeV]	5.92	5.98	8.51	5.98
b_1	$14.51{\cdot}10^{-3}$	$18.92{\cdot}10^{-3}$	$22.90{\cdot}10^{-3}$	$28.79{\cdot}10^{-3}$
b_2	$-0.868{\cdot}10^{-3}$	$-1.037{\cdot}10^{-3}$	$1.56801{\cdot}10^{-3}$	$0.935167{\cdot}10^{-3}$
b_3	$-0.424{\cdot}10^{-3}$	$-0.825{\cdot}10^{-3}$	$-2.124{\cdot}10^{-3}$	$-2.655{\cdot}10^{-3}$
b_4	$32.36{\cdot}10^{-6}$	$83.57{\cdot}10^{-6}$	$71.32{\cdot}10^{-6}$	$250.25{\cdot}10^{-6}$
b_5	8.82	1.29	1.19	-59.46
b_6	-10.55	-7.13	-7.81	-19.68

Table 5.1: *The values of the fit parameters of the TRF η and E_T parameterizations, $f(E_T)$ and $g(\eta)$, for four different H_T bins.*

The jet TRF has been normalized to predict the total number of observed tagged jets. The normalization is fixed by the requirement:

$$N_{tagged}^{jets} = \sum_{jets} p^{jet} = \sum_{jets} f(E_T)g(\eta), \tag{5.5}$$

which is determined for each H_T bin separately, on the entire data sample. This normalization also ensures that the absolute number of jets is predicted properly.

Figure 5.5 shows the TRF performance as a function of jet pseudo-rapidity and transverse energy. The figure shows the number of observed and predicted b jet candidates. Figure 5.5 also shows that the TRFs predict the shape of the tagged jet η and E_T distribution within reasonable limits.

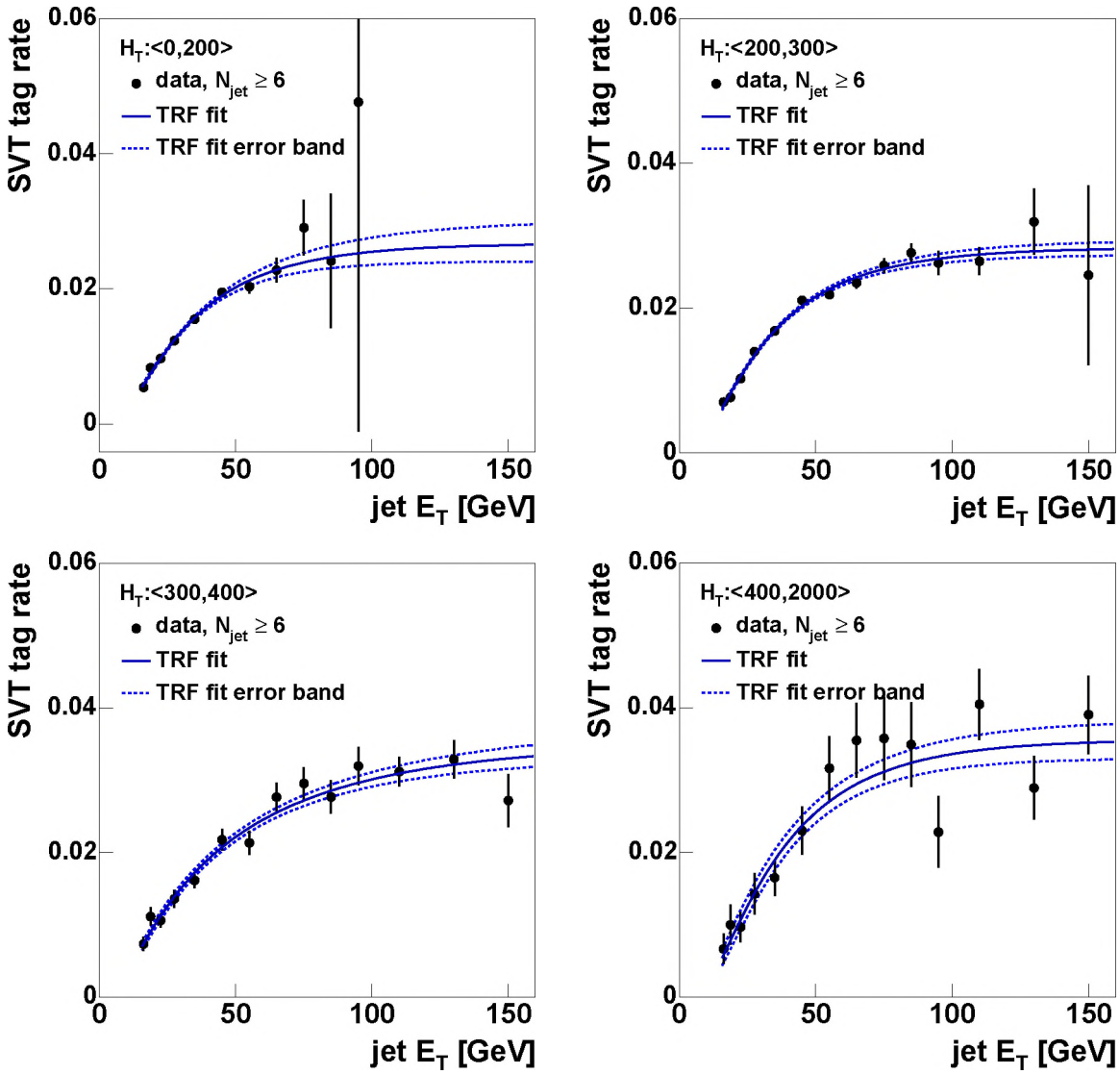

Figure 5.3: *The tag rate function as a function of E_T, for different H_T bins as indicated. The markers are the observed distributions in multijet data, the curves describe the TRF fit of $f(E_T)$ (solid line) and its uncertainty is indicated by the dashed curves.*

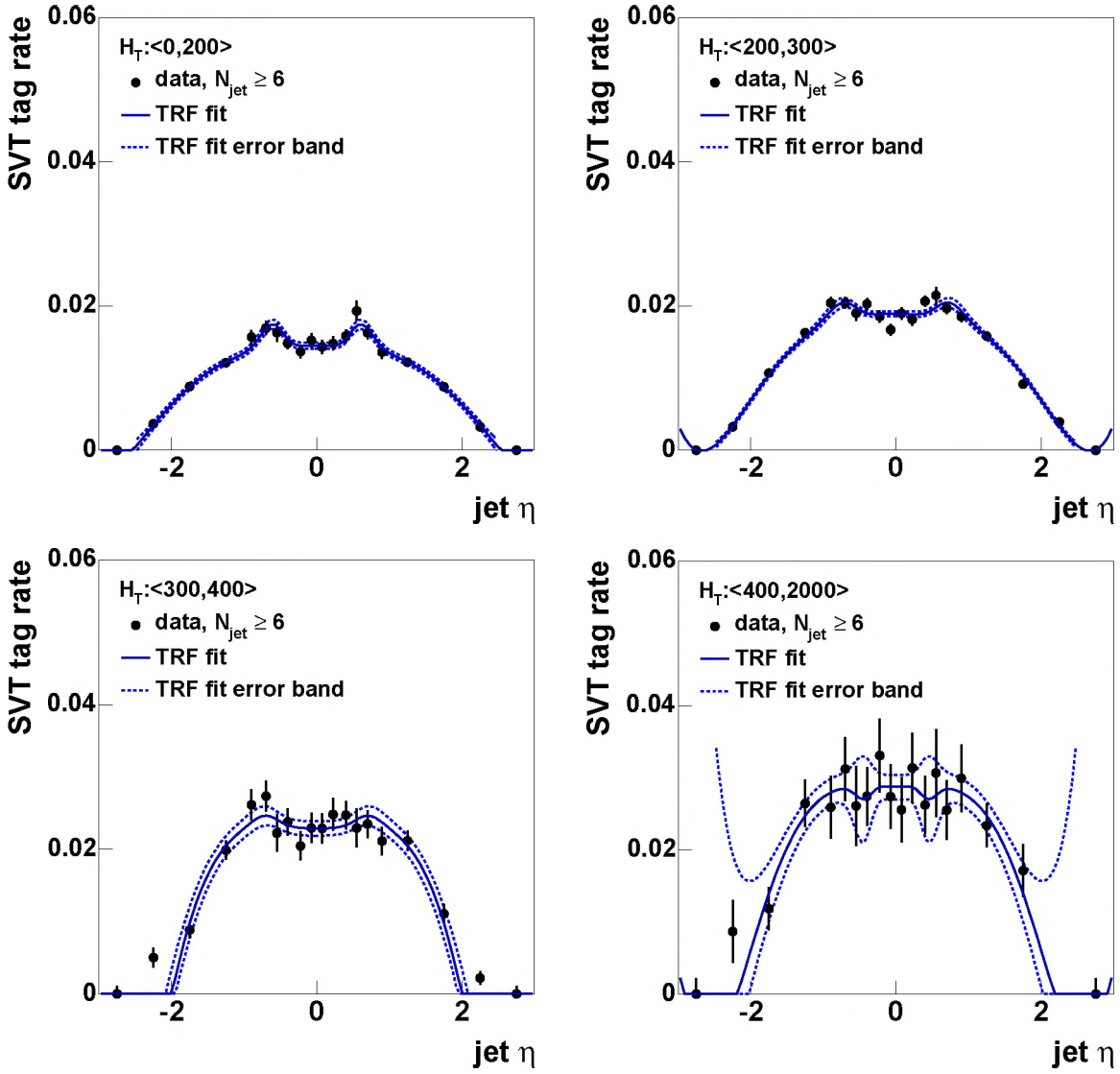

Figure 5.4: *The tag rate function as a function of η, for different H_T bins as indicated. The markers are the observed distributions in multijet data, the curves describe the TRF fit of $g(\eta)$ (solid line) and its uncertainty is indicated by the dashed curves. Jets with $|\eta| > 2.5$ do not pass the jet identification, and the points outside this range are only used for fit purposes.*

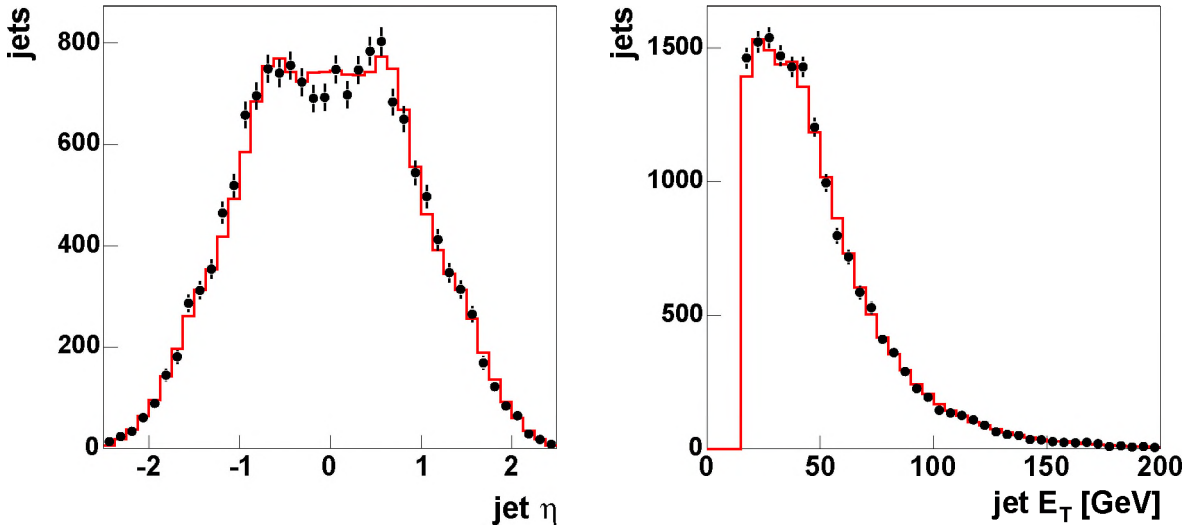

Figure 5.5: *Number of predicted and observed SVT tagged jets as a function of jet η and jet E_T. The histogram is the absolute number of predicted jets, the markers represent the observed jets with a secondary vertex.*

5.2.3 Jets from $b\bar{b}$ events

As mentioned previously, there also is an overwhelming number of tagged background events.

In events with two jets that contain secondary vertices[2] it is possible to study the angular correlation between the tagged jets. When an event contains two b jet candidates we refer to it as a double-tagged event. Most double-tagged events are expected to originate from QCD heavy quark production. If the two b candidate jets in the event behave like created by an isotropic process, they are presumed to come from mis-tagged light jets or other processes (like $t\bar{t}$) where the b quarks are randomly distributed with respect to each other.

To use the TRF method to predict the behavior of background in the tagged sample, the jets with a secondary vertex tag in the sample need to be randomly distributed. To calculate the probability that a background event is tagged, the probability for any jet to be tagged is used. The assumption is that there is no correlation between the b candidates in the event, so the probability is independent of the number of b candidates in the event. This has as a consequence that, if there is a significant contribution of $b\bar{b}$ content in the sample, the TRF method is biased.

Figure 5.6 shows the distribution in $dR_{tags} = \sqrt{(\Delta\phi)^2 + (\Delta\eta)^2}$, the distance in η, ϕ space between the two b candidate jets in double-tagged events. The markers represent the double-tagged data events. The histogram (+error band) is obtained by applying the TRF prediction to the individual jets in the events. There are about twice as many double-tagged events observed between $0.5 < dR_{tags} < 1.5$ as can be expected from

[2]The number of events with three jets with secondary vertices is negligible. There are 53 of such events in the sample, of which approximately 2 are expected to originate from $t\bar{t}$ production.

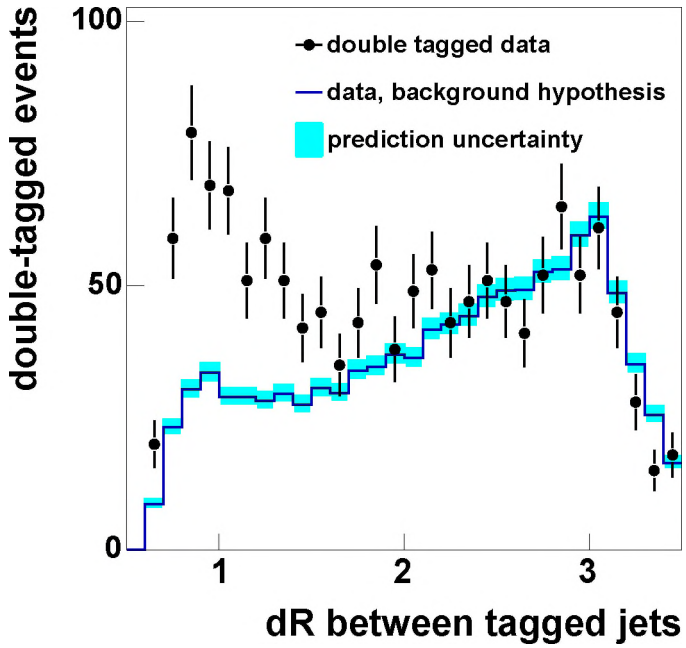

Figure 5.6: *dR_{tags} between two tagged jets, for both observed double-tagged data events (markers) and absolute number of predicted events if the double-tagged sample consisted of completely random tags (histogram). The uncertainty on the background prediction is given by the error band.*

random tags. On the other hand, the data above $dR_{tags} > 1.5$ can be described, within statistical limits, by random tags.

The excess of double-tagged events at low dR_{tags} is consistent with the presence of genuine b jets originating from gluon splitting $g \to b\bar{b}$. In this standard QCD process, a hard gluon is produced, which subsequently decays to two b-quarks. The higher the gluon momentum, the closer the b-jets will be.

$t\bar{t}$ MC	$\varepsilon(dR_{tags} > 1.5)$
$\varepsilon(b)$ data	0.8017 $\pm$ 0.0047
2×SVT	0.8059 $\pm$ 0.0045
b-quark jet match	0.8003 $\pm$ 0.0067

Table 5.2: *Exclusive efficiency of $dR_{tags} > 1.5$ cut on $t\bar{t}$ all-jets Monte Carlo events, for different methods of b-identification. The efficiencies are normalized to be 100% if all double-tagged events are included. Errors are from MC statistics.*

The hypothesis that the excess events at $dR_{tags} < 1.5$ are actually coming from $t\bar{t}$ is very unlikely. This is illustrated in Figure 5.7. The distance dR_{tags} between two jets in $t\bar{t}$ six-jet events tends to populate the larger values. In addition, only a few tens of double-tagged events are expected. The shape of the distribution in Figure 5.7 is almost completely determined by phase space and does not depend on the type of b identification, where both realistic efficiencies as measured in data (line) and jet-b-quark matching (dashed) were considered. To reduce the contribution from gluon splitting background we chose to cut on $dR_{tags} > 1.5$. Table 5.2 lists the efficiency of this cut, measured on Monte Carlo events, using three different methods:

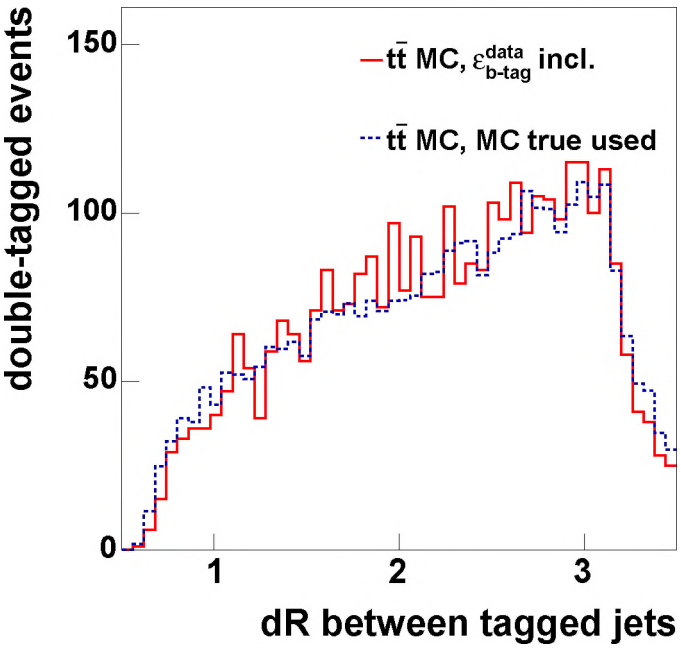

Figure 5.7: *dR_{tags} between two tagged jets, for signal Monte Carlo. Shown are both the expected distribution (solid) with data-based b identification folded in, and b-quark matched jets (dashed). The distributions are normalized to contain the same number of events.*

- folding in the b tagging efficiency as measured on data (most realistic);
- observation of secondary vertices in Monte Carlo jets;
- direct b jet-parton matching (least realistic).

However, these methods only measure the relative efficiency of the cut after already requiring double-tagged events. The relevant efficiency for $t\bar{t} \rightarrow$ all-jets signal events with at least one tag is measured to be

$$\varepsilon(dR_{tags} > 1.5) = 0.985 \pm 0.001. \tag{5.6}$$

After application of the dR_{tags} cut the b-jets in the remaining double-tagged background events are expected to be uncorrelated, which allows the use of one TRF to predict the number of tagged background events.

5.3 Quantities used for event selection

This section discusses the various variables used in the kinematic $t\bar{t}$→all-jets analysis. Even in the b tagged dataset, the background dominates the $t\bar{t}$ signal by two orders of magnitude. For all variables, the behavior of tagged background and expected $t\bar{t}$ signal is presented. As will be shown, the TRF method predicts the tagged background distributions reasonably well.

5.3.1 Definition of used variables

Variables used to distinguish hadronic top signal from QCD multijet background can be separated into five categories:

(i) Event energy scale. QCD background tends to have an overall lower transverse energy distribution, jets are less energetic and the total invariant mass of the event is smaller than in $t\bar{t}$ events;

(ii) Soft non-leading jets. As the QCD background mainly consists of hard 2-jet processes with extra soft gluon jets, the additional jets are expected to be softer for background than in $t\bar{t}$ signal. Even though the average jet energy is smaller in multijet QCD events, the leading jets tend to be more energetic in QCD than in $t\bar{t}$ events with comparable total transverse energy;

(iii) Event Shape. These quantities describe the event topology and the behavior of the angles of jets in the event as a whole. Top events have a different shape compared to QCD background. The jets are almost spherically distributed in top events, while QCD events usually have a more back-to-back jet distribution;

(iv) Pseudo-rapidity distribution. These quantities are used to identify where the jets in the event are observed in the detector. The typical hard scatter origin causes the jets in QCD background events to be more back-to-back than top signal, while QCD events are also more likely to be boosted in the direction of the beam-line. Thus fewer jets in the event are expected to be central. As $t\bar{t}$ production at the Tevatron is typically near the mass threshold, the $t\bar{t}$ system is expected to have a relatively small boost in the beam direction. Top pair events are hence expected to be more central;

(v) Top event properties. There are properties which are very typical for top event structure, like the presence of W-bosons and b-quarks.

These properties will be discussed in detail in the following paragraphs, and are also shown in Figures 5.8 through 5.22, where the observed tagged events and predicted distribution for tagged background are shown. The expected background in tagged events is predicted with the use of TRFs. The distribution is created by applying event weights (from the TRFs) to the complete (tagged and untagged) sample. For comparison, the shape of the $t\bar{t}$ signal is also shown. To make the top content visible, the number of $t\bar{t}$

events is scaled to be equal to the number of tagged events in the figures. In practice, this means that the $t\bar{t}$ signal distribution should be divided by approximately a factor 100 to get a reasonable prediction for the number of $t\bar{t}$ events expected in the sample. All variables are shown both on a linear and logarithmic scale.

(i) Parameters Sensitive to Event Energy Scale

Parameters sensitive to the event energy scale are generally also sensitive to the top mass. For all Monte Carlo simulations, the top mass of value $m_t = 175$ GeV/c^2 is used.

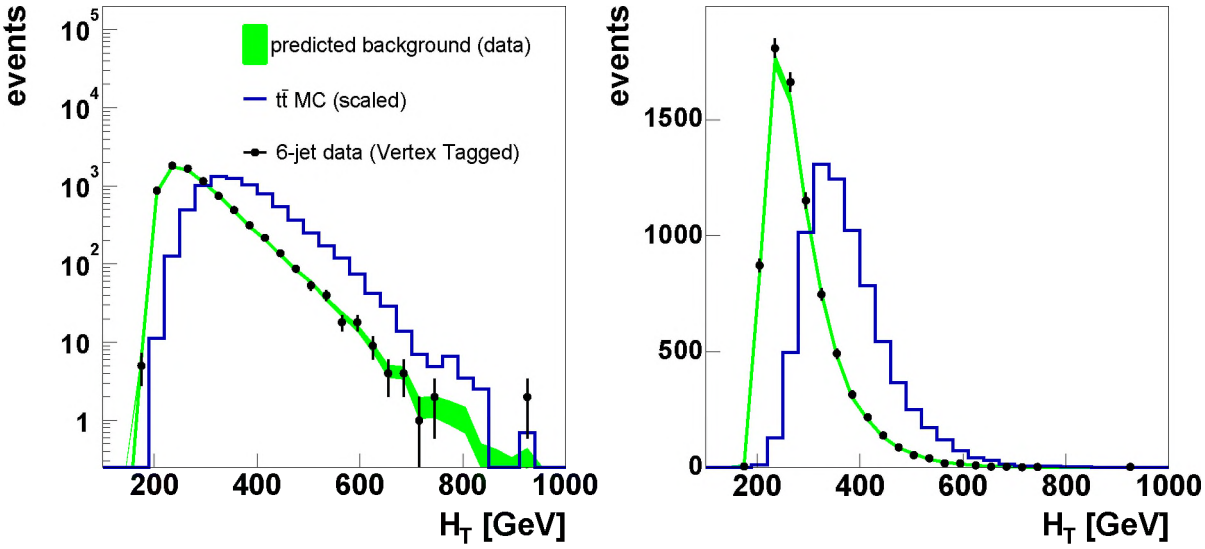

Figure 5.8: *H_T distribution for tagged data (markers) and $t\bar{t}$ →all-jets Monte Carlo (histogram). Also shown is the (predicted) distribution for tagged background (band).*

1. H_T. This parameter is defined as the scalar sum of the transverse energy of the jets in the event, and is also used for triggering. Only energy contained in jets is used for the calculation of H_T. H_T is one of the quantities that is sensitive to changes in the top mass, jet multiplicity and jet energy scale. The H_T distribution for background and signal (normalized to contain the same number of events) can be observed in Figure 5.8.

2. $\sqrt{\hat{s}}$. The invariant mass of the jet system. Figure 5.9 presents the distribution for tagged events, expected background and signal. The background is expected to come from QCD processes, which prefer small values of $\sqrt{\hat{s}}$. The significant difference between the two distributions is explained by the creation of two heavy objects (the $t\bar{t}$ quarks) in signal events.

(ii)Parameters Sensitive to Additional Radiation

The QCD background consists of $2 \rightarrow 2$ parton processes with additional QCD radiation. The following observables are mainly used because they provide good distinction

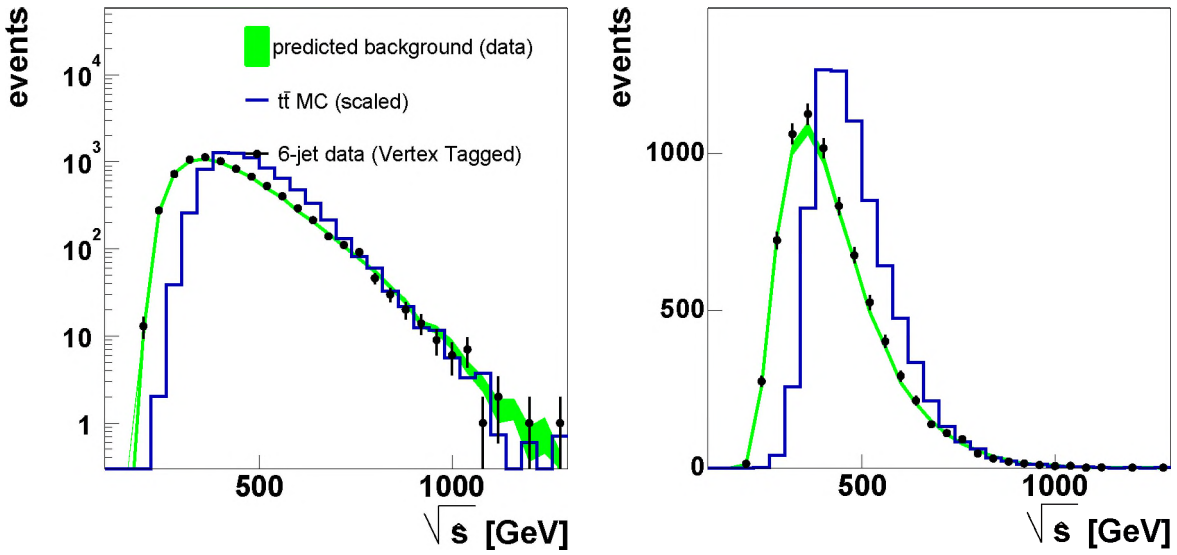

Figure 5.9: $\sqrt{\hat{s}}$ *distribution for tagged data (markers) and* $t\bar{t}$ *→all-jets Monte Carlo (histogram). Also shown is the (predicted) distribution for tagged background (band).*

between the hard $2 \rightarrow 2$ scatter with extra jets and events where all jets originate from $t\bar{t}$ production.

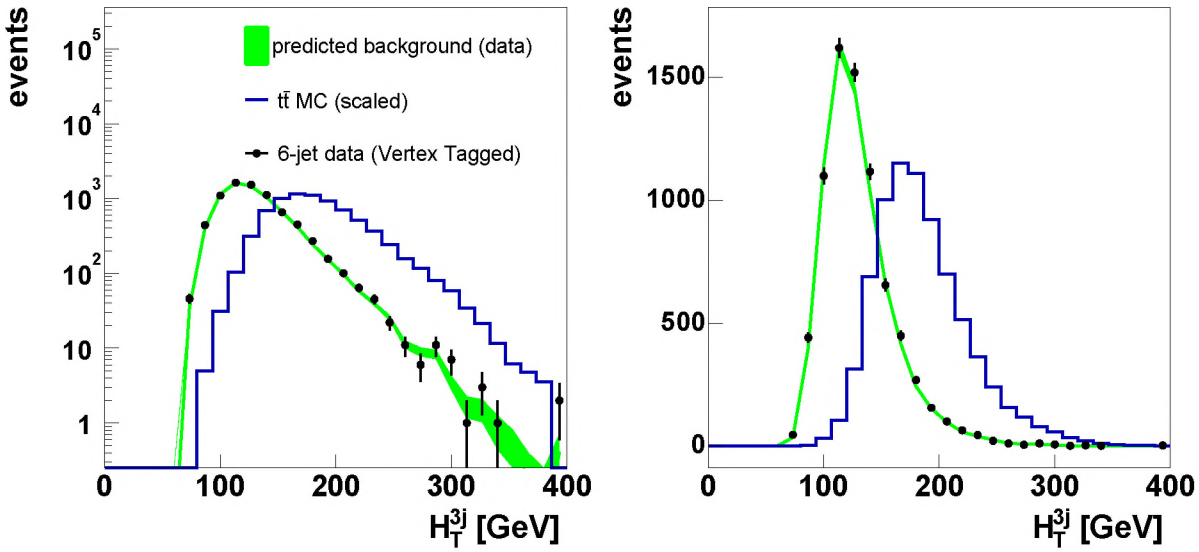

Figure 5.10: H_T^{3j} *distribution for tagged data (markers) and* $t\bar{t}$ *→all-jets Monte Carlo (histogram). Also shown is the (predicted) distribution for tagged background (band).*

3. H_T^{3j}. This variable is defined as

$$H_T^{3j} = H_T - E_T(\text{jet 1}) - E_T(\text{jet 2}), \tag{5.7}$$

where jet 1 and jet 2 are the leading and second-leading jet, respectively. By subtracting the energies of the leading jets, the remaining transverse energy sum becomes more sensitive to the difference between gluon radiation and the jets from W and b decay. Figure 5.10 shows the distributions for background data and $t\bar{t}$ Monte Carlo simulated events, where the latter are expected to have a significantly higher H_T^{3j} spectrum.

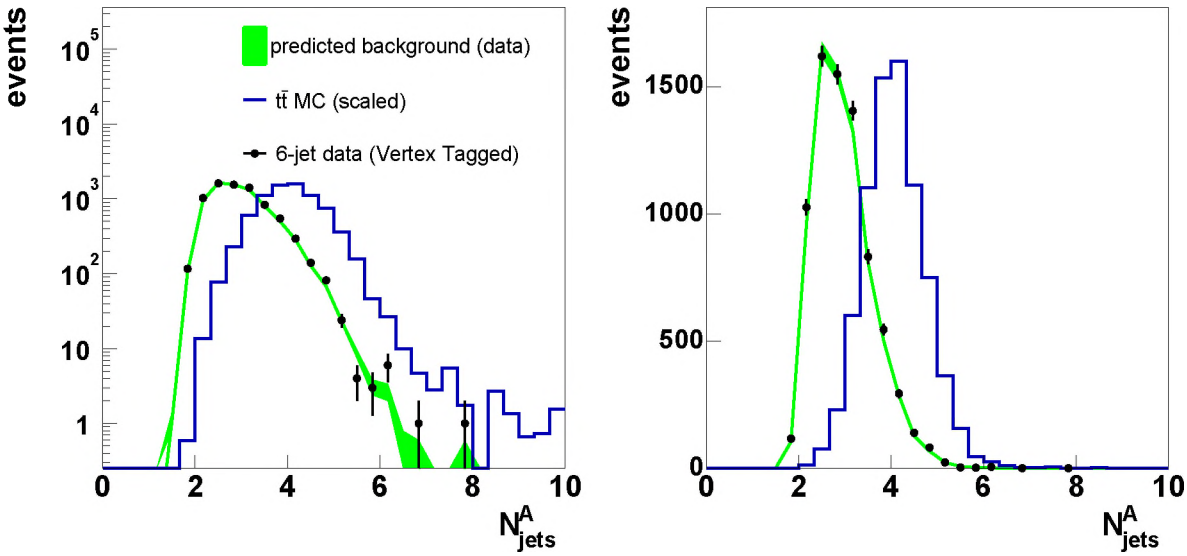

Figure 5.11: *N^A_{jets} distribution for tagged data (markers) and $t\bar{t}$ →all-jets Monte Carlo (histogram). Also shown is the (predicted) distribution for tagged background (band).*

4. N^A_{jets} is the jet E_T weighted average over the number of jets, which is defined as

$$N^A_{jets} = \frac{\int_{15}^{55} \mathrm{d}E_T^{thr}\, E_T^{thr}\, N(E_T^{thr})}{\int_{15}^{55} \mathrm{d}E_T^{thr}\, E_T^{thr}}, \tag{5.8}$$

where $N(E_T^{thr})$ is the number of jets in a given event with $|\eta| < 2.5$ and E_T greater than the threshold value E_T^{thr}. An average jet count parameter like N^A_{jets} provides a way to parametrize the number of jets in the event, while taking into account the hardness of these jets. In particular, this variable is more sensitive to the number of jets with energies expected for $t\bar{t}$ production than just a simple count of the jets. For the expected $2 \to 2$ scattering process of the background, N^A_{jets} is expected to be close to 2, as can be observed in Figure 5.11. The choice of integration boundaries for E_T^{thr} (15 and 55 GeV) is motivated by the difference in jet spectra for $t\bar{t}$ and QCD events in this region [61].

5. $E_{T_{5,6}}$ is defined as the geometric mean of the transverse energies of the fifth and sixth leading jet:

$$E_{T_{5,6}} = \sqrt{E_T(\text{jet } 5) \cdot E_T(\text{jet } 6)} \tag{5.9}$$

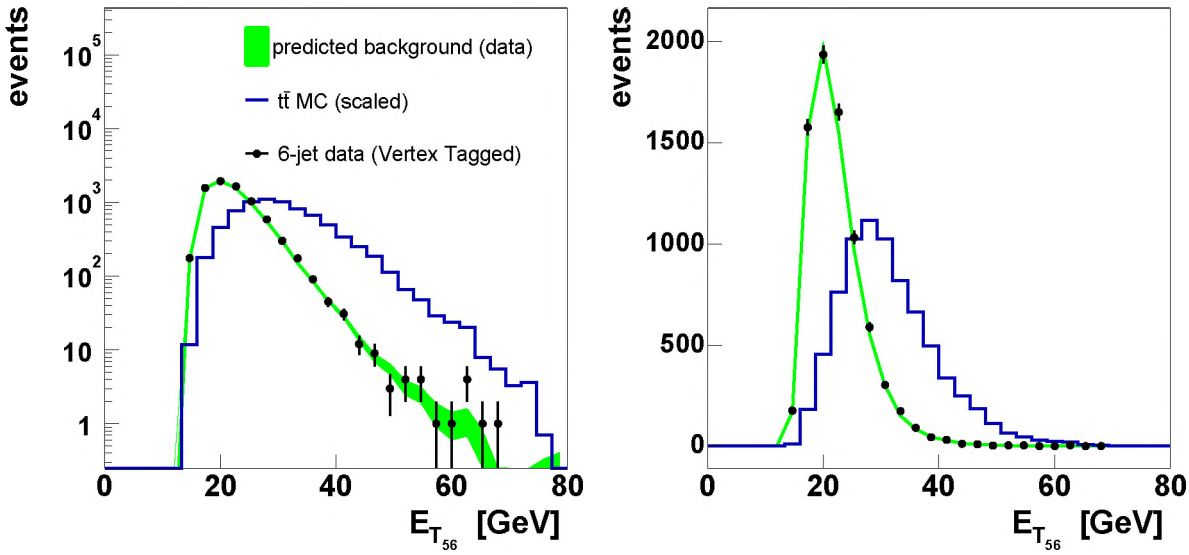

Figure 5.12: $E_{T_{5,6}} = \sqrt{E_T(jet\ 5) \cdot E_T(jet\ 6)}$ *distribution for tagged data (markers) and* $t\bar{t}$ *→all-jets Monte Carlo (histogram). Also shown is the (predicted) distribution for tagged background (band).*

This observable is effectively rejecting events of which the fifth and sixth jet are much less energetic than expected in $t\bar{t}$ signal events. Figure 5.12 shows that the distribution of $E_{T_{5,6}}$ is indeed much softer for background than for $t\bar{t}$ Monte Carlo events.

(iii)Event shape

The shape of the event can be quantified in terms of the normalized momentum tensor M_{ab}:

$$M_{ab} = \frac{\sum_{j=1}^{N_{jets}} p_{ja} p_{jb}}{\sum_{j=1}^{N_{jets}} p_j^2} \tag{5.10}$$

where a and b are the spatial coordinates x, y, z of the jet momentum-vectors p and j runs over the number of jets in the event. M_{ab} is, by definition, a symmetric 3×3 matrix, whose eigenvalues Q_1, Q_2 and Q_3 can be used to quantify the momentum flow of the jets in the event. Because of the normalization and the requirement that there are positive-definite solutions of the eigenvalues, the sum of the eigenvalues is equal to unity: $Q_1+Q_2+Q_3 = 1$. The eigenvalues are arranged such that $0 \leq Q_1 \leq Q_2 \leq Q_3$.

The size of any Q_i represents the momentum flow in the direction of the ith eigenvector. This way, the leading eigenvector, with size Q_3, points to the direction at which most jet energy points. The other two eigenvectors (with sizes Q_1 and Q_2) span an orthogonal coordinate system with respect to this maximal momentum flow. Aplanarity and sphericity are defined as different combinations of the eigenvalues of the normalized momentum tensor, where the aplanarity is

$$\mathcal{A} = \frac{3}{2} Q_1, \tag{5.11}$$

and the sphericity is defined as

$$\mathcal{S} = \frac{3}{2}(Q_1 + Q_2). \tag{5.12}$$

As $\mathcal{A}$ and $\mathcal{S}$ are calculated from the jet three-momenta, they are sensitive to the Lorentz frame that they are calculated in. Here, the laboratory ($p\overline{p}$) frame is used. The physical interpretations of the two variables are:

6. Aplanarity, $\mathcal{A}$, defines how the collection of jets in the event is placed with respect to a plane. If the event system spans only one plane, the Aplanarity is zero. An event is maximally aplanar when $\mathcal{A} = 0.5$. Figure 5.13 shows that $t\bar{t}$ Monte Carlo events tend to be more aplanar than background events.

7. Sphericity, $\mathcal{S}$, defines how spherically the jets are situated in the event. A perfectly spherical event has $\mathcal{S} = 1$. Top events are expected to be more spherical than QCD background events, as can be seen in Fig 5.14.

(iv) Pseudo-rapidity sensitive parameters

Top events are expected to have pseudo-rapidity distributions different from the QCD background. The following variables provide a handle on this characteristic:

8. Centrality, $\mathcal{C}$, is defined as

$$\mathcal{C} = \frac{H_T}{H}, \tag{5.13}$$

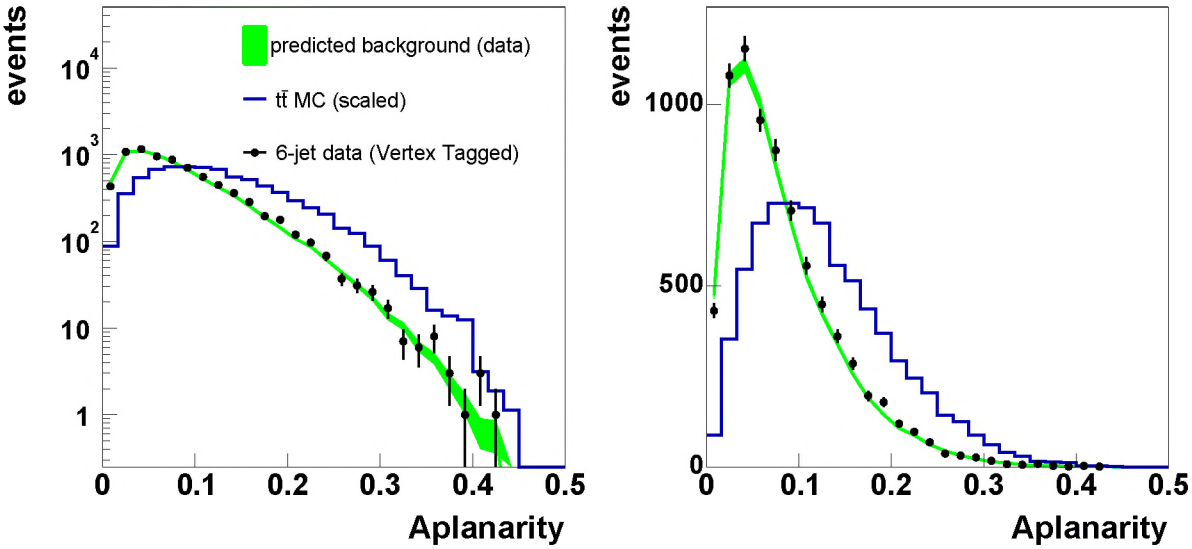

Figure 5.13: *Aplanarity distribution for tagged data (markers) and $t\bar{t}$ →all-jets Monte Carlo (histogram). Also shown is the (predicted) distribution for tagged background (band).*

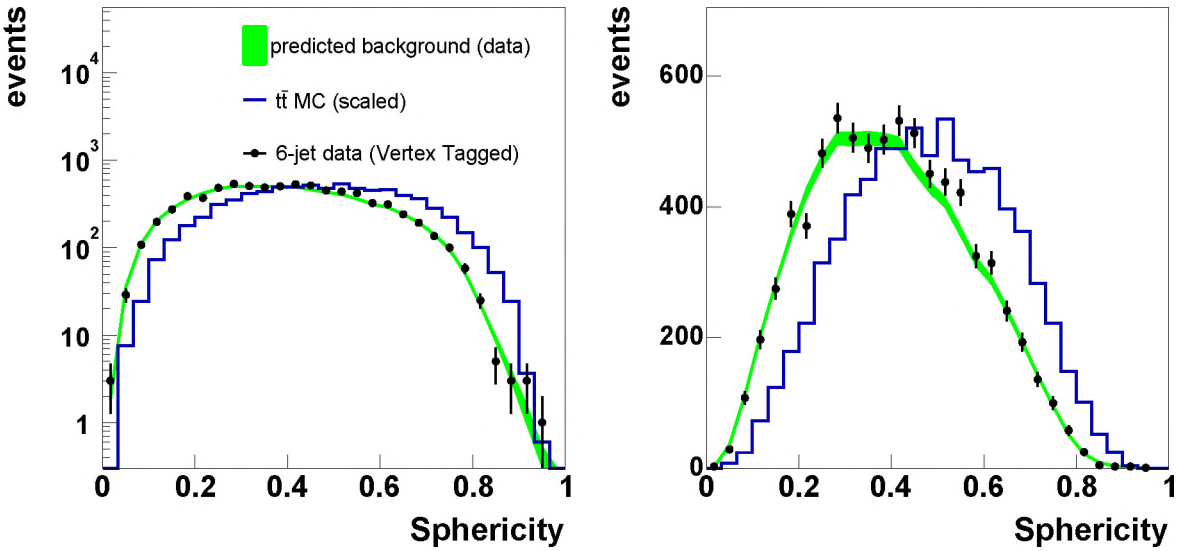

Figure 5.14: *Sphericity distribution for tagged data (markers) and $t\bar{t}$ →all-jets Monte Carlo (histogram). Also shown is the (predicted) distribution for tagged background (band).*

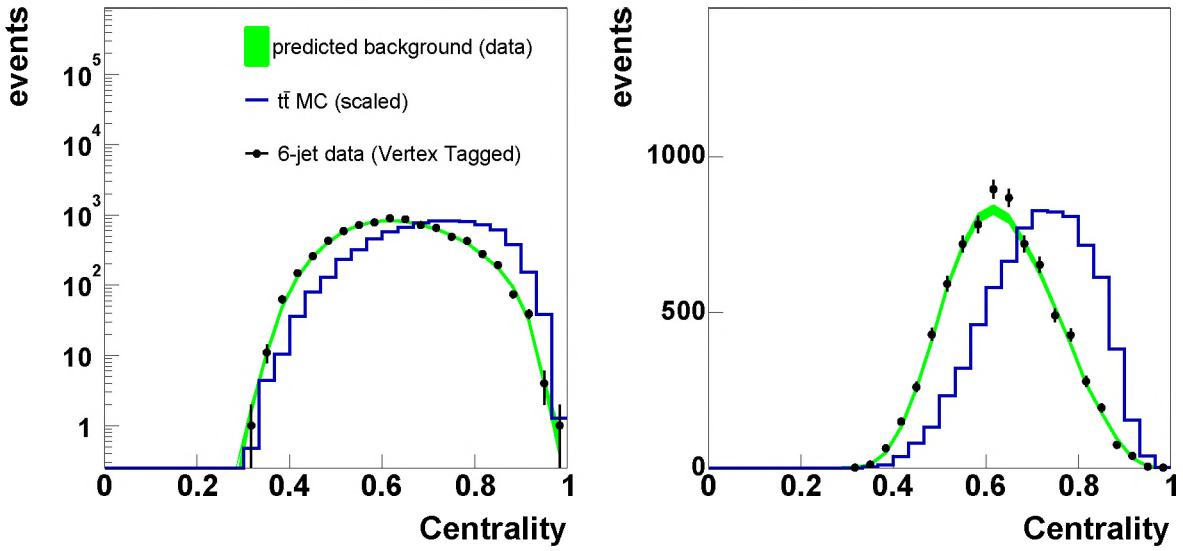

Figure 5.15: *Centrality distribution for tagged data (markers) and $t\bar{t}$ →all-jets Monte Carlo (histogram). Also shown is the (predicted) distribution for tagged background (band).*

where $H = \sum_{i=1}^{N_{jet}} E_i$ is the sum of all the jet energies in the event, similar to H_T but including the longitudinal energy. The centrality measures which fraction of the energy deposited in the proton-antiproton collision is transverse energy. By construction, $\mathcal{C}$ is to first order not dependent on the energy scale. Figure 5.15 shows the centrality distributions for data and $t\bar{t}$ Monte Carlo events. The signal tends to have higher values of $\mathcal{C}$.

9. $\langle\eta^2\rangle$ is the weighted root-mean-square (RMS) of the η of the six leading jets in the event, and is defined as

$$\langle\eta^2\rangle = \frac{\sum_{jet=1}^{6} \mathcal{W}(E_T)(\eta_{jet} - \bar{\eta})^2}{\sum_{jet=1}^{6} \mathcal{W}(E_T)}. \tag{5.14}$$

The jet weight $\mathcal{W}(E_T)$ and average value, $\bar{\eta}$, are defined as

$$\mathcal{W}(E_T) = \frac{\sigma^{t\bar{t}}(E_T) - \sigma^{bg}(E_T)}{\sigma^{t\bar{t}}(E_T)} \tag{5.15}$$

and

$$\bar{\eta} = \frac{1}{H_T} \sum_{j=1}^{N_{jets}} E_{T_j} \eta_j. \tag{5.16}$$

The quantities $\sigma^{t\bar{t}}(E_T)$ and $\sigma^{bg}(E_T)$ are the expected RMS of the jet η distribution, as a function of the jet E_T. Figure 5.17 shows the observed distributions of $\sigma^{t\bar{t}}(E_T)$

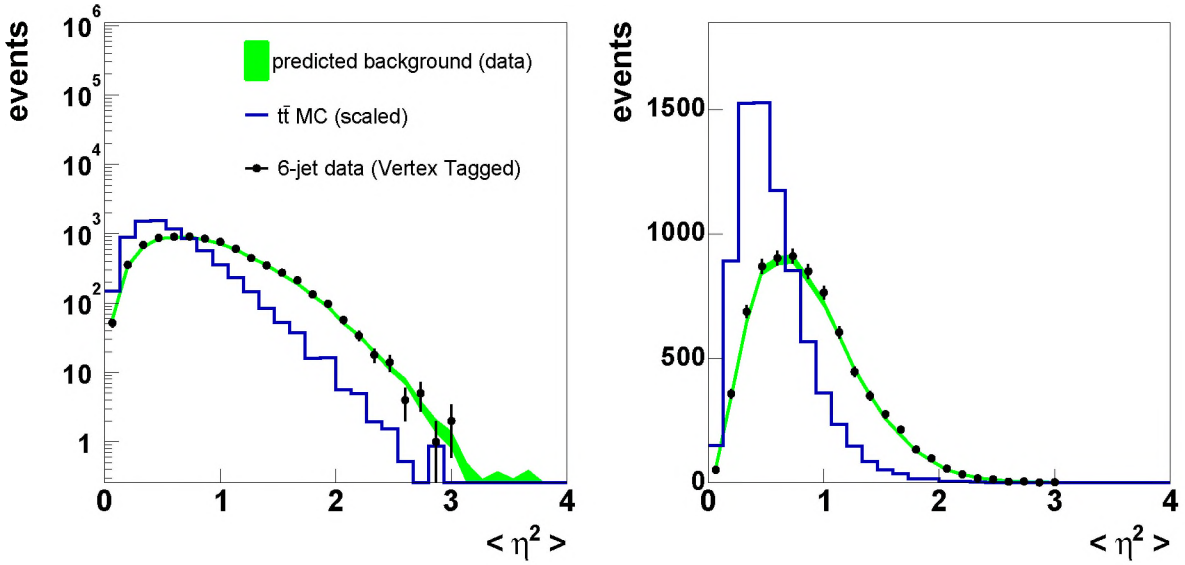

Figure 5.16: $\langle\eta^2\rangle$ *distribution for tagged data (markers) and* $t\bar{t}$ $\rightarrow$*all-jets Monte Carlo (histogram). Also shown is the (predicted) distribution for tagged background (band).*

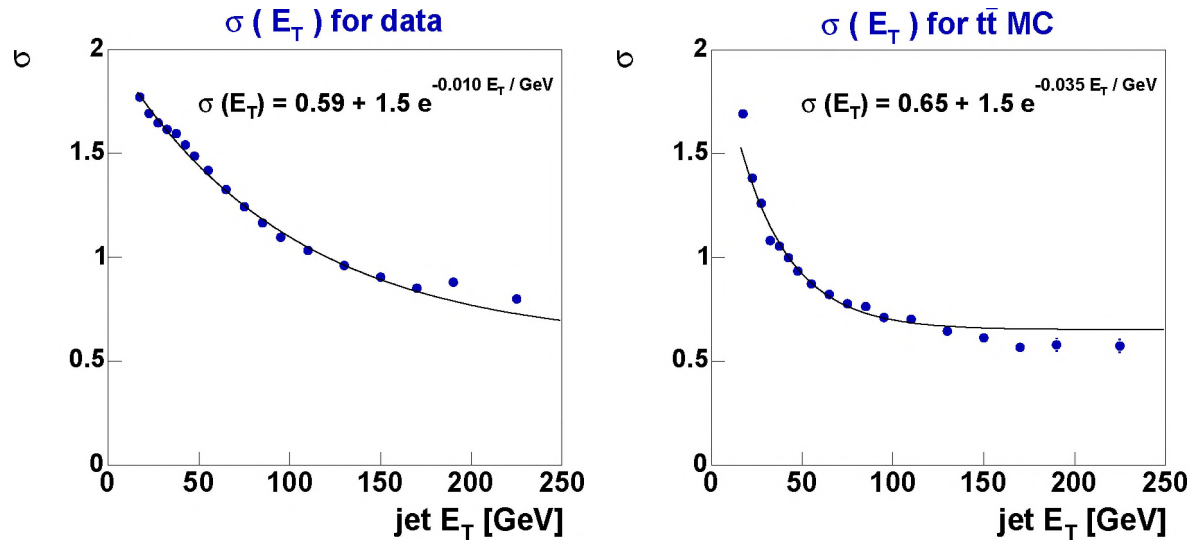

Figure 5.17: *Distribution of* $\sigma(E_T)$*. Left plot gives the behavior for data, right plot for* $t\bar{t}$ *Monte Carlo. The curves represent the fits that are used in equation (5.15).*

and $\sigma^{bg}(E_T)$ with respect to the center of the detector ($\eta = 0$), as a function of jet E_T. We use functions of type

$$\sigma(E_T) = c_0 + c_1 \cdot \exp(c_2 E_T) \tag{5.17}$$

to parametrize $\sigma^{t\bar{t}}(E_T)$ and $\sigma^{bg}(E_T)$.

As can be observed in Figure 5.17, the QCD multijet background falls slower than the $t\bar{t}$ signal distribution. The η distribution of a typical $t\bar{t}$ event is expected to be normally distributed around the center of the detector. As $t\bar{t}$ events are expected to be produced almost at rest, the number of jets above and below $\eta = 0$ is expected to be equal. Hence, $\langle \eta^2 \rangle$ is expected to be smaller for signal with respect to background, as can also be observed in Figure 5.16.

(v) Top event properties

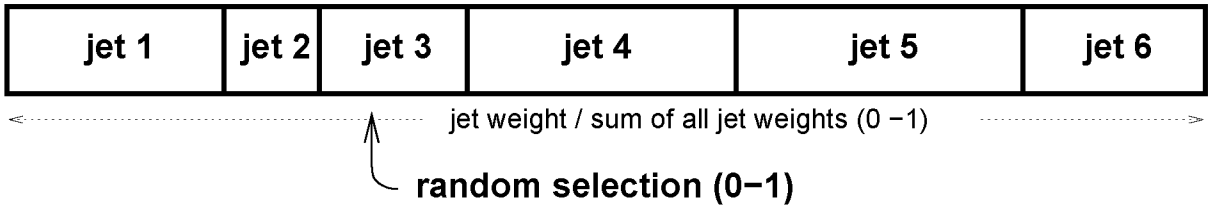

Figure 5.18: *Random selection of candidate b jets. All jets in the event have a certain probability to be tagged, represented by the size of the corresponding field shown above. A random number between 0 and 1 labels a b jet candidate.*

This class of variables contains quantities which are specific to the presence of high-mass particles that decay to three jets, of which one is expected to be a b jet candidate.

10. E_T^b, the E_T of the jet that is the most likely b candidate. The jets coming from b decay of top quarks are typically more energetic than the b jets coming from QCD b production. In untagged events used for the background prediction this quantity is not à priori available. Hence, the TRF is used for the untagged data prediction. In Monte Carlo events, the efficiencies for b, c and light jets are taken into account. To select the b jet candidate in untagged events, we adopted the following method:

    - if the event contains no tagged jets, a b candidate is selected by a random draw. Each jet in the event is given a probability proportional to the tagging probability of the jet. The probabilities are normalized by dividing each jet probability by the sum of the jet probabilities. A random number between 0 and 1 selects the b candidate jet. Figure 5.18 gives a graphical representation of this method;
    - if a data event contains one tagged jet, that jet is used as the b candidate;

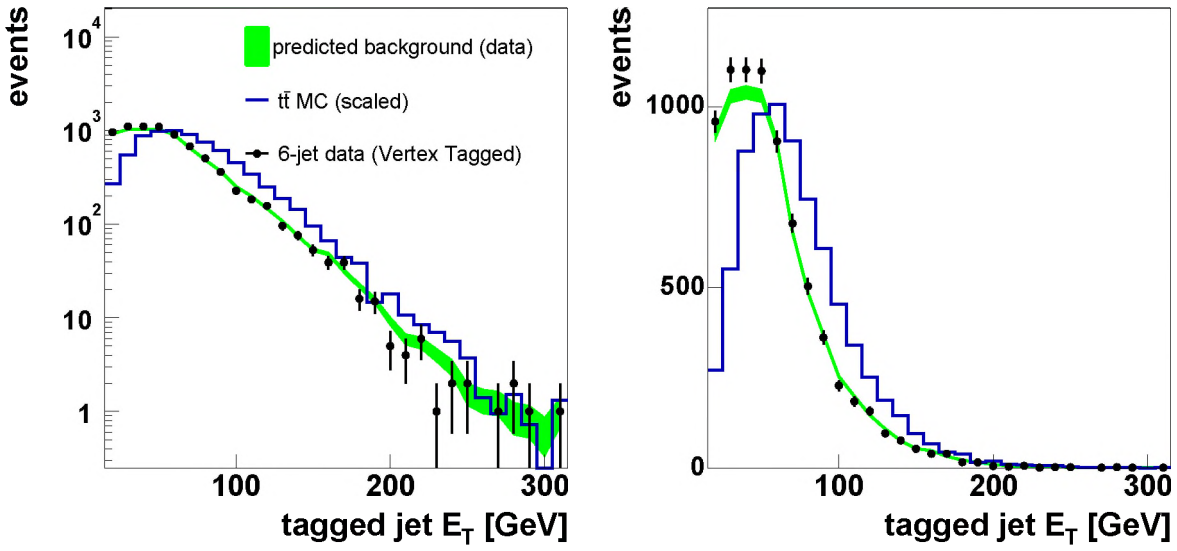

Figure 5.19: *Distribution of E_T^b, the b jet candidate for tagged data (markers) and $t\bar{t}$ →all-jets Monte Carlo (histogram). Also shown is the (predicted) distribution for tagged background (band).*

– if the event has several tagged jets, the random draw method is used again, but now only for the tagged jets.

Figure 5.19 shows the E_T^b distribution for tagged data and the expected Monte Carlo. The E_T^b in $t\bar{t}$ events tends to be larger than for background.

11, 12. The top mass likelihood of the event, $\mathcal{M}_{t\bar{t}}$, is a χ^2 variable defined as:

$$\mathcal{M}_{t\bar{t}} = \frac{(m_{t_1} - m_{t_2})^2}{\sigma_t^2}, \tag{5.18}$$

where m_{t_1} and m_{t_2} are the invariant masses of the two (three-jet) top candidates, and σ_t is the width of the top mass peak as measured on $t\bar{t}$ Monte Carlo events. All possible permutations of the six leading jets in the event are used. The combination that gives the smallest value of $\mathcal{M}_{t\bar{t}}$ is used. A jet that is a b candidate cannot be used in the reconstructed W. The b candidate is selected with the method described in the definition of E_T^b (variable 10).

A similar variable can also be constructed for the W boson mass. The W mass likelihood $\mathcal{M}_{WW}$ is defined as

$$\mathcal{M}_{WW} = \frac{(M_{W_1} - M_W)^2}{\sigma_W^2} + \frac{(M_{W_2} - M_W)^2}{\sigma_W^2}, \tag{5.19}$$

where M_W and σ_W are the expected central value and standard deviation of the W boson mass peak, obtained from $t\bar{t}$ all-jets Monte Carlo distributions as shown in

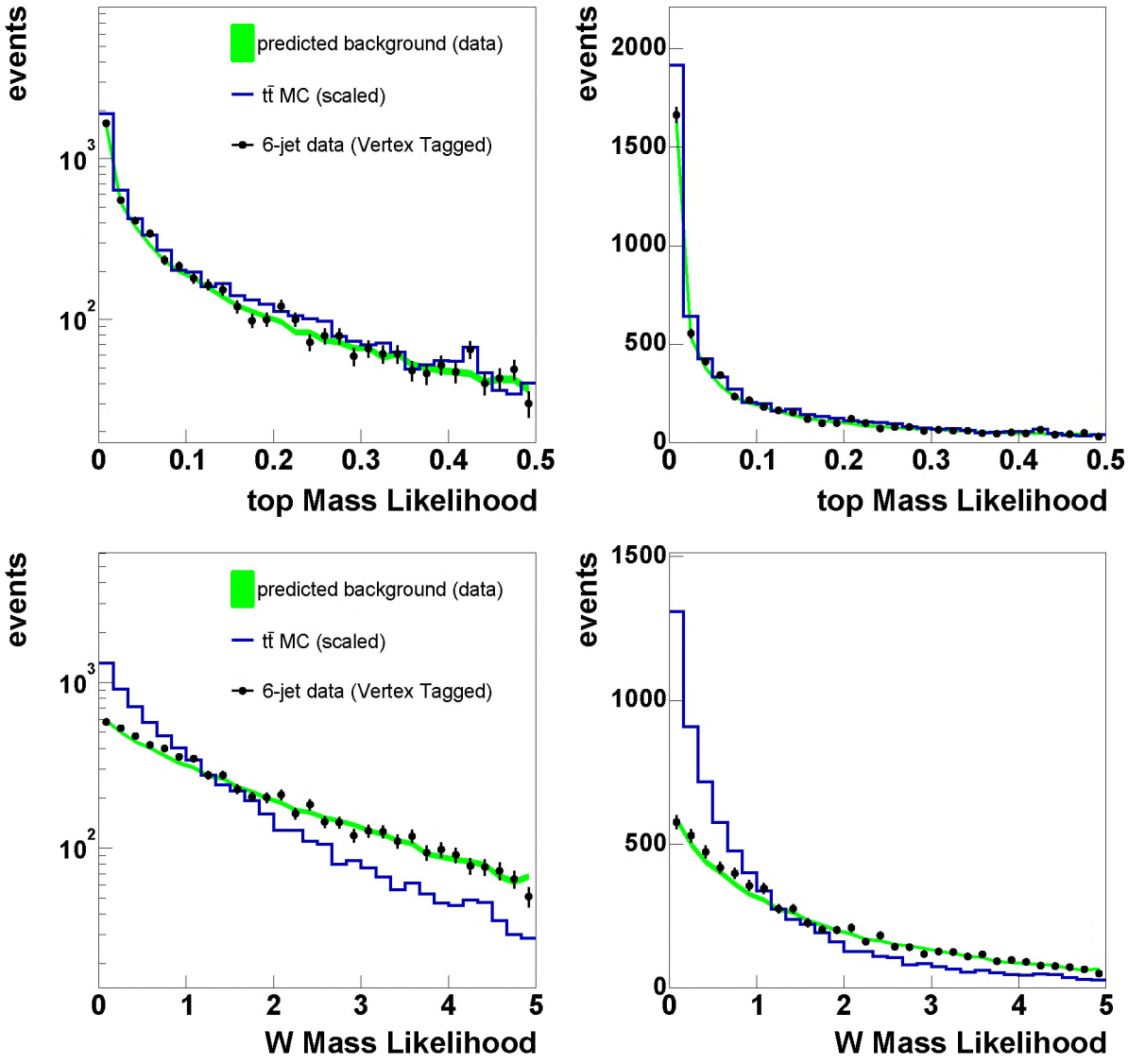

Figure 5.20: *Distribution of the mass likelihood variables $\mathcal{M}_{t\bar{t}}$ (top) and $\mathcal{M}_{WW}$ (bottom) for tagged data (markers) and $t\bar{t}$ →all-jets Monte Carlo (histogram). Also shown is the (predicted) distribution for tagged background (band).*

Figure 4.11 and 4.14, with values $\sigma_t = 22$ GeV/c^2, $\sigma_W = 13$ GeV/c^2 and $M_W = 83$ GeV/c^2. These are similar to the values used in the Run 1 analysis. M_{W_1} and M_{W_2} are the invariant masses of the two candidate W bosons. For both $\mathcal{M}_{t\bar{t}}$ and $\mathcal{M}_{WW}$, the jet permutation with the smallest value are used, after consideration of all different jet permutations. This means it is likely that different jet permutations are used for $\mathcal{M}_{WW}$ and $\mathcal{M}_{t\bar{t}}$.

Figure 5.20 shows the distribution of $\mathcal{M}_{t\bar{t}}$ and $\mathcal{M}_{WW}$, which differ by about one order of magnitude: it is more difficult to reconstruct two W bosons than it is to find two three-jet objects with a similar mass. Moreover, the difference of $\mathcal{M}_{t\bar{t}}$ for signal and background is only marginal, while $\mathcal{M}_{WW}$ exhibits obvious differences.

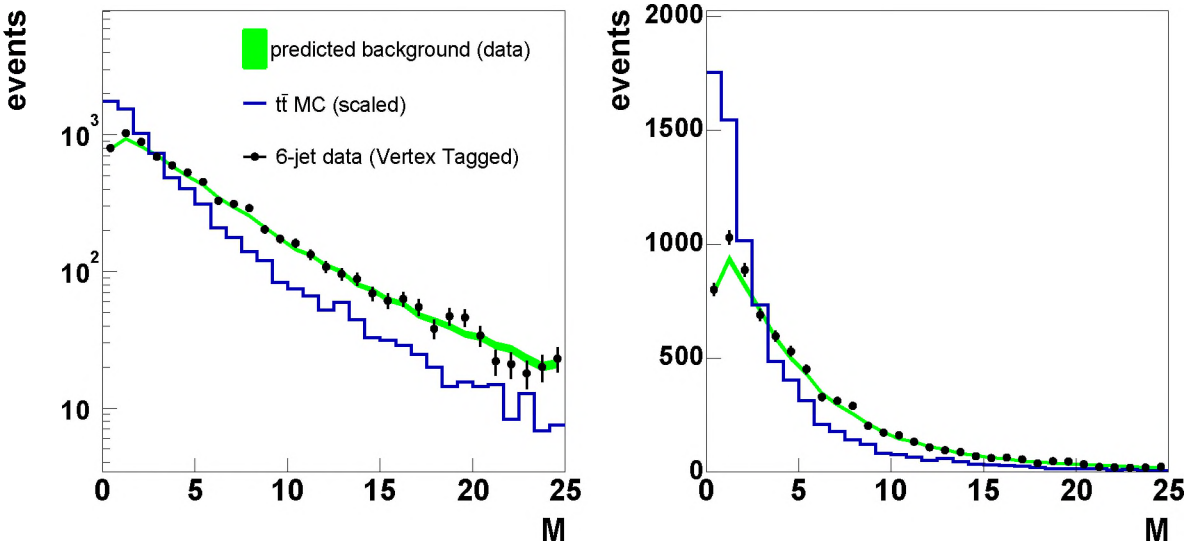

Figure 5.21: *Distribution of the mass likelihood variable $\mathcal{M}$ for tagged data (markers) and $t\bar{t}$ →all-jets Monte Carlo (histogram). Also shown is the (predicted) distribution for tagged background (band).*

13. It is also possible to combine $\mathcal{M}_{WW}$ and $\mathcal{M}_{t\bar{t}}$ in one variable, $\mathcal{M}$

$$\mathcal{M} = \frac{(M_{W_1} - M_W)^2}{\sigma_W^2} + \frac{(M_{W_2} - M_W)^2}{\sigma_W^2} + \frac{(m_{t_1} - m_{t_2})^2}{\sigma_t^2}, \tag{5.20}$$

which is the minimized mass likelihood variable used in the Run 1 analysis [61]. Here, obviously there is no ambiguity to what jet combinations are used for the W and t reconstruction: the smallest χ^2 of $\mathcal{M}$ is used. The distribution for $\mathcal{M}$ can be seen in Figure 5.21. The background has a relatively large tail towards higher values of $\mathcal{M}$. The initial Run 2 analysis used the two separate variables [71], but in this thesis we do an optimization on all topological variables, so both the combined and separate configuration will be considered.

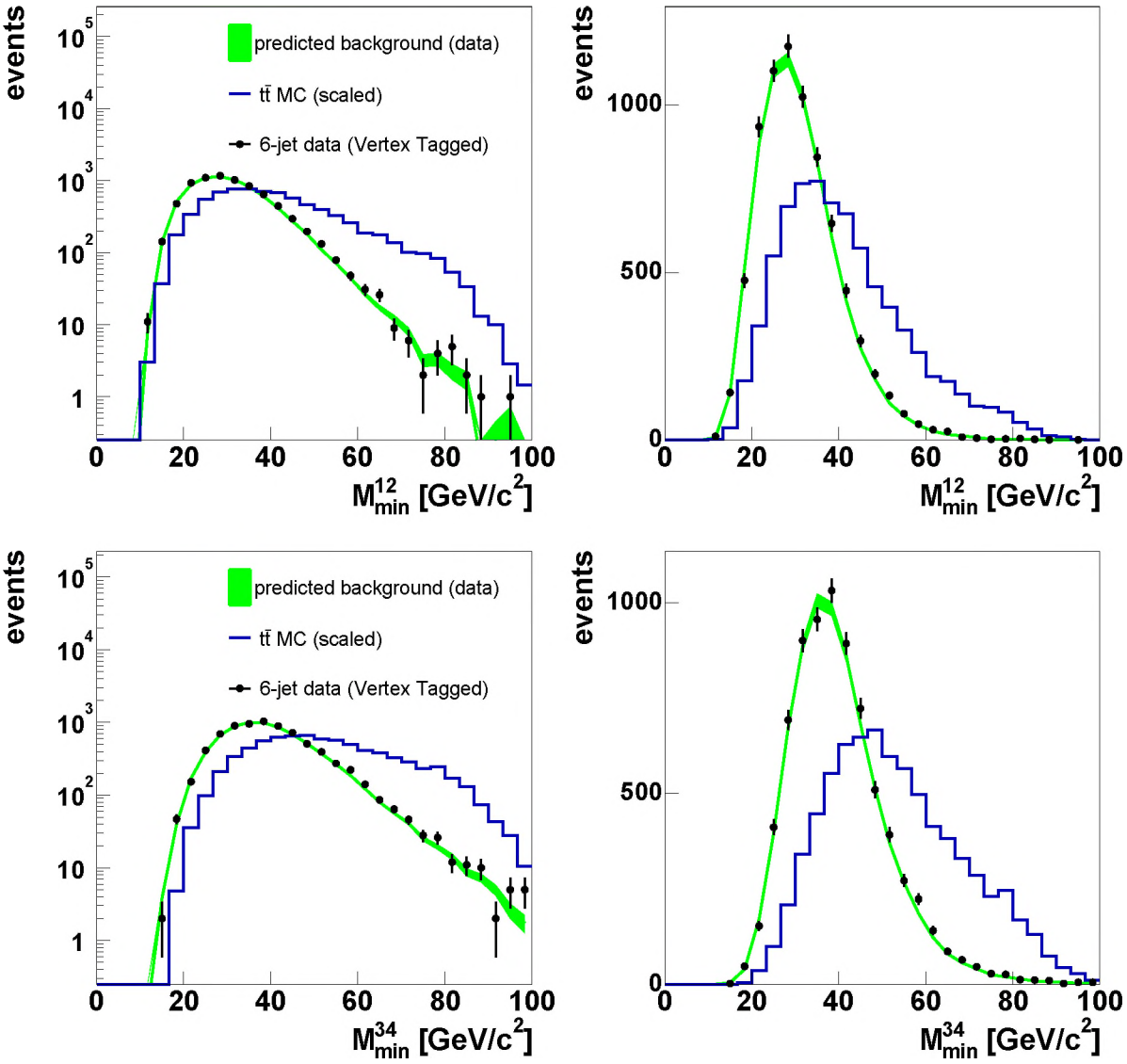

Figure 5.22: *Distribution of the two minimal di-jet mass variables $M^{1,2}_{min}$ and $M^{3,4}_{min}$ for tagged data (markers) and $t\bar{t}$ →all-jets Monte Carlo (histogram). Also shown is the (predicted) distribution for tagged background (band).*

14, 15. The smallest di-jet masses in the event. As all jets in $t\bar{t}$ events are associated with high-mass objects, both the smallest di-jet mass $M_{min}^{1,2}$ and the second smallest di-jet mass $M_{min}^{3,4}$ can be useful variables to distinguish $t\bar{t}$ events from QCD events. $M_{min}^{1,2}$ and $M_{min}^{3,4}$ are expected to be a smaller for QCD than for top events. When calculating $M_{min}^{3,4}$, jets that were already used for $M_{min}^{1,2}$ are ignored. There is no veto on the use of b candidate jets, they are included in the permutations. Figure 5.22 shows the distributions of $M_{min}^{1,2}$ and $M_{min}^{3,4}$. Both variables peak at lower values and more sharply for background than for $t\bar{t}$ events.

5.3.2 Correlations between the topological variables

The variety of quantities as described in Section 5.3.1 are correlated. To quantify the correlation between two variables x_i and y_i, the (linear) correlation is calculated, which is defined as:

$$r = \frac{\bar{xy} - \bar{x}\bar{y}}{\sigma_x \sigma_y} = \frac{(\frac{1}{N}\sum_i^N x_i y_i) - (\frac{1}{N}\sum_i^N x_i)(\frac{1}{N}\sum_i^N y_i)}{\sqrt{(\frac{1}{N}\sum_i^N x_i^2) - (\frac{1}{N}\sum_i^N x_i)^2} \cdot \sqrt{(\frac{1}{N}\sum_i^N y_i^2) - (\frac{1}{N}\sum_i^N y_i)^2}}, \tag{5.21}$$

where the summation over i runs over all N events. The results of this correlation study are listed in Table 5.3 for data, and Table 5.4 for Monte Carlo $t\bar{t}$ events. The event samples used were $t\bar{t}$ all-jets Monte Carlo events with six or more jets, and data events with six or more jets. There were no requirements on events being b tagged.

Variables with r values under 0.1 are considered to be mildly correlated. Variables with r values over 0.2 are considered correlated, while strong correlations are expected to have $r > 0.4$. Looking at the tables, it can be noted that most variables are strongly correlated with H_T, the most sensitive variable in the analysis. Variables from the same category tend to be more correlated. The correlations are expected to be different for background and $t\bar{t}$ signal. The variables which show a large difference in correlation are expected to be most efficient at discriminating between background and signal. We combine the quantities in an artificial neutral network , which takes these correlations into account.

5.4 Neural networks

Artificial neural networks (ANNs), like other complex multivariate techniques, provide the best possible discriminating power by accounting for the correlations between the various input variables. We use feed-forward ANNs, trained by back propagation as implemented in the JETNET [63] program. All the ANNs used have one output node and one middle layer with twice the number of nodes as the input layer (Figure 5.23). Based on the value of the input nodes, the hidden nodes decide whether or not to 'fire'. The decision to fire is made through the evaluation of a function, in the case of JETNET

$$N(x) = \frac{1}{1 + \mathrm{e}^{-2x}}, \tag{5.22}$$

where x is the weighted sum of the input node values. There are several functions of this type that can be used in ANNs, but the critical requirement is that the function has a

	$\sqrt{\hat{s}}$	H_T^{3j}	N_{jets}^A	$E_{T_{5,6}}$	$\mathcal{A}$	$\mathcal{S}$	$\mathcal{C}$	$\langle\eta^2\rangle$	E_T^b	$\mathcal{M}_{t\bar{t}}$	$\mathcal{M}_{WW}$	$\mathcal{M}$	M_{12}^{min}	M_{34}^{min}
H_T	0.76	0.64	0.67	0.36	-0.28	-0.25	-0.02	0.20	0.43	0.27	0.20	0.36	0.25	0.34
$\sqrt{\hat{s}}$	1	0.60	0.63	0.36	-0.45	-0.52	-0.53	0.74	0.31	0.30	0.28	0.46	0.30	0.40
H_T^{3j}		1	0.84	0.73	-0.02	-0.20	-0.16	0.18	0.12	0.13	0.10	0.19	0.32	0.34
N_{jets}^A			1	0.60	-0.16	-0.29	-0.19	0.22	0.20	0.14	0.12	0.22	0.41	0.48
$E_{T_{5,6}}$				1	0.02	-0.12	-0.13	0.13	0.01	0.07	0.06	0.11	0.39	0.38
$\mathcal{A}$					1	0.59	0.43	-0.45	-0.17	-0.13	-0.15	-0.22	-0.05	-0.08
$\mathcal{S}$						1	0.57	-0.49	-0.10	-0.09	-0.18	-0.23	-0.10	-0.13
$\mathcal{C}$							1	-0.76	0.01	-0.10	-0.13	-0.20	-0.16	-0.21
$\langle\eta^2\rangle$								1	0.11	0.22	0.18	0.32	0.20	0.29
E_T^b									1	0.06	0.09	0.09	0.09	0.14
$\mathcal{M}_{t\bar{t}}$										1	0.08	0.62	0.04	0.06
$\mathcal{M}_{WW}$											1	0.61	0.05	0.06
$\mathcal{M}$												1	0.08	0.11
M_{12}^{min}													1	0.70

Table 5.3: *Average correlations among the variables, for data events, which are dominated by QCD background.*

	$\sqrt{\hat{s}}$	H_T^{3j}	N_{jets}^A	$E_{T_{5,6}}$	$\mathcal{A}$	$\mathcal{S}$	$\mathcal{C}$	$\langle\eta^2\rangle$	E_T^b	$\mathcal{M}_{t\bar{t}}$	$\mathcal{M}_{WW}$	$\mathcal{M}$	M_{12}^{min}	M_{34}^{min}
H_T	0.80	0.73	0.63	0.43	-0.15	-0.20	0.33	-0.17	0.44	0.24	0.12	0.28	0.33	0.38
$\sqrt{\hat{s}}$	1	0.64	0.54	0.39	-0.31	-0.41	-0.15	0.40	0.33	0.31	0.19	0.40	0.33	0.39
H_T^{3j}		1	0.88	0.73	0.12	0.02	0.17	-0.16	0.20	0.17	0.06	0.19	0.38	0.40
N_{jets}^A			1	0.78	0.15	0.05	0.17	-0.17	0.17	0.12	0.03	0.12	0.48	0.50
$E_{T_{5,6}}$				1	0.14	0.04	0.08	-0.09	0.06	0.09	0.01	0.10	0.48	0.46
$\mathcal{A}$					1	0.69	0.29	-0.34	-0.11	-0.08	-0.09	-0.15	0.05	0.04
$\mathcal{S}$						1	0.36	-0.37	-0.09	-0.07	-0.11	-0.15	-0.01	-0.03
$\mathcal{C}$							1	-0.69	0.17	-0.06	-0.05	-0.09	0.02	0.01
$\langle\eta^2\rangle$								1	-0.08	0.17	0.08	0.20	0.06	0.10
E_T^b									1	0.02	0.06	0.04	0.11	0.14
$\mathcal{M}_{t\bar{t}}$										1	0.08	0.66	0.05	0.07
$\mathcal{M}_{WW}$											1	0.53	-0.00	-0.01
$\mathcal{M}$												1	0.03	0.04
M_{12}^{min}													1	0.79

Table 5.4: *Average correlations among the variables, for signal Monte Carlo events.*

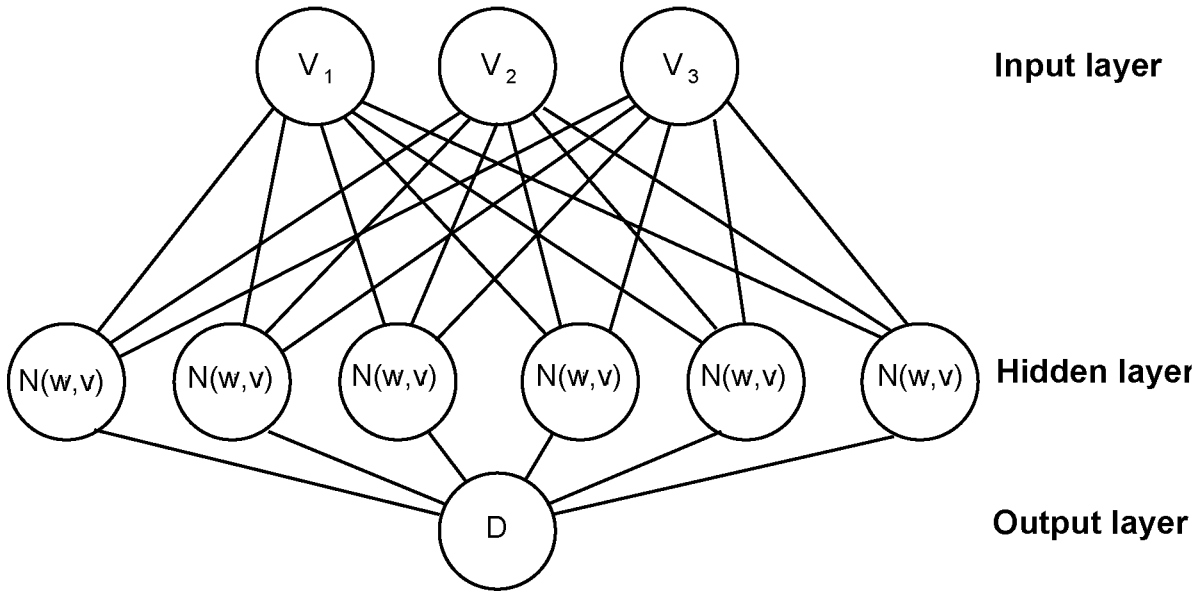

Figure 5.23: *A schematic view of a simple, three-layer neural network.*

sharp 'turn-on', to simulate neuron-like firing behavior. The outputs of the hidden nodes are collected, and passed on to the output node, which returns a number that can be used to distinguish between different sets of input variables.

5.4.1 Neural network training

Neural networks contain weights for the different input variables and nodes. The determination of these weights is known as training. A good description of ANNs and the training process in JETNET can be found in [63, 64].

During training, the neural net is tested on samples for which the desired output is known. In this thesis we use the definition that for signal the ANN should return '1', while for background the output should be '0'. In the training process, the weights between the nodes are adjusted in order to obtain the (known) output result. In principle this is just a fit of a high-dimensional discriminant D, that is a function of the node weights and inputs. Because of the many necessary iterations, JETNET uses a minimization algorithm that searches for the minimum of D by taking the gradient and searching for a gradient value close to zero. Once all weights are set, D is re-calculated. This fit continues until the gradient of D is close to zero. Each step where all weights are determined for D is called an epoch. Once the training is completed, the output discriminant D can be used to quantify the similarity to the training sample for a set of input variables.

Over-training

When ANNs are used, one of the common buzzwords is over-training. Over-training an ANN has to do with the node weights not being set properly, which results in the neural network discriminant having an unintended bias toward a certain input variable. The bias

typically consists of effects where the neural network becomes sensitive to very specific information in the training sample, which not necessarily exist in the data set the neural network is applied to. Three possible ways to over-train an ANN are listed below [64]:

1. Too many input parameters: if too many input parameters are used, any combination of the event weights will be able to generate a minimum that is sufficient for the minimization. One can think of this as the errors being so large that any value of the node weights will be considered to be 'within specifications'.

2. Too many epochs: if a neural network is trained over too many training cycles, it becomes sensitive to the statistical fluctuations in the training samples. Or simply: the neural network gets to know the training sample too well.

3. Samples too small: as the training is done on samples, it is very important that the samples are large enough. Usually, the rule of thumb is that the number of training events is much larger than the number of parameters. If the sample is too small, there is again the risk that the discriminant is trained to identify the statistical fluctuations in the training sample.

These three ways to over-train can be used as guidelines on how not to over-train: use as few input variables as possible, limit the number of epochs and use large training samples.

For the neural networks used in this thesis, the input variables were chosen from the 15 variables discussed previously. Only a subset of those 15 is used in the final analysis. The selection of the final set of variables is done by optimization of the expected analysis sensitivity.

The training samples

The neural networks are trained on a small, randomly chosen fraction of the main samples, consisting of 2500 events for both signal or background. The training sample is equivalent to around 2% of the data sample or 15% of the $t\bar{t}$ all-jets Monte Carlo sample with six or more jets. Data events that contain a b jet candidate are never used for ANN training.

5.4.2 Two different neural networks, two different goals

In the analysis presented in this thesis, two different neural networks are used, which are labeled NN_0 and NN_{all}. The first ANN, NN_0, is used for the preselection. The aim is to reject obvious background without rejecting signal. NN_0 is identical to the ANN used in the Run 1 $t\bar{t}$ to all-jets cross section analysis [61] and is not optimized for anything but background rejection. As there is only a very mild cut made on the output discriminant of NN_0, no influence on the number of observed $t\bar{t}$ signal events is expected. See Section 7.1 for the stability of the expected cross section as a function of the NN_0 selection cut.

The second neural network, NN_{all}, is used to isolate the signal. NN_{all} is tuned extensively and many different configurations are considered. The final configuration is determined by optimization of the expected statistical uncertainty on the cross section measurement (Section 6.2.1), a method also described in [62]. This method consists of

rejecting input variables until a figure of merit (in this case the statistical uncertainty on the cross section analysis) starts deteriorating rapidly.

5.5 NN_0

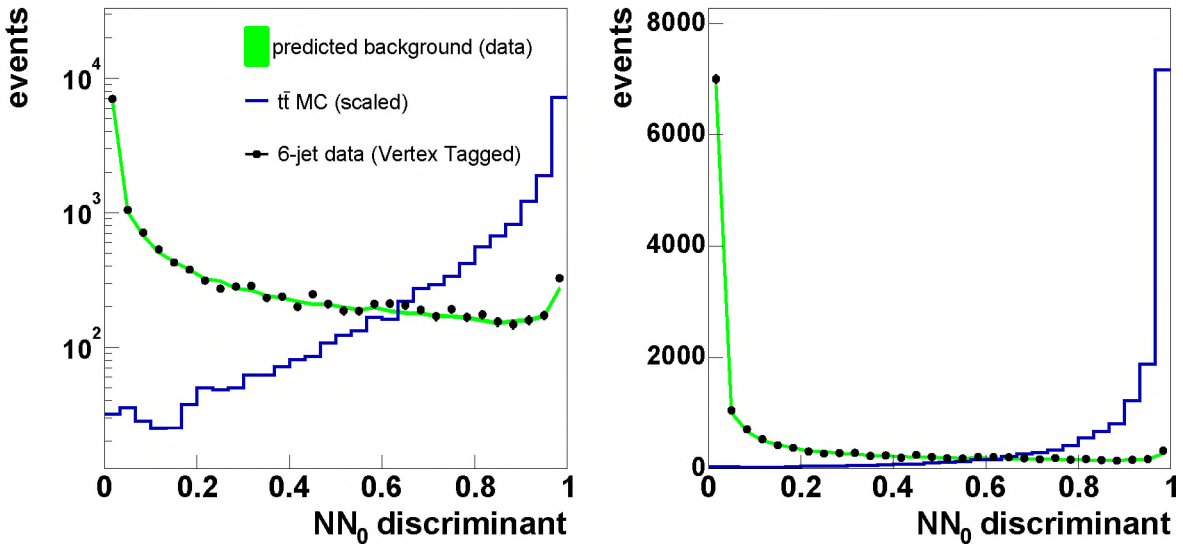

Figure 5.24: *The output distribution of NN_0 for tagged data (markers) and background prediction (band). Also shown is the distribution shape for $t\bar{t}$ all-jets Monte Carlo events (histogram).*

The signal sample to train NN_0 consists of 2.5k randomly picked $t\bar{t}$ all-jet Monte Carlo events. Untagged data is used to provide a background sample, which also consists of 2.5k events. The number of epochs is set to 50. NN_0 is trained on the identical set of variables that were used in DØ's Run 1 $t\bar{t}$ all-jets cross section measurement [61], which were selected to get maximal background rejection without affecting the $t\bar{t}$ signal: H_T, $\sqrt{\hat{s}}$, H_T^{3j}, N_{jets}^A, $\mathcal{S}$, $\mathcal{A}$ and $\mathcal{C}$. The output distribution of NN_0 is shown in Figure 5.24. As can be observed from the markers and error band, the TRF prediction of the tagged sample also works after application of NN_0. A requirement of

$$NN_0 > 0.05 \tag{5.23}$$

is made on the NN_0 discriminant. This cut has only a marginal effect on $t\bar{t}$ signal, but reduces the background by more than a factor two, as is listed in Table 5.5.

5.5.1 The TRF prediction versus NN_0

In this section the behavior of the TRF-predicted background is studied as a function of the NN_0 discriminant. To get a reliable background prediction it is important that there is no significant topological dependence of the TRF prediction on the neural network

	tagged data	all data	MC ($t\bar{t}$) efficiency
$NN_0 > 0.05$	45.62 ± 0.54 %	40.24 ± 0.14 %	99.68 ± 1.13 %

Table 5.5: *Efficiency of the $NN_0 > 0.05$ requirement for the entire data sample, the tagged data sample, and for $t\bar{t}$ signal Monte Carlo events.*

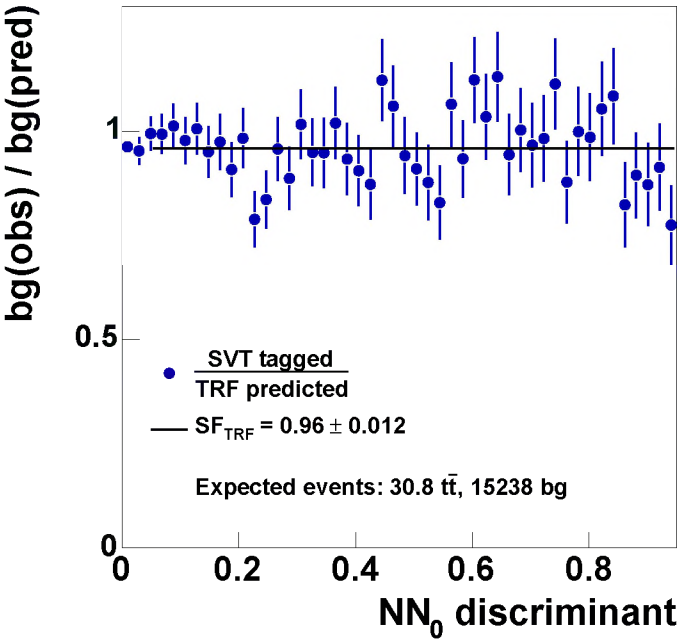

Figure 5.25: *Determination of SF_{TRF} for the SVT tag analysis. Shown per bin is the number of observed events divided by the number of predicted events. The line is the result of a fit of the data points to a horizontal line.*

discriminants. At the same time, this method is used to provide an absolute prediction of the number of background events in the tagged data sample.

Figure 5.25 shows the number of observed tagged events divided by the number of background tagged events as predicted by the TRF, as a function of the NN_0 discriminant. In the ideal case, the ratio of these should be '1' in each bin. However, we observe that the absolute normalization of the TRFs on event-by-event basis is slightly too large: We predict more events than we observe. The difference from unity is probably caused by correlations between the first and second vertex tagged jet, caused by a remnant of $b\bar{b}$ events in the sample. All these effects are small, so can easily be corrected for by scaling the TRF prediction so it predicts the correct number of tagged events[3].

For the region $NN_0 > 0.05$, a value of $SF_{TRF} = 0.960 \pm 0.012$ is observed[4]. The line shown in Figure 5.25 represents the fit of this normalization factor. Contamination by $t\bar{t}$ events does not affect the value of SF_{TRF}. The effect of the $t\bar{t}$ contribution was determined to be of the order of 0.002. All TRF predicted background distributions in this thesis are corrected with SF_{TRF}. The background prediction in the figures of the ANN input variables (Figure 5.8 through 5.22) also already include this correction, just like Figure 5.24. The uncertainty on this normalization will be taken into account as a systematic uncertainty on the cross section analysis.

The fact that the correction factor is small, leads us to believe that the factorization of the η and E_T dependence in the TRF is justified.

5.6 The final neural network and choice of input variables

The second ANN, NN_{all}, is used to enrich the $t\bar{t}$ content in the data sample. The training requirements for NN_{all} are more stringent, as the obvious background has already been removed from the training sample by NN_0. Besides the veto on tagged events in the training sample selection, the choice is made to bias the selection of data and Monte Carlo events, based on how likely the event is to have a secondary vertex tag. The goal of this procedure is to create training samples which are enriched with events with top production characteristics. Particularly the background training sample should be as similar to tagged data as possible, without actually containing any tagged events.

Events are assigned a weight between 0 and 1 which quantifies how likely the event is to end up in the tagged sample. Events with large probabilities are more likely to be used for the training of NN_{all}. For data, this means that the weight for the (untagged) sample is the event tag probability as derived from the TRF. For Monte Carlo events, the weight includes the trigger efficiency and the SVT efficiency on the event level. If the event weight is larger than a random number drawn from a uniform distribution between 0 and 1, the event is used for training.

[3]Note that the small number of correlated double-tagged events is the result of the $dR_{tags} > 1.5$ requirement. Without this requirement the TRFs perform significantly worse [71].

[4]This value is compatible with the value obtained if SF_{TRF} is measured without the $NN_0 > 0.05$ requirement. As the NN_0 cut is applied throughout the entire analysis, we also use it here.

The event selection is repeated until samples of 5k Monte Carlo events and untagged data events are collected, of which 2.5k are used for training. The other 2.5k events are used for the optimization of the neural network output during the training process, which reduces the risk of over-training NN_{all}. It turns out that this selection method produces ANNs that are around 4% more sensitive for the difference between $t\bar{t}$ and QCD events. This is mainly caused by the suppression of data events that can be classified as obvious background.

Choice the input variables for NN_{all}

The best choice of input variables for NN_{all} is determined by the rejection method: starting from the 15 variables defined in Section 5.3, input variables are rejected until the expected statistical significance of the NN_{all} analysis increases drastically. The expected significance, $\sigma_{frac}(\text{stat})$, is derived with the use of $t\bar{t}$ Monte Carlo events and the background prediction from the TRFs, and is defined as:

$$\sigma_{frac}(\text{stat}) = \frac{\sqrt{s_{exp} + b_{pred}}}{s_{exp}}, \tag{5.24}$$

where s_{exp} and b_{pred} represent the number of expected signal and predicted background events above a certain NN_{all} threshold. The expected best achievable analysis sensitivity for a certain ANN is equivalent to the minimum value of $\sigma_{frac}(\text{stat})$, see also Section 6.2.1.

The minimal value of $\sigma_{frac}(\text{stat})$ for different ANNs does not change much until only six variables are left. A relatively small number of input variables allows us to better understand and control systematic effects. Compared to the configuration with 15 variables [71] the observed increase, 4 % of the expected statistical error, is considered acceptable. Removing one extra variable increases the fractional error by around 7 %.

After optimization, NN_{all} uses the following input variables: H_T, $E_T^{5,6}$, $\mathcal{A}$, $\langle\eta^2\rangle$, $\mathcal{M}$ and $M_{min}^{3,4}$. Though there was no à priori requirement on this, now NN_{all} includes at least one input variable for every class of discriminating quantities as defined in Section 5.3.1. Note that the transverse energy sum H_T and the aplanarity $\mathcal{A}$ are used by both NN_0 and NN_{all}.

Stability of NN_{all}

After the choice of input variables for NN_{all}, the behavior of the neural network discriminant is studied for different training configurations. Again, the figure of merit used for these sensitivity studies is the expected statistical significance of a cross section measurement. The number of epochs for the training of NN_{all} is 100, which is observed to be a conservative value. When the expected statistical significance is studied as a function of the number of internal nodes of NN_{all}, the expected analysis sensitivity remains stable when the number of internal nodes is varied between 2 and 20. This suggests that NN_{all} does not make much use of the inter-correlations between its input variables.

Options other than neural networks

The suspicion that NN_{all} makes little use of the correlations between the input variables is investigated through application of a more simple multivariate method. If the expected sensitivity does not become worse, NN_{all} can in principle be replaced by these more simplistic methods. For instance, it is possible to construct a linear likelihood discriminant. However, it should be noted that it would not be possible to easily select this particular combination of input variables without the convenience of the NN_{all} pruning and the preselection with NN_0.

A linear likelihood discriminant is defined as a function of a set of variables $\vec{v}$ and their probability density functions (PDF) for signal $S(\vec{v})$ and background $B(\vec{v})$ (See also [16, 54]). Here, the variables $\vec{v}$ are the same variables as used for NN_{all}. A simple likelihood discriminant is defined as

$$D(\vec{v}) = \frac{S(\vec{v})}{S(\vec{v}) + B(\vec{v})}, \tag{5.25}$$

where $D(\vec{v})$ is expected to be close to zero for background and close to unity for signal events. The PDFs used for $S(\vec{v})$ and $B(\vec{v})$ are one-dimensional, so no correlations between the input variables are taken into account.

A cross section measurement that uses a likelihood discriminant of type $D(\vec{v})$ is expected to have a statistical significance that is 3% worse than using a neural network. Even though the expected statistical error is thus only marginally worse, we decided to continue with an analysis with NN_{all}.

5.6.1 The output of NN_{all}

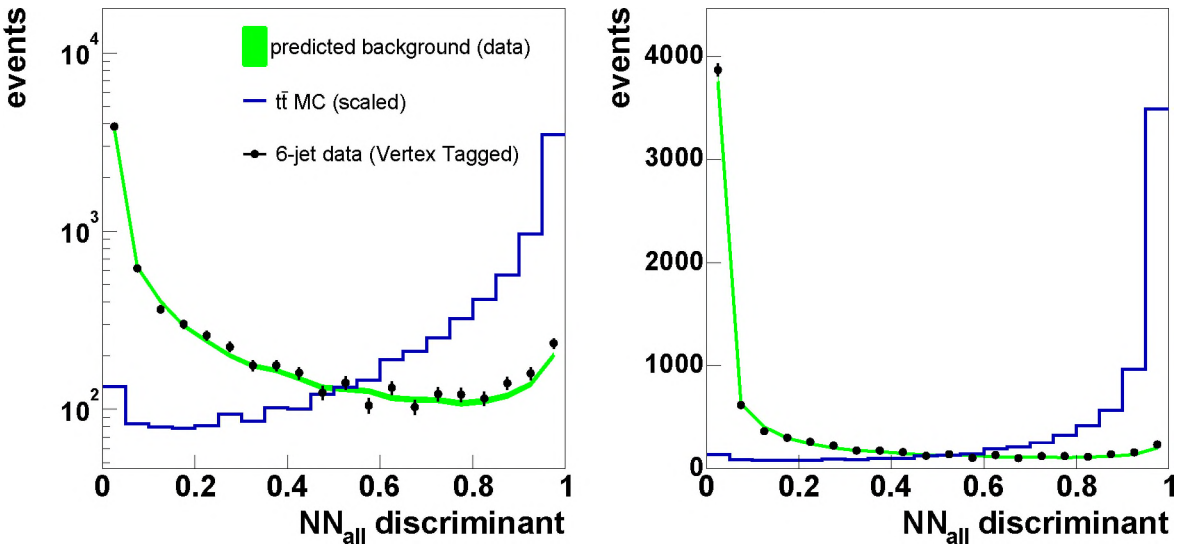

Figure 5.26: *The output distribution of NN_{all} for tagged data (markers) and TRF predicted tagged background (band). Also shown is the expected distribution for $t\bar{t}$ all-jets Monte Carlo events (histogram).*

The output discriminant of NN_{all} is presented in Figure 5.26. Shown are the observed tagged events, the prediction of the (tagged) background and the behavior for $t\bar{t}$ all-jets Monte Carlo events. There is a small excess of around a 100 events in the higher NN_{all} values. The excess events are attributed to $t\bar{t}$ production.

In the next chapter we use NN_{all} to determine the number of $t\bar{t}$ all-jets candidate events in the total data sample.

Chapter 6

Top pair cross section measurement

This Chapter discusses the $p\overline{p} \rightarrow t\bar{t}$ cross section measurement in the all-jets channel, using topological event information and the secondary vertex tag algorithm for b identification. An artificial neural network, NN_{all}, is used to discriminate between $t\bar{t}$ signal and tagged QCD background. We will determine the optimal cut on NN_{all}, which is used to count the number of events above the cut threshold and compare this to the predicted number of background events. The observed excess events are used to calculate the $t\bar{t}$ production cross section.

6.1 Signal efficiency

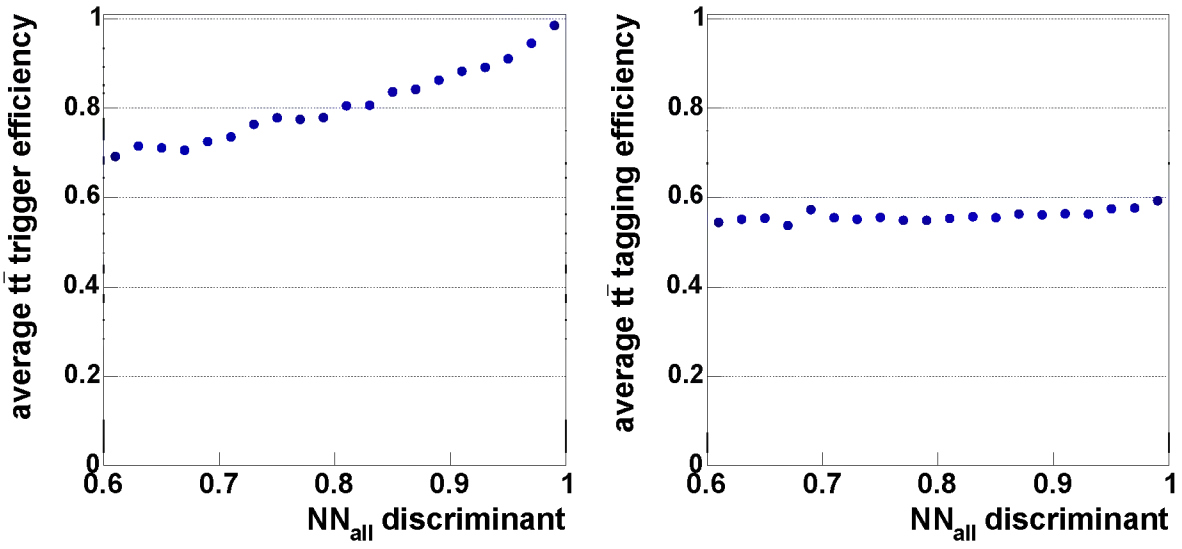

Figure 6.1: *The trigger efficiency (left) and SVT tagging efficiency (right) as a function of the NN_{all} discriminant in the signal region. These efficiencies have been measured on data. The Monte Carlo predictions are corrected for data efficiencies.*

The efficiency to detect a $t\bar{t}$ all-jets event depends on the location of the jets in the DØ

detector and on the transverse energy of the jets. As the jet E_T and η are also used as input for the various kinematic variables that are the input to NN_{all}, we expect a dependence of the efficiency to find a $t\bar{t}$ all-jets event as a function of the NN_{all} discriminant.

Figure 6.1 shows the trigger efficiency and SVT tagging efficiency as a function of NN_{all}. As can be observed, particularly the trigger efficiency increases near the NN_{all} region where most of the signal is expected, which is above $NN_{all} > 0.8$. We will account for this dependence in the determination of the efficiency for $t\bar{t}$ signal.

6.2 Cross section using counting method

6.2.1 Optimization of the NN_{all} discriminant cut

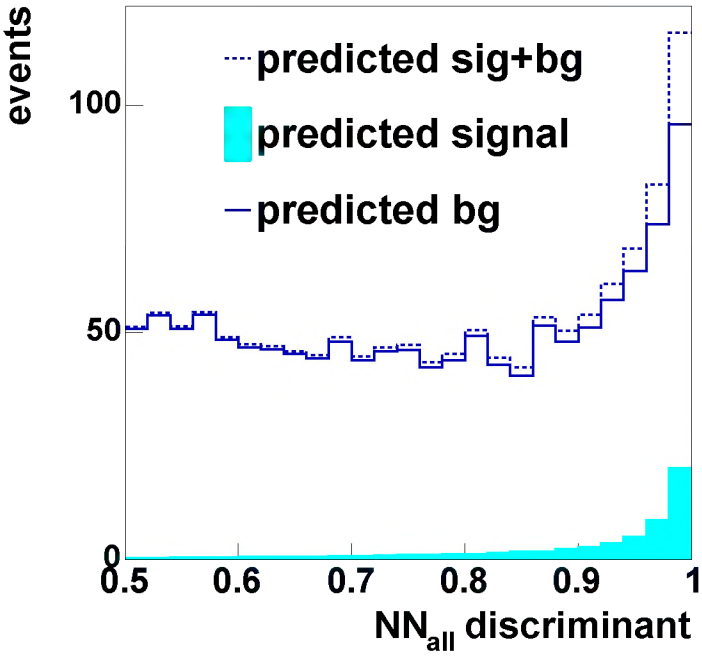

Figure 6.2: *Expected NN_{all} output distribution for background (line histogram) and expected background with additional $t\bar{t}$ signal (dashed histogram). The expected $t\bar{t}$ signal (filled histogram) is obtained from Monte Carlo simulated events (using a cross section of 6.5 pb).*

Figure 6.2 shows the predicted number of background events, together with the total number of expected events, which include $t\bar{t}$ signal and background. The number of signal events is obtained from Monte Carlo simulation, where a $t\bar{t}$ cross section of 6.5 pb is presumed. The simulated signal distribution is corrected for the trigger- and SVT tagging efficiencies. The optimal value of the cut on NN_{all} is determined by minimizing the expected statistical error on the measurement, σ_{frac}(stat). See Equation 5.24 for the definition of σ_{frac}(stat).

As can be seen in Figure 6.3, σ_{frac}(stat) is optimal at an NN_{all} cut of 0.91, which is used in the final analysis.

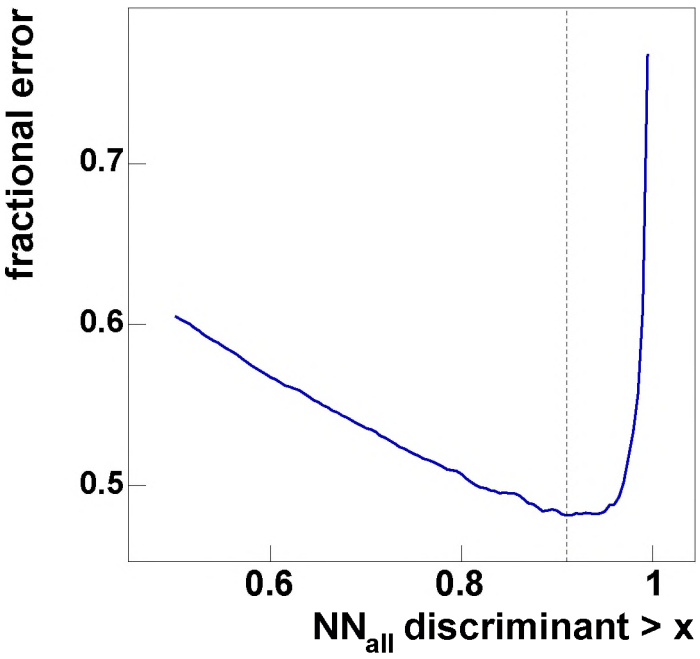

Figure 6.3: *Relative statistical error on the cross section measurement for different NN_{all} discriminant cuts. The dashed line indicates the cut at $NN_{all} = 0.91$.*

	tagged events
$N_{tag} \geq 1$	15851
$dR(tags) > 1.5$	15238
$NN_0 > 0.05$	7649
$NN_{all} > 0.91$	357

Table 6.1: *Numbers of tagged events after consecutive analysis cuts. The effect of the preselection has already been listed in Table 4.3.*

6.2.2 Observed events

In the tagged sample, the following number of events are observed above the NN_{all} cut:

$$N_{obs} = 357 \text{ events.} \tag{6.1}$$

For completeness, we list the effect of all analysis cuts on the tagged sample in Table 6.1.

The tagged background is predicted to contribute:

$$N_{bg}^{raw} = 315.9 \pm 6.6 \text{ events,} \tag{6.2}$$

where the error comes from statistical fluctuations in the TRF input events.

The number of *real* background events is lower than the observed number. As the predicted background distribution has to be corrected for $t\bar{t}$ tagged events that are used in the background prediction, the corrected prediction will be lower than the TRF prediction.

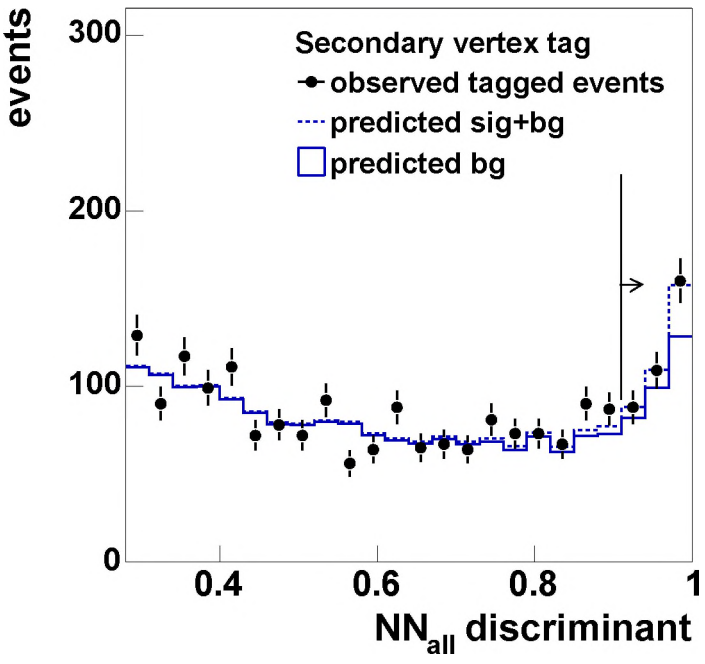

Figure 6.4: *NN_{all} output distribution for tagged events (markers), predicted background (histogram) and expected signal+background (dashed histogram).*

The correct number of background events if a cross section of $\sigma_{t\bar{t}} = 6.5$ pb is taken into account is 1.9% smaller:

$$N_{bg}^{corr} = 310.0 \pm 6.6 \text{ events.} \tag{6.3}$$

The uncertainty on this correction due to the $t\bar{t}$ cross section will be taken into account as a systematic uncertainty. The probability that the 357 observed events originate from a statistical fluctuation of the predicted 310 background events is equivalent to $\frac{357-310}{\sqrt{310}} = 2.67$ standard deviations. This implies a Gaussian probability of $P = 3.8 \cdot 10^{-3}$ that the observed excess of events is caused by a statistical fluctuation of the background.

Figure 6.4 shows the observed NN_{all} distribution, together with the distribution predicted if background and $t\bar{t}$ all-jets signal (dashed histogram) or only background (solid histogram) were present in the dataset. The binning has been chosen such that the last three bins contain all events above the cut of $NN_{all} > 0.91$.

The efficiency for the selected cut is measured on $t\bar{t}$ all-jets Monte Carlo events, which is corrected for the efficiency of the trigger and the probability to have one SVT tag. The efficiency for each individual cut (exclusive efficiency) and the total efficiency (inclusive efficiency) are listed in Table 6.2:

$$\epsilon_{\text{all-jets}} = 0.0806 \pm 0.0010 \text{ (stat)}, \tag{6.4}$$

where the errors are due to Monte Carlo statistics. This efficiency still has to be corrected for events from the other $t\bar{t}$ decay channels, particularly the τ+jets channel is expected to have an event topology that is similar to the fully hadronic top decays. From Monte Carlo simulation we obtain:

$$\epsilon_{\ell\text{+jets}} = 0.0026 \pm 0.0003 \text{ (stat)}. \tag{6.5}$$

ε for $t\bar{t}$	all-jets		lepton+jets	
	inclusive	exclusive	inclusive	exclusive
trigger	0.2537 ± 0.0022	0.7725 ± 0.0066	0.0169 ± 0.0008	0.5305 ± 0.0255
$N_{SVT} \geq 1, dR_{tags} > 1.5$	0.1430 ± 0.0012	0.5635 ± 0.0045	0.0095 ± 0.0005	0.5628 ± 0.0275
$NN_0 > 0.05$	0.1426 ± 0.0012	0.9971 ± 0.0007	0.0093 ± 0.0005	0.9831 ± 0.0095
$NN_{all} > 0.91$	0.0806 ± 0.0010	0.5652 ± 0.0060	0.0026 ± 0.0003	0.2831 ± 0.0336

Table 6.2: *Inclusive and exclusive efficiencies for $t\bar{t}$ all-jets signal. Shown are the efficiencies for both the all-jets and lepton+jets decay channel. The preselection efficiency has already been listed in Table 4.2.*

Note that the exclusive SVT tagging efficiency is very similar for both $t\bar{t}$ decay channels, as the number of b jets is the same for both decay channels.

Combining the efficiencies for the different $t\bar{t}$ decay channels has to be done according to the expected branching ratios. The branching ratios are respectively, BR= 0.4619 ± 0.0048 for the all-jets and BR= 0.4349 ± 0.0027 for all three lepton+jets channels combined, see Table 1.3. This gives us a final signal efficiency of

$$(\epsilon \cdot \mathrm{BR})_{t\bar{t}} = (\varepsilon \cdot \mathrm{BR})_{\mathrm{all-jets}} + (\varepsilon \cdot \mathrm{BR})_{\ell+\mathrm{jets}} = 0.0384 \pm 0.0012 \tag{6.6}$$

6.2.3 Cross section calculation

The $t\bar{t}$ production cross section, measured in the all-jet channel, is calculated from

$$\sigma_{t\bar{t}} = \frac{N_{obs} - N_{bg}}{\mathcal{L} \cdot (\mathrm{BR} \cdot \epsilon)_{t\bar{t}}} \tag{6.7}$$

where the integrated luminosity was measured to be $\mathcal{L} = 162.5 \pm 10.6$ pb^{-1} (see also Table 4.1).

The (Poisson) logarithmic likelihood $-2 \ln Q$ of the cross section probability Q can be constructed using:

$$-2 \ln Q = \ln \left(\frac{N_{exp}^{N_{obs}}}{N_{obs}!} e^{-N_{exp}} \right), \tag{6.8}$$

which gives the likelihood to observe a certain number of events N_{obs}, as a function of the number of expected events N_{exp}. N_{exp} is the number of events that are predicted for a (running) hypothetic cross section value. N_{exp} is only dependent on the cross section if all other observables in Equation 6.7 are known. The minimal value of the Poisson likelihood is identical to $\sigma_{t\bar{t}}$, and the standard deviation is given by the values where $-2 \ln Q$ is exactly one higher than the minimal value. Figure 6.5 shows the distribution of $-2 \ln Q$.

Using the observed events (6.1), the predicted background (6.3) and efficiency (6.6), the cross section is measured to be:

$$\sigma_{t\bar{t}} = 7.5^{+3.1}_{-3.0}(\mathrm{stat})\ \mathrm{pb} \tag{6.9}$$

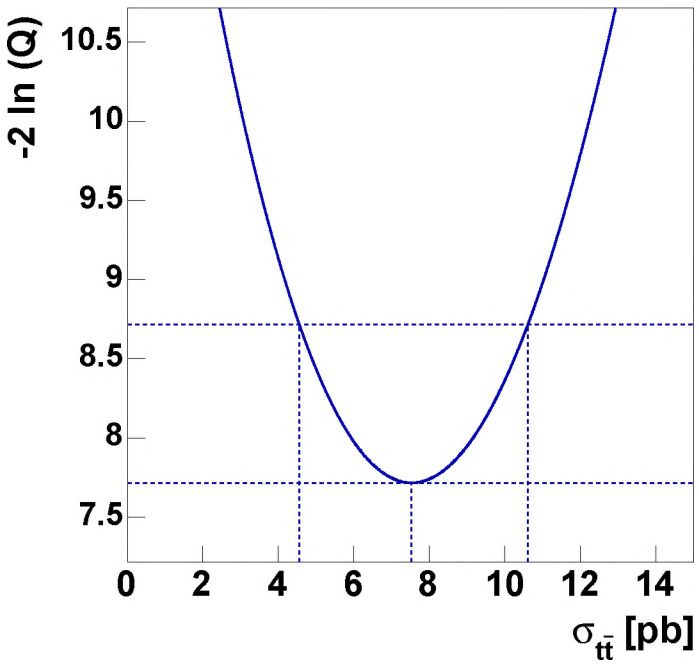

Figure 6.5: *The Poisson likelihood of the $t\bar{t}$ cross section measurement.*

6.3 Event Display

We use the DØ viewing environment [69] to visualize tagged events at large NN_{all} discriminants. All events with large NN_{all} values have only one, well defined primary vertex, but the six-jet environment in combination with high track multiplicities make the candidate events not very interesting for aesthetic purposes.

We selected an event with two secondary vertex tags, which increases the probability that it is a top candidate. In addition, it is possible to identify all six jets and both secondary vertices in the event display. Some additional information concerning this event and its jets is listed in Table 6.3. The reconstructed invariant masses of the top quarks and W bosons are the values coming from the jet permutation with the smallest value of $\mathcal{M}$ (Equation 5.20).

Figure 6.6 shows the separate six jets in the event in the η, ϕ plane, where the energy contained in the calorimeter is represented on the vertical axis. This type of representation is very useful for studying the calorimeter information and jets in the event. A threshold of $E_T > 1.0$ GeV on the calorimeter towers was applied for noise reduction.

When the busy six-jet environment is projected to a two-dimensional plane, it is usually difficult to identify the separate jets in the x, y plane, like is shown in Figure 6.7. The jets tend to overlap when the event is projected on to the transverse plane, it is only possible to identify 5 jets in this projection. Figure 6.8 is a detail of the central detector region in Figure 6.7. The secondary vertices that have been reconstructed in the track-jets are marked by an ellipse. The hits in the inner layer of the SMT are also shown in Figure 6.8. These are located on a cylinder with a radius approximately 2.6 cm from the interaction point.

General information			
	event number	41213373	
	run number	176305	
	date	Tuesday April 29, 2003	
Topological variables and ANN			
H_T	457 GeV	$E_{T_{5,6}}$	37.4 GeV
$\mathcal{A}$	0.28	$\langle\eta^2\rangle$	0.31
$\mathcal{M}$	1.29	$M_{min}^{3,4}$	71.3 GeV/c^2
NN_0	0.999	NN_{all}	0.998
The jets			
jet 4	$E_T = 61.9$ GeV $\eta = -0.9$ $\phi = 236°$	jet 1	$E_T = 114.2$ GeV $\eta = -0.1$ $\phi = 240°$
jet 2	$E_T = 111.2$ GeV $\eta = -0.5$ $\phi = 38°$	jet 5	$E_T = 41.9$ GeV $\eta = -1.3$ $\phi = 329°$
M_{W_1}	71.3	M_{W_2}	78.1
jet 6*	$E_T = 33.4$ GeV $\eta = 0.4$ $\phi = 75°$	jet 3*	$E_T = 94.8$ GeV $\eta = -0.4$ $\phi = 126°$
m_{t_1}	175.4	m_{t_2}	188.1

Table 6.3: *Additional information of the event shown in Figures 6.6 through 6.8. The jets marked with $\star$ have a secondary vertex assigned to them. The three jets within a column correspond to the listed M_{W_i} and m_{t_i} in the same column. The W mass resolution is approximately 15 GeV/c^2, the resolution for the triple-jet invariant mass of the top candidates is around 24 GeV/c^2, see also Appendix A.*

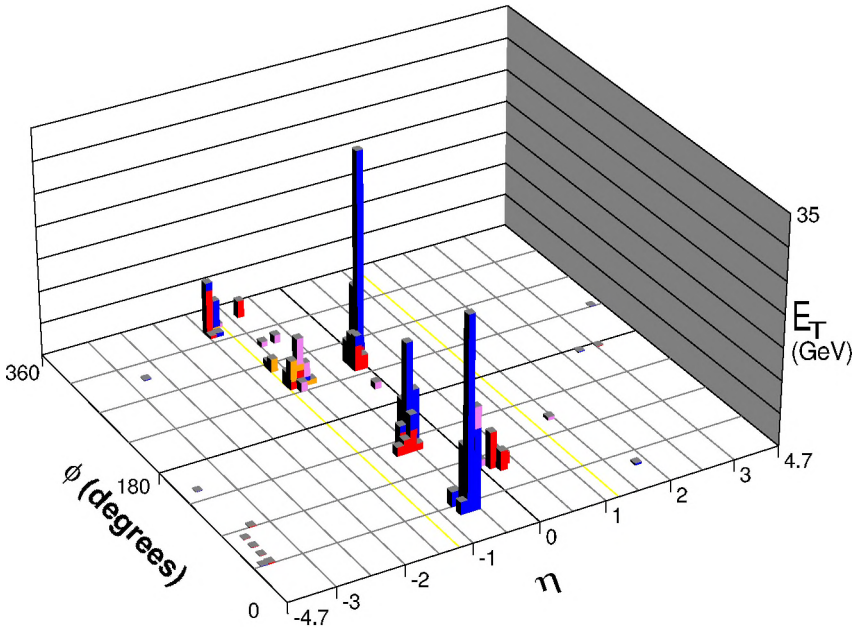

Figure 6.6: *Calorimetric transverse energy in the η, ϕ plane, of a six-jet, double-tagged $t\bar{t}$ candidate event.*

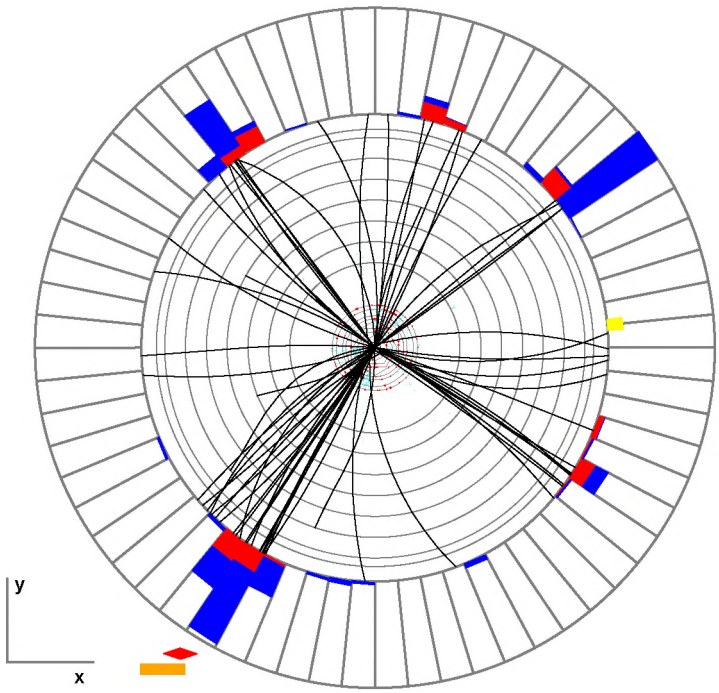

Figure 6.7: *The calorimeter and tracking view. A double-tagged $t\bar{t}$ candidate event shown in the plane perpendicular to the beam. Shown is a projection on the xy plane at $z = 0$.*

6.4 Systematic uncertainties

In this section the systematic uncertainties on the measured cross section will be described. There are several uncertainties that affect the cross section extraction. Some influence the signal efficiency, others the number of background events.

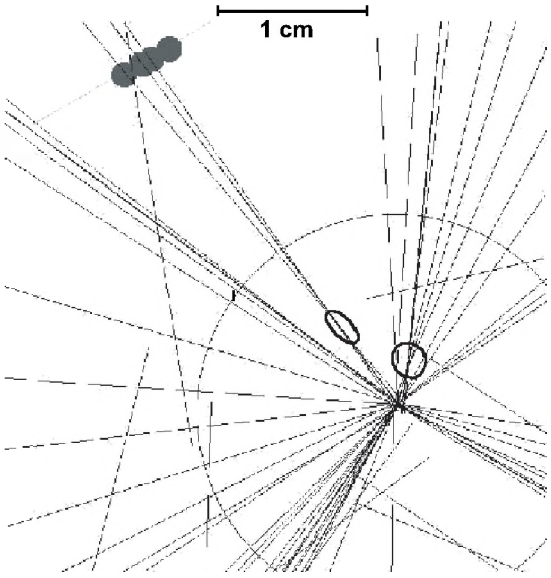

Figure 6.8: *Detail of the double-tagged $t\bar{t}$ candidate event. Shown is a projection on the xy plane at $z = 0$, focused on the interaction region near the beam pipe. The dots in the upper left corner represent hits in the inner layers of the silicon tracker, approximately 2.6 cm from the interaction point. The two secondary vertices are also indicated.*

Below, we list the uncertainties in decreasing order of importance based on the size of their effect on the measured cross section:

- the uncertainty on the jet energy scale for calorimeter energy measurements both in data and Monte Carlo events;
- the uncertainty coming from the (fixed) input top mass in the Monte Carlo simulation;
- the uncertainty coming from the jet energy resolution and the jet identification;
- the uncertainty coming from the SVT tag efficiency parameterizations;
- the uncertainty coming from the trigger parameterizations;
- the uncertainty on the background prediction using the tag rate functions.

6.4.1 Jet Energy Scale

Any change in the behavior of the Jet Energy Scale influences the efficiency for signal and background. The total uncertainty on the jet energy scale depends on the choice of the parameterizations (systematic error) and the accuracy of the determination of the parameters (statistical error). There are different JES corrections for data and Monte Carlo events. The dominant systematic error comes from the showering correction $\mathcal{S}$ (See Equation 3.5). The systematic and statistical errors are taken to be uncorrelated, and the total error on the energy of a jet is defined as

$$\sigma^{JES} = \sqrt{\sigma^2_{stat} + \sigma^2_{syst}}. \tag{6.10}$$

σ^{JES} depends on the jet energy and η_{det}. The typical value of the jet energy scale uncertainty is $\sigma^{JES} = 7\%$. The uncertainty on the JES for data and that for the Monte Carlo are uncorrelated and should both be taken into account. The uncertainty in the JES affects the efficiency for signal in two places:

1. the preselection efficiency is sensitive to the number of jets over an E_T threshold;

2. the ANN analysis is sensitive to the variations in the (energy-sensitive) input variables, particularly H_T, $E_T^{5,6}$, $\mathcal{M}$ and $M_{min}^{3,4}$.

Table 6.4 lists the fractional changes of the measured efficiency for signal when the jet energy scale is varied by $\pm\sigma^{JES}$, and by the average value of the correction uncertainty, that amounts to 7%. Shown are both the influence of the JES on the preselection efficiency and on the total analysis efficiency for $NN_{all} > 0.91$.

	preselection		$NN_{all} > 0.91$	
	$-\sigma$	$+\sigma$	$-\sigma$	$+\sigma$
data JES	-10.8	10.7	-20.2	20.7
MC JES	-10.8	10.7	-20.1	20.7
$\sigma^{JES} \equiv 7\%$	-7.5	7.00	-24.8	23.9

Table 6.4: *Systematic uncertainties (in %) on the efficiency for signal as caused by the uncertainty on the jet energy scale. Shown are the effect of the JES on the preselection efficiency, and the effect of the JES on the efficiency after the NN_{all} cut.*

The uncertainties listed in Table 6.4 show that the JES influences the analysis uncertainty in two ways: Low-energy jets have large uncertainties on the jet correction. These jets are also most likely to be cut away in the preselection, and as such the JES correction of low-energy jets influences the preselection efficiency. At NN_{all} values near unity, all jets are relatively energetic. This is caused by the set of kinematic and topological variables which are used to select $t\bar{t}$-like events. The NN_{all} cut efficiency is very sensitive to fluctuation in the energies of the jets that are used for the calculation of the various variables. Here, the small errors on jets with transverse energies around 50-100 GeV create an uncertainty on the analysis efficiency which is even larger than the effect that is caused by the preselection.

The result of this effect is presented in a graphical way in Figure 6.9, which shows the efficiencies when the JES is varied by $\pm\sigma$ or, alternatively, by $\pm 7\%$. Figure 6.9 shows the behavior of the efficiency of the complete analysis under JES variations, as a function of the NN_{all} cut. The left plot shows the fractional change in analysis efficiency as a function of the NN_{all} cut. The right plot shows the efficiency of the NN_{all} cut after preselection and $NN_0 > 0.05$ requirement, which hence is equal to unity if no NN_{all} cut is applied. Figure 6.9 only shows the uncertainty for a $\pm 1\sigma$ variation of the Monte Carlo JES. Adding the same curves for variation of the data JES would not add any information; as listed in Table 6.4, the uncertainties introduced are almost identical. Although the absolute

corrections for the data and Monte Carlo JES are different, the identical uncertainty confirms that the JES in the simulation provides a realistic model of the data.

The total uncertainty is obtained by adding the data and Monte Carlo JES uncertainty in quadrature:

$$\sigma_{JES}(\text{tot}) = \sqrt{\sigma_{JES}^{MC}(\text{tot})^2 + \sigma_{JES}^{data}(\text{tot})^2}. \tag{6.11}$$

The values of $\sigma_{JES}(\text{tot})$ are +29.3% for changes towards larger efficiency values, and -28.5% for the lower shift. The influence of the JES error on the total efficiency is a significant fraction of the analysis uncertainty.

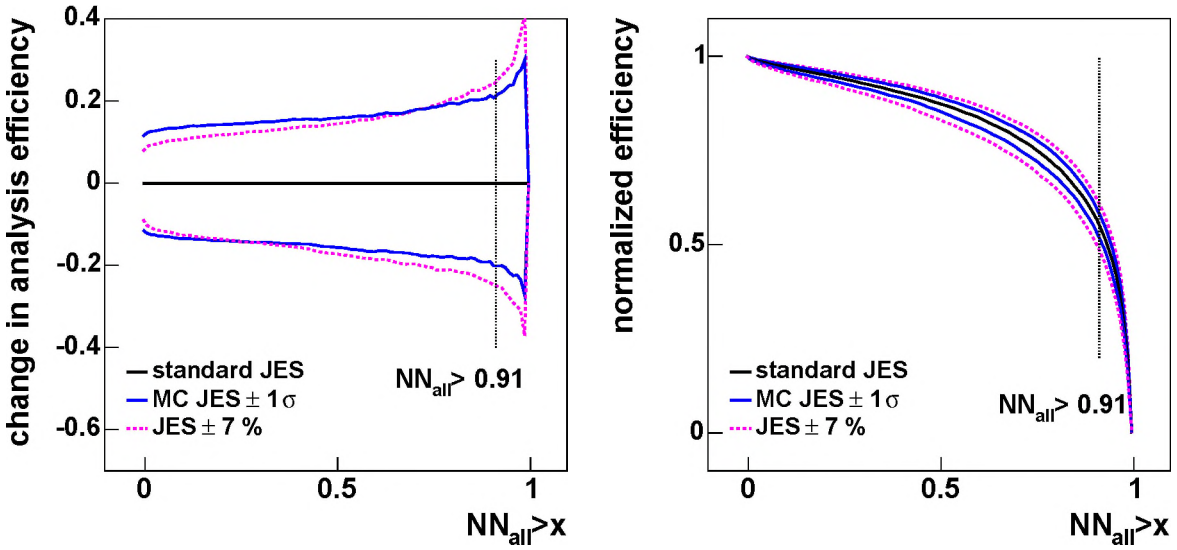

Figure 6.9: *The relative change in efficiency (left) and efficiency of the cut on NN_{all} (right) for changes in JES. Shown are the efficiencies for the JES varied by $\pm\sigma$, which are similar for the data and Monte Carlo jet energy scale. Also shown is the result of the $\pm$7% JES variation.*

6.4.2 Top mass

The extracted efficiency for signal is dependent on the top mass that was used in the Monte Carlo simulation. Figure 6.10 shows the nominal signal efficiency for a top mass of 175 GeV/c^2, together with the result obtained from control samples with top masses of 165 and 185 GeV/c^2. We determine the efficiency for $m_t = 178.0 \pm 4.3$ GeV/c^2 (the current preliminary world average, see [9, 13]) through interpolation, also shown in Figure 6.10.

As the value of m_t used in the Monte Carlo is still within one standard deviation of the world average, we decided not to correct to the current world average. Instead, the variation of the efficiency as a function of the $\pm 1\sigma$ uncertainty of the world average is taken as the limit. These limits are also indicated in the Figure. The efficiency for $t\bar{t}$ varies between -2.0% and $+9.0\%$, which is taken into account as a systematic uncertainty from the top mass.

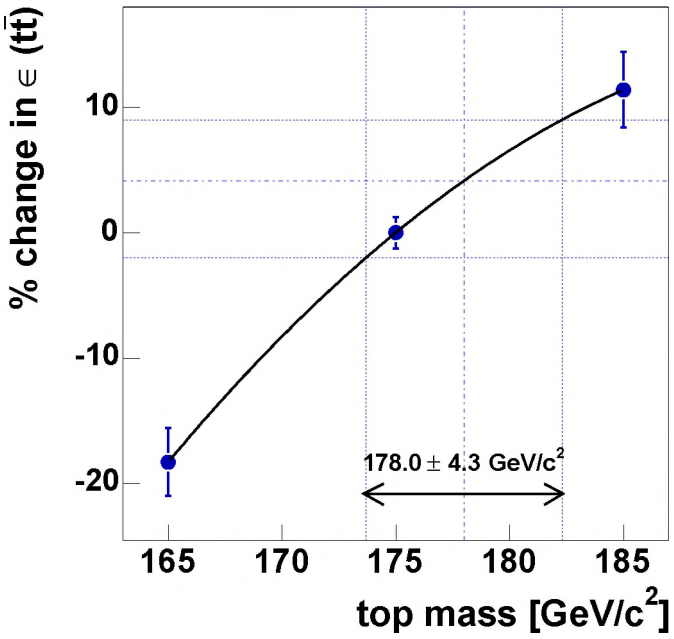

Figure 6.10: *Top mass dependence of the efficiency for signal, for the vertex tag analysis. The dashed lines are the current (preliminary) limits on the top mass,* $m_t = 178.0 \pm 4.3$ *GeV/*c^2.

6.4.3 Jet identification

The current jet identification and reconstruction uses a first-level trigger confirmation in its selection criteria, as discussed in Section 3.1.6. In the Monte Carlo simulation, this effect is not taken into account and therefore the efficiency of the identification and reconstruction is typically 1% higher than in data. We have made a conservative parametrization of this effect, and apply it in the Monte Carlo. This leads to a change of -5.2% in efficiency for $t\bar{t}$ all-jets events, which we take into account as a systematic uncertainty.

6.4.4 Jet resolution

The Monte Carlo jets are smeared according to the measured jet energy resolution in data. There is an uncertainty on this smearing correction, which is of the order of a few tenths of a percent. This effect is taken into account by over- or under-smearing the simulated jets. We observe an effect between -0.2% and 0.5% on the signal efficiency.

6.4.5 Tag rate functions and background

Uncertainty on TRF fit

The uncertainties on the TRF fits are shown in Figures 5.3 and 5.4, and include all correlations between the fit parameters. We modify the TRF to the upper and lower values. Determination of the number of background events with these modified turn-on TRF parameterizations gives us a different number of expected background events. We use the change as a systematic uncertainty on the TRF fit, which is listed in Table 6.5.

$NN_{all} > 0.91$	$-\sigma$	$+\sigma$	change in N_{bg} [events]	
TRF fits	-1.29 %	0.87 %	-4.0	2.7
SF_{TRF}	-1.20 %	1.20 %	-3.7	3.7
$t\bar{t}$ content	0.88 %	-0.88 %	2.8	-2.8

Table 6.5: *Uncertainty on the number of predicted background events. Listed are the uncertainties caused by the error on the TRF fit functions, the error on the TRF normalization and the presence of $t\bar{t}$ events in the TRF prediction of the background.*

The TRF scale factor

The tag rate functions are normalized to predict the exact number of tagged events in the background region. There is an uncertainty on the fit of the normalization factor SF_{TRF}, which is used as the systematic error on the background normalization. The effect on the number of predicted background events is listed in Table 6.5.

The presence of $t\bar{t}$ in the background

The number of background events is corrected for the (expected) number of $t\bar{t}$ all-jets events in the sample, where the theoretical value of $\sigma_{t\bar{t}} = 6.5$ pb is used. We estimate the systematic error by varying the cross section by ± 3 pb, which is the statistical error on the measured cross section in this analysis. The effect is listed in Table 6.5.

6.4.6 The b-identification

The b jet identification efficiency in data and Monte Carlo simulation has sizable uncertainties. The systematic error on the efficiency to tag b jets is around 3 %. The largest contribution comes from the size of the muon tagged sample, which is used to measure the efficiency on data. There also is a similar effect from Monte Carlo statistics, particularly in μ-tagged jets. Another effect that has an influence on the efficiency for $t\bar{t}$ all-jets signal is the uncertainty on the taggability of jets. There are also marginal effects coming from the difference in taggability as a function of (Monte Carlo) quark flavor and the assumption that the secondary vertex tag behaves identical if a muonic jet is present in the event. The changes in efficiency for signal are categorized in simulation and data effects, and are listed in Table 6.6.

6.4.7 Other systematic uncertainties

Monte Carlo statistics

The uncertainty on the efficiency is limited by the number of Monte Carlo simulated $t\bar{t}$ all-jets events. This introduces an additional systematic uncertainty of 1.2% on the cross section measurement.

$NN_{all} > 0.91$	$+\sigma$	$-\sigma$
Monte Carlo Statistics	+1.2 %	-1.2 %
Vertex reconstruction	+1.0 %	-1.0 %
Trigger Efficiency	+3.0 %	-0.0 %
Trigger fit	+1.0 %	-1.2 %
JES $\pm\sigma_{JES}$	+29.3 %	-28.5 %
$m_t \pm \sigma_t$	+9.0 %	-2.0 %
jet identification	+0.0 %	-5.2 %
jet energy resolution	+0.2 %	-0.5 %
b tag efficiency (data)	+3.0 %	-3.8 %
b tag efficiency (MC)	+0.6 %	-0.9 %
total uncertainty on $\varepsilon_{t\bar{t}}$	+31.0 %	-29.4 %

Table 6.6: *The changes in the efficiency (in %) for $t\bar{t}$ signal for different systematic uncertainties that affect the efficiency measurement.*

Primary vertex reconstruction

The preselection also includes a vertex multiplicity cut. The uncertainty on this selection cut is $\pm 1.0\%$, which is a combination of the uncertainty caused by the difference in efficiency between data and Monte Carlo events, and Monte Carlo statistics [46].

Determination of the trigger efficiency

The method to determine the trigger efficiency neither accounts for the correlations between triggered jets, nor the possibility that a jet might trigger more than one L1 trigger tower. The size of this effect is derived from the difference between the application of the jet turn-on curves and the efficiency as measured on Monte Carlo $t\bar{t}$ events with a simulated trigger (Section 4.3.2). The effect on this efficiency is +3 %.

Uncertainty of the trigger fits

The signal trigger inefficiency is almost completely dominated by the first trigger level, the efficiency for $t\bar{t}$ signal at the first trigger level is not saturated like in L2 and L3. The trigger efficiency was re-calculated by varying the trigger turn-on curves on all trigger levels by $\pm 1\sigma$. The effect of the total trigger efficiency is 1%.

6.4.8 Total systematic uncertainty

The contributions from all effects to the systematic uncertainty of the signal efficiency are listed in Table 6.6. The effect due to the JES appears to dominate the systematic uncertainty. The different systematic effects on the signal efficiency are considered uncorrelated, and are added in quadrature to obtain the total systematic uncertainty. We do the same to obtain the systematic uncertainty on the number of background events.

	$+\sigma$	$-\sigma$	change in cross section	
total error on efficiency	31.0%	−29.4%	-1.8 pb	+3.1 pb
total error on background	1.72%	−1.97%	-0.9 pb	+1.0 pb
total systematic error			-2.0 pb	+3.3 pb
error on the luminosity	+6.5%	−6.5%	-0.5 pb	+0.5 pb
statistics			-3.0 pb	+3.1 pb

Table 6.7: *Summary of the total systematic, statistical and luminosity uncertainties and the result on the cross section measurement.*

Table 6.7 lists the total systematic uncertainty on the efficiency and the number of background events. Also listed in Table 6.7 are the uncertainty on the luminosity and the statistical error.

The total systematic uncertainty on the cross section is determined to be -2.0 pb for contributions which lower the cross section. The cross section is raised by 3.3 pb for contributions which increase the measured value. The uncertainty due to the error on the luminosity can be considered small, while the statistical error is of comparable size to the total systematic error.

6.5 The $t\bar{t}$ production cross section

The $t\bar{t}$ production cross section measured on events with a secondary vertex tag and six or more jets is

$$\sigma_{t\bar{t}} = 7.5^{+3.1}_{-3.0}(\text{stat})\ ^{+3.3}_{-2.0}(\text{syst})\ \pm 0.5(\text{lumi})\ \text{pb}. \tag{6.12}$$

When all uncertainties are combined in quadrature, we obtain

$$\sigma_{t\bar{t}} = 7.5^{+4.5}_{-3.6}\ \text{pb}, \tag{6.13}$$

slightly more than two standard deviations from 0. An excess of 47 events is observed in a sample with an integrated luminosity of 162.5 pb^{-1}. The probability that these 47 events originate from a statistical fluctuation of the background is $P = 3.8 \cdot 10^{-3}$. The invariant mass of the $t\bar{t}$ candidates is examined in Appendix A.

6.6 Comparison

Figure 6.11 shows the preliminary measurements of the $t\bar{t}$ production cross section in a variety of analyses, presented at high energy physics conferences in the spring of 2004 [70], including a cross section result for the all-jets channel measured on the same dataset but without optimizations in the background sample and neural network procedure [71]. Figure 6.11 also includes the result presented in this thesis. The uncertainty on the measurement in this thesis is smaller than the previous DØ Run 2 cross section measurement in the all-jets channel.

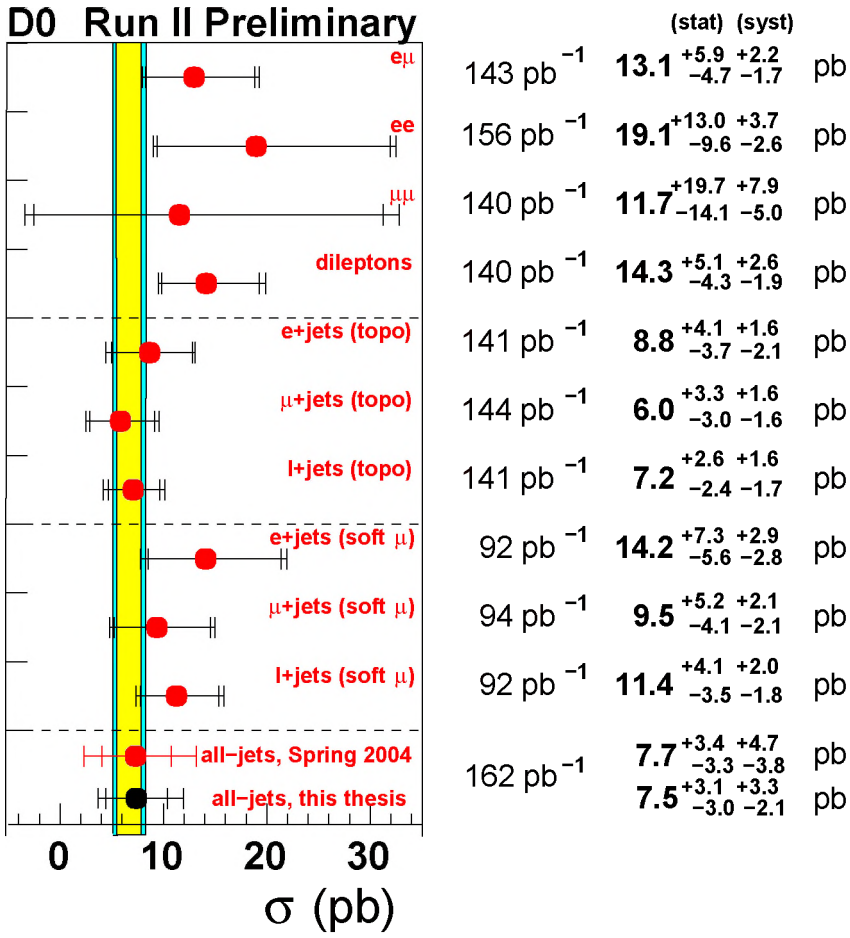

Figure 6.11: *The preliminary DØ results for the different $t\bar{t}$ cross section analyses [70]. The bands represent the theoretical predictions for the $t\bar{t}$ cross section, for $m_t = 174.3 \pm 5.1$ GeV/c^2. Listed are the measured cross sections from the different analyses, with their statistical and systematic uncertainty listed separately. Also shown is the integrated luminosity on which each measurement is based.*

The measurement presented in this thesis has comparable errors to the measurements in the other decay channels. Most measurements are dominated by the statistical uncertainty, unlike the measurement in this thesis which has a statistical and systematic uncertainty of comparable size. Analyses which focus on $t\bar{t}$ decays with few jets are less dependent of the uncertainty on the jet energy scale. Therefore, the different channels with a lepton and jets in the final states are measured with relatively small systematic errors.

The competing preliminary result of the $t\bar{t}$ cross section in the all-jets channel as presented by the CDF collaboration [67] has a similar central value, and comparable statistical and systematic uncertainties.

6.6.1 Theoretical prediction

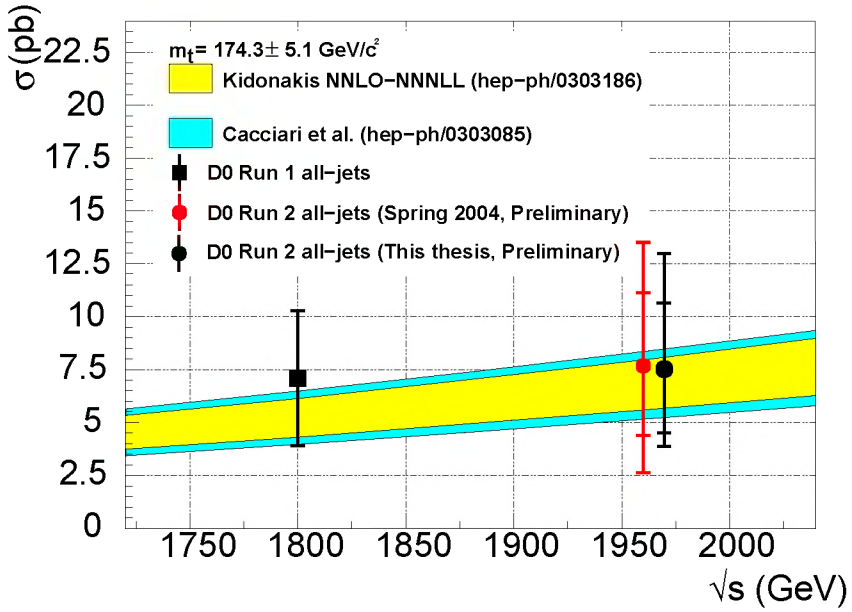

Figure 6.12: *The Run 1 and Run 2 DØ $t\bar{t}$ production cross section result for the measurements in the all-jets channel. Both Run 2 cross section measurements were done on data with a center of mass energy of 1.96 GeV, but for clarity the second point is shifted toward higher values of $\sqrt{s}$.*

Figure 6.12 shows the NNLO QCD predictions for the $t\bar{t}$ cross section, for a top mass of $m_t = 174.3 \pm 5.1$ GeV/c^2 [9, 70]. The result presented in this thesis and previous $t\bar{t}$ cross section measurements in the all-jets channel are also shown in Figure 6.12. The measurements agree well with the theoretical predictions.

Chapter 7

Stability and consistency of the result

In the previous Chapter we have measured the $t\bar{t}$ production cross section. In this Chapter we will further examine the data used to determine the $t\bar{t}$ production cross section. The stability of the result will be investigated by application of alternative analysis methods.

7.1 The neural network analysis

In the cross section estimate, the analysis efficiency and number of events are determined for a fixed NN_{all} cut. The NN_{all} cut is optimized by tuning to the expected lowest statistical error as described in Section 6.2.1. All systematic uncertainties are derived for this particular NN_{all} cut. The main other uncertainty of the neural network analysis is the dependence on the NN_0 background rejection cut.

The neural network NN_0 is used for an intermediate selection, as discussed in Section 5.5. Figure 7.1 shows the minimal fractional error σ_{frac} of the analysis as a function of the preselection cut on NN_0. The cut of $NN_0 > 0.05$ appears to lie 'safely' on the plateau region. Consequently the fractional error does practically not depend on the value of the NN_0 cut.

7.2 Tighter jet criteria

Another quantity which affects the measurement is the minimal E_T requirement, used in the jet identification. The expected analysis efficiency and uncertainty depends on the jet E_T requirements near the used requirement of $E_T > 15$ GeV. Naïvely one could expect an improvement when the E_T cut is tightened (See also Table 6.4). The current sample, however, is too small to do this in an effective way: the (expected) statistical uncertainty increases rapidly when the jet requirements are tightened.

Table 7.1 gives the (expected) statistical fractional error on the cross section as a function of the jet E_T requirement. The table also lists the relative systematical errors coming from the jet energy scale uncertainty. As the lower-energy jets have larger JES

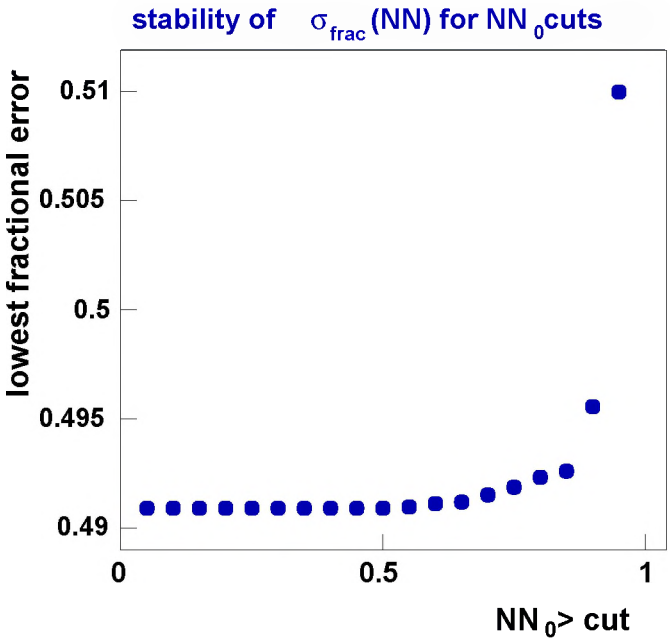

Figure 7.1: *The expected fractional error of the cross section measurement, as a function of the cut on the discriminant of the preselection neural network NN_0.*

E_T cut [GeV]	σ_{frac}(stat,$\sigma_{t\bar{t}} = 6.5$pb)	σ_{frac}(JES)	
15	0.476	+0.293	-0.285
20	0.502	+0.343	-0.308
25	0.547	+0.333	-0.308
30	0.645	+0.373	-0.301
35	0.780	+0.427	-0.346

Table 7.1: *The expected fractional error on the cross section measurement, as a function of the jet E_T cut in the preselection. Also shown is the dependence of the JES systematic errors as a function of the jet E_T cut.*

uncertainties, tightening the jet requirements could in principle reduce the systematic uncertainty on the measured cross section. As can be seen in the table, the fractional error due to the JES does not improve as a function of the jet E_T cut. This is due to the fact that, in the final sample, events which consist only of low energetic jets are already rejected by the neural network analysis.

7.3 Linear likelihood discriminant

As discussed in Section 5.6, it is possible to construct a linear likelihood discriminant $D(\vec{v})$ instead of a neural network. $D(\vec{v})$ is expected to be close to zero for background and close to unity for signal. The likelihood method performs optimal when the input PDFs are uncorrelated, so this analysis can be considered a cross-check on how the neural network analysis uses the correlations in the six input variables. We use one-dimensional

PDFs to construct $D(\vec{v})$, using the same quantities (H_T, $E_T^{5,6}$, $\mathcal{A}$, $\langle\eta^2\rangle$, $\mathcal{M}$ and $M_{min}^{3,4}$) as for the neural network SVT analysis. The same preselection is used, but the NN_0 cut is tightened to $NN_0 > 0.1$ to increase the sensitivity of this study. Figure 7.2 shows the predicted distribution of $D(\vec{v})$ and the expected fractional error.

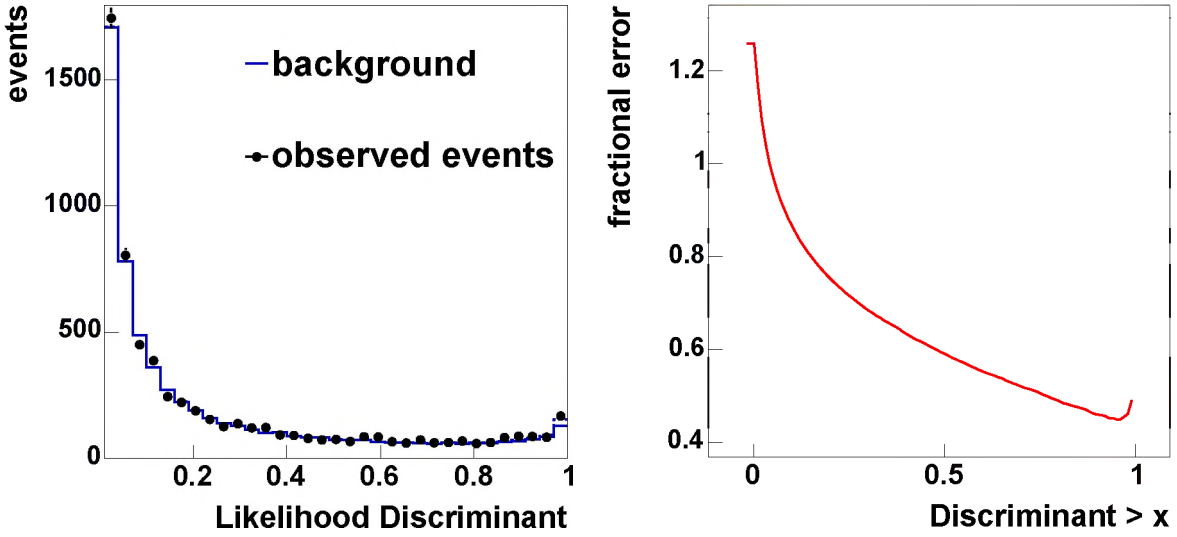

Figure 7.2: *Left: Distribution of top discriminant $D(\vec{v})$ for observed tagged data (markers) and predicted tagged background(histogram). Right: Fractional error as a function of the cut value for $D(\vec{v})$.*

The *predicted* optimal fractional error of $\sigma_{frac} = 0.44$ is obtained for $D(\vec{v}) > 0.95$[1], comparable to the fractional error observed in the neural network analysis. Figure 7.3 shows the distribution for the higher values of $D(\vec{v})$.

Above the cut of $D(\vec{v}) > 0.95$, the following numbers are observed:

$$N_{obs} = 254 \text{ events}, \tag{7.1}$$

$$N_{bg} = 214.7 \pm 5.5 \text{ events}, \tag{7.2}$$

which is already corrected for $t\bar{t}$ content, and a signal efficiency of

$$\varepsilon_{all-jets} = 0.0724, \tag{7.3}$$

approximately 0.01 smaller than in the NN_{all} analysis. The number of observed events and the number of predicted background events is smaller than in the NN_{all} analysis. The figure of merit, the *observed* fractional error, is slightly larger; 0.40 for the neural network analysis and 0.41 for the discriminant analysis. This results in the calculated value for the $t\bar{t}$ cross section (Equation 6.7):

$$\sigma_{t\bar{t}} = 7.3^{+3.0}_{-2.9}(\text{stat}) \text{ pb}, \tag{7.4}$$

[1]Note that the *value* of the minimal fractional error depends on the cross section used in the Monte Carlo prediction. However, the cut value does not depend on the Monte Carlo cross section.

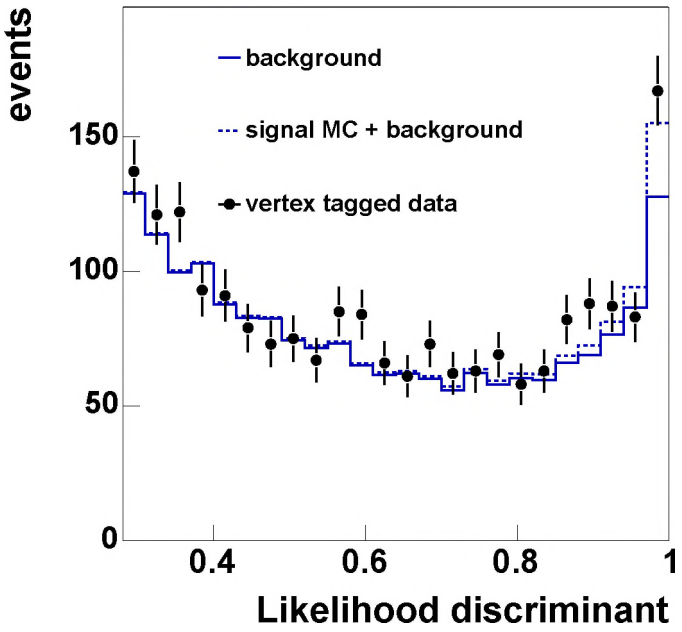

Figure 7.3: *Linear likelihood for tagged data (markers), expected background (line) and expected signal+background (dashed line).*

consistent with the neural network analysis, but with a somewhat smaller central value.

It should be noted that the construction of the linear likelihood discriminant relies heavily on the knowledge gained from the NN_{all} analysis. Thus, treating the likelihood discriminant analysis as a completely independent method is unjustified: without the cut on NN_0 and knowledge of the optimally discriminating input variables of NN_{all}, it is practically impossible to construct a discriminating linear likelihood discriminant.

7.4 Cross section using neural network fits

It is also possible to use the shape of the background and signal distributions to determine the relative $t\bar{t}$ content in the tagged sample. The data excess and signal efficiency can then be determined by integrating over the NN_{all} distribution. To fit the background and signal contribution, a binned Poisson likelihood fit is used [68]. This method has the additional advantage that it accounts for all statistical fluctuations of the tagged data sample, Monte Carlo simulated signal and TRF predicted background (see also [61]).

Events with $NN_{all} < 0.1$ are not considered in the fit. The fit determines the fraction of signal, f_s, and background, f_b, in the tagged sample. Figure 7.4 shows the result of the binned likelihood fit. Shown are the tagged events, the fitted distribution that describes the tagged events and the fitted background contribution. The fit result is that $f_s = (2.70 \pm 1.04)$ % of the 3158 tagged events, N_{tag}, are consistent with the $t\bar{t}$ hypothesis.

The number of observed excess events is

$$N_{excess} = f_s \cdot N_{tag} = 85.44 \pm 32.96 \text{ events}, \tag{7.5}$$

where N_{excess} is equivalent to the difference $N_{obs} - N_{bg}$ in the cut-based analyses. Only the uncertainty of the fitted fraction f_s is used for the uncertainty of the number of observed

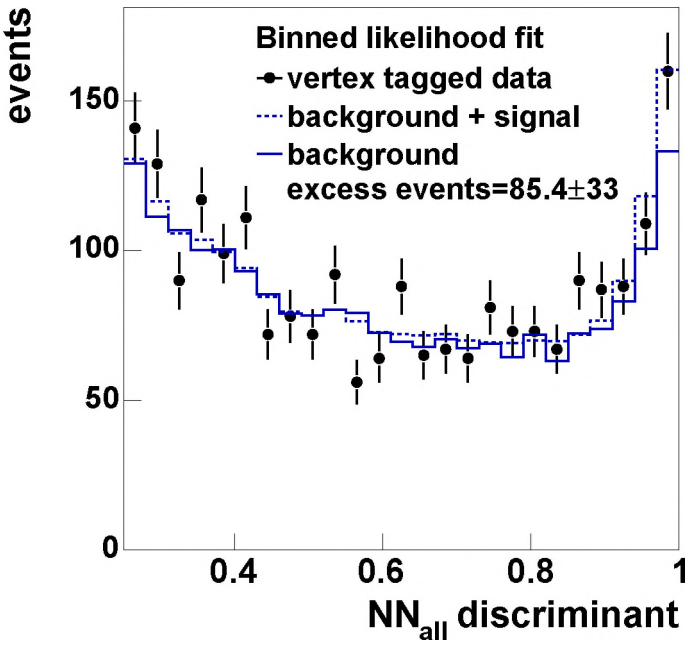

Figure 7.4: *Result of the binned likelihood fit (dashed line), the fitted background content (line) and the observed distribution (markers)*

ε for $t\bar{t}$	all-jets		lepton+jets	
	inclusive	exclusive	inclusive	exclusive
trigger	0.2537 ± 0.0022	0.7725 ± 0.0066	0.0169 ± 0.0008	0.5305 ± 0.0255
$N_{SVT} \geq 1, dR_{tags} > 1.5$	0.1430 ± 0.0012	0.5635 ± 0.0045	0.0095 ± 0.0005	0.5628 ± 0.0275
$NN_0 > 0.05$	0.1426 ± 0.0012	0.9971 ± 0.0007	0.0093 ± 0.0005	0.9831 ± 0.0095
$NN_{all} > 0.1$	0.1385 ± 0.0012	0.9716 ± 0.0020	0.0084 ± 0.0005	0.8964 ± 0.0227

Table 7.2: *Inclusive and exclusive efficiencies for $t\bar{t}$ all-jets signal. Shown are the efficiencies for both the all-jets and lepton+jets decay channel, for a mild $NN_{all} > 0.1$ cut. These efficiencies are used in the binned likelihood fit on the NN_{all} output.*

events. The efficiency for $t\bar{t}$ signal for the considered NN_{all} range shown is

$$\varepsilon_{\text{all-jets}} = 0.1385 \pm 0.0012, \tag{7.6}$$

and

$$\varepsilon_{\ell\text{+jets}} = 0.0084 \pm 0.0005. \tag{7.7}$$

Combining these, the total efficiency for $t\bar{t}$ signal is

$$(\varepsilon \times \text{BR})_{t\bar{t}} = 0.068 \pm 0.001, \tag{7.8}$$

a higher efficiency as the cut on $NN_{all} > 0.91$ is loosened to $NN_{all} > 0.1$. The inclusive and exclusive efficiencies for the trigger and b identification, together with the final NN_{all} cut efficiency are listed in Table 7.2.

The fit gives a normalization of the background which is:

$$f_b = 0.973 \pm 0.021. \tag{7.9}$$

The cross section can be calculated by using Equation 6.7, where $N_{obs} - N_{bg}$ now obviously can be replaced by N_{excess}. The resulting estimate for the cross section is

$$\sigma(t\bar{t}) = 7.7 \pm 3.0 \text{ (stat) pb.} \tag{7.10}$$

The observed fractional error, the statistical error divided by the central value of the cross section, is 0.39, of similar size as the value 0.4 from the neural network cut analysis. This is caused by the fact that the statistical fluctuations in the background from the TRF prediction are also included in the fit. This result is consistent with the cross section measurement as described in Chapter 6.

7.5 Methods used by other experiments

The CDF collaboration has also measured the $t\bar{t}$ cross section in the all-jets channel, using a comparable dataset [67]. The CDF measurement counts the number of vertex tagged jets as a function of jet multiplicity, after the following kinematic cuts:

$$6 \leq N_{jets} \leq 8; \tag{7.11}$$

$$H_T \geq 320 \text{ GeV}; \tag{7.12}$$

$$\mathcal{C} \geq 0.77; \tag{7.13}$$

and

$$\mathcal{A} + \frac{0.0037}{\text{GeV}} H_T^{3j} \geq 0.85. \tag{7.14}$$

These requirements were optimized for the best statistical significance of the CDF analysis, and have not been re-optimized for use on the DØ dataset. The dominant systematic error in the CDF measurement is the jet energy scale, which introduces an uncertainty in the signal efficiency of 30 %, equivalent to the result presented in this thesis.

Figure 7.5 shows the behavior of the dataset used in this thesis, after preselection, for H_T, $\mathcal{C}$ and $\mathcal{A}$ versus H_T^{3j}, the variables used in the CDF analysis. The CDF cuts are also indicated. Figure 7.6 shows the distribution of the number of predicted and observed secondary vertex tags, as a function of the number of jets in the event, after the kinematic cuts, and the number of tagged jets expected for a cross section of $\sigma_{t\bar{t}} = 6.5$ pb.

The cross section can be calculated from the results in Table 7.3. The efficiency for the kinematic cut analysis is defined as ε_k. The efficiency, ε_k, already contains the inefficiency caused by the all-jets branching ratio, and the preselection and trigger efficiencies. The cross section is calculated from:

$$\sigma_{t\bar{t}} = \frac{N_{obs} - N_{bg}}{\varepsilon_k \langle n_{tag} \rangle \mathcal{L}}, \tag{7.15}$$

where N_{obs} and N_{bg} are the numbers of observed tagged jets and expected background jets, respectively. To obtain the cross section from the number of tagged jets the efficiency has to be multiplied by the average number of tags expected in a $t\bar{t}$ event, $\langle n_{tag} \rangle$.

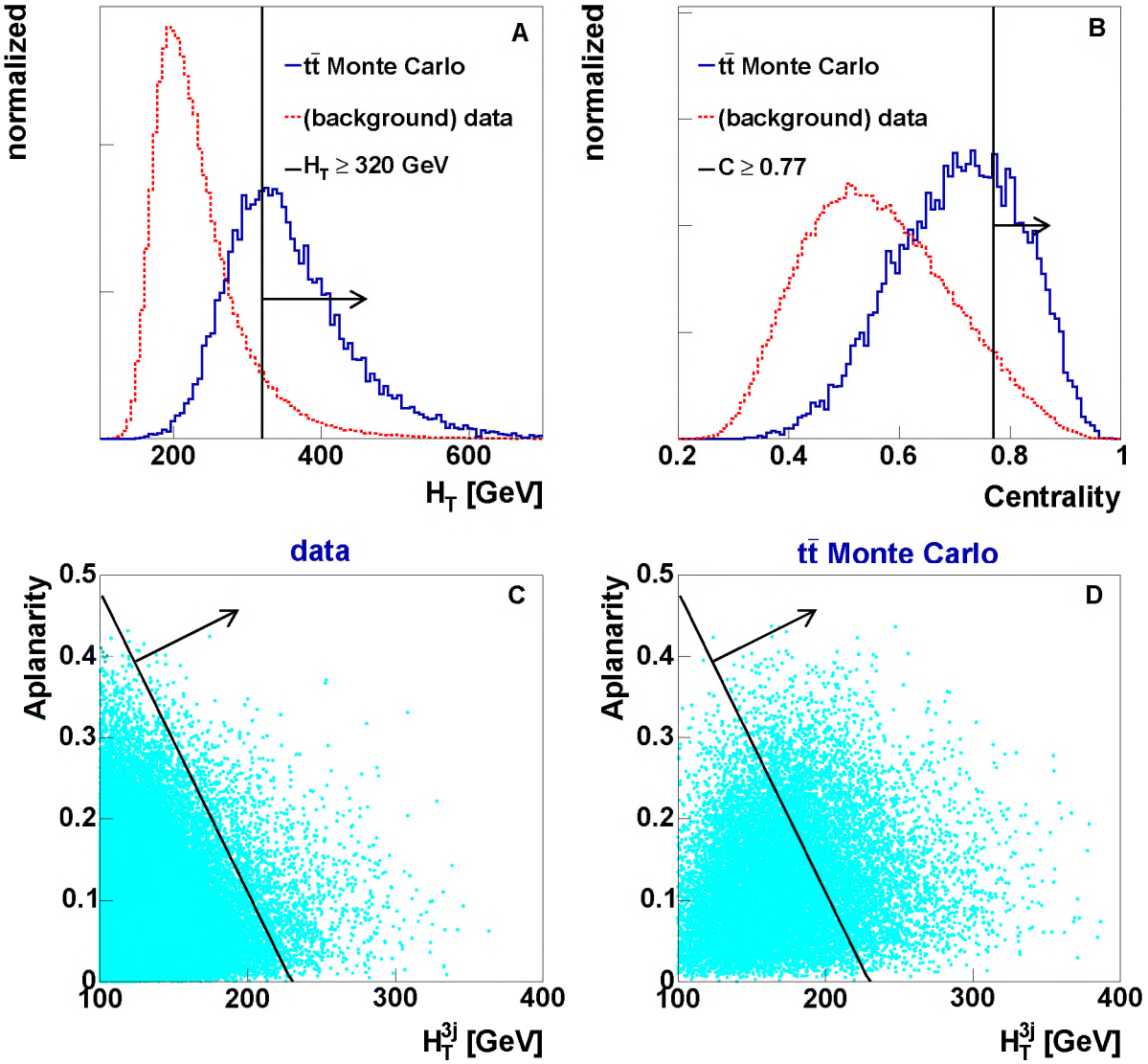

Figure 7.5: *Variables used in the CDF-style analysis. Shown are: (A) the transverse energy H_T, (B) the centrality $\mathcal{C}$ and the aplanarity $\mathcal{A}$ versus the non-leading transverse energy H_T^{3j} for data (C), which is dominantly background, and $t\bar{t}$ signal Monte Carlo (D). The lines shown are the kinematic cuts as listed in equations 7.12 through 7.14.*

Using the values for the CDF measurement as listed in Table 7.3, the CDF preliminary Run 2 cross section [67] measured in the $t\bar{t}$ all-jets decay channel is:

$$\sigma_{t\bar{t}} = 7.8 \ \pm 2.5(\text{stat})^{+4.7}_{-2.3} \ (\text{syst}) \ \text{pb}; \tag{7.16}$$

while the same method applied on the DØ dataset yields:

$$\sigma_{t\bar{t}} = 8.2 \ \pm 3.3 \ (\text{stat})^{+3.6}_{-2.0} \ (\text{syst}) \ \text{pb}. \tag{7.17}$$

The DØ and CDF measurements are consistent within both statistical and systematic uncertainties, and the measurement on the DØ dataset is also consistent with the neural

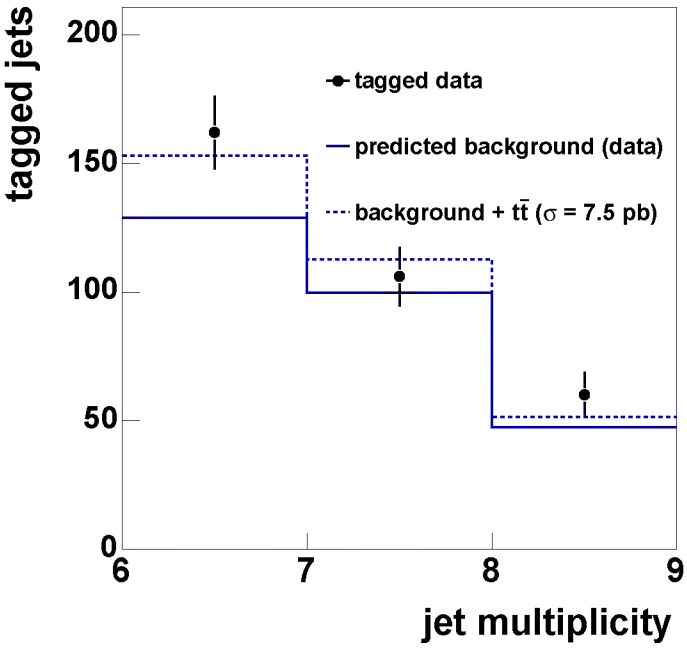

Figure 7.6: *The number of observed tags (markers) as a function of the jet multiplicity. Also shown is the predicted number of tags consistent with background (line) and the expected contribution when $t\bar{t}$ content is added to the background (dashed line). A $t\bar{t}$ cross section of $\sigma = 6.5$ pb is used as the input of the signal+background distribution.*

variable	symbol	CDF analysis	This dataset
Integrated luminosity [pb^{-1}]	$\mathcal{L}$	165 $\pm$ 10	162 $\pm$ 11
Candidate tags	N_{obs}	326	328
Expected background	N_{bg}	264.7 $\pm$ 17.2	276.1 $\pm$ 17.6
Kinematic efficiency for $t\bar{t}$ [%]	ε_k	6.2 $\pm$ 1.9	4.6 $\pm$ 1.4
average number of tags per $t\bar{t}$	$\langle n_{tag} \rangle$	0.763 $\pm$ 0.065	0.844 $\pm$ 0.062

Table 7.3: *Input values for the CDF cross section measurement, and the numbers derived on the DØ dataset. The values from the CDF analysis are taken from [67].*

network cross section analysis as presented in Chapter 6. To compare the neural network analysis to the tag counting 'CDF-style' analysis on DØ data, the statistical error divided by the central value of the cross section is considered. The observed fractional error is equivalent to 0.40 for both analyses.

The main difference between the CDF and DØ measurements is that the number of background events is higher in the DØ data set. As the average number of tags per event $\langle n_{tag} \rangle$ is also higher, this can be attributed to a difference in efficiency and purity of the vertex tagger. The DØ secondary vertex tagger has a higher efficiency than the CDF tagger, when using the nominal selection parameters. However, this has the disadvantage of the introduction of a larger background in the DØ analysis.

7.6 Cross section measurement with soft muon tagging

It is interesting to study the stability of the $t\bar{t}$ cross section measurement using an alternative method to the secondary vertex tag discussed in Chapter 6. Here, soft muon b-jet identification is used. At present no electron tags are used. Nevertheless, soft muon tagging is referred to as soft lepton tagging (SLT). This measurement is also useful for comparison to the Run 1 results [61, 64, 65], where SLT was also used.

7.6.1 Dataset

For the soft muon analysis, the requirements on the muon detector system are more tight than for the vertex tagged dataset (See Section 4.1.1, particularly Table 4.1). The integrated luminosity of the dataset after the detector quality requirements is equivalent to:

$$\mathcal{L} = 149.9 \text{ pb}^{-1} \tag{7.18}$$

7.6.2 b identification

After preselection, the requirement that at least one jet contains a soft muon is used to increase the b content of the sample. Soft muon tagging has as an advantage that the fake rate is low, but unfortunately at a cost of efficiency compared to the SVT tag.

The efficiency to tag a b jet with a muon is approximately the same for Monte Carlo as for data (See Section 3.4.3). As only around 11% of b jets decay to a muon[2], the maximum efficiency is limited to 11%. The average efficiency to tag a b jet in a $t\bar{t}$ Monte Carlo event is 7.7%. The equivalent efficiency for c quark jets is 3.3%. The fake rate in data is of the order of 0.5%.

7.6.3 Background prediction

To predict the number of muon tagged events, the method described in Section 5.2 is used, but now for muon tagged events.

The obvious background is removed by making a cut on $NN_0 > 0.05$. Figure 7.7 shows the TRF fit distributions as a function of jet η_{det} and p_T. Shown are the number of jets with a muon in the jet divided by the total number of jets, per η_{det} and E_T bin. The TRF fits are shown as solid curves, while the uncertainty on the fit is shown as a dashed curve. The fraction of tagged jets is about 10 times smaller than in the SVT analysis. (The corresponding figures for the SVT analysis are shown in Figure 5.3 and 5.4.)

[2]Only a fraction of all b-jets decays to a muon, either directly, $b \to \mu + X$ (approximately 1/10), or indirectly, $b \to c \to \mu + X$ (approximately 1/100). If both are taken into account, the combined efficiency is 11%.

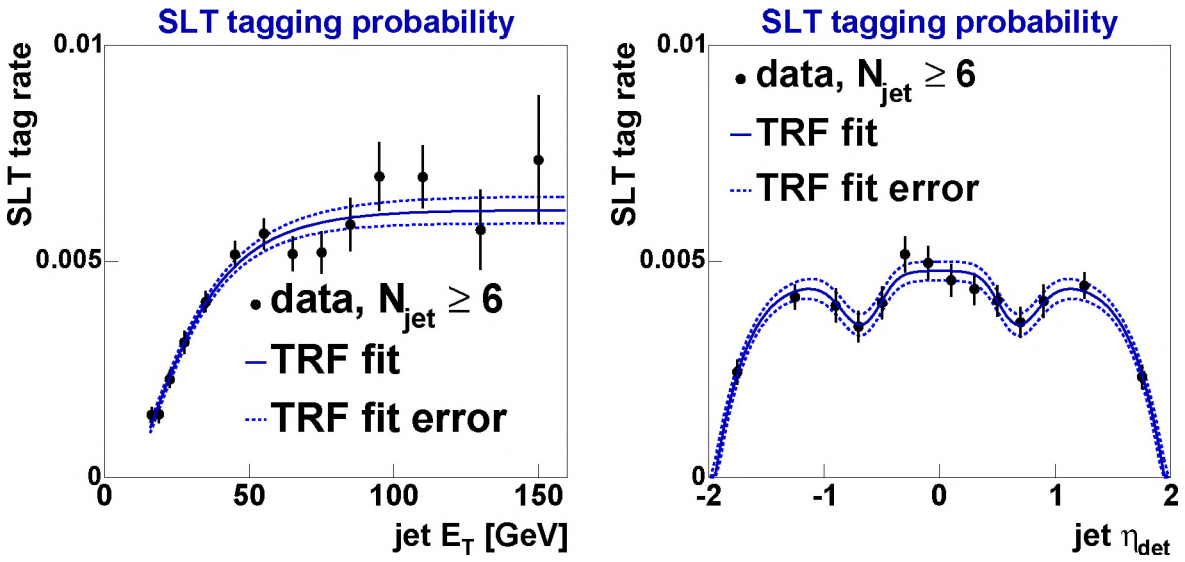

Figure 7.7: *TRF determination for jets with a soft muon tag, as a function of jet p_T (left) and η_{det} (right). The markers are the number of jets with a μ inside divided by the number of total jets, on a bin-by-bin basis. The TRF fits are shown as the solid curve, with the dashed curves the uncertainty on the fit.*

Background normalization

Analogous to the SVT analysis, the TRF prediction of the number of muon tagged events is adjusted to give the correct number of events in the background region: $0.3 < NN_0 < 0.9$. The distribution of tagged events as a function of NN_0 is shown in Figure 7.8. The TRFs describe the data in the background region within statistical uncertainties. The result for $t\bar{t}$ Monte Carlo events, normalized for visualization, is also shown.

Figure 7.9 shows the fraction of observed tagged and predicted events as a function of NN_0, for the background region of the neural net. The value of $SF_{TRF} = 1.037 \pm 0.036$ is consistent with unity within errors and stays within the error if cross sections between $\sigma_{t\bar{t}} = 1$ and 20 pb are considered.

7.6.4 Neural Network

We use the same neural networks as used in the SVT analysis. The same preselection and NN_0 cut are used. The distributions of H_T, $E_{T_{5,6}}$, $\mathcal{A}$, $\langle\eta^2\rangle$, $\mathcal{M}$ and $M_{min}^{3,4}$ are shown in Figures 7.10 and 7.11 for muon tagged data (markers) and the predicted background distribution (band). The normalized Monte Carlo distributions are also shown, as histograms. The distributions seem to be predicted reasonably well by the TRF, but contain fewer events than in the SVT analysis.

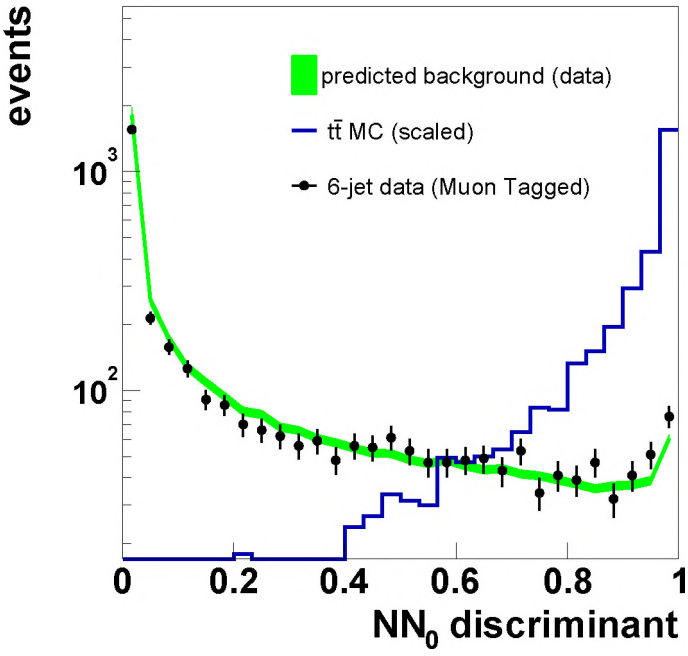

Figure 7.8: *Output of NN_0 for tagged data (markers) and predicted background (error band). The shown histogram gives the distribution of NN_0 for $t\bar{t}$ signal, normalized to contain the same number of events as the tagged data.*

7.6.5 Cross section using counting method

Figure 7.12 shows the expected fractional error as a function of the cut on the NN_{all} discriminant. The expected statistical significance of the measurement is substantially lower than for the vertex tag analysis. The optimal NN_{all} cut is obtained at a value of

$$NN_{all} > 0.9, \tag{7.19}$$

and results in a fractional error of $\sigma_{frac} = 0.79$.

7.6.6 Efficiency

The efficiency for the NN_{all} cut is measured on $t\bar{t}$ all-jets Monte Carlo events, which are already corrected for the efficiency of the trigger:

$$\epsilon_{\text{all-jets}} = 0.0260 \pm 0.0007, \tag{7.20}$$

where the errors are due to Monte-Carlo statistics. This efficiency still has to be corrected for events from the other $t\bar{t}$ production channels, especially the τ+jets channel can be expected to have an event topology that is similar to the fully hadronic top decays:

$$\epsilon_{\ell\text{+jets}} = 0.0009 \pm 0.0002. \tag{7.21}$$

Combining these two efficiencies according to the branching fractions for lepton+jets and all-jets $t\bar{t}$ events leads to a signal efficiency of

$$\epsilon \cdot \text{BR} = 0.0120 \pm 0.0008. \tag{7.22}$$

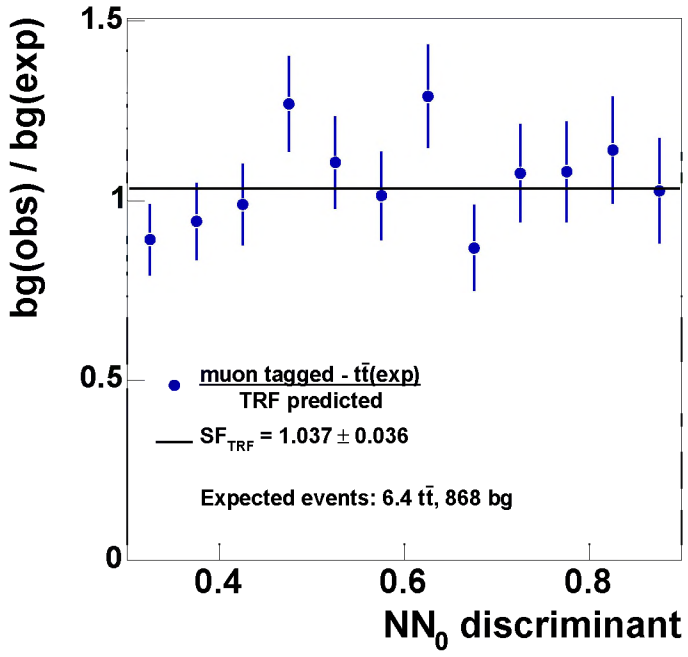

Figure 7.9: *The fraction of observed tagged events and the predicted events as a function of NN_0. The average value SF_{TRF} is also indicated.*

The analysis efficiency for the muon tag analysis is about three times lower than for the SVT analysis (Equation 6.6).

7.6.7 Observed and expected events

From the TRF prediction, the number of soft muon tagged background events is expected to be

$$N_{bg} = 75.45 \pm 1.57 \text{ events}, \tag{7.23}$$

where the error comes from statistical fluctuations in our background distribution only. Figure 7.13 shows the observed NN_{all} distribution in muon tagged events, the predicted background and the prediction for $t\bar{t}$ signal and background. The number of observed tagged events above $NN_{all} > 0.90$ is

$$N_{obs} = 91 \text{ events}. \tag{7.24}$$

The probability that these 91 events originate from a statistical fluctuation of the 75.45 background events is equal to 1.8 standard deviations. This is equivalent to a Gaussian probability of $P = 3.7 \cdot 10^{-2}$.

7.6.8 Result of the soft muon tag analysis

The systematic uncertainties for a cross section measurement with muon tagging are mostly identical to the uncertainties introduced when the SVT is used for b identification. The differences are mainly caused by the change from vertex tagging to muon tagging and TRF determination. The JES is still the dominant uncertainty. Table 7.4 lists the systematic and statistical uncertainties.

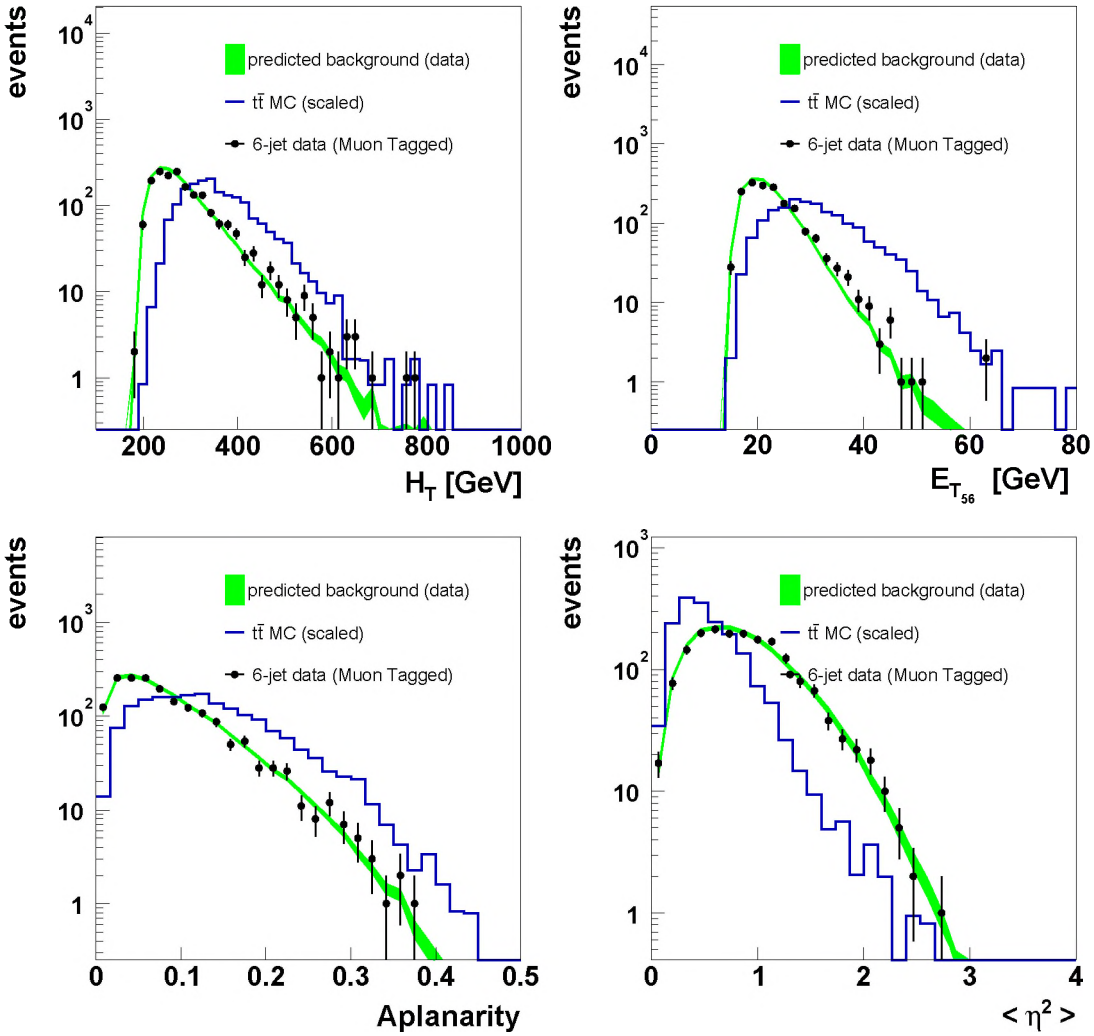

Figure 7.10: *The NN_{all} input variables H_T,$E_{T_{5,6}}$, $\mathcal{A}$ and $\langle\eta^2\rangle$, for muon tagged events. Shown are the observed distribution in muon tagged data (markers) and the predicted background distribution from the TRFs (band). For comparison, the normalized distribution for $t\bar{t}$ all-jets events is also shown (histogram).*

	$+\sigma$	$-\sigma$	change in cross section	
total error on efficiency	32.6%	−30.7%	-2.1 pb	+3.8 pb
total error on background	3.53%	−3.83%	-1.5 pb	+1.6 pb
total systematic error			-2.6 pb	+4.2 pb
error on the luminosity	6.5%	-6.5%	-0.6 pb	+0.6 pb
statistics			-5.1 pb	+5.5 pb

Table 7.4: *Systematic uncertainties on the cross section measurement using muon tagging.*

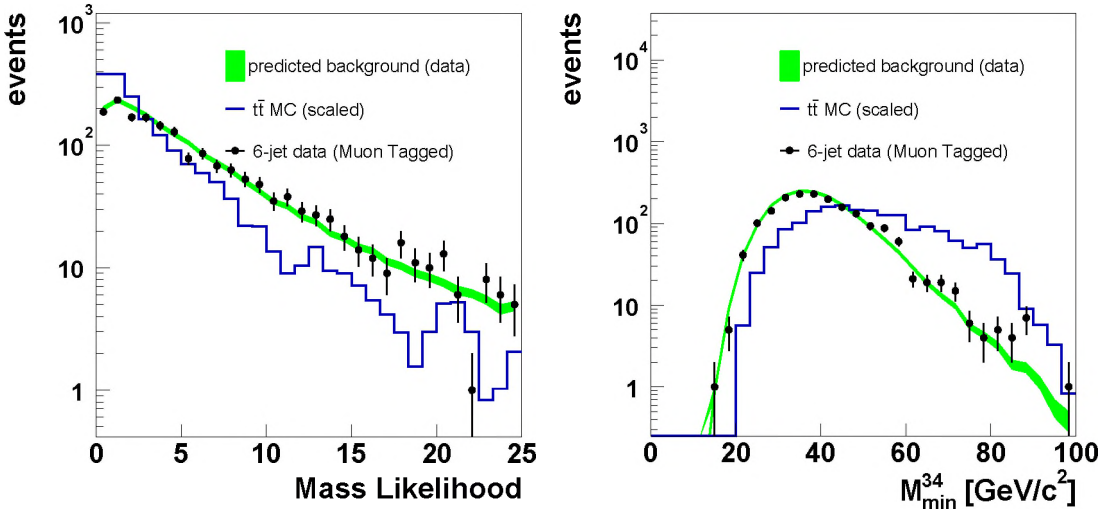

Figure 7.11: *The NN_{all} input variables $\mathcal{M}$ and $M^{3,4}_{min}$, for muon tagged events. Shown are the observed distribution in muon tagged data (markers) and the predicted background distribution from the TRFs (band). For comparison, the normalized distribution for $t\bar{t}$ all-jets events is also shown (histogram).*

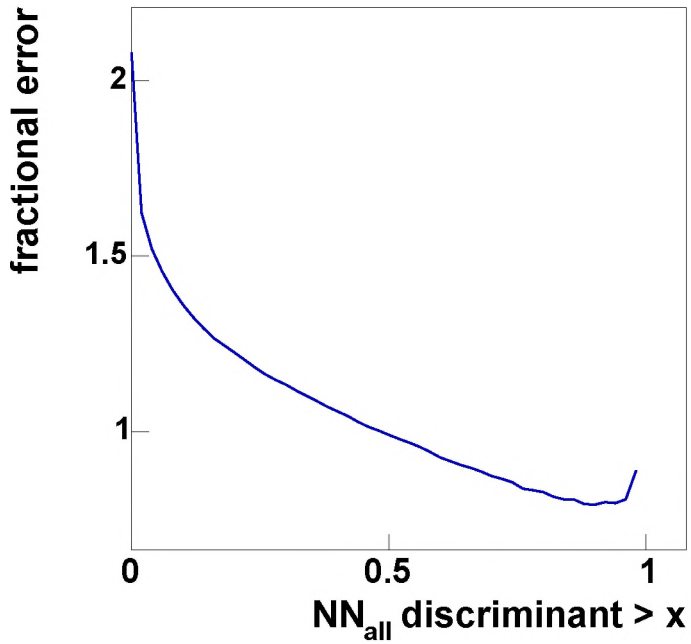

Figure 7.12: *Expected fractional error on the measured $t\bar{t}$ cross section as a function of the cut on NN_{all}.*

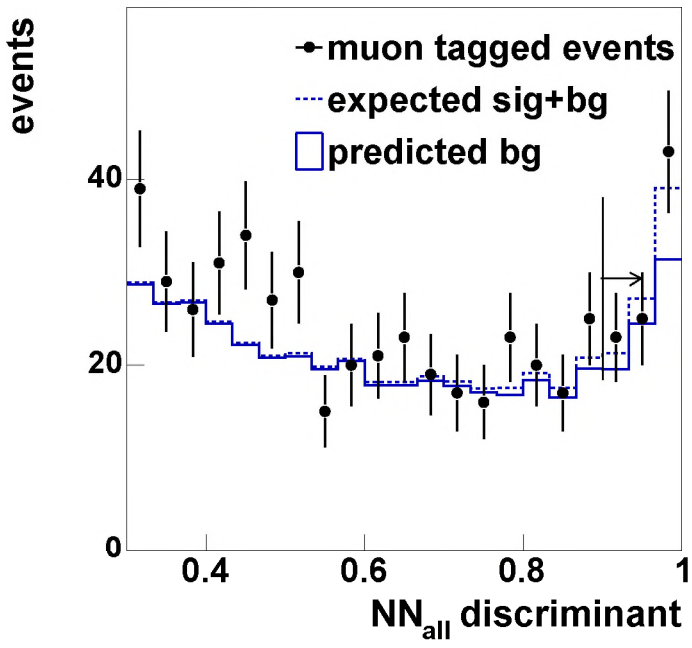

Figure 7.13: *NN_{all} distribution for the soft muon tag analysis. Shown are tagged events (markers), the predicted background (solid histogram) and the expected distribution (dashed histogram).*

Using soft muon identification, we measure:

$$\sigma_{t\bar{t}} = 8.6^{+5.5}_{-5.1}(\text{stat})^{+4.2}_{-2.6}(\text{syst}) \pm 0.6(\text{lumi}) \text{ pb}, \tag{7.25}$$

consistent with the secondary vertex tag measurement, but with significantly larger errors.

One should note that the result in Equation 7.25 is not independent of the cross section analysis with secondary vertex tagging. Not only is the SLT analysis performed on a subset of the dataset used for the main measurement, but there also are no requirements on the presence of secondary vertex tags in the muon analysis or vice versa. Above the $NN_{all} > 0.91$ threshold, 32 events have both a muonic and a secondary vertex tag.

7.7 Overview

In this chapter, we investigated the stability of the $t\bar{t}$ cross section result as measured in Chapter 6:

$$\sigma_{t\bar{t}} = 7.5^{+3.1}_{-3.0}(\text{stat})\ ^{+3.3}_{-2.0}(\text{syst}) \pm 0.5(\text{lumi}) \text{ pb}. \tag{7.26}$$

This result was obtained from an analysis which used a cut on an artificial neural network discriminant, $NN_{all} > 0.91$. The following analysis methods were used to examine the sample of tagged events with at least six jets:

- Section 7.3: Application of a linear likelihood discriminant instead of an artificial neural network. This method has as a main advantage that no neural networks were used. The analysis yielded a cross section of:

$$\sigma_{t\bar{t}} = 7.3^{+3.0}_{-2.9}(\text{stat}) \text{ pb}, \tag{7.27}$$

consistent with the neural network analysis, but with a somewhat smaller central value. The linear likelihood analysis is only possible because the correct kinematical and topological quantities were chosen in the NN_{all} analysis;

- Section 7.4: A binned likehood fit to the NN_{all} distributions for Monte Carlo signal events and background events . This analysis has as a main advantage that the entire distribution is taken into account, so the statistical fluctuations in the sample can be included in the fit. The result of the binned likelihood fit is:

$$\sigma_{t\bar{t}} = 7.7 \pm 3.0 \text{ (stat) pb;} \tag{7.28}$$

- Section 7.5: The CDF experiment has performed a cross section measurement on a similar size dataset. This analysis does not use multivariate methods. When the CDF analysis is performed on the DØ dataset, the following result is obtained:

$$\sigma_{t\bar{t}} = 8.2 \ \pm 3.3 \text{ (stat)}^{+3.6}_{-2.0} \text{ (syst) pb;} \tag{7.29}$$

- Section 7.6: A soft muon tag is used for b jet identification. The NN_{all} analysis is repeated with a muonic jet requirement instead of secondary vertex tagging. The soft muon analysis yields:

$$\sigma_{t\bar{t}} = 8.6^{+5.5}_{-5.1}\text{(stat)}^{+4.2}_{-2.6}\text{(syst)} \pm 0.6\text{(lumi) pb,} \tag{7.30}$$

  where no veto is applied on events that contain two different types of b tags.

As can be observed, the measurement proves to be robust when different analysis methods are applied. As all these analyses were applied to the same data sample, the results are considered correlated.

Chapter 8

Conclusions

This thesis presents a measurement of the $t\bar{t}$ cross section in the all-jets channel, measured in $p\bar{p}$ collisions at a center of mass energy of 1.96 TeV, using data collected with the DØ detector. The dataset used for this analysis has an integrated luminosity equivalent to $\mathcal{L} = 162.5 \pm 10.6$ pb^{-1}.

A $t\bar{t}$ cross section measurement is a test of the Standard Model predictions for heavy quark production, and the first step towards measurements of the mass and other properties of the top quark. The presented measurement of the cross section for the process $p\bar{p} \rightarrow t\bar{t}$ uses the decay channel where both top quarks decay to quarks. The top quark first decays to a b quark and a W boson, and then, for this particular channel, the W boson decays hadronically. Hence, events with six energetic quarks are expected, which ideally leads to events with six jets. These so called all-jets events have a significantly larger branching fraction than other $t\bar{t}$ decay channels. The large branching fraction in the all-jets channel means that a significant sample of $t\bar{t}$ candidates can be extracted, which can subsequently be used for studies of top quark properties, like the top mass. The background, multijet production through Quantum Chromo Dynamics (QCD) has a cross section three to four orders of magnitude larger than expected for $t\bar{t}$ production.

The analysis presented in this thesis uses the decay vertices of long-lived b-flavored mesons to identify the b jets. With the silicon detector installed at the start of Run 2 of the Tevatron, the DØ experiment is now able to use this method for b identification. The presence of b quarks in the event makes it possible to reduce the background to a few percent of the original sample, while only rejecting around 45% of the $t\bar{t}$ content in the sample.

Even after b jet identification, the background dominates the $t\bar{t}$ signal by about two orders of magnitude. A variety of kinematic and topological quantities of the measured jets are studied. A combination of six of these quantities is fed into an artificial neural network, which is configured to discriminate between the $t\bar{t}$ signal and the background. The six quantities are H_T, which is sensitive to the energy scale of the event; $E_T^{5,6}$, a quantity sensitive to the presence of gluonic jets in QCD multijet processes; $\mathcal{A}$, which quantifies how the event shape compares to a plane; $\langle\eta^2\rangle$, which quantifies how the jets are placed in the DØ detector; $\mathcal{M}$, a quantity tuned to identify the presence of W bosons and top quark candidates and $M_{min}^{3,4}$, sensitive to heavy objects in the event. The efficiency

to collect $t\bar{t}$ pairs that decay to only hadrons was determined to be 0.08. The relative uncertainty on this efficiency is 30%, which is dominated by the accuracy with which the scale of the jet energies in the event is known. A total of 357 events were observed in a sample where 310 ± 6.6 events were expected if no $t\bar{t}$ content was present. The background prediction is derived from multijet data, and has a relative uncertainty of 2%. The excess of events are assigned to $t\bar{t}$ decay. This sample is the largest ever isolated, in comparison to any other individual DØ analysis that involved top quarks. The cross section is extracted to be

$$\sigma_{t\bar{t}} = 7.5^{+3.1}_{-3.0}(\text{statistic})\ ^{+3.3}_{-2.0}(\text{systematic}) \pm 0.5(\text{luminosity})\ \text{pb}. \tag{8.1}$$

The stability of the measured cross section is investigated by application of different analysis methods. The applied methods include the use of cut-based analyses and a linear likelihood discriminant instead of neural networks. The measurement proved to be robust. When an alternative method for b identification is used, a comparable result is obtained. The result agrees with cross section measurements in other $t\bar{t}$ decay channels and has errors of comparable size. The results are consistent with theoretical predictions using NLO perturbation QCD calculation.

In Appendix A, it is also shown that the observed excess of events behaves in a manner which is consistent with the presence of top quarks in the sample. The excess above background, 47 top quark candidates, behaves as two objects with an invariant mass near the top mass. A dedicated measurement of the top quark mass in this channel would be useful using larger datasets. The investigation in this thesis hints that the expected uncertainty would be competitive with other top mass measurements.

Appendix A

Top mass measurement

It is interesting to investigate whether the excess of events that is observed in the NN_{all} analysis is consistent with the production of $t\bar{t}$ events. The 357 tagged events used to calculate the $t\bar{t}$ all-jets cross section can be used to extract the top mass. This provides a powerful consistency check: the distribution of the invariant mass of the appropriate jets should exhibit a top mass peak above the background. The background is expected to behave different from $t\bar{t}$ events, though a bias coming from the neural network selection is expected.

The mass likelihood, as described in Section 5.3.1(v), runs over all the permutations of the six leading jets. Permutations which assign the jet with vertex tag to the W boson are ignored. Monte Carlo studies of the W boson mass and width are used for the input values for $\mathcal{M}$. The permutation which leads to the smallest value of $\mathcal{M}$ is used to provide the two invariant di-jet masses of the W boson candidate and the two invariant triple-jet masses of the top quark candidates in the event.

Studies of the $t\bar{t}$ all-jets reconstruction efficiency are performed on Monte Carlo simulated events. It turns out that often it is not possible to assign the two b quarks and all partons from W decay to jets. Jets disappear into the beam pipe, or are too close together to be identified as separate jets. Through QCD effects it is also possible to move the jet axis away from the hadronizing quark which created the jet. We find that in $t\bar{t}$ all-jets Monte Carlo events with six or more jets, only 16% of the events have all partons matched to a jet. In this clean sample of reconstructible events, the mass likelihood selects the correct permutation in 80% of the events. This is equivalent to 13% of the total number of $t\bar{t}$ events. In 30% of the events at least one top quark is correctly reconstructed, while in 58% of $t\bar{t}$ events at least one W boson is identified.

A.1 The mass of the W boson

Figure A.1 shows the observed distribution of the invariant mass of the W boson candidates. Shown are the distributions for tagged data, together with the predicted background distribution and the expected signal + background distribution. The $t\bar{t}$ all-jets excess represents a presumed cross section of 7.5 pb, the estimate for the $t\bar{t}$ cross section as obtained in Chapter 6. As Figure A.1 shows, the background distribution has its max-

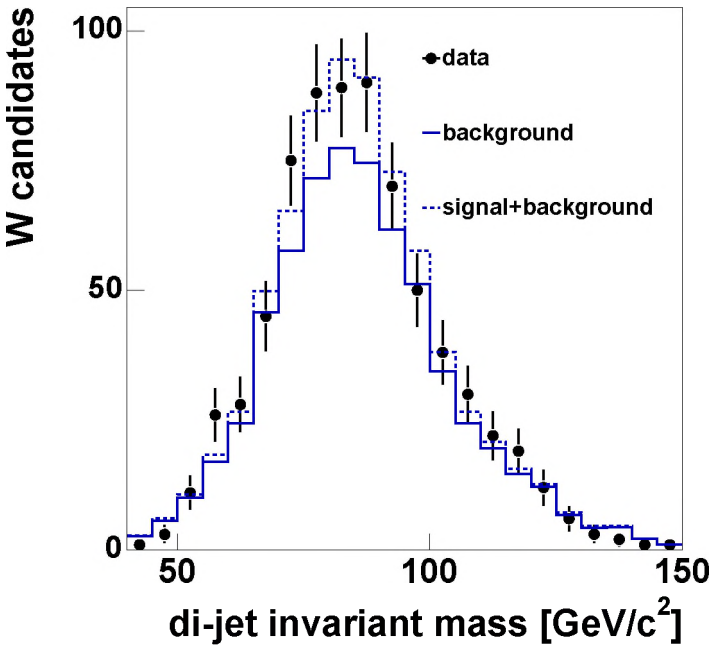

Figure A.1: *Mass distribution of the reconstructed W bosons candidates. Shown are the predicted background distribution (solid histogram), the expected distribution if $t\bar{t}$ signal is added (dashed histogram), and the observed di-jet invariant mass distribution for the tagged sample with $NN_{all} > 0.91$ (points).*

imum around the W mass, but is broader. The excess in the data is described well by the predicted distribution.

Figure A.2 shows the mass distributions for the W boson candidates for background subtracted data and from $t\bar{t}$ Monte Carlo events. Also shown is a Breit-Wigner distribution fit to the distributions, where the width of the peak in data is fixed to the value obtained from the Monte Carlo simulation. The fit to the distributions in Figure A.2 yields the following values for the central value M_W:

$$M_W(\text{data}) = 79.86 \pm 4.87 \text{ GeV/c}^2, \tag{A.1}$$

and

$$M_W(\text{MC}) = 84.54 \pm 0.11 \text{ GeV/c}^2 \tag{A.2}$$

The W boson mass from Monte Carlo is compatible with our expectation, as has been discussed in Section 4.4.1. It should be noted that the error quoted does not include any systematic uncertainty.

One could consider to re-calibrate the JES using the measured W boson mass. If the JES is varied by one standard deviation, the W boson mass as observed in Monte Carlo events shifts by ± 3 GeV/c^2. The statistical uncertainty in data and systematic uncertainty in Monte Carlo are of similar size. As a consequence, the re-calibration of the jet energy scale to yield the known W mass introduces errors that are comparable to the current errors caused by the jet energy scale.

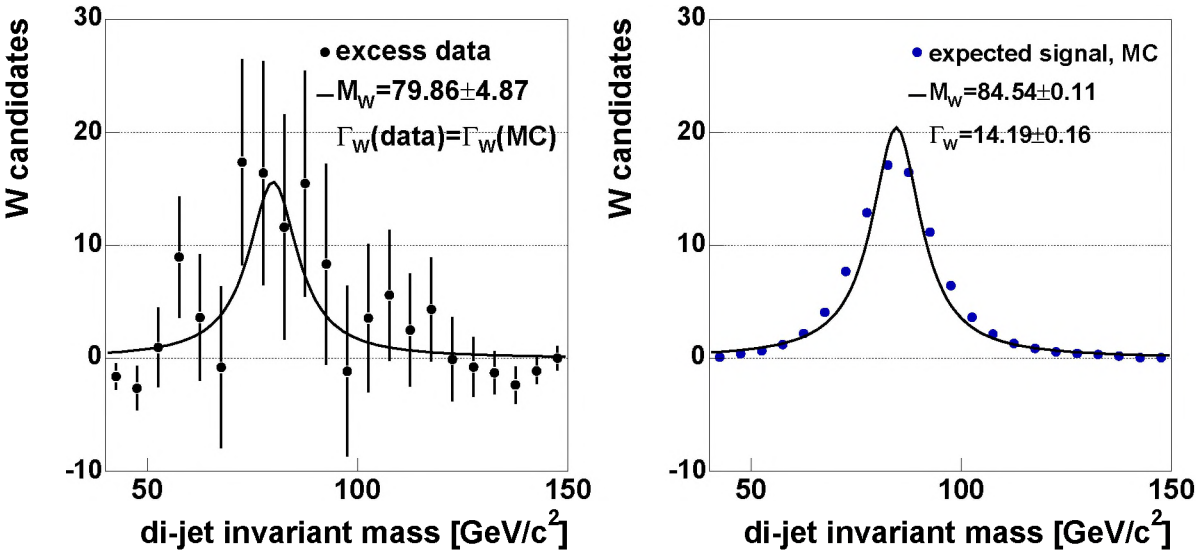

Figure A.2: *The reconstructed mass of the W boson, the predicted distribution for $\sigma_{t\bar{t}}$ = 7.5 pb for tagged data with $NN_{all} > 0.91$ after background subtraction (left) and from Monte Carlo $t\bar{t}$ all-jets events (right). The lines shown are fits of a Breit-Wigner distribution to the mass peak.*

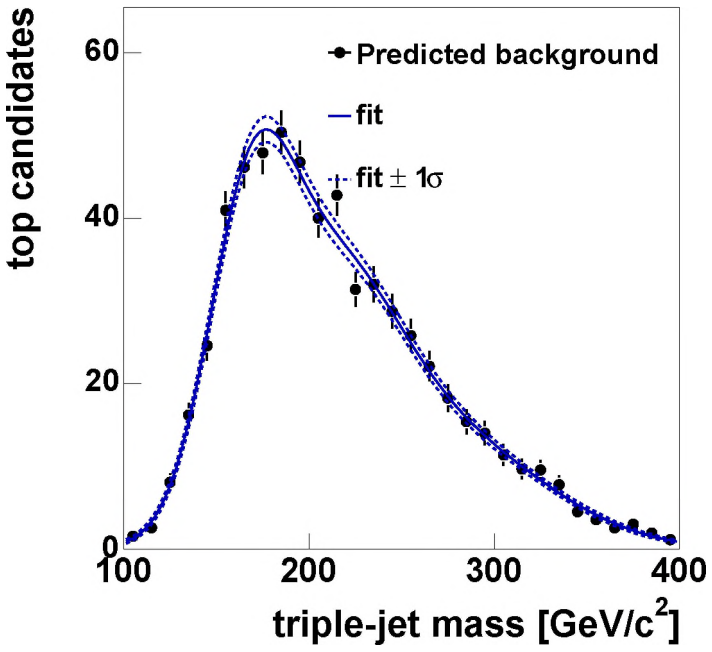

Figure A.3: *Prediction of the background distribution (markers) and fit (curve) with errors (dashed curves) for triple-jet invariant masses in QCD events. The fit uses a sum of three Gaussian distributions.*

A.2 Triple-jet invariant mass

This section discusses the triple-jet invariant mass distribution that is expected for the QCD background. For each event we consider two systems of three jets provided by the mass likelihood. The background content in the tagged sample is predicted with the TRF method. This is identical to the method in the cross section analysis. Figure A.3 shows the predicted mass distribution for the background content above $NN_{all} > 0.91$. Also shown is a fit and errors of the sum of three Gaussian distributions

$$b(m) = c_1 G(m, \mu_1, \sigma_1) + c_2 G(m, \mu_2, \sigma_2) + c_3 G(m, \mu_3, \sigma_3), \tag{A.3}$$

where $G(m, \mu, \sigma)$ is a Gaussian distribution with mean μ and width σ, that depends on the triple-jet invariant mass m. This function was selected because the fit seemed to represent the observed distribution and resulted in a low χ^2. Other functions that were considered were high order polynomials and two Gaussian distributions.

The background distribution peaks around the expected top mass but has a large spread. This behavior is expected as the neural network selection prefers (background) events that are kinematically similar to $t\bar{t}$ events. For a 'stand-alone' top mass measurement one has to consider possible biases and account for resulting systematic uncertainties. A study of these uncertainties is beyond the scope of this thesis. Our purpose is just to show that the excess events are consistent with the presence of top quarks in the sample.

A.3 The excess and its invariant mass

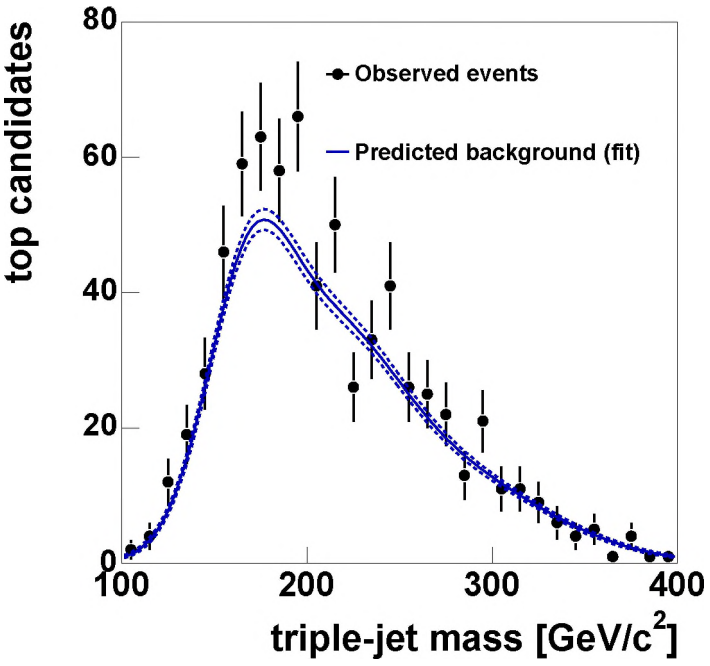

Figure A.4: *Invariant triple-jet mass of the tagged sample (markers), and the predicted background from fit (dashed line).*

After parametrization of the predicted background, we are now ready to consider the triple-jet mass distribution in the tagged data. Figure A.4 shows the results for

top candidates in tagged events that passed the $NN_{all} > 0.91$ cut. Also shown is the predicted background contribution obtained from the triple-Gaussian fit, as discussed above. At low and high invariant masses, the tagged sample seems to be consistent with background. There is a small excess of events in the invariant triple-jet mass spectrum. Before considering the central value of the excess, the predictions from Monte Carlo simulation will be compared to the observed triple-jet mass distribution.

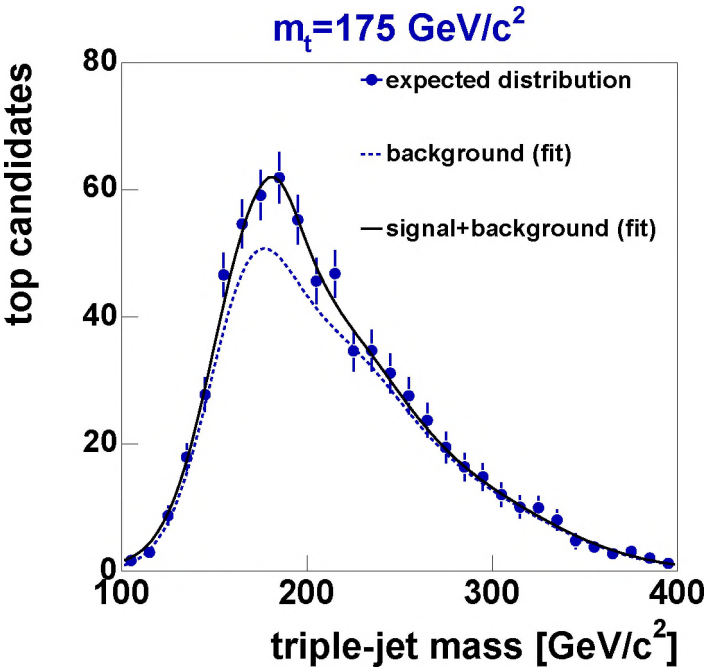

Figure A.5: *The expected tagged data distribution (markers) for a Monte Carlo top mass of 175 GeV/c^2. Also shown are the expected background from fit (dashed line), and the fit to the combined signal and background (line).*

The expected excess above background is studied by adding Monte Carlo $t\bar{t}$ events to the predicted background, using the measured cross section of 7.5 pb. Figure A.5 and A.6 show the expected $t\bar{t}$ contribution. The markers represent the distribution for predicted signal and background for three different top masses: 165, 175 and 185 GeV/c^2. Also shown are fits to the distributions using the sum of the background and a Breit-Wigner function. The central values are listed in Table A.7. The central value of the peak above background follows the input top mass, but there is a bias towards larger masses. We have made no attempt to correct for this shift.

We now return to the excess observed in data. Figure A.8 shows the invariant triple-jet mass in tagged events, after subtraction of the predicted background. Also shown is the fit of a Breit-Wigner distribution (and its $\pm 1\sigma$ uncertainty), which yields an average value of

$$m_t = 181.8 \pm 3.7 \text{ GeV/c}^2, \tag{A.4}$$

where only the statistical uncertainty on the fit is given. The main systematic uncertainty is expected to come from the JES and biases in the selection and reconstruction of the event. Although systematic effects were not taken into account in this study, we conclude that the observed excess of events is consistent with the production of top quarks.

In addition, as a closure test we performed the following check. The number of events and the width of the Breit-Wigner distribution are left free in the fit. The fitted excess

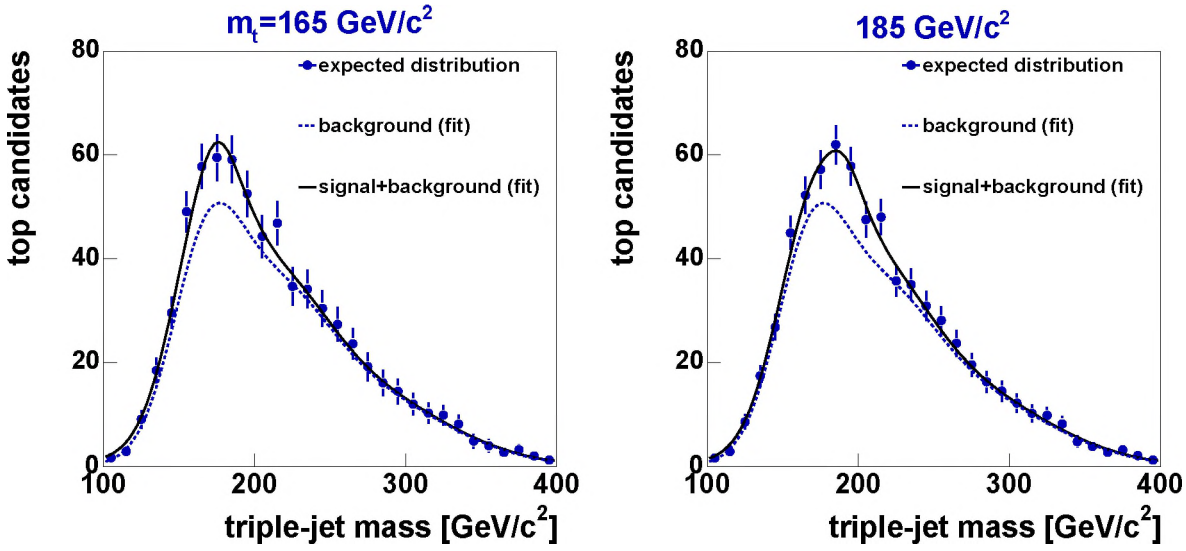

Figure A.6: *The expected tagged data distributions (markers) for two different input top masses: 165 (left) and 185 GeV/c^2 (right). Also shown are the expected background from fit (dashed line), and the fit to the combined signal and background (line).*

MC m_t [GeV/c^2]	observed m_t [GeV/c^2]
165	176
175	185
185	192

Figure A.7: *The peak value of the excess, as predicted by Monte Carlo simulation for different input values of m_t.*

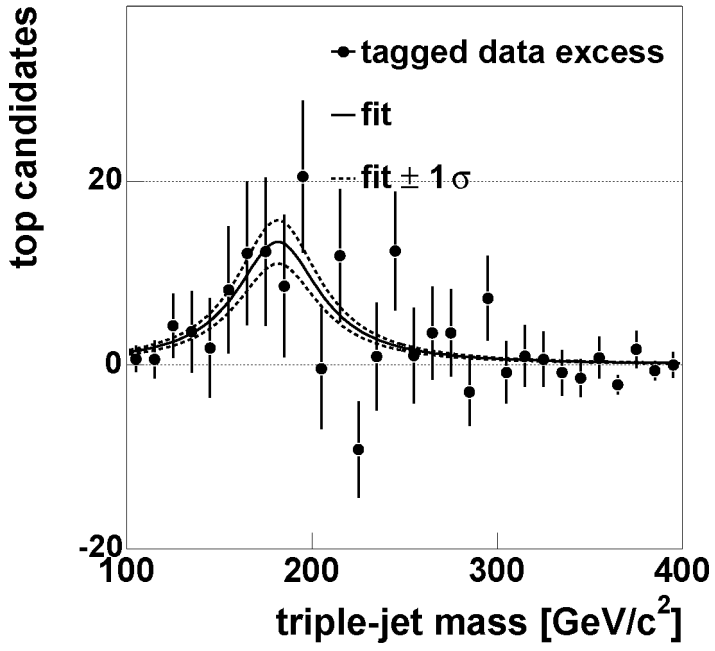

Figure A.8: *Invariant triple-jet mass of the tagged sample, after background subtraction. Shown are the tagged data (markers), the fit through the excess events (solid curve) and fit uncertainty (dashed curves).*

distribution contains 105 top quark candidates (52 events), the background distribution contains 610 candidates (305 events). The observed excess corresponds to a $t\bar{t}$ cross section of $\sigma_{t\bar{t}} = 8.4$ pb , consistent with the cross section measurement as presented in Chapter 6.

A.4 Comparison to previous measurements

The Run 1 mass measurement in the $t\bar{t}$ all-jets channel by the DØ collaboration [65] yields a value of

$$m_t = 178.5 \pm 13.5(\text{stat}) \pm 7.7(\text{syst}) \text{ GeV/c}^2, \tag{A.5}$$

which was measured on a relatively small sample of 16.6 ± 7 candidate events in a sample of 65 tagged events collected in the Run 1 period, using soft muon tagging for b-identification.

The CDF measurement of the top mass in the all-jets channel in Run 1 [66], which used vertex identification, resulted in a measurement of

$$m_t = 186 \pm 10(\text{stat}) \pm 7(\text{syst}) \text{ GeV/c}^2, \tag{A.6}$$

in a sample containing 19 signal events and a background of 63 vertex tagged events.

Although the mass measurement in this thesis is only used to confirm that the observed excess in the cross section measurement is consistent with $t\bar{t}$ signal, the observed statistical error from the fit on the top mass is already a significant improvement over the Run 1 measurement. The small statistical error indicates that a top mass measurement with significantly lower uncertainty in this channel is possible. No study of systematic effects was done. If the systematic uncertainty is around the same value as the Run 1 CDF and DØ measurements, a mass measurement in this particular $t\bar{t}$ decay channel will also contribute substantially to the combined top mass measurements.

Samenvatting

Dit proefschrift beschrijft een meting van top quark paar ($t\bar{t}$) productie bij de Tevatron proton-antiproton ($p\overline{p}$) versneller. De proton op antiproton botsingen hebben een zwaartepuntsenergie van 1.96 TeV. Om de botsingen te registreren wordt gebruik gemaakt van de DØ detector.

De hier gepresenteerde meting van de werkzame doorsnede voor het proces $p\bar{p} \rightarrow t\bar{t}$ bekijkt het vervalskanaal waar beide top quarks vervallen naar hadronen. De experimentele signatuur voor dit type $t\bar{t}$ creatie zijn interacties waarbij zeer veel (zes of meer) jets worden geproduceerd. Deze hadronische vervallen gebeuren vaker dan de andere $t\bar{t}$ vervalskanalen. Het nadeel van dit vervalskanaal is echter dat er ook zeer veel achtergrond is. Deze achtergrond, multi-jet Quantum Chromo Dynamische productie (QCD), waarbij ook zes of meer jets geproduceerd worden, komt vele duizenden malen vaker voor dan het top paar signaal. Dat het toch mogelijk is om een meting te doen in dit moeilijke kanaal komt doordat top quarks naar b quarks vervallen. Door de aanwezigheid van b quarks in een jet te eisen, wordt de achtergrond drastisch gereduceerd, maar niet volledig verwijderd daar b quarks ook gevormd kunnen worden via QCD processen. Tevens is het mogelijk om een fout te maken in de identificatie, en dus een niet-b jet te 'labelen' als een b jet.

De meting in dit proefschrift identificeert b quarks met behulp van de reconstructie van de vervalsvertex van de gehadroniseerde b quark. Dit is de eerste keer dat deze methode wordt gebruikt bij een $t\bar{t}$ analyse van door het DØ experiment geregistreerde botsingen. De gebruikte dataset bestaat uit bijna 300.000 Tevatron botsingen, die allen zes of meer jets in de DØ detector hebben gecreeërd. Deze dataset is equivalent aan een geïntegreerde luminositeit van $\mathcal{L} = 162.5 \pm 6.5\%$ pb^{-1}. De sub-dataset waar b jets in zijn gevonden bevat 18.000 botsingen.

Na de identificatie van b quarks bevat de dataset nog steeds ongeveer honderd keer meer achtergrond dan $t\bar{t}$ signaal. Vele kinematische en topologische grootheden zijn bestudeerd, deze worden berekend op basis van de gemeten jets. Uiteindelijk combineren we zes van deze grootheden in een artificieel neuraal netwerk. Het neuraal netwerk is zo geconfigureerd dat het onderscheid maakt tussen $t\bar{t}$ signaal en multi-jet achtergrond. Om de achtergrond te beschrijven wordt gebruik gemaakt van de veel grotere dataset waarop geen b-identificatie op is toegepast.

Er zijn 357 gebeurtenissen geïsoleerd, waarvan we voorspellen dat er 310 ± 6.6 achtergrond zijn. De 47 extra gebeurtenissen worden aan hadronisch $t\bar{t}$ verval toegeschreven, de grootste $t\bar{t}$ dataset ooit geobserveerd in een DØ $t\bar{t}$ analyse. Uit simulaties is gebleken dat deze methode een efficientie heeft van 0.08 ± 0.024 voor hadronische $t\bar{t}$ events. De system-

atische onzekerheid van 30% komt bijna geheel voort uit onzekerheden op de schatting van de energie schaal van de DØ calorimeter.

Als we alle gegevens combineren, resulteert dit in een gemeten waarde voor de werkzame doorsnede van

$$\sigma_{t\bar{t}} = 7.5^{+3.1}_{-3.0}(\text{statistisch})\ ^{+3.3}_{-2.0}(\text{systematisch}) \pm 0.5(\text{luminositeit})\ \text{pb}. \qquad \text{(A.7)}$$

Verschillende tests zijn toegepast om aan te tonen dat de gebruikte methode robuust is. De gemeten waarde komt goed overeen met theoretische voorspellingen, en is tevens vergelijkbaar in precisie met metingen van $\sigma_{t\bar{t}}$ in andere vervalskanalen.

In Appendix A is aangetoond dat de geobserveerde extra gebeurtenissen zich gedragen zoals verwacht wordt als er top quarks aanwezig zijn in de data. De botsingen met top kandidaten kunnen worden gekarakteriseerd als twee massieve objecten met een invariante massa in de buurt van de topmassa. De studie laat doorschemeren dat het mogelijk is om een concurrerende topmassameting uit te voeren in het hadronische $t\bar{t}$ vervalskanaal.

Bibliography

[1] "Introduction to elementary particles", Griffiths, ISBN 0-471-60386-4.

[2] "Quarks and leptons, Halzen and Martin", ISBN 0-471-88741-2 .

[3] "An Introduction to Quantum Field Theory", M. Peskin and D. Schroeder, ISBN 0-201-50397-2.

[4] "Top quark physics at the Tevatron", P.C. Bhat, H. Prosper, S.S. Snyder, Int.J.Mod.Phys. A**13**:5113-5218 (1998).

[5] "Top Quark Production Cross Section", E. Laenen et.al., Phys.Lett. B **321** (1994) 254-258.

[6] "High order corrections for top quark and jet production at the Tevatron", N. Kidonakis, hep-ph/0110145, 2002.

[7] "NLL resummation of the heavy-quark hadroproduction cross-section", R. Bonciani, S. Catani, M.L. Mangano and P. Nason, Nucl. Phys. B **529**,424 (1998).

[8] "Sudakov resummation and finite order expansions of heavy quark hadroproduction cross sections", N. Kidonakis, E. Laenen, S. Moch, R. Vogt, NIKHEF/2001-01.

[9] "The review of particle physics", S. Eidelman *et al.*, Physics Letters B**592**, 1 (2004).

[10] "Techniques and Concepts of High-Energy Physics XII", H.B. Prosper and M. Danilov (eds.), ISBN 1-4020-1591-7.

[11] "p14 local muon momentum resolution", J. Butler, Muon ID/Algorithms meeting (February 2004).

[12] "Measurement of the b-jet cross section at $\sqrt{s}$ = 1.96 TeV", Onne Peters, PhD thesis, University of Amsterdam (2003).

[13] "LEP Electroweak Working Group",// http://lepewwg.web.cern.ch/LEPEWWG/

[14] "An improved measurement of the top mass", DØ Collaboration, Nature 429, 638-642 (2004).

[15] "Spin Correlation in $t\bar{t}$ Production from $p\overline{p}$ Collisions at $\sqrt{s}$=1800 GeV", DØ Collaboration, Phys. Rev. Lett. **85** 256 (2000).

[16] "Top quark production at hadron colliders", L. Phaf, NIKHEF / Universiteit van Amsterdam PhD thesis (2004).

[17] "ALPGEN, a generator for hard multiparton processes in hadronic collisions", M.L.Mangano et al., JHEP 0307:001, 2003, hep-ph/0206293.

[18] "Next-to-leading order calculation of three-jet observables in hadron-hadron collision", Z. Nagy, Phys. Rev. D. 68, 094002 (2003).

[19] "Multiple jet production at low transverse energies in $p\overline{p}$ collisions at $\sqrt{s}$=1800 GeV", DØ Collaboration, Phys. Rev. D**67** 052001, 2003.

[20] "Properties of High-Mass Multijet Events at the Fermilab Proton-Antiproton Collider", CDF Collaboration, Phys. Rev. Lett. **75**, 608 (1995).

[21] "Properties of Six-jet Events with Large Six-jet Mass at the Fermilab Proton-Antiproton Collider", CDF Collaboration, Fermilab-PUB-97/093-E.

[22] "What to do with multijet events?", T. Hebbeker, DØ note 4465.

[23] "W and Z (plus jets) cross sections at 1.96 TeV", Gavin Hesketh, hep-ex 0405067 (2004) *Contributed to 39th Rencontres de Moriond on QCD and High-Energy Hadronic Interactions.*

[24] "Study of the heavy flavor content of jets produced in W events at the Tevatron collider", G. Apollinari, FERMILAB-CONF-02-123-E (2002), *Presented at 16th Les Rencontres de Physique de la Vallee d'Aoste.*

[25] "Current Tevatron beam status web page", http://www-bd.fnal.gov/notifyservlet/www .

[26] "PYTHIA 6.2, Physics and Manual", T.Sjoestrand et al., LU TP 01-21, hep-ph/0108264.

[27] "New Generation of Parton Distributions with Uncertainties from Global QCD Analysis", CTEQ6 Collaboration, hep-ph/0201195.

[28] "Global QCD analysis of parton structure of the nucleon: CTEQ5 parton distributions," CTEQ5 Collaboration, hep-ph/9903282

[29] "The EvtGen particle decay simulation package", D.J. Lange, Nucl. Instr. Meth. A 462 (2001) 152-155 .

[30] "D0gstar web documentation", http://www-d0.fnal.gov/computing/MonteCarlo/simulation/d0gstar.html .

[31] "Geant3", R. Brun *et al.*, CERN-DD/EE/81-1, (1987).

[32] The DØ simulation web page, http://www-d0.fnal.gov/computing/production.html .

[33] "The DØ Upgrade, The Detector and Its Physics", DØ Collaboration, Fermilab Pub 96/357-E.

[34] "Search for high mass top quark production in p anti-p collisions at $\sqrt{s}$= 1.8 TeV,", DØ Collaboration, Phys. Rev. Lett. **74** (1995) 2422 .

[35] "Main Ring Deadtime", J. Butler, DØ note 1682.
"Main Ring Veto Counters for Run 1b", N. Amos, DØ note 2072.

[36] "Averaging of the inelastic cross sections measured by the CDF and the E811 experiments", Klimenko *et al.*, Fermilab FN-741.

[37] "The updated DØ luminosity determination", T. Edwards *et al.*, DØ note 4328.

[38] "DØ Silicon Tracker Technical Design Report", DØ upgrade Collaboration, DØ note 2169.

[39] "Luminosity monitor design report", Lo A. *et al.*, DØ note 3320.

[40] "The SVX2 readout chip", SVXII design Group, FERMILAB-TM-1892.

[41] "Numbering schemes for the D0 SMT", F. Blekman, DØ note 3899.

[42] "Beam Tests of the DØ Uranium Liquid Argon End Calorimeter", DØ Collaboration, Nucl. Instr. and Methods, **A324**, 53 (1993).

[43] "Vertex Fitting by means of the Kalman Filter techinque", A. Schwartzman, M. Narian, DØ note 3907 .

[44] "Finding Tracks", D. Adams, DØ note 2958-2 .
"Central Track Extrapolation Through the D0 Detector", G. Hesketh, DØ note 4079.

[45] "Tracking efficiency overview",
http://www-d0.fnal.gov/global_tracking/results/p14.00.00_index.html .

[46] "Measurement of the $t\bar{t}$ production cross-section at $\sqrt{s}$ = 1.96 TeV using lifetime tagging", L. Shabalina *et al.*, DØ note 4141.

[47] "Towards a Coherent Treatment of Calorimetric Energies: Missing Transverse Energy, Jets, E.M. Objects and the T42 Algorithm", Ursula Bassler and Gregorio Bernardi, DØ note 4124.

[48] "Improvements from the T42 Algorithm on Calorimeter Objects Reconstruction", G. Bernardi *et al.*, DØ note 4335 .

[49] "Run II Jet Physics", G. Blazey *et al.*, DØ note 3750 .

[50] "Determination of the Mass of the W Boson Using the D0 Detector at the Tevatron", The DØ Collaboration, Phys. Rev. D 58 12002 (1998).
"Determination of the Absolute Jet Energy Scale in the D0 Calorimeters", The DØ Collaboration, Nuclear Instruments and Methods A424, 352 (1999).

[51] "DØ Top Analysis and Data Sample for the Winter conferences 2004", Top physics group, DØ note 4419 .

[52] "Jet reconstruction efficiency", S. Kulik, DØ CALGO workshop, (2003).

[53] "MuonID Certification for p14", C. Clément *et al.*, DØ note 4350.

[54] "Electron likelihood in p14", J.Kozminski *et al.*, DØ note 4449 .

[55] "Measurement of the $B^{\pm}$ lifetime and top quark identification using secondary vertex b-tagging", A. Schwartzman, PhD thesis Universidad de Buenos Aires, 2004.

[56] The DØ Run Quality Database and Common Samples Group, http://www-d0.fnal.gov/Run2Physics/cs/index.html

[57] "Top Trigger Selection and Application of Turn On Curves to the Monte Carlo", R. Schwienhorst, http://www-d0.fnal.gov/Run2Physics/top/d0_private/wg/triggers /Note_Reinhard_Jan2004.pdf .

[58] "Top Trigger Efficiency Measurements and the top_trigger package", Top trigger group, DØ note 4512.

[59] "Trigger Simulator home page", http://www-d0.fnal.gov/computing/trigsim/trigsim.html .

[60] "Measurement of the $t\bar{t}$ Production Cross section at $\sqrt{s}$ = 1.96 TeV in the Lepton+jets Final States using Soft Muon Tags", DØ Collaboration, DØ note 4026 (2003) .

[61] "Measurement of the top quark pair production cross section in $p\bar{p}$ collisions using multijet final states", DØ Collaboration, Phys. Rev. **D 60**, 012001 (1999).

[62] "Benefits of minimizing the number of discriminators used in a multivariate analysis," S. Towers, *Proceedings of the workshop on Advanced Statistical Techniques in Particle Physics, Durham (2002).*

[63] "JETNET 3.0: A Versatile artificial neural network package", C. Peterson, T. Rognvaldsson and L. Lonnblad, Comput. Phys. Commun. **81**, 185 (1994).

[64] "Measurement of the Top mass in the all-jets channel with the DØ detector at the Fermilab Tevatron collider", B.M. Connolly, PhD thesis, Florida State University (2002).

[65] "Measurement of the Top Quark Mass in Alljets Events", DØ Collaboration, Fermilab-Pub-04/305-E (2004), Accepted by Phys. Lett. B .

[66] "First Observation of the All Hadronic Decay of tt-bar Pairs", CDF Collaboration, Phys. Rev. Lett. 79, 1992 (1997).
"Measurement of the Top Quark Mass with the Collider Detector at Fermilab", CDF Collaboration, Phys. Rev. D**63**, 032003 (2001).

[67] "Measurement of the $t\bar{t}$ production cross section in the all-hadronic channel", CDF Collaboration, CDF note 7075 (2004)

[68] "Fitting using finite Monte Carlo samples", R. Barlow and C. Beeston, Comput. Phys. Commun. **77** (1993) 219.
see also http://root.cern.ch/root/html/TFractionFitter.html

[69] "The d0_ve Event Viewer",
http://www-d0.fnal.gov/computing/graphics/graphics_d0ve.html

[70] "Preliminary results in top physics",
http://www-d0.fnal.gov/Run2Physics/WWW/results/top.htm .

[71] "Dataset and topological analysis for the ttbar to hadrons production cross section measurement on p14 data", F. Blekman and M. Vreeswijk, DØ note 4333.
"Measurement of the ttbar to all-jets production cross section using Secondary Vertex Tagging", F. Blekman and M. Vreeswijk, DØ note 4346.
"Measurement of the $t\bar{t}$ production cross section in the all-jets channel", DØ Collaboration, DØ note 4428.

About the author

[redacted]

After attending primary education, Freya was accepted at the Montessori Lyceum in Amsterdam. Besides the standard academical activities at this exceptionally liberal high school, she was the editor of the (award winning) school newspaper and active in the committee that organized school parties. Her favorite subjects were Dutch, Art, Biology and Philosophy, but an overly enthusiastic physics teacher convinced her to enter the physics course at Universiteit van Amsterdam.

At U.v.A. she served as a member of the Faculty of Physics executive committee for two terms. She also actively contributed to the U.v.A. outreach program, which provided the possibility to give experimental physics demonstrations all over the Netherlands and Belgium and also at the 40th anniversary of CERN. This was her first contact with particle physics, and mainly because of the cool machines and detectors, interesting physics and paid student allowance she got motivated to do her Masters thesis research at NIKHEF, the Dutch National institute of Nuclear and High Energy Physics.

After a short, introductory, experiment on trying to break HERA-B drift chambers, she continued as a Masters student in the LHCb group, where she worked on drift chamber prototyping for the outer tracker. Meanwhile, she spent part of her time teaching small groups of high school students at the P.P.I., the city of Amsterdam's institute for remedial, psychological and academic guidance for children. She also attended the CERN summer student program, where she worked both on the development of the CMS silicon assembly robot and the summer student web pages.

After acquiring her U.v.A. degree in the winter of 2000, she continued at NIKHEF with a PhD studentship at the DØ experiment. The result of the 5 years of research is presented in this thesis. Two years were spent at the experiment at Fermi National Accelerator Laboratory, where Freya learned that not all European prejudice about Americans is true. She was an officer of Fermilab's Graduate Student Association, served in Fermilab's User Executive Committee, lobbied the American congress and senate, and gave presentations and tours to high school students. While at NIKHEF, she enjoyed teaching a nuclear physics lab to second year physics students at Universiteit van Amsterdam.

Besides work, Freya has been playing hockey (on AstroTurf, not ice) at A.M.H.C. Pinoké since she was 9 years old. During her high school and university years, she contributed to the club as hockey trainer, coach and member of the admittance committee. Freya also enjoys watching live music in the small club scene, which her parents already

introduced her to at a young age. Her other hobbies are meeting her friends, reading, drawing and painting, traveling (particularly cities), listening to music and playing computer games.

Freya will continue to do particle physics at Imperial College London. She will continue work on $t\bar{t}$ physics for the DØ experiment and will also work on the higher level track trigger for the CMS experiment, due to start at CERN's Large Hadron Collider in the near future.

Acknowledgments

Een proefschrift schrijven doe je niet alleen, al voelt dat af en toe wel zo. In de vijf kalenderjaren die mijn promotie heeft geduurd, heb ik vele nieuwe vrienden gemaakt en met een heleboel mensen samengewerkt. Ere wie ere toekomt:

Traditioneel worden als eerste de promotores bedankt. Daar kan ik natuurlijk niet bij achterblijven: Marcel Demarteau en Frank Linde, jullie hebben met jullie adviezen mijn promotieonderzoek relatief gemakkelijk laten verlopen. Het is natuurlijk fantastisch dat je als je zeven uur van je ene promotor af zit, je toch nog even bij je andere kan binnenlopen! Marcel D. bedankt voor je zeer nuttige wekelijkse bezoekjes, vaak is alleen uitleggen dát iets niet werkt al genoeg om de oplossing te vinden. Tevens ook heel hartelijk bedankt voor jouw suggesties wat betreft het manuscript. Frank, bedankt voor het creeëren van een promotieplaats bij DØ, ik was tenslotte al bijna naar Nijmegen verhuisd toen jij de suggestie deed dat er ook in Amsterdam hardware-werk gedaan zou kunnen worden.

Mijn co-promotor Marcel Vreeswijk is een van de belangrijkste invloeden geweest bij de totstandkoming van dit promotiewerk. We hebben, vooral direct na mijn terugkomst uit de Verenigde Staten, zeer intensief samengewerkt, en dit leidde al snel tot resultaat. Na de intensieve samenwerking was het voor mij dan ook gelukkig niet zo lastig om zelfstandig door te werken aan de analyse toen het allemaal wat minder met je ging. Het feit dat er in de lente van 2004 al een concurrerende DØ crosssectie meting in het 'altijd moeilijke' hadronische $t\bar{t}$ kanaal lag, is daar het bewijs van. Marcel, vanzelfsprekend ook heel erg bedankt voor het lezen van mijn manuscript. Het ging misschien niet altijd precies zoals we allebei wilden, maar uiteindelijk is het toch gelukt om binnen zeer korte tijd een gestructureerd proefschrift samen te stellen. Dat hebben we goed gedaan.

Naast mijn 'echte' (co-)promotores, zou ik ook Frank Filthaut, Paul de Jong en Sijbrand de Jong willen bedanken voor hun adviezen en ondersteuning. Vooral tijdens de totstandkoming van de eerste versies van mijn all-jets analyse zijn jullie commentaren erg nuttig geweest.

When I arrived at Fermilab in the summer of 2000, I was lucky enough to work with Marian Zdrazil, Aurelio Juste and Harald Fox. I would like to thank them all for the enervating experience, it was great to get the first 10% (actually 11%!!!) of the DØ silicon detector working. My arrival at Fermilab also was a change in another way. I had to learn how to drive. Rick Jesik saved mankind by letting me practise in MJ. Thank you, the world is a safer place now!

In the following months I mainly worked on the creation of silicon monitoring software, together with Breese Quinn and Harald Fox. You made the (not so interesting) subject of mapping cables, detectors and readout cards into a database a lot more enjoyable.

Dugan O'Neil introduced me to the marvels of the DØ programming framework. My first task, locating memory leaks in wonderful d0trigsim, provided me with knowledge I needed further on in my PhD. Our cooperation led to the installation of a whole series of (relatively) complex $t\bar{t}$ multijet triggers, which I actually used in this thesis. Dugan, you provided access to a lot of knowledge that would have otherwise been incredibly difficult to obtain. Thanks for making it a bit easier!

The analysis phase at Fermilab I worked in close cooperation with a lot of people in the top group. I think there are an almost unlimited number of people that contributed something to my work, but some of you really need some extra credit: Elisabeta Shabalina, Bob Kehoe, Arnulf Quadt, Ela Barberis, Cecilia Gerber and Aurelio Juste, thanks for all the advice. Jonas Strandberg and Tobias Golling, thanks for the fruitful collaboration. I think we set an example for the way international collaboration should be done, particularly if trans-Atlantic.

De meeste tijd spendeer je toch eigenlijk in je kantoor. Dat was in de eerste helft van mijn verblijf op FNAL het nogal luidruchtige NIKHEF office in DØ portercamp 151. Vooral de zeer strategische lokatie tussen de herentoiletten, de damestoiletten en de keuken, in combinatie met de deuren van de portercamp en de naastliggende vergaderzaal die in mijn herinnering continu open stonden, hebben een onuitwisbare indruk gemaakt. Onne, Paul en Bram, volgens mij ging het eigenlijk allemaal nog relatief vlekkeloos: Eén jaar lang vier mensen op zes vierkante meter en we leven allemaal nog!

'Elk Voordeel Hep Z'n Nadeel', zoals de Verlosser placht te zeggen. Dat is zeker waar, de volgende kantoren leken een oase van rust, ruimte en gezelligheid. Marcel DeM., Paul B., Onne, Axel, Silke, Lukas en Bram, het was een genoegen met jullie samen te werken. Ik denk dat we allemaal veel aan elkaar gehad hebben, zowel qua werk als wat betreft het broodnodige inburgeren in de Verenigde Staten, toch niet per sé het gemakkelijkste wat er is. Ook Mieke en Johanna hebben daar zeker aan bijgedragen. Dank jullie allemaal!

I would also like to apologize to Andrew, Angela, Brian, Daniela, Greg, Ian, Jon, Kyle and Satish for not wanting to go to the East China Inn again. Trust me, I did the right thing for all of us, we will live longer! The daily lunch ceremony is one of the things I miss most. Thanks for your company and I think I will run into most of you again soon.

All my life I have been socially engaged in some organization. During my PhD this was mainly the GSA, the Graduate Student Association at Fermilab. Heather, Kirby, Michel and Nate: I think we did a great job, particularly considering how we managed our time. The cooperation with the Fermilab Users Committee was also enjoyable, particularly with John Conway and Robin Erbacher. I'm sure we will be together in some meeting again. See you there!

When not working I spent most of my time in the wonderful city of Chicago. Here I particularly would like to thank Rick Jesik, Lara Lasky, Beate Heinemann, Joel Goldstein, Jonathan Hays, Harald Fox, Kyle Stevenson (when he could find the meeting point) and Michele Petteni, without you it just wouldn't have been the same. It's wonderful to have concert-buddies who are willing to go to obscure music even they don't know what it is. Or try to find a good restaurant. Thank all of you for being able to just go and drink beer without having to drive, which is something you only learn to appreciate after a while of not being able to do it. When in need of a quieter note, I could always depend on my

good friend Gregory Davis. Thanks for the friendship and hospitality, both in Aurora and New Rochelle. That also counts for Madelyn, Michael, Beth and Adam!

I would also like to thank the always enigmatic Chicago Hash House Harriers, and Smell This and Full Term in particular: thank you for introducing me to a way of life I never realized existed. Particularly, I enjoyed the experience of crossing waist-deep rivers in the middle of winter, only to find a big fat 'F' on the other side. On-On to the next big event.

Back in Amsterdam I quickly managed to make my way to the also-enigmatic-but-in-a-different-way Amsterdam Hash House Harriers. Here I met so many good, open, friendly people, I will definitely miss you when I move again: Doggy Style, Chihuahua Growler, Five Pack, Paparassi, Pussy Galore, Premature Withdrawal, Wide Open, Postman Prat and (of course) Smeghead The Fornicating Physicist. Boy, I'm happy I didn't get that name! I probably forgot some here, my sincere apologies; you will be able to provide me with liquid punishment soon.

Op het NIKHEF neemt de communicatie over en weer met je collega's toch wat mij betreft een belangrijke taak in. Sterker nog, ik denk dat het een van de dingen is die NIKHEF maakt tot het instituut wat het is! De gezellige lunches en koffie/thee pauzes met Aart, Mieke, Daan B, Bram vR, Patrick, Duncan, Ivo, Paul B, Lukas, Wouter, Niels, Sasha, Paul deJ, Stan, Marcel V, Frank L, Jeroen H, Pieter H en Pieter vdB slaagden er in om het nuttige met het aangename te combineren. En laten we over de vrijdagmiddag borrels maar niet beginnen, die liepen regelmatig uit tot zaterdagmorgen borrels. Kees Huyser wil ik graag bedanken voor zijn hulp met het ontwerp van de omslag van dit proefschrift.

Tijdens mijn promotie (en daarvoor) heb ik ook met veel genoegen gehockeyd in Pinoké Dames X (voorheen XI-XIII-XVI-XVII). Dames, het was heerlijk om twee keer (het laatste halfjaar meestal maar een keer) per week te hockeyen met jullie. En ik vind ons nog steeds een van de gezelligste teams in het Amsterdamse Bos. Ik zal de TD-tjes en voornamelijk jullie missen in Londen, maar misschien kunnen we wat regelen wat betreft toernooien of zo. Ik blijf in ieder geval niet spelend lid, dus jullie horen nog van me.

De etentjes met Kirsten, Joris PZ en Joostje waren ook altijd gezellig. Het is leuk om te kijken hoe onze levens langzamerhand andere wendingen nemen, maar er blijft gelukkig toch altijd nog wel wat om over te praten. En zo hoort het ook!

Dat geldt natuurlijk ook voor Ruari, Lisa, Bente en Monica. Ja, jullie mogen in het Nederlands, tenslotte ben ik verantwoordelijk voor een deel van de inburgeringscursus. Het was altijd fijn om gezellig te lunchen in het weekend. Of 'als afleiding' uit in Amsterdam, met soms een biertje te veel. Jullie zijn schatten, en ik ben vereerd jullie tot mijn vrienden te rekenen.

When I wasn't playing hockey in weekends, I was usually visiting friends abroad. Joel, Finne, Jaap (sorry, the rest doesn't understand Dutch), Michele and Sam, it was always great to enjoy your hospitality. I hope you agree that the best way to visit cities is to visit your friends!

Voor sommige mensen is één woord genoeg: Mogge. Wist u bijvoorbeeld dat je Mogguh op een heleboel verschillende manieren kan spellen? Bram, Vins, Len, Alec, Torst, Tom, Joost, Peet, het is fijn om zeker te weten dat je elke dag in ieder geval e-mail krijgt die

gaat over de belangrijke zaken des levens. Of over de wat minder belangrijke zaken des levens. Of over niet zo belangrijke zaken. Of gewoon over het weer. Of ècht nergens over. Is dit trouwens het eerste proefschrift waar alle spammers ook met naam in staan? We spammen er wel over.

Met Len en Janna heb ik veel goede gesprekken en etentjes (met of zonder kaas) mogen hebben. Jullie waren, net zoals Joris vdH, Aart, Daan en Mark en Ellie, bijna altijd wel te porren voor een portie gitaargeweld. Vergeet niet te mailen wanneer er weer een decibel-extravaganza in de Melkweg plaats vindt, ik ben benieuwd of ze erin slagen hun record te breken.

Aan het einde van een promotie moeten de mensen die het meeste om je geven ook het meeste lijden. Sjerry, Jantje en Jet, zonder jullie steun was het allemaal een stuk moeilijker gegaan. Ook de rest van de familie wil ik bedanken: Dick, Anneke, Enid, Kees, Oma van Vlerken en Oma Blekman hebben allemaal bijgedragen aan mijn welzijn. En nu kan ik jullie zelfs af en toe zien, dat helpt vast ook. Ik blijf hier kort maar krachtig: Bedankt!

Als allerlaatste wil ik graag mijn broer en zus bedanken. Sjoerd en Myrte, ik ben heel blij dat jullie mijn paranimfen willen zijn. Na alle traumatische familiegebeurtenissen hebben we alledrie soms nog wel onze pieken en dalen, maar ik ben trots op wat jullie hebben bereikt. Ik denk dat Ineke en Henk ook trots zouden zijn geweest, op ons alle drie, want zoals jullie weten vonden zij een goed en volledig mens zijn veel belangrijker dan een of ander papiertje.